The University of Hull

Study of Scale Modelling, Verification and Control of a Heaving Point Absorber Wave Energy Converter

being a thesis submitted for the degree of Doctor of Philosophy

at the University of Hull

by

Bingyong Guo

MSc (Northwestern Polytechnical University, China)

BEng (Northwestern Polytechnical University, China)

October 2017 the thesis submitted

I would like to dedicate this thesis to my beloved and loving.

Acknowledgements

My deepest gratitude goes first and foremost to my academic supervisor, Professor Ron Patton, a respectable, responsible and resourceful scholar, who has been carefully guiding and meticulously helping me in research since I registered as a PhD student. He has led me to an interesting and promising research field with his solid background, creative mind and extensive experience in academic research. It is my honour to do research under his rigorous supervision.

I am deeply indebted to my second supervisor, Professor Jim Gilbert, for his valuable guidance, timely support and constant encouragement during my PhD research and investigation. I would like to show my special thanks to Professor Dan Parsons who has enlightened me for hydrodynamics and supplied me facilities for wave tank tests. Special thanks owe to Dr. Stuart McLelland and Mr. Brendan Murphy of the School of Environmental Sciences for their help and supervision in using the Hull University wave tank. Thanks are expressed to Dr. Antony Wilkinson, Mr. David Wright, Ms. Joanna Arnett, Mr. Steve Coopland and Mr. Stuart Butterick for their great advices for the electro-mechanical design of a $1/50$ prototype.

I also would like to thank all my colleagues of the Control and Intelligent Systems Engineering (C&ISE) research group in the School of Engineering and Computer Science at the University of Hull, Dr. Shaodong Ma, Dr. Xiaoran Feng, Mr. Zhihuo Wang, Mr. Jianglin Lan, Mr. Mustafa Abdelrahman, Ms. Siya Jin, Ms. Yanhua Liu and Mr. Shuo Shi, who have helped me with many useful discussions.

I gratefully acknowledge the financial support from the China Scholarship Council (CSC) and the University of Hull, providing me the maintenance and tuition fees for my PhD study, respectively.

Finally, a special acknowledgement owes to my family for their understanding, support and encouragement during all these years.

Abstract

This study focuses on scale modelling of a heaving Point Absorber Wave Energy Converter (PAWEC), model verification via wave tank tests and power maximisation control development. Starting from the boundary element method simulation of the wave-PAWEC interaction, linear and non-linear modelling approaches of Wave-To-Excitation-Force (W2EF), Force-To-Motion (F2M), Wave-To-Motion (W2M) are studied. To verify the proposed models, a $1/50$ scale PAWEC has been designed, simulated, constructed and tested in a wave tank under a variety of regular and irregular wave conditions. To study the coupling between the PAWEC hydrodynamics and the Power Take-Off (PTO) mechanism, a Finite Element Method (FEM) is applied to simulate and optimise a Tubular Permanent Magnet Linear Generator (TPMLG) as the PTO system and control actuator. Thus linear and non-linear Wave-To-Wire (W2W) models are proposed via combining the W2M and PTO models for the study and development of power maximisation control.

The main contributions of this study are summarised as follows:

Linear and non-linear F2M models are derived with the radiation force approximated by a finite order state-space model. The non-linear friction is modelled as the Tustin model, a summation of the Stribeck, Coloumb and damping friction forces, whilst the non-linear viscous force is simulated as the drag term in the Morison equation. Thus a non-linear F2M model is derived considering the non-linear friction and viscous forces as a correction or calibration to the linear F2M model. A wide variety of free-decay tests are conducted in the wave tank and the experimental data fit the non-linear F2M modelling results to a high degree. Further, the mechanism how these non-linear factors influence the PAWEC dynamics and energy dissipations is discussed with numerical and experimental results.

Three approaches are proposed in this thesis to approximate the wave excitation force: (i) identifying the excitation force from wave elevation, referred to as the W2EF method,

(ii) estimating the excitation force from the measurements of pressure, acceleration and displacement, referred to as the Pressure-Acceleration-Displacement-To-Excitation-Force (PAD2EF) approach and (iii) observing the excitation force via an unknown input observer, referred to as the Unknown-Input-Observation-of-Excitation-Force (UIOEF) technique. The W2EF model is integrated with the linear/non-linear F2M models to deduce linear/non-linear W2M models. A series of excitation tests are conducted under regular and irregular wave conditions to verify the W2EF model in both the time- and frequency-domains. The numerical results of the proposed W2EF model show a high accordance to the excitation test data and hence the W2EF method is valid for the $1/50$ scale PAWEC. Meanwhile, a wide range of forced-motion tests are conducted to compare the excitation force approximation results between the W2EF, PAD2EF and UIOEF approaches and to verify the linear and non-linear W2M models. Comparison of the PAWEC displacement responses between the linear/non-linear W2M models and forced-motion tests indicates that the non-linear modelling approach considering the friction and viscous forces can give more accurate PAWEC dynamic representation than the linear modelling approach.

Based on the $1/50$ scale PAWEC dimension and wave-maker conditions, a three-phase TPMLG is designed, simulated and optimised via FEM simulation with special focus on cogging force reduction. The cogging force reduction is achieved by optimise the TPMLG geometric design of the permanent magnets, slots, pole-shoe and back iron. The TPMLG is acting as the PTO mechanism and control actuator. The TPMLG is connected with the buoy rigidly and hence the coupling is achieved by the PTO force. Linear and non-linear W2W models are derived for the study of power maximisation control. To investigate the control performance on the linear and non-linear W2W models, reactive control and phase control by latching are developed numerically with electrical implementation on the TPMLG. Further, a W2W tracking control structure is proposed to achieve power maximisation and displacement constriction under both regular and irregular wave conditions.

Table of contents

List of figures xiv

List of tables xxii

List of symboles and abbreviations xxiii

List of publications xxxi

1 Introduction 1

1.1 Introduction 1

1.2 Wave energy utilisation 1

1.3 Challenges of wave energy utilisation 6

1.4 Research motivations, aim and objectives 9

1.5 Contributions and thesis layouts 13

2 Literature review 18

2.1 Introduction 18

2.2 Review of WEC systems 20

2.2.1 WEC devices 20

2.2.2 Heaving PAWEC devices . . . 22
2.3 Review of modelling approaches . . . 25
2.4 Review of control strategies . . . 28
2.5 Summary . . . 31

3 WEC linear modelling approach 33

3.1 Introduction . . . 33
3.2 Wave properties . . . 33
3.2.1 Linear wave theory . . . 34
3.2.2 Regular waves . . . 38
3.2.3 Irregular waves . . . 40
3.3 Wave-PAWEC interaction . . . 42
3.4 Linear PAWEC modelling . . . 45
3.4.1 NEMOH simulation . . . 45
3.4.2 Linear PAWEC model with frequency-determined parameters 49
3.5 Optimum condition for power maximisation . . . 54
3.5.1 Complex amplitude expressions . . . 54
3.5.2 Optimum power conversion condition . . . 57
3.6 Summary . . . 59

4 Linear and non-linear F2M modelling 61

4.1 Introduction . . . 61
4.2 Radiation force approximations . . . 61

4.2.1 Frequency-domain identification of radiation force 64
4.2.2 Time-domain identification of radiation force 65
4.2.3 Linear force-to-motion modelling 68
4.3 Non-linear force-to-motion modelling 70
4.3.1 Modelling of viscous force 70
4.3.2 Modelling of friction force 71
4.3.3 Non-linear force-to-motion modelling 72
4.4 Wave tank tests 73
4.4.1 Free-fall tests 74
4.4.2 Free-decay tests 75
4.5 Model verification 77
4.5.1 Model verification of lumped non-linear force 77
4.5.2 Displacement response comparison 80
4.5.3 Energy dissipation comparison 82
4.6 Summary and conclusion 85
4.6.1 Summary 85
4.6.2 Conclusion 86

5 Excitation force approximations 88

5.1 Introduction 88
5.2 Analytic modelling approach 89
5.3 W2EF modelling approach 90
5.3.1 Methodology 90

5.3.2 System identification of causalised kernel function 93
5.3.3 Wave prediction 94
5.4 PAD2EF modelling approach 95
5.4.1 Methodology 95
5.4.2 Pseudo-velocity measurement 96
5.5 UIOEF modelling approach 98
5.5.1 Methodology 98
5.5.2 Unknown input observer design 98
5.6 Wave-to-motion modelling 100
5.7 Results and discussion 101
5.7.1 Results of excitation tests 101
5.7.2 Results of forced-motion tests 104
5.7.3 Results of W2M modelling 108
5.7.4 Parameters of numerical simulation 111
5.8 Summary and conclusion 112
5.8.1 Summary 112
5.8.2 Conclusion 113

6 PAWEC design and wave tank tests 114

6.1 Introduction 114
6.2 Scaling problem 114
6.2.1 Froude number 114
6.2.2 Scale ratio 117

6.2.3 Design parameters 118
6.3 Mechanical design 119
6.3.1 Buoy design and sketch 119
6.3.2 Connection joints 119
6.4 Electrical design 122
6.4.1 Sensing subsystem 123
6.4.2 Power supply and circuits sketch 126
6.5 Data acquisition and signal processing 127
6.5.1 Data acquisition hardware 127
6.5.2 LABVIEW™ programming 128
6.5.3 Signal processing 131
6.6 Wave tank tests 133
6.6.1 Wave tank properties 133
6.6.2 Free-fall test procedure 138
6.6.3 Free-decay test procedure 139
6.6.4 Excitation test procedure 140
6.6.5 Forced-motion test procedure 141
6.7 Summary and Conclusion 143
6.7.1 Summary 143
6.7.2 Conclusion 144

7 TPMLG modelling **145**

7.1 Introduction 145

7.2 Reivew of power take-off systems 146
7.2.1 Hydraulic PTO systems 147
7.2.2 Direct-drive PTO systems 148
7.2.3 Elastomer PTO systems 151
7.3 TPMLG geometric design 152
7.3.1 Rated power 153
7.3.2 Initial geometric parameters 154
7.4 Finite element analysis of TPMLG 157
7.4.1 Basic equations in MAXWELL™ 158
7.4.2 Convergence verification 159
7.4.3 Cogging force reduction and design optimisation 163
7.5 TPMLG mathematical representation 173
7.5.1 State-space model of TPMLG 173
7.5.2 Design specifications 174
7.6 Wave-to-wire modelling 176
7.7 Summary and conclusion 178
7.7.1 Summary 178
7.7.2 Conclusion 179

8 Power maximisation control **180**

8.1 Introduction 180
8.2 Development of reactive control strategy 180
8.2.1 Reactive control principle 181

8.2.2 Mechanical tuning approaches 182
8.2.3 Electrical tuning approaches 191
8.3 Development of phase control by latching 197
8.3.1 Phase control principle 198
8.3.2 Electrical latching 200
8.3.3 Non-linear effects on electrical latching performance 202
8.4 W2W tracking control structure 205
8.4.1 Reference generation 207
8.4.2 Tracking control 210
8.4.3 Results and discussion 210
8.5 Summary and conclusion 214
8.5.1 Summary 214
8.5.2 Conclusion 215

9 Conclusion and future work 217
9.1 Summary 217
9.2 Contribution 219
9.3 Conclusion 220
9.4 Future work 221

References 224

Appendix A Mechanical design 242

Appendix B Electrical sketch 252

Appendix C Material properties for TPMLG design 257

List of figures

1.1 Global distribution of wave power estimated by Thorpe (1999). The wave power density is calculated based on wave front given as kW/m. 2

1.2 Aim and objectives of this study. 11

1.3 Thesis structure. 15

2.1 Classification of prevailing WEC devices based on their operating principles. 20

2.2 Examples of one-body PAs, including the Seabased buoy, AWS and CETO buoy (Eriksson, 2007; Polinder et al., 2005a; Rafiee and Fiévez, 2015). 23

2.3 Example of two-body PAs, including the PowerBuoy and Wavebob (Edwards and Mekhiche, 2013; Mouwen, 2008). 24

2.4 Wavestar in operation and protection modes (Kramer et al., 2011). . . 24

3.1 Sketch of wave parameters. 34

3.2 Sketch of a semi-submerged cylindrical buoy constrained in heave mode. 42

3.3 The principle of NEMOH simulation. 46

3.4 Convergence verification of radiation damping coefficient in NEMOH. 47

3.5 Added mass and radiation damping coefficient from NEMOH. 48

3.6 Frequency response function of the wave excitation force from NEMOH. 48

3.7 Curve-fitting results of the added mass in Eq. (3.53). 51

3.8 Curve-fitting results of the radiation damping coefficient in Eq. (3.55). 51

3.9 Curve-fitting results of the amplitude response of wave excitation force in Eq. (3.56). 52

3.10 Curve-fitting results of the phase response of wave excitation force in Eq. (3.57). 52

3.11 Electromechanical analogue. 54

4.1 The radiation IRF obtained from NEMOH simulation. 64

4.2 Comparison of added mass between NEMOH and frequency-domain identified results. 66

4.3 Comparison of radiation damping coefficient between NEMOH and frequency-domain identified results. 66

4.4 Comparison of IRFs between NEMOH and time-domain identified results. 67

4.5 Sketch of the Tustin model with continuous approximation (inset). . . 71

4.6 Free-fall tests to determine the Coulomb and damping coefficients. . . 74

4.7 Zero-crossing point to determine the Stribeck force parameters. 76

4.8 Comparison of power dissipations by the Coulomb, Stribeck and damping friction forces and viscous force. 78

4.9 Comparison of the lumped non-linear force between the measured and simulated data. 79

4.10 Normalised displacement response comparison between numerical and experimental results of a free-decay test with initial displacement -0.20 m. 81

4.11 Power dissipation comparison among the dissipative forces of free-decay tests with initial displacements of -3 cm, -8 cm and -18 cm. . 83

4.12 Dissipated energy comparison among the dissipative forces. 85

5.1 Schematic diagram of the W2EF modelling approach. 90

5.2 Comparison of the excitation force IRFs. 91

5.3 Goodness of fit with varying causalisation time t_c and system order number n. 93

5.4 Comparison of wave elevations between the experimental measurement and the numerical prediction with an AR model. 95

5.5 Schematic diagram of the PAD2EF modelling approach. 96

5.6 Pseudo-velocity estimations. 97

5.7 Schematic diagram of the UIOEF modelling approach. 98

5.8 W2M modelling approach. 100

5.9 Comparison of the excitation forces between the measurement and the estimation via the W2EF method. 102

5.10 Amplitude response comparison between the excitation tests, NEMOH computations and W2EF simulations. 103

5.11 Phase response comparison between the excitation tests, NEMOH computations and W2EF simulations. 104

5.12 Comparison of the excitation force between the excitation tests and the W2EF modelling under the irregular wave conditions. 105

5.13 Comparison of the excitation force approximations in a forced-motion test under regular wave. 106

5.14 Comparison of the excitation force approximations in a forced-motion test under irregular wave. 107

5.15 Comparison of the displacement between the linear, non-linear W2M models and forced-motion tests. 108

5.16 Comparison of the RAOs between the linear, non-linear simulations and forced-motion tests. 109

5.17 Displacement comparison among the linear/non-linear W2M simulations and experimental data of a forced-motion test under irregular wave. 110

6.1 Scaling down sketch of the experimental buoy. 118

6.2 Impression view of the 1/50 scaled PAWEC in SOLIDWORKS®. . . . 120

6.3 Five pressure sensors installed at the bottom of the buoy. 120

6.4 Impression view of the top component in SOLIDWORKS®. 121

6.5 Linear bearings and their connection to the wave tank gantry. 121

6.6 The connection of the LVDT to the PAWEC and wave tank gantry. . . 122

6.7 The sealing of the pressure sensors. 124

6.8 Wave gauge installation for wave tank tests. 126

6.9 Calibration procedure and results of the LVDT. 128

6.10 Calibration procedure of the accelerometer. 129

6.11 Data acquisition GUI coded in LABVIEW™. 131

6.12 Synchronisation of the two DAQ subsystems. 132

6.13 Comparison of the pressure measurements between the filtered and unfiltered data from PS2. 133

6.14 Sketch of the wave tank, the installation of the 1/50 scale prototype and the configuration of the sensing subsystem. 134

6.15 Wave elevation and its harmonic approximation of numerical simulation according to Eq. (6.16). 136

6.16 Wave elevation collected from the wave tank tests (WG2) and its harmonic approximation. 137

6.17 Spectrum verification of the numerical and experimental wave elevations via the PM spectrum comparison among the theoretical PM spectrum in Eq. (3.27) and estimated spectrum from numerical wave elevation in Eq. (6.16) and the experimental data of collected from WG2. 138

6.18 Diagrammatic sketch of the free-fall tests. 139

6.19 Diagrammatic sketch of the free-decay tests. 140

6.20 Diagrammatic sketch of the excitation tests. 140

6.21 Diagrammatic sketch of the forced-motion tests. 141

7.1 The Wells, the Denniss-Auld and the impulse turbines (López et al., 2013) are applied as PTO mechanisms for OWC devices. Conventional rotating generators are driven by these turbines to produce electricity. 146

7.2 Water turbines for the over-topping devices, including the Pelton, Kaplan and Francis turbines (López et al., 2013). 147

7.3 Hydraulic PTO systems with the variable pressure type on the left and the constant pressure type on the right (Costello et al., 2011). 148

7.4 Direct-drive PTO system for the AWS device (Prado and Polinder, 2011). 149

7.5 PTO system with a gear box and rotating machine (Rhinefrank et al., 2012). 150

7.6 DEGs applied as PTO systems for the PA and OWC types WEC devices (Chiba et al., 2010; Vertechy et al., 2013). 152

7.7 Comparison of the working principles between the PMSM and TPMLG. 154

7.8 TPMLG geometric structure. 155

7.9 Convergence tests of phase A induced voltages. 160

7.10 Convergence tests of the cogging forces. 161

7.11 Magnet flux density distribution in the air gap for the initial design in Table 7.2. 161

7.12 Induced phase voltages for the initial design in Table 7.2. 162

7.13 Cogging force for the initial design in Table 7.2. 162

7.14 Co-energy distribution of the TPMLG. 164

7.15 Cogging force reduction via pole-shoe parametric analysis of L_c. . . . 165

7.16 Pole-shoe parametric analysis of W_t and W_c. 166

7.17 Pole-shoe parametric analysis of H_0 and H_1. 166

7.18 Permanent magnet parametric analysis of T_{pm} and L_{pm}. 167

7.19 Auxiliary teeth parametric analysis of T_a and T_{ae}. 168

7.20 Back-iron/yoke parametric analysis of T_{bi} and T_y. 168

7.21 Cost function varies against the optimisation evaluations. 170

7.22 Comparison of the induced phase voltages between the initial and optimised designs. 171

7.23 Comparison of the cogging force between the initial and optimised designs. 171

7.24 Cogging force and its fitted formulation of the optimised design. . . . 172

7.25 Sketch of the TPMLG *dq-axis* model. 173

7.26 Comparison of the induced phase voltages between the MAXWELL™and MATLAB® simulations for $v_r = 0.24$ m/s. 175

7.27 Comparison of the induced phase voltages between the MAXWELL™and MATLAB® simulations for $v_r = 0.34\sin(\pi t)$ m/s 176

7.28 W2W modelling approach. 178

8.1 Reactive control performance via mechanical resistance tuning. 183

8.2 Reactive control performance via mechanical impedance tuning. . . . 185

8.3 Reactive control performance via mechanical impedance tuning considering displacement constraints. 187

8.4 Mass tuning approach. 188

8.5 Average density of the PAWEC with tuned mass. 189

8.6 Required stiffness to achieve resonance via mechanical impedance tuning. 190

8.7 Relationship of parameters in the electro-mechanical analogue. 192

8.8 Electrical resistance tuning performance. 194

8.9 Electrical impedance tuning performance. 195

8.10 Electrical impedance tuning performance considering the displacement constraints. 196

8.11 Control performance comparison between the mechanical and electrical latching implementations in terms of displacement, velocity and captured energy. 201

8.12 *Dq-axis* currents evaluations for the electrical latching implementation. 202

8.13 Comparison of power conversion efficiencies between the linear and non-linear models by electrical latching. 204

8.14 Comparison of the buoy displacements between the linear and non-linear models by electrical latching. The constraints are selected as 0.28 m, which is half of the buoy height. 205

8.15 A W2W tracking control structure. 206

8.16 Real-time estimates of wave excitation force instantaneous magnitude and frequency via the TEO method. 209

8.17 Decoupling of *dq-axis* currents. 211

8.18 W2W tracking control performance based on linear/non-linear W2W models under regular wave conditions. 211

8.19 W2W tracking control performance based on linear/non-linear W2W models under irregular wave condition of $H_s = 0.06$ m and $f_p = 0.80$ Hz. 212

8.20 W2W tracking control performance based on linear/non-linear W2W models under irregular wave condition of $H_s = 0.11$ m and $f_p = 0.60$ Hz. 213

8.21 W2W tracking control performance based on linear/non-linear W2W models under irregular wave condition of $H_s = 0.25$ m and $f_p = 0.40$ Hz. 214

A.1 Sketch of the bottom component. 243

A.2 Sketch of the end-protection component. 244

A.3 Sketch of the hex-bar1 component. 245

A.4 Sketch of the hex-bar2 component. 246

A.5 Sketch of the lid component. 247

A.6 Sketch of the disc component. 248

A.7 Sketch of the side component. 249

A.8 Sketch of the top component. 250

A.9 Sketch of the circular-bar component. 251

B.1 Sketch of the power supply board. 253

B.2 Sketch of the interface board. 254

B.3 Sketch of the connectors. 255

B.4 Connection of the sensing system. 256

C.1 B-H curve of the NdFeB35 material. 258

C.2 B-H curve of the B50A470 material. 259

C.3 AWG wire electro-mechanical standard. 260

List of tables

1.1 Global wave power installed and consented capacities (OES, 2014). . 4

4.1 Parameters of the friction/viscous models in Eqs. (4.35) and (4.29). . 77

4.2 Normalised modelling error of the lumped non-linear force. 80

4.3 Modelling goodness of the non-linear model referred to the experimental data. 82

6.1 Orders of magnitude of the inertial, gravitational and viscous forces. . 116

6.2 Design parameters of the scaled down prototype. 118

6.3 Calibration results on July 4th, 2016. 130

7.1 Maximum average absorbed power under regular/irregular waves. . . 153

7.2 TPMLG initial design parameters. 157

7.3 TPMLG mesh convergence verification with $t = 0 : 0.005 : 0.3$ s and $v = 0.24$ m/s. 160

7.4 TPMLG parameters for the design optimisation. 170

7.5 Parameters for cogging force fitting. 172

7.6 TPMLG electromagnetism parameters 175

A.1 List of mechanical components. 242

List of symboles and abbreviations

Roman Symbols

FN	Froude number
H_m	Modal wave height of deign sea state
H_e	Excitation force FRF
I_d, I_q	*Dq-axis* currents of the TPMLG
K_e	Back electromotive force constant of the TPMLG
K_f	Thrust force constant of the TPMLG
L_d, L_q	*Dq-axis* inductances of the TPMLG
P_g	Power captured by the TPMLG
R_s	Synchronising resistance of the TPMLG
t_c	Causalisation time
T_m	Modal wave period of deign sea state
U_d, U_q	*Dq-axis* voltages of the TPMLG
$\ddot{z}$	Vertical acceleration
$\dot{z}$	Vertical velocity
$\hat{F}_e$	Complex amplitude of wave excitation force
$\hat{F}_r$	Complex amplitude of radiation force
$\hat{F}_{pto}$	Complex amplitude of power take-off force

$\hat{v}$	Complex amplitude of buoy velocity
$\hat{z}$	Complex amplitude of buoy displacement
$\vec{n}$	Unit normal vector on wet surface
$\vec{u}$	Solid body moving velocity
$\vec{v}$	Fluid velocity
a_m	Measured buoy acceleration
A_∞	Added mass at infinite frequency
A_{fe}	Amplitude-frequency response of wave excitation force
b	Buoy height
C_d	Viscous coefficient
d	Draught, half of the buoy height
$d_{c,max}$	Theoretical maximum power capture width
E_c	Energy dissipated by Coulomb friction force
E_d	Energy dissipated by damping friction force
E_p	Potential energy stored in the system at the free-decay releasing time
E_r	Energy dissipated by radiation force
E_s	Energy dissipated by Stribeck friction force
E_v	Energy dissipated by viscous force
E_{rms}	Rated induced phase voltage
f	Wave frequency
f_d, C_f	Damping friction force and its coefficient
f_f	Non-linear total friction force
f_n	Natural frequency of the PAWEC device
f_v	Non-linear viscous force

F_{cog}	Cogging force
f_c, F_c	Coulomb friction force and its coefficient
F_e	Wave excitation force
$f_{f,m}$	Pseudo measured friction force during free-fall tests
F_f	Friction force
F_{hs}	Hydrostatic force
$f_{ln,m}$	Pseudo measured lumped non-linear force during free-decay tests
f_{ln}	Lumped non-linear force $f_{ln}(t,x) = f_v(t,x) + f_f(t,x)$
F_{pto}	Power take-off force
F_r	Radiation force
$F_r^{'}$	Convolution term of the radiation force
$f_{s,g}$	Synchronising frequency of the TPMLG
f_s, F_s, C_s	Stribeck friction force and its coefficients
F_v	Viscous force
g	Gravity constant
$G_{fit,r}$	Goodness of fit for radiation identification
G_{fit}	Goodness of fit function of curve fit
H	Wave height
h	Water depth
H_s	Significant wave height of irregular wave
I_{rms}	Rated phase current
J	Power transform
k	Wave number
k_e, $k_{e,c}$	Excitation force IRF and its causalised formation

K_r	Radiation force FRF
k_r	Radiation force IRF
K_{hs}	Hydrostatic stiffness
K_{pto}	Spring stiffness of power take-off system
M_a	Added mass
M_b	Mass of the buoy
m_n	n^{th} order spectral moment
M_{pto}	Mass of power take-off system
p	Pressure
P_c	Power dissipated by Coulomb friction force
P_d	Power dissipated by damping friction force
P_e	Captured power from the excitation force to the PAWEC motion
P_r	Radiated power due to the PAWEC oscillation
P_s	Power dissipated by Stribeck friction force
P_v	Power dissipated by viscous force
P_w	Wave power passing by the buoy
P_{pto}	Converted power by the power take-off mechanism
R	Mechanical resistance
r	Buoy radius
R_r	Radiation damping coefficient
R_{e2m}	Mechanical equivalent of the electrical resistance
R_{m2e}	Electrical equivalent of the mechanical resistance
R_{pto}	Damping coefficient of power take-off system
T	Wave period

T_e	Energy period of irregular wave
t_r	Releasing time of free-decay tests
t_s	Settling time of free-decay tests
v_m	Measured buoy velocity
X	Mechanical reactance
X_{e2m}	Mechanical equivalent of the electrical reactance
X_{m2e}	Electrical equivalent of the mechanical reactance
Z	Mechanical impedance defined as $\hat{F}_e/\hat{v}$
z	Vertical displacement
z_i	Initial displacement for free-decay tests
Z_{e2m}	Mechanical equivalent of the electrical impedance
Z_i	Internal PAWEC mechanical impedance
Z_{m2e}	Electrical equivalent of the mechanical impedance
Z_{pto}	Mechanical impedance of the power take-off mechanism

Greek Symbols

η_p	Predicted wave elevation of t_c in advance
ω_e	Electrical angular velocity of the TPMLG
ϕ_{pm}	Flux linkage constant referred to permanent magnets of the TPMLG
η	Wave elevation
η_c	W2W efficiency defined by capture width
$\hat{\eta}$	Complex amplitude of wave elevation
λ	Wave length
∇	Vector differential operator
∇^2	Laplace operator

ν	Kinematic viscosity coefficient
ω	Wave angular frequency
ϕ	Fluid velocity potential function
ϕ_w	Initial phase angular of harmonic waves
ϕ_{fe}	Phase-frequency response of wave excitation force
ρ	Water density, 1000 $\mathrm{kg/m^3}$
τ_p	Pole pitch of the TPMLG
τ_s	Slot pitch of the TPMLG

Other Symbols

$\bar{X}$	Mean value of X
$\tilde{X}$	Estimation of X
$\Re(X)$	Real operation of X
$\tanh(X)$	Hyperbolic tangent function of X
$S(\omega)$, $S(f)$	PM spectrum
$X * Y$	Convolution operation between X and Y
X^*	Complex-conjugate operation of X

Acronyms / Abbreviations

Acc	Accelerometer
AR	Auto-Regressive
AWS	Archimedes Wave Swing
BEM	Boundary Element Method
BPF	Band-Pass Filter
CFD	Computational Fluid Dynamic
CoE	Cost of Energy

DAQ	Data AcQuisition
DEG	Dielectric Elastomer Generator
DoF	Dimension of Freedom
F2M	Force-To-Motion
FEM	Finite Element Method
FRF	Frequency Response Function
FSI	Fluid-Structure Interaction
FTC	Fault Tolerant Control
FVR	Force-to-Velocity Ratio
GUI	Graphic User Interface
IRF	Impulse Response Function
LCoE	Levelised Cost of Energy
LVDT	Linear Variable Displacement Transducer
MSD	Mass-Spring-Damper
NMSE	Normalised Mean Square-Error
O&M	Operation and Maintenance
OES	Ocean Energy Systems, a technology collaboration programme operating under the framework of the International Energy Agency (IEA)
OWC	Oscillating Water Column
PAD2EF	Pressure-Acceleration-Displacement-To-Excitation-Force
PA	Point Absorber
PAWEC	Point Absorber Wave Energy Converter
PMLG	Permanent Magnet Linear Generator
PM	Pierson-Moskowitz

PMSM	Permanent Magnet Synchronous Machine
PS	Pressure Sensor
PTO	Power Take-Off
R&D	Research and Development
RAO	Response Amplitude Operation
RLC	Resistance-Inductance-Capacitance
RMS	Root-Mean Square
TPMLG	Tubular Permanent Magnet Linear Generator
UIOEF	Unknown-Input-Observation-of-Excitation-Force
UIO	Unknown Input Observe
VPP	Peak-to-Peak Value
W2EF	Wave-To-Excitation-Force
W2M	Wave-To-Motion
W2W	Wave-To-Wire
WEC	Wave Energy Converter
WG	Wave Gauge

List of publications

1. **B. Guo**, R. Patton, M. Abdelrahman and J. Lan (2016). A continuous control approach to point absorber wave energy conversion. Proc. UKACC on Control, Queen's University, Belfast, UK, IEEE.

2. S. Jin, **B. Guo**, R. Patton, J. Gilbert and M. Abdelrahman (2016). Non-linear analysis of a point absorber wave energy converter. Proc. International Conference on Offshore Renewable Energy, Glasgow, UK.

3. M. Abdelrahman, R. Patton, **B. Guo** and J. Lan (2016). Estimation of wave excitation force for wave energy converters. Proc. SysTol, Barcelona, Spain, IEEE.

4. **B. Guo**, R. Patton (2017). Non-linear viscous and friction effects on a heaving point absorber dynamics and latching control performance. IFAC World Congress, Toulouse, France.

5. **B. Guo**, R. Patton and S. Jin (2017). Identification and validation of excitation force for a heaving point absorber wave energy converter. Proc. EWTEC, Cork, Ireland.

6. **B. Guo**, R. Patton, S. Jin, J. Gilbert and D. Parsons (2016). Non-linear modelling and verification of a heaving point absorber for wave energy conversion. IEEE Transactions on Sustainable Energy. DOI: 10.1109/TSTE.2017.2741341.

7. **B. Guo**, R. Patton, S. Jin and J. Lan (2017). Numerical and experimental studies of excitation force approximations for wave energy conversion. Renewable Energy. **Submitted**.

8. S. Jin, R. Patton and **B. Guo** (2017). Viscosity influence on the non-linear hydrodynamics of a designed point absorber wave energy converter validated by simulations and experiments. Renewable Energy. **Submitted**.

Chapter 1

Introduction

1.1 Introduction

With the emergence of fossil fuel crisis and global attention on climate change and CO_2 emissions, renewable energy has been becoming an important research area and researchers have been turning to the value of harnessing power from ocean waves. This Chapter expresses the research background of this thesis. Section 1.2 describes the global status of wave energy utilisation. Section 1.3 emphasises current technical challenges of wave energy conversion. Based on the promising potentials and existing barriers, research motivations, aim and objectives of this work are outlined in Section 1.4. The contributions and layouts of this thesis are given in Section 1.5.

1.2 Wave energy utilisation

Wave energy is a concentrated form of wind energy, or ultimately solar energy (McCormick, 1981). An example given by McCormick (1981) is "at a latitude 15°N (northeast trades) the solar insolation is 0.17 kW/m^2. the average wind speed over ocean may be approximately 10 m/s and thus have a power intensity of 0.58 kW/m^2. The average wave generated by this wind has a power intensity of 8.42 kW/m^2." Compared with the utilisation of other renewable energy resources, such as solar, wind and biomass energy, wave energy conversion techniques are immature but have promising potential for renewable energy harvesting, due to their favourable characteristics: (i)

the reserve of wave energy is huge; (ii) wave energy is widely distributed worldwide (Thorpe, 1999); (iii) ocean waves provide higher power density than wind and solar power (McCormick, 1981); (iv) ocean waves can offer more stable and continuous power production than other renewable energy resources and (v) less environmental impact is caused by wave energy conversion (Drew et al., 2009; Ilyas et al., 2014; López et al., 2013).

Commercial and industrial applications of Wave Energy Converter (WEC) technologies are rather immature and raw, probably due to (i) higher Cost of Energy (CoE) compared with other energy resources (Carbon-Trust, 2011), (ii) difficulties in WEC modelling, design, construction, installation, maintenance and optimal control strategies (Drew et al., 2009; Falcão, 2010; McCormick, 1981), and (iii) constraints of wave power distribution, extreme sea conditions, and WEC physical dimensions (Carbon-Trust, 2011). This Section outlines the state of art in global wave energy distribution and capacity installation with emphasis on the Research and Development (R&D) activities.

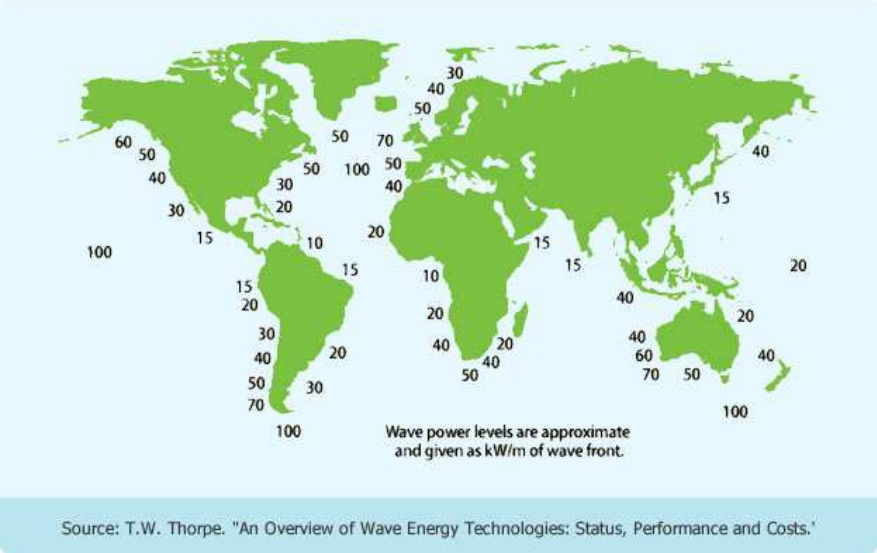

Fig. 1.1 Global distribution of wave power estimated by Thorpe (1999). The wave power density is calculated based on wave front given as kW/m.

The global distribution of wave energy is studied by Thorpe (1999), shown in Fig. 1.1. Among the theoretical estimate of the global wave power, the applicable part is defined as *practical wave power*, considering the constraints of power density levels, environmental influences and extreme sea conditions. According to the estimation by Gunn and Stock-Williams (2012); WEC-Commission (1993)[1], the practical wave power

[1] World Energy Council (WEC).

resource worldwide is more than 2 TW. The wave energy distribution shown in Fig. 1.1 indicates that wave power is not evenly distributed globally but is concentrated within the latitudes between 30° and 60° in both northern and southern hemispheres, due to strong prevailing western wind. The wave power density is computed according to wave front with the unit of kW/m.

The first upsurge of wave energy deployment happened during the 1970s and 1980s after the fossil fuel crisis (Clément et al., 2002; Evans, 1981; Falnes, 2007). On this subject, R&D work abated in the 1990s when the fuel price dropped dramatically but once again became active after the agreement of the Kyoto Protocol in 1997 (Falcão, 2010; Vantorre et al., 2004). For the past 20 years, wave energy capture has been a "hot-spot" for academic research and industrial developments and hence various types of WEC devices bloom up with innovations of WEC concepts, components, subsystems and material (WES, 2017b). As summarised by OES (2014)[2], recently installed and planned wave capacity is described in Table 1.1. From the comparison of installed and consented wave capacities, it is fair to say that R&D activities of wave energy are animated in European countries and UK is in a leading position for wave power capture.

Up to date, remarks and achievements are listed out, taking country as unit, as:

- **Belgium**: The FlanSea I WEC achieved a high conversion efficiency up to 81% in the North Sea test. Undertaking work is to develop FlanSea II with larger scale and alternative Power Take-Off (PTO) machine (De Koker et al., 2016a,b; Pelfrene, 2011).

- **China**: Three sea test sites are of under-construction in Weihai, Hangzhou and Guanzhou cities. Several WEC devices have been tested in open sea, including the Sharp Eagle I (efficiency 16.76%), Jida I (efficiency 15%), FLB (efficiency 14%) and Haiyuan I (efficiency 16.4%) (OES, 2014, 2015; Wang et al., 2011). The wave power density is quite low in the Chinese sea. The annual average of power density is about 1.5 kW/m (Zhou et al., 2015).

- **Denmark**: The 1.5 MW Wave Dragon (Kaźmierkowski et al., 2008) and the 1/10 Crestwing device (Kofoed and Antonishen, 2009) have been tested as demonstration prototypes. Resent projects emphasis on the development of digital hydraulic PTO mechanism for the WaveStar and *negative spring* techniques for

[2]The Ocean Energy System Technology Collaboration Programme (OES) is an intergovernmental collaboration between countries, which operates under framework established by the International Energy Agency in Paris.

Table 1.1 Global wave power installed and consented capacities (OES, 2014).

Country	**Installed Capacity** (kW)	**Consented Capacity** (kW)
Belgium	N/A	Up to 20000
China	350	2860
Denmark	N/A	115
Norway	200	N/A
Portugal	700	5000
Republic of Korea	500	500
Singapore	16	N/A
Spain	296	300
Sweden	180	10400-10600
USA	N/A	1365
UK	3730	40000
Total	**5972**	**up to 80540**

generic WEC devices (Hansen and Kramer, 2011; Kramer et al., 2011; Sinha et al., 2016). The Wavestar has been tested with 2 paddles in open sea in 2009 and is heading to its full scale prototype test.

- **France**: Great work has been done by the Hydrodynamic and the Ocean Engineering Group in the Université de Nantes. A pitch/surge device called SEAREV has been simulated and tested in a wave tank with sub-optimum control strategies (latching and declutching) (Babarit et al., 2009; Ruellan et al., 2010). An open source Boundary Element Method (BEM) package, called NEMOH, is developed and released by the Université de Nantes to compute the first order wave load on offshore structures (Babarit and Delhommeau, 2015).

- **Ireland**: There are two sea test sites, the Galway Bay Quarter Scale Test Site and the Atlantic Marine Energy Test Site (SEAI, 2017). A $1/4$ scale model, Wavebob, was tested in the Galway Bay in 2006 (Weber et al., 2009). Lots of R&D work, including numerical and experimental modelling, simulation and control system design, has been conducted in the Centre for Ocean Energy Research at National University Ireland Maynooth (COER, 2017).

- **Japan**: Japan has a lack of conventional energy resources and has a long coast line of 350,000 km (Bricker et al., 2017). Wave energy conversion research work dates back to the early 1940s and the Oscillating Water Column (OWC) type WEC was first invented by Yoshio Masuda (Falnes, 2007). Up to date, there are more than one thousand near-shore OWC devices have been installed for navigation. Current work focuses on OWC devices and the Pendulors. An offshore floating OWC device, the "Mighty Whale", is still under operation now (Clément et al., 2002; Washio et al., 2001).

- **Norway**: There are two sea test sites, the Runde Environmental Centre (REC) and the Stade Towing Tank (OES, 2014, 2015). Norwegian University of Science and Technology (NTNU) is one of the most active academic groups in ocean energy research. The Havkraft Wave Energy Converter (H-WEC) has been tested in the open sea (Ovadia, 1995).

- **Portugal**: The devices, the Pico (OWC type) and the WaveRoller (terminator type), have been tested in the sea (Brito-Melo et al., 2008; Neumann et al., 2007). There are two famous and active research groups, the Institute of Mechanical Engineering at the University of Lisbon and the Centre for Marine Technology and Engineering, focusing on the marine energy harnessing.

- **Sweden**: The applicable resource surrounding the Swedish waters varies from 5 to 10 TWh/year. The IPS buoy is the first full scale Point Absorber Wave Energy Converter (PAWEC) that has been tested in open sea with an efficiency fluctuating from 30% to 35% (Clément et al., 2002). The world largest 10 MW offshore wave farm is under construction and test with the Sea-Based type PAWECs (OES, 2014, 2015).

- **USA**: There are four sea test sites, including the Navy's Wave Energy Test Site (WETS), the Pacific Marine Energy centre-South Energy Test Site (PMEC-SETS), the California Wave Energy Test Centre (CWETC) and the National Marine Renewable Energy Centre (NMREC) (OES, 2014, 2015). Several projects have been conducted in the Sandia National Laboratories (SNL), the National Renewable Energy Laboratory (NREL), the Pacific Northwest National Laboratory (PNNL) and the Oak Ridge National Laboratory (ORNL) (OES, 2014, 2015). The devices, the TDU2 and the Azura, were tested in 2014 and 2015, respectively.

- **UK**: There are three sea test sites, including the European Marine Energy Centre (EMEC), the WaveHub test site and the Falmouth Bay Test (FaBTest) site (EMEC,

2016; FaBTest, 2016; WaveHub, 2016). Several pre-commercial devices have been tested in open sea, including the Oyster 800, the P2-001, the P2-002, the Oceanus and the Penguin (EMEC, 2016; OES, 2014; O'Hagan et al., 2016). Resent R&D programmes give priority to the CoE reduction, novel PTO mechanism and wave farm operation (EPSRC, 2015).

1.3 Challenges of wave energy utilisation

For industrial application, CoE is the most significant factor which impedes the commercial development and operation of WEC systems. Based on the statistical report from DECC (2013), the electricity generation costs by fuel types are 8 p/kWh for gas, 10-12 p/kWh for coal, 8 p/kWh for nuclear power, 11-12 p/kWh for biomass conversion, 16-17 p/kWh for solar energy and 9-13 p/kWh for wind power [3]. However, according to the marine energy assessment report by Carbon-Trust (2011), offshore wave CoE is about 38-48 p/kWh and tidal stream CoE is around 29-33 p/kWh [4]. Hence the CoE for offshore wave energy is about 5 times of the CoE for conventional energy resources and the CoE reduction corresponding to wave energy still has a long way to go.

The main factors resulting in high CoE of wave energy include the high installation cost in offshore environment, high Operation and Maintenance (O&M) cost due to extreme sea states and low overall energy conversion efficiency due to untapped WEC technology. Hence, technical innovations, such as innovative WEC concepts, subsystems, components and materials, show great potential to overcome the barriers mentioned above and hence for CoE reduction. Carbon-Trust (2011) has planned the innovation roadmap to reduce offshore energy CoE from current high level to a competitive level by 2020. Carbon-Trust (2011) concludes that, with continuous progress on technology innovation, wave power CoE can come down to 18 p/kWh by 2020 (estimated with 800 MW of installed capacity), providing competitive CoE of ocean renewable energy to power consumers.

The reduction of wave energy CoE mainly depends on two factors, the installation capacity and the technology innovation which overlap and produce mutual benefit. As to the technology issues, R&D challenges are (EPSRC, 2015; Ilyas et al., 2014):

[3] The CoE is cumulated with 10% discount rate in DECC (2013).
[4] The CoE is cumulated with 15% discount rate in Carbon-Trust (2011).

- **Modelling of Fluid-Structure Interaction (FSI)**: Linear numerical modelling methods for ship motion and sea-keeping are commonly adopted to predict WEC hydrodynamics. However, linear methods may not satisfy the requirements of WEC motion prediction. For ship design and see-keeping applications, the structure is optimised to avoid resonance and it is easy to achieve with a huge characteristic dimension. However, in contrast to ship systems, a typical WEC structure has a much smaller dimension and its motion is maximised by control. In operation close to resonance, the often used linear assumptions cannot be satisfied any more for WEC hydrodynamics and in so doing will exaggerate WEC motion and hence give incorrect prediction of captured power. In this situation, non-linear Computational Fluid Dynamic (CFD) methods are necessary and required to provide accurate approximations of WEC hydrodynamics. However, CFD methods are computationally expensive and their results are inconvenient for real-time control system design. The CFD results are not intuitive and call for sophisticated post-process to give more general representations. In control studies, the model is generally presented in the transfer function or state-space formula. Hence, system identification and parameter estimation methods are applied in this work to derive more applicable and generally used mathematical models considering non-linear phenomena in a transfer function or state-space formulation, as a precursor to control system development.

- **Validation of Numerical Models**: Validation of numerical models is essential before PTO and control system studies can be conducted. The performance of variable WEC devices is not fully proven and understood since there are few devices tested in the open sea with a full scale prototype. For offshore devices, scale prototype tank tests and full scale model sea trials are especially essential to gain certainty of WEC behaviour and to gain confidence for control systems design. In this thesis, a 1/50 scale PAWEC is tested in a wave tank to validate the proposed linear and non-linear numerical modelling approaches of wave-PAWEC interaction.

- **Improvement of Energy Conversion Efficiency**: Due to the irregularity of sea waves (such as irregularities of the wave amplitude, phase, frequency and direction), inferior energy conversion performance of WEC devices has been impeding the industrial and commercial applications. To improve the energy capture, resonance theory has been proposed to maximise the power output for WEC devices operating in harmonic waves (Evans, 1976, 1981). Nevertheless, in random sea, the wave frequency, height, direction and phase vary slowly and

continuously, which makes the resonance phenomenon hard to achieve without properly designed control systems. In random sea states, control systems are necessary to tune the WEC devices to the incoming wave adaptively for real-time WEC power maximisation. The control systems are also vital to make sure that the WEC devices can survive under extreme sea conditions and in the presence of faults. Thus, enhanced efficiency will lead to dramatical reduction of CoE. Hence in this work, power maximisation control strategies are adopted to achieve WEC devices resonance under conditions of both regular and irregular waves.

- **Reduction of O&M cost**: It is estimated by Carbon-Trust (2011) that the O&M cost is about one quarter of the Levelised Cost of Energy (LCoE). To achieve O&M cost reduction, control technologies can be applied on single device or array levels, to improve operation performance under moderate sea sates for the reduction of operation cost and to decrease manual intervention under extreme sea conditions for the reduction of maintenance cost. Additionally, appropriately designed control system has great potential to improve the survivability and reliability of WEC devices under storm weather and hence to achieve low life-time O&M costs.

- **Elevation of Survivability and Reliability**: Extreme sea conditions, such as the Tsunami, severe storm, generate very rough sea surfaces and huge waves with consequently giant hydrodynamic forces acting on WEC devices. These extreme conditions may destroy the WEC systems and hence survivability and reliability are extremely important for successful proliferation of wave energy installation. The subject of Fault Tolerant Control (FTC) has large potential in helping to mitigate the damaging effects of extreme environment as well as device components faults to elevate the WEC survivability and reliability for the purpose of life-time CoE reduction. Hence, properly designed control methods can reduce the life-time CoE by (i) improving the overall energy conversion efficiency via power maximisation control under moderate sea states and (ii) reducing system or component failures via advanced control methods under extreme sea states to handle system or component constraints.

- **Novel Components, Subsystems and Materials**: Novel components, subsystems and material are needed to maintain WEC performance and to reduce the LCoE. These may include novel design of PTO mechanisms (such as permanent magnet linear generators, digital hydrophilic systems and etc.), built-in control systems, power regulators (e.g. flexible AC transmission systems for grid connec-

tion) and etc. These components or subsystems are critical factors to achieve CoE reduction for the next generation of WEC devices. Another innovative concept is the “co-design” idea, which tries to make a compromise among the hydrodynamic design/optimisation, PTO design/optimisation, power electronics circuits design, built-in control system development and the cost of WEC system cost. High efficiency does not always mean low CoE. Hence the co-design concept has a great potential to promote the commercialisation process of WEC technologies.

This thesis focuses on linear and non-linear numerical modelling approaches of wave-WEC interaction, model verification via wave tank tests and WEC power maximisation control strategies development based on a 1/50 cylindrical heaving PAWEC to overcome some of the challenges detailed above. This study addresses the PAWEC behaviour validation to derive convenient and straightforward non-linear numerical models for the FSI analysis and control system design. Based on the verified non-linear models, power maximisation control strategies are investigated in this study.

1.4 Research motivations, aim and objectives

As described in Section 1.2, the global reserve of wave energy is huge and showing promising potential for electricity generation without green house gas emissions. This is one of the main motivations. As summarised in Section 1.3, some technical challenges to some extent impede commercial development of wave energy conversion. One main challenge is that the subject of control engineering is little understood by wave energy experts. It is now well known that modern control strategies are essential to tune a WEC device close to resonance for power maximisation, hence reducing the CoE. Thus wave energy conversion can be said to be a "fertile" domain of R&D for control applications (WES, 2017a). Hence, another motivation of this thesis is to provide a suitable modelling framework for facilitating the use of well chosen optimising control.

Whilst wave energy capture is a multi-discipline topic involving mechanical, civil, electrical and control engineering as well as environmental and material sciences, there are "gaps" between different subjects since the researchers from different backgrounds tend not to communicate effectively. For example, experts from mechanical engineering background (and to some extend civil engineering) tend to focus on numerical and experimental WEC hydrodynamics, their results are often not in suitable format for the development of control systems. On the other hand people working in the

control community prefer to use numerical models based on either frequency-domain representations (transfer functions) or time-domain formulations (state-space models). However, most of these models are simplified or linearised with some theoretical or ideal assumptions and very few are verified experimentally. The numerical models used in hydrodynamics are not the same as those used in control system design and hence a knowledge gap is present when these disciplines attempt to interact. Similar discipline gaps also exist when mechanical, electrical and control systems engineers try to work together within a system engineering framework. In this research an attempt is made in the Control and Intelligent Systems Engineering (C&ISE) research group at Hull to be immersed in a combination of hydrodynamics, electrical technology and control science. This is achieved in this project through the modelling, construction and "co-design" development of a benchmark for the $1/50$ PAWEC system. This benchmark and exciting work testing the PAWEC performance in Hull University wave tank at the Deep aquarium has been an essential motivation of this study.

The aim of this thesis is thus to deduce and verify linear and non-linear Wave-To-Wire (W2W) models of the dynamics and electrical characteristics of the $1/50$ scale PAWEC prototype. With this a strategy for power maximisation control design has also been developed. The PAWEC has been constructed to harvest energy from wave fluctuation to buoy motion using a good quality steel cylindrical structure. This form of heaving point absorber or heaving buoy is a good basis for initial modelling, control and wave tank experiments. The cylindrical shape has been chosen for simplicity. The dynamics of this PAWEC device have been derived based on an appropriate combination of hydrodynamics and Newtonian physics. The model has been verified using data derived from the wave tank tests using a suitable sensor suite and a LABVIEW™ data acquisition system. The buoy and the development of the sensing and data acquisition systems have all been developed as a part of this PhD study.

Since only the heaving motion is studied in this study, the PTO system to generate electricity uses a Tubular Permanent Magnet Linear Generator (TPMLG) attached to the buoy with the simplifying assumption that the most significant degree of “energy freedom” is in heaving motion. The TPMLG has been investigated extensively using finite element physical simulation MAXWELL™ package in ANSYS®. Based on the numerical models of the mechanical and electrical system, a specific control strategy has been applied on the TPMLG to regulate the PTO force aimed to keep the PAWEC resonant with the incident waves.

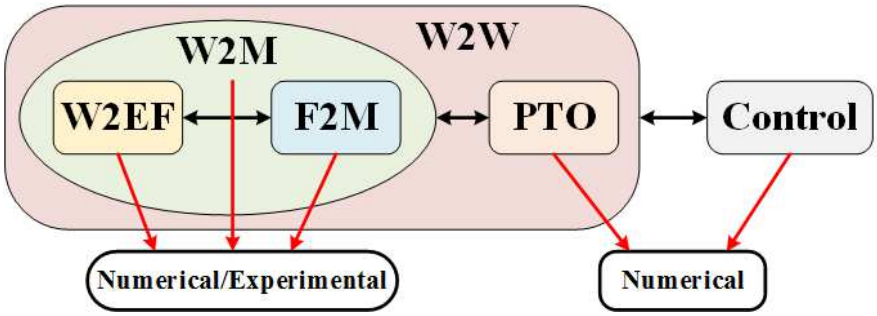

Fig. 1.2 Aim and objectives of this study.

To fulfil the aim of linear/non-linear W2W modelling, the objectives are divided into (i) F2M modelling, (ii) W2EF modelling, (iii) prototype design and wave tank tests for model verification, (iv) PTO modelling and W2W modelling as a combination of the W2EF, F2M and PTO modelling and (v) control system development based on the W2W modelling. The relationship between the aim and the objectives are illustrated in Fig. 1.2. Each of the objectives is separated into a couple of tasks and the details are given as follows:

- **Modelling and Verification of Force-To-Motion (F2M) Models**:
  - Conduct linear numerical simulation via BEM code NEMOH to compute the wave-PAWEC interaction, based on the $1/50$ scale prototype;
  - Identify state-space models of the radiation force from BEM results;
  - Model the non-linear viscous and friction forces;
  - Derive F2M models considering the non-linear forces; and
  - Verify the linear and non-linear F2M models via wave tank (free-decay) tests.
- **Modelling and Validating of Excitation Force**:
  - Investigate the non-causality of the Wave-To-Excitation-Force (W2EF) process;
  - Identify wave excitation force from wave elevation according to the W2EF Frequency Response Function (FRF), referred to as the W2EF modelling approach;
  - Estimate the excitation force from the pressure, acceleration and displacement measurements, referred to as the Pressure-Acceleration-Displacement-To-Excitation-Force (PAD2EF) modelling method;

  - Observe the excitation force from the displacement measurement via Unknown Input Observer (UIO), referred to as the Unknown-Input-Observation-of-Excitation-Force (UIOEF) technique;
  - Derive linear and non-linear Wave-To-Motion (W2M) models via combining the W2EF and F2M models.
  - Verify the proposed W2EF, PAD2EF, UIOEF and W2M models via wave tank tests.

- **PAWEC Prototype Design and Construction**:
  - Design a $1/50$ scale PAWEC as the mechanical subsystem;
  - Sketch a sensing subsystem (including accelerometer, displacement and pressure sensors) and a Data AcQuisition (DAQ) subsystem;
  - Code Graphic User Interface (GUI) to cooperating with the DAQ subsystem; and
  - Conduct a wide variety of wave tank tests for model verification, including free-fall, free-decay, excitation and forced-motion tests.

- **Modelling and Optimising of the TPMLG**:
  - Simulate the electromagnetic coupling of the TPMLG in Finite Element Method (FEM) package ;
  - Optimise the mechanical design of the TPMLG to reduce the cogging force;
  - Identify a TPMLG state-space model from FEM simulation results;
  - Derive linear and non-linear Wave-To-Wire (W2W) models for control system design.

- **Control System Development**:
  - Apply reactive control to the proposed W2W models;
  - Study phase control by latching on the proposed W2W models; and
  - Develop a W2W tracking control structure for power maximisation and displacement constriction of the proposed W2W models.

1.5 Contributions and thesis layouts

Compared to the research work in the literature, the main contributions of this work include the linear/non-linear modelling of the PAWEC hydrodynamics, wave tank tests for model verification, modelling and optimisation of TPMLG and control development of power maximisation algorithm. The details are given as follows:

- **Non-linear Modelling of PAWEC:** Linear modelling of the PAWEC are based on the assumptions of ideal fluid (irrotational, inviscid and incompressible), linear (or Airy's) wave theory and small motion amplitude. Ignoring some important non-linear effects, linear models always exaggerate the PAWEC motion and its power output and cannot represent the PAWEC true behaviour if excited by waves. Hence, non-linear phenomena, like viscous, friction and cogging forces are modelled to derive more realistic numerical models. Since CFD simulations are expensive in computing and inconvenient for PAWEC motion analysis and control system design, system identification techniques are adopted to derive non-linear state-space models based on CFD results. These non-linear state-space models are generally accepted and commonly used for dynamic system analysis and control strategies design. The non-linear modelling approaches are detailed in Chapters 4 and 5.

- **Experimental Verification of Non-linear Models:** In the literature, most of the state-space models of PAWEC are derived from and validated by CFD results and few are verified via wave tank tests or sea trials. To verify the proposed non-linear models, a 1/50 scale PAWEC has been designed, constructed and tested in this work. The prototype compromises a semi-submerged cylindrical buoy and a sensing system with hardware and software design. A wide variety of free-fall, free-decay, excitation and forced-motion tests are conducted in the University of Hull advanced wave tank. The experimental data are compared with the numerical simulation results of the proposed linear and non-linear F2M, W2EF, W2M models for the purpose of model varification. The details of the prototype sketch and experimental configuration are given is Chapter 6.

- **TPMLG Modelling and Optimisation:** For a heaving PAWEC, a TPMLG is selected as the PTO mechanism after the comparison with other PTO systems, e.g. hydraulic PTO, rotational machine and elastomer PTO systems. One main drawback of the TPMLG is that the cogging force is relatively large due to the stator topological structure (mainly the end-effect). The cogging force reduction

is investigated numerically in MAXWELL™ via the optimsation of the stator length, pole-shoe shape and permanent magnet length and width. Based on the physical field simulation in MAXWELL™ a optimised TPMLG model is obtained and applied as the PTO system for the 1/50 scale PAWEC to derive W2W models. This part of study is given in Chapter 7.

- **Development of Power Maximisation Control Strategies:** Based on the proposed linear/non-linear F2W and W2W models, reactive control and phase control by latching are studied and developed with implementation acting on the TPMLG for power maximisation and displacement constriction. A W2W tracking control structure is proposed with a three-level tracking control system and simulated under both regular and irregular wave conditions. The proposed W2W tracking control can achieve almost the same performance as the reactive control and latching control in terms of energy conversion efficiency and displacement constriction. This part of work is illustrated in Chapter 8.

The structure of the nine chapters of the thesis is shown in Fig. 1.3:

- **Chapter 2** briefly reviews the historical development of wave energy conversion techniques. Various WEC systems are discussed and classified, with focus on the Point Absorber (PA) type WEC devices. Numerical modelling methods are studied and compared, including (i) analytical and empirical methods, (ii) linear numerical modelling methods, (iii) non-linear extension of linear numerical modelling approaches and (iv) fully non-linear CFD approaches. Different control strategies are briefly introduced. A PA type WEC device is selected as the main target in this research. All work undertaken and contributions to the research fit within the context of the current state of the art of wave energy harvesting techniques.

- **Chapter 3** succinctly expresses the mathematical fundamentals of linear wave theory, linear modelling of wave-PAWEC interaction and linear PTO mechanism. Based on BEM simulation results, a linear F2M model with frequency-determined parameters is derived. Power maximisation condition is studied via electromechanical analogue according to maximum power transfer theorem. The basic definitions and terminology are detailed in this Chapter.

- **Chapter 4** concerns the radiation force approximation with finite order system and modelling of non-linear mechanical friction and fluid viscous forces. The radiation force is expressed by the Cummins equation, but there is a convolution

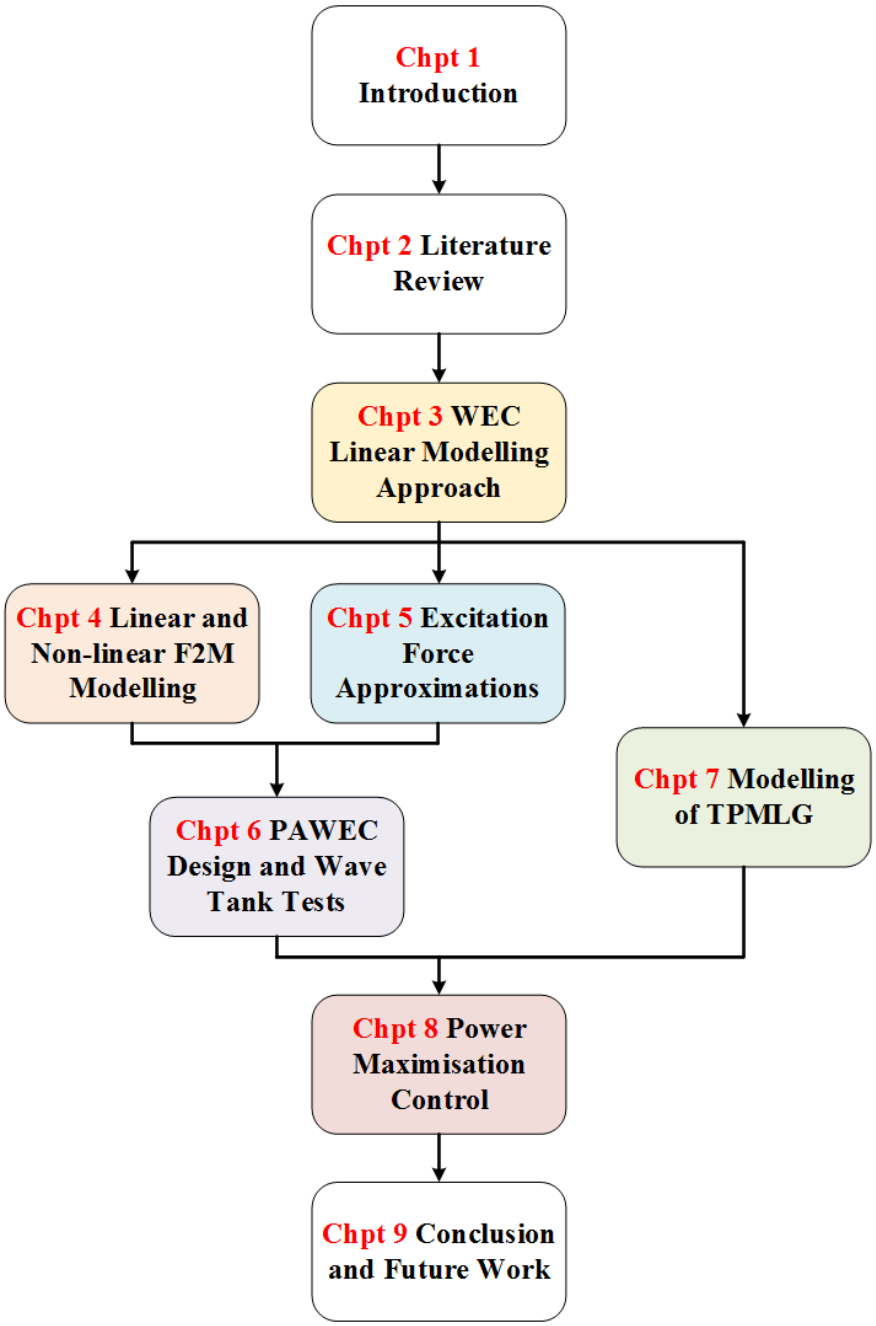

Fig. 1.3 Thesis structure.

term which is inconvenient for control system design. Both frequency- and time-domains system identification techniques are applied to approximate the convolution term with finite order state-space models. Thus a linear F2M model is derived viewing the excitation force as system input and the PAWEC displacement as system output. To investigate the non-linear phenomena influences on the PAWEC performance, the viscous force is modelled as the drag force term in the Morison equation and the friction force is simulated as the Tustin model (a summation of Stribeck, Coulomb and linear damping friction forces). The viscous and friction forces are lumped and their summation is referred to as a lumped non-linear force. Thus a non-linear F2M model in state-space formulation is derived by taking into account these non-linear forces. A set of free-decay tests are conducted in the wave tank to verify the proposed linear and non-linear F2M models. The simulation results of the non-linear F2M model shows a much higher correspondence to the measured data than the linear F2M model.

- **Chapter 5** is concerned with the relationship between the incoming wave elevation and the wave excitation force acting on the cylinder. The physical meaning of the non-causality is expressed and then a causalisation method is proposed to identify a W2EF model from wave elevation in the state-space formulation to approximate the excitation force. The W2EF model is verified by excitation tests. Combined with the F2M models proposed in Chapter 4, linear and non-linear W2M models are derived. Forced-motion tests are configured and conducted to validate the proposed W2M models. For the forced-motion tests, the measurements of pressure, acceleration and displacement are available and hence the PAD2EF and UIOEF methods are studied to approximate the excitation force as comparisons of the W2EF approach.

- **Chapter 6** details the design, construction and testing of the $1/50$ scale PAWEC. The cylindrical buoy has a diameter 0.3 m and height 0.58 m designed in SOLIDWORKS® and constructed in the Hull University mechanical workshop. The electrical circuits are sketched in ALTIUM DESIGNER™ and assembled to connect sensing subsystem (6 Pressure Sensors (PSs), 1 Linear Variable Displacement Transducer (LVDT) and 1 accelerometer), DAQ and power supply subsystems. To cooperate with the DAQ card, a GUI is coded in LABVIEW™ for sensor calibration, data collection and visual monitoring. This prototype has been tested in the wave tank under both regular and irregular wave conditions, including free-decay, free-fall, excitation and forced-motion tests. All the experi-

mental data are adopted to validate the proposed linear/non-linear F2M, W2EF and W2M models.

- **Chapter 7** compares several PTO mechanisms and introduces a TPMLG as the PTO device. The TPMLG model is designed using first principles from the machine's electromagnetic function. The physical model has then been simulated using MAXWELL™. The geometrical design of the TPMLG is optimised via an internal optimisation analyser in MAXWELL™ to reduce the so-called cogging force (Krishnan, 2010). A *dq-axis* state-space model of the TPMLG is extracted based on the electromagnetic simulation and is combined with the F2M models resulting in F2W models or with the W2M models leading to W2W models.

- **Chapter 8** discusses power maximisation control strategies and their implementations on the proposed F2W and W2W models. Reactive control and phase control by latching are developed to regulate the TPMLG *dq-axis* currents electrically to increase of the energy conversion efficiency and to constrict the PAWEC displacement within physical constraints. Furthermore, a W2W tracking control structure is proposed and simulated under regular and irregular wave conditions to maximise power capture and to bound PAWEC displacement response.

- **Chapter 9** summarises the thesis contributions and comments on the achievements made during the PhD study. Future work is outlined to study the PAWEC co-design, to investigate advanced control strategies and to verify the W2W models.

Chapter 2

Literature review

2.1 Introduction

The first patent of wave energy conversion was applied for in France by Girard (1799). McCormick (1981) reported that there were more than 1000 WEC patents registered by 1980. Modern wave energy utilisation dates back to the 1940s. Yoshio Masuda invented the first OWC type WEC for supplying power for navigation lights (Masuda, 1986). Falcão (2010) regarded Yoshio Masuda as the father of modern wave energy technology. After the oil crisis in 1973, the Salter Duck was proposed (Salter, 1974) marking a major landmark commencing a new era of wave energy conversion.

During the 1970s, the understanding that resonance theory was important to achieve optimum power capture based on the concept of potential flow theory became established (Budal and Falnes, 1975b; Evans, 1976; Mei, 1976). Hydrodynamic modelling methods for ship design and sea-keeping, developed by Cummins (1962); McCormick (1973); Newman (1977); Ogilvie (1964); Timman and Newman (1962), were applied to analyse WEC hydrodynamics using both experimental and numerical simulations. For optimising the power products of WEC devices, control strategies, including reactive control and phase/amplitude control, were proposed and tested during this time span by Budal and Falnes (1975b); Evans (1976); Falnes and Budal (1978).

In the 1980s, research interest and activities decreased dramatically as the oil price dropped rapidly due to the oil glut. However, even during this time there were some important studies undertaken in Norway (Mehlum, 1986; Sarmento, 1993). Onshore

devices, an over-topping device (TAPCHAN) and an OWC type WEC, were installed and tested in Toftestallen in 1985 (Mehlum, 1986; Sarmento, 1993).

Since the 1990s wave energy utilisation once again became a research "hot-spot", especially after the agreement of the Kyoto Protocol in 1997. All the member states turned to renewable energy to achieve their roadmaps for CO_2 emission reduction. The current situation is that various R&D projects are being undertaken worldwide. Researchers and companies in Belgium, China, Denmark, France, Ireland, Japan, Norway, Portugal, Sweden, UK, USA and etc. have a growing interest in wave power capture activities. Numerical simulation via commercial CFD packages and scale model tests are being conducted in parallel. A wide range of research topics are being conducted including wave power distribution and marketing, LCoE, environmental impact, advanced control strategies, survivability and reliability, mooring techniques, novel components and subsystems, modelling, etc.

More recently, there is a growing contribution by control experts attracted by this fertile field for control application. Consequently, several advanced control strategies have been developed and tested which achieve power maximisation under moderate sea states and WEC system survival under extreme sea states. Also, the optimum WEC performance achieved by advanced control approaches stimulates the WEC modelling of non-linear effects, like viscosity, vortices, slamming, over-topping, etc.

These references provide a rich source of background for WEC research and development by Babarit et al. (2012); Clément et al. (2002); Drew et al. (2009); Evans (1981); Falcão (2010); Falnes (2007); Langhamer et al. (2010); Li and Yu (2012); Ringwood et al. (2014). There are also several books dealing with all perspectives of WEC technology, written by Alcorn and O'Sullivan (2013); Cruz (2007); Evans and de O Falcao (1985); Falnes (2002); Korde and Ringwood (2016); McCormick (1981).

In this Chapter, Section 2.2 gives a brief introduction of currently prevailing WEC systems, which are classified into six predominant types in this thesis. Section 2.3 discusses several numerical modelling methods of wave-WEC interaction and their pros and cons. Prevalent control strategies, including reactive control, phase/amplitude control and advanced control, are discussed in Section 2.4.

2.2 Review of WEC systems

2.2.1 WEC devices

According to OES (2015), more than 1000 WEC devices have been described. Clément et al. (2002) discussed the main WEC types in Europe and Babarit et al. (2012) recognised that there are eight main WEC types which were compared numerically in terms of overall efficiency and hydrodynamic performance. According to the WEC properties and working principles, several categorisation methods have been developed. Thorpe (1999) classified the WEC devices into three types, shoreline, near-shore and offshore devices, according to the WEC deployment locations. Drew et al. (2009) studied three classification methods according to installation locations, design concepts and operation modes. Falcão (2010) classified WEC devices into three predominant types as OWC devices, oscillating bodies and over-topping devices. Li and Yu (2012); Tiron et al. (2015) catalogued the WEC systems into five basic concepts as OWC devices, over-topping systems, pitch devices, membranes and PAs.

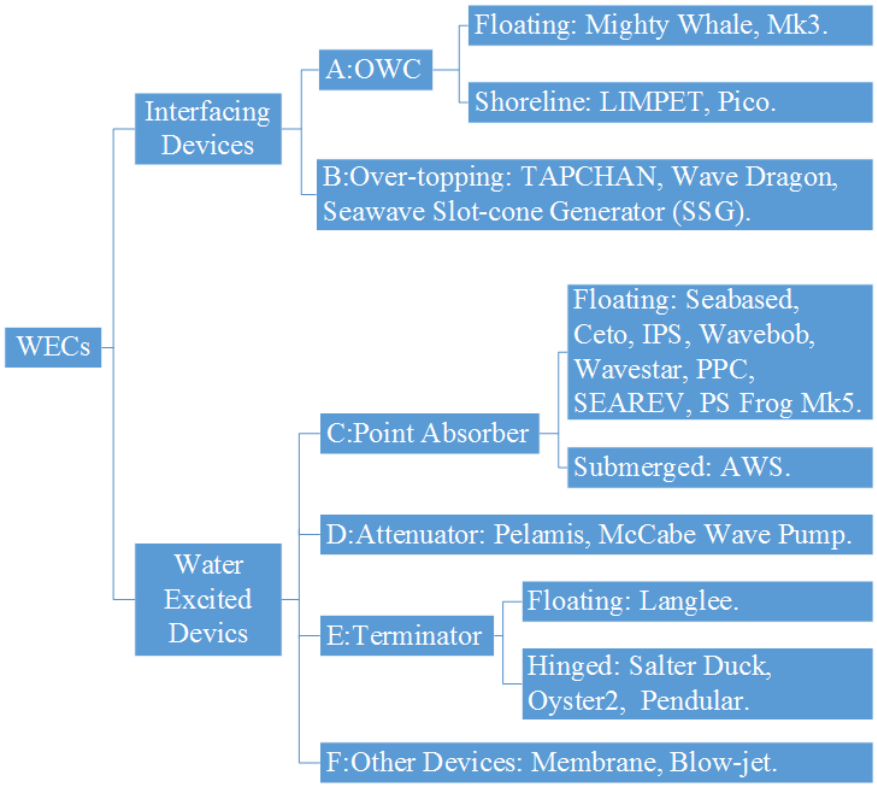

Fig. 2.1 Classification of prevailing WEC devices based on their operating principles.

In this Chapter, existing WEC devices are further classified into six types, including the OWCs[1], over-topping devices, PAs, attenuators, terminators and novel WEC devices, shown in Fig. 2.1. Among the existing devices, the dominant WEC systems are categorised as follows:

- **Type A OWC Devices**: The first generation of OWC devices were invented in 1940s for navigation light by Yishio Masuda and commercialised in 1965 (Falcão, 2010). When the sea waves hit the OWC structure the water inside the chamber oscillates to compress or decompress the air. Thus the motion of the air drives a turbine to generate electricity. The most notable OWC devices are the Mighty Whale (Washio et al., 2000), the Oceanlinx Mk3 (Baghaei, 2010), LIMPET (Boake et al., 2002), and Pico (Le Crom et al., 2009).

- **Type B Over-Topping Devices**: This type devices have collectors to concentrate wave energy using reflection phenomenon. Ramps are built to transform wave kinetic energy into potential energy and reservoirs are used to store the water which is above the average sea surface. The water goes back to the sea due to the gravity and drives a hydroelectric generator to produce electricity. The most notable systems are the TAPCHAN (Mehlum, 1986), the Seawave Slot-cone Generator (SSG) (Margheritini et al., 2009; Vicinanza and Frigaard, 2008) and the Wave Dragon (Kofoed et al., 2006; Tedd and Kofoed, 2009).

- **Type C PA Devices**: PA devices are wave energy converters with small dimensions relative to the incoming wave length (tenth or twentieth). PAs may operate in heave, pitch, even multiple Dimensions of Freedom (DoFs) and situate nearshore or offshore environment. PAs can be simply classified into two subgenera: (i) floating PAs, e.g. the Seabased buoy (Eriksson, 2007), IPS buoy (Eidsmoen, 1995), Wavebob (Weber et al., 2009), Wavestar (Marquis et al., 2010), the Pontoon Power Converter (PPC) (Babarit et al., 2012), SEAREV (Durand et al., 2007) and the PS Frog Mk5 (McCabe et al., 2006), and (ii) submerged PA devices, such as the Archimedes Wave Swing (AWS) (De Sousa Prado et al., 2006), CETO buoy(Rafiee and Fiévez, 2015). Numerical simulations by Babarit et al. (2012) indicates that the energy capture efficiency of PA systems varies from 1% to 30%. However, the theoretical efficiency can be 50 % for one DoF devices and 100 %

[1]The OWCs are ultimately excited by the wave fluctuation. However, the wave fluctuation interface with the air and then the air drives the turbine to generate electricity. Hence the OWCs are classfied as the interfacing devices rather than the water excited devices.

for multiple DoFs PA systems. Therefore control can play an essential role for this specific type WEC devices.

- **Type D Attenuators**: Attenuators are the WECs which can align themselves paralleling to the incident wave direction. The Pelamis (Henderson, 2006) and the McCabe Wave Pump (Pontes and Falcão, 2001) are the typical examples of the attenuators. The devices operate in pitching mode. The relative motion between different bodies are captured by hydraulic rams to generate electricity.

- **Type E Terminators**: The terminators are the devices which are perpendicular to the wave front. These devices operate in pitch/surge mode to drive hydraulic PTO mechanisms to generate electricity. The most notable terminators are the Salter Duck (Salter, 1974), the Langlee (Pecher et al., 2010) and Oyster II (Cameron et al., 2010).

- **Type F Other Novel Devices**: Up to date, some novel WEC design and concepts are proposed and simulated, including the Membrane (Li and Yu, 2012), the Blow-jet (Mendoza et al., 2015), hinged-raft WEC (MoceanEnergy, 2017).

2.2.2 Heaving PAWEC devices

The PAWEC definition is determined by the geometric dimension rather than its operation DoFs and hence the PAWECs can operate in single or multiple DoFs. Hence the Salter Duck (Salter, 1974) in pitch mode, the PS Frog Mk 5(McCabe et al., 2006) in pitch/roll mode and the SEAREV (Ruellan et al., 2010) in pitch/roll mode can be sorted as the PAWEC devices. However, this study has a specific focus on PAWEC devices in heaving mode. For the heaving PAs, there are three subtypes including one-body PAs, two-body PAs and PA arrays. Their properties are compared as follows:

- **One-body PAs:** One-body PAs are always fixed to a reference, such as the sea bed. There are two type of one-body PAs, the floating one-body PAs and submerged one-body PAs. A floating PA device usually comprises a symmetrical structure floating on the sea surface and a PTO system anchored on the sea bed. A taut cable is required to connect the floating structure with the PTO system. Excited by incident waves, the floating structure oscillates and drives the PTO system to generate electricity. The most notable floating one-body PA is the Seabased Buoy (Eriksson, 2007), shown in Fig. 2.2. A submerged one-body PA

is usually standing on or referenced to the sea bed and excited by the pressure variations due to wave troughs and crests. The famous representatives are the AWS degined in Holland but tested in full scale in Portugal (De Sousa Prado et al., 2006; Polinder et al., 2005a) and the CETO buoy tested in Australia (Rafiee and Fiévez, 2015), shown in Fig. 2.2.

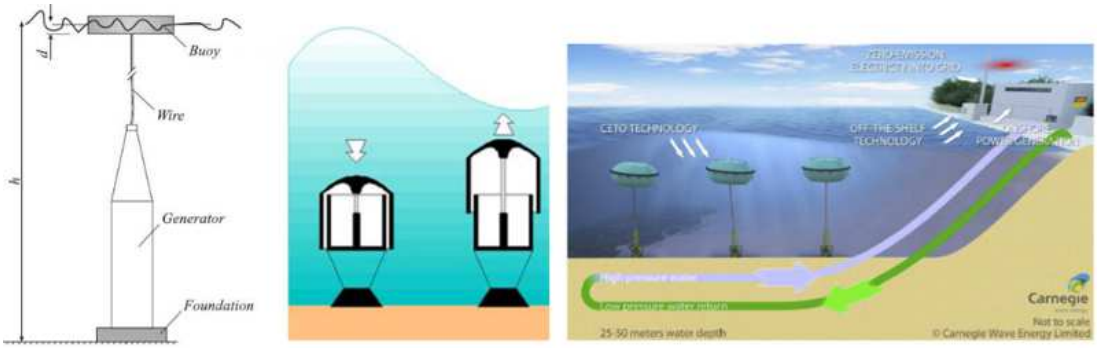

Fig. 2.2 Examples of one-body PAs, including the Seabased buoy, AWS and CETO buoy (Eriksson, 2007; Polinder et al., 2005a; Rafiee and Fiévez, 2015).

The floating one-body PA devices show good potential to harvest most of the wave energy since 96% of wave energy is distributed within $1/4$ wave length under the sea surface (Falnes, 2007). However, the floating one-body PAs surfer from extreme sea states and have high requirements on survivability and anchor system. On contrast, the submerged PA devices show more reliability and tolerance to severe sea states. However, the submerged one-body PAs cannot achieved as high energy conversion efficiency as the floating devices (Mann, 2011). For both the floating and submerged PAs, their energy capture efficiencies have a narrow bandwidth and hence power maximisation control is essential to achieve high energy conversion efficiency under varying sea states.

- **Two-body PAs:** Two-body PAs are characterised with the self-referenced property and the relative motion between two bodies drives PTO system to generate electricity. Since the two-body PAs are not attached to a fixed reference, the mooring system is easy to achieve and hence two-body PAs are suitable for deep sea applications. Some of the well known devices are the OPT PowerBuoy in USA (Edwards and Mekhiche, 2013) and Wavebob in Ireland (Mouwen, 2008), as shown in Fig. 2.3. Compared with the one-body devices, the two-body PAs show a much wider energy capture bandwidth.

- **PA Arrays:** Several PAs can be attached to a jacked up frame or structure to form a PA array to harvest wave power. The notable arrays are the Wavestar developed

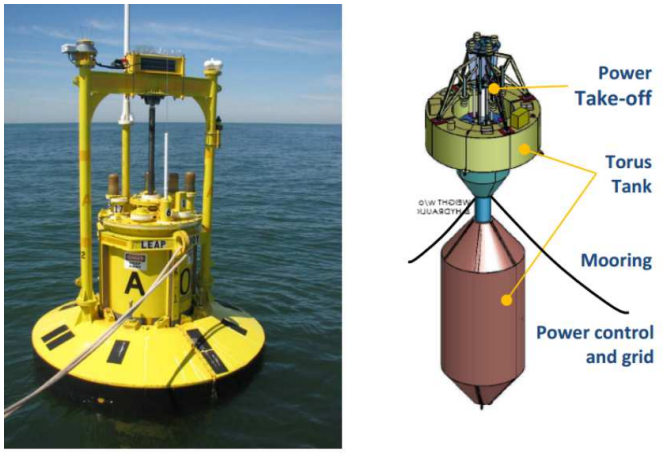

Fig. 2.3 Example of two-body PAs, including the PowerBuoy and Wavebob (Edwards and Mekhiche, 2013; Mouwen, 2008).

and tested in Denmark (Kramer et al., 2011) and the FO3 tested in Norway (Gao and Moan, 2009). As shown in Fig. 2.4, the Wavestar shows good survivability to storms by pulling the buoys up to the frame. The sea trials of the 1/40 and 1/10 scale Wavestar show a energy conversion efficiency up to 40-60% (Kramer et al., 2011).

Fig. 2.4 Wavestar in operation and protection modes (Kramer et al., 2011).

Compared with all the other types of WEC devices, the floating one-body heaving PAWEC is selected in this thesis. The main advantages of the one-body heaving PAWEC device are: (i) The structure is simple and economic to manufacture and hence it is cost saving. (ii) The mooring system is simple to design and install for the saving of installation cost. (iii) The PAWEC is low in system complexity with less components or subsystems and hence it is high in system reliability. (iv) The PAWEC shows good survivability under extreme wave conditions and has little requirement on manual maintenance. The shortcoming of low energy conversion efficiency can be overcome by well-designed control strategies.

2.3 Review of modelling approaches

This Section outlines the modelling methods of the wave-WEC interaction. The most generally used methods include the analytical/empirical methods, linear numerical methods, non-linear extension of the linear model methods, non-linear CFD methods and other hydrodynamic modelling methods. To some extent, the hydrodynamics of wave-WEC interaction are similar with wave-ship interaction and thus some modelling approaches of ship design can be applied to WEC hydrodynamic modelling.

- **Analytical and empirical methods** are wildly used for the modelling and prediction of WEC motion. For a floating body, its motion can be represented analytically as a Mass-Spring-Damper (MSD) system with empirically determined added mass, radiation damping coefficient and hydrostatic stiffness (Budal and Falnes, 1975a,b; Falnes, 2002; McCormick, 1981). These methods can provide accurate simulation for some specific device shapes, such as spheres and cylinders. However, they are not valid for arbitrary structures since the empirical parameters are not available for arbitrary structures. One main advantage of these analytical and empirical methods is that second order MSD models are convenient and intuitive to understand with all the parameters showing their physical meaning directly. Thus, WEC systems can be analysed by electromechanical analogue approaches. Based on the analogue concept (e.g. equivalence between electrical and mechanical systems), resonance theory and optimal power conditions are proposed and derived by Budal and Falnes (1975a,b). Therefore, the reactive (or complex conjugate) control approach and phase/amplitude control (including latching and declucthing control) methods are proposed and derived to achieve resonance and optimal conditions. These analytical/empirical approaches also allow the inclusion of other forces, like viscous, friction, mooring and PTO forces, to be superposed in to form more applicable extended representations. However, these analytical/empirical methods cannot provide accurate solutions for arbitrary WEC structures. For such cases only numerical methods can deal with this problem.

- **Linear numerical modelling methods** can provide accurate numerical solutions for arbitrary WEC systems in terms of first order hydrodynamics and wave loads, including the strip theory, panel method, BEM and etc. The first numerical solution is proposed by Korvin-Kroukovsky and Jacobs (1957), called the strip theory, and developed by Newman (1977); Ogilvie and Tuck (1969). More presently,

BEM packages are widely applied for WEC hydrodynamic simulations, including the frequency-domain packages (WAMIT™, AQWA™, NEMOH) and the time-domain codes (ACHIL3D). Similar with the analytical/empirical methods, the linear numerical modelling methods show clear the physical meanings of excitation force, radiation damping coefficient and added mass. Also, these methods are based on harmonic wave conditions in the frequency-domain. The time-domain responses can be gained according to the Ogilvie relation, which is proposed by Ogilvie (1964) to transform system responses mutually between the time- and frequency-domains. For irregular waves, the responses can be obtained from the regular wave simulations based on superposition principle (Ogilvie, 1964; St Dinis and Pierson Jr, 1953). The BEM code NEMOH (Babarit et al., 2012) is adopted in this study to calculate the hydrodynamic parameters, detailed in Chapter 3. However, these methods focus on linear hydrodynamics only and fail to simulate the WEC motion under harsh sea states. To improve modelling validity, some non-linear effects can be considered as corrections or calibrations based on superposition principle. Also, more complete approaches to CFD modelling should include non-linearity to provide more accurate hydrodynamic representations of wave-WEC interaction.

- **Non-linear extension of linear numerical modelling approaches** generally offer a compromise between modelling validity and fidelity. Thus, non-linear excitation, radiation, PTO and mooring forces can be used to extend the linear model (Giorgi et al., 2015; Merigaud et al., 2012). Non-linear viscous force is applied to extend the linear models and the numerical simulation shows a good accordance to the total non-linear CFD results (Bhinder et al., 2015) and wave tank tests data (Guo et al., 2017; Jin et al., 2016). Non-linear models considering both viscous and friction forces usually fit the experimental data to a higher degree. An example of this strategy is given in Chapter 4, focusing on the importance of including non-linear viscous and friction forces.

- **Fully non-linear CFD approaches** can provide precise prediction and hydrodynamics of WEC devices considering all kinds of non-linear phenomena during wave-WEC interaction, including viscosity, vortex shedding, slamming, turbulence, wave breaking and over-topping effects. Finite Element Method (FEM) or Finite Volume Method (FVM) are implemented to solve the Navier-Stokes equation via temporal-spatial discretisation, which can be achieved by CFD packages, like COMET®, OpenFOAM®, Flow3D®, CFX™ and so on. Several simulation techniques and algorithms are developed to satisfy various design and simulation

requirements, including the Reynolds-Averaged Navier-Stokes (RANS), Direct Numerical Simulation (DNS), Detached Eddy Simulations (DES), Large Eddy Simulations (LES) methods (Agamloh et al., 2008; Li and Yu, 2012; Peñalba et al., 2015; Wolgamot and Fitzgerald, 2015; Yu and Li, 2011). The drawbacks of these methods are: (i) Fully non-linear CFD is expensive in computation. (ii) The CFD results is not as intuitive as the analytical/empirical methods. (iii) the CFD can only provide distribution of the resultant pressure and velocity. Special simulation design or post process are necessary to separate the excitation, radiation, viscous forces from the resultant force.

Recently, there are some numerical modelling approaches proposed for wave-WEC hydrodynamic modelling, including the bond-graph modelling approach (Kurniawan et al., 2012), spectral modelling approach (Folley and Whittaker, 2010), Smoothed Particle Hydrodynamics (SPH) approach (Marjani, 2008) and linear/non-linear data-based model determination method (Davidson et al., 2016; Giorgi et al., 2016). These methods are reviewed by Li and Yu (2012); Peñalba et al. (2015); Wolgamot and Fitzgerald (2015). The book by Folley (2016) has a special focus on numerical modelling of WEC devices, illustrating the fundamental principles, case studies and limitations of various modelling methods.To gain a whole scope of WEC systems and their control requirements, W2W models are proposed by Bailey et al. (2014); Ferri (2014); Forehand et al. (2016); Garcia-Rosa et al. (2014); Josset et al. (2007) and reviewed by Penalba and Ringwood (2016). In the W2W models, the incident wave is viewed as the input and the WEC generated electricity is viewed as the output.

As pointed out by Folley (2016), the key challenge in the numerical modelling of WECs is to identify the most appropriate method for a specific WEC concept and modelling objectives. Intimately linked to this challenge is model verification. In this study, a hybrid modelling method is applied to represent the hydrodynamic behaviour of the 1/50 scale heaving PAWEC with comparative study between linear and non-linear modelling approaches. A wide range of wave tank tests are conducted for the purpose of model verification and comparison of linear/non-linear modelling approaches. This part of work is detailed in Chapters 3, 4, 5 and 6.

2.4 Review of control strategies

Awareness of the importance of control has been present since the time when WEC concepts were first proposed. Based on the analytical/empirical models and experimental tests, a separate way of thinking using resonance concept was proposed and tested in the 1970s by Budal and Falnes (1975b); Evans (1976); French (1979); Mei (1976); Salter (1979). WEC devices always have narrow frequency bandwidth and their efficiency performance generally remains low. When resonance is achieved, WEC motion (velocity) tracks the variations in the incident wave excitation force closely. Thus the WEC motion is amplified even though the wave height is small. Hence, more energy can be captured from waves. Although it is strictly applicable to harmonic waves to achieve resonance, optimal phase and amplitude conditions are derived by Budal and Falnes (1977), which indicate basic concepts of reactive control and phase/amplitude control. More recently, control experts simulated and tested several advanced control strategies for wave energy maximisation that can be applicable to both regular and irregular wave conditions (Bacelli et al., 2009; Beirao et al., 2007; Cretel et al., 2011; Da Costa et al., 2007; Genest and Ringwood, 2016a,b; Hals et al., 2011b).

- **Reactive control** (Salter, 1979), sometimes referred to as the complex-conjugate control (Nebel, 1992), is often used to derive certain optimal phase and amplitude conditions for WEC devices via continuous adjustment of PTO system parameters, such as mass, stiffness and damping. During the reactive control process, for a part of a given wave induced cycle some power is fedback to the water by the PTO mechanism (e.g. a generator now momentarily working as a motor). In this case the power is reactive (rather than real or active) and thus this approach is named “reactive control”. The concept of reactive control in the context of WEC devices was first investigated numerically and experimentally on the Salter Duck (Fusco and Ringwood, 2014; Nebel, 1992; Salter, 1979).

  For harmonic waves, it is easy to determine the PTO parameters since the added mass, radiation damping coefficient and hydrostatic stiffness can be determined from frequency-domain numerical simulation. From this the tuning of the corresponding PTO parameters can be achieved in a mechanical way (Korde, 1999; Nebel, 1992). Reactive control implementation on a permanent magnet linear generator is achieved via an electrical tuning approach by Shek et al. (2007). However, for irregular waves, the optimal PTO parameters are not straightforward to determine since the wave prediction is required to overcome the non-causality

of the wave-WEC FSI. The required prediction horizon for real-time reactive control is analysed by Fusco and Ringwood (2011b). Suboptimal causal reactive control for a heaving point absorber is discussed by Fusco and Ringwood (2011c). For some specific PTO systems, the reactive power (from device to wave) is not allowed, the optimal resistive loading (passive load) control can be applied (Hals et al., 2011a). Also this optimal resistive loading is adopted for latching control realisation.

- **Phase and amplitude control** is proposed by Budal and Falnes (1977) to achieve the optimal phase and amplitude conditions for a heaving sphere. However, this strategy is difficult to implement on PTO systems since the system cannot be realistically tuned in real-time due to significant parameter variations under irregular wave conditions. A rather old but nevertheless simple suboptimal strategy, known as "latching control", was proposed by Falnes and Budal (1978) and tested by Budal et al. (1981), which is easy to implement via mechanical or hydraulic PTO systems, although as wave prediction is necessary to determine the switching or releasing time instant. The optimum phase condition is achieved by latching the WEC when its velocity vanishes and unlatching the WEC after an optimal time interval when the phase shift between the excitation force and WEC velocity is minimised. To achieve optimum amplitude condition, the PTO resistive load is optimised as a pure damper equalising with the radiation damping coefficient at the resonant frequency.

  The latching performance relies on how to determine the latching duration. Babarit and Clément (2006) analytically calculated the optimal latching duration in order to maintain WEC velocity in phase with wave excitation force or to maximise the captured power in a given horizon. In their work, a short-term prediction of wave excitation force is assumed available and accurate. Various latching strategies are compared by Babarit et al. (2004); Lopes et al. (2009). Non-prediction latching control is proposed by Lopes et al. (2009) to determine the optimum instant for unlatching the WEC when the wave excitation force changes its direction or when the wave elevation exceeds a pre-determined threshold. To achieve this, a pressure transducer is installed to provide real-time wave elevation measurement. More recently, Sheng et al. (2015) explained the physical meaning of latching control mathematically via a time-out technique and derived a simple statistic way to determine latching interval under irregular wave conditions without excitation force prediction.

As a extension of latching control, Babarit et al. (2009) proposed declutching control with implementation on a hydraulic PTO system. The Pontryagin principle is used to calculate the optimal instant to switch on or off a by-pass valve to couple or decouple the PTO system. The comparison between latching and declutching control strategies are investigated by Clément and Babarit (2012). They also combined these two control methods to form a hybrid control structure called latching-operating-declutching control.

- **Advanced control approaches** are applied on WEC systems to deal with constraints, non-linear effects and power maximisation, including Model Predictive Control (MPC), Internal Model Control (IMC), Pseudo-Spectrum (PS) control, Sliding Model Control (SMC) and etc. IMC is applied on a AWS device by Beirao et al. (2007); Da Costa et al. (2007). PS control is investigated numerically by Genest and Ringwood (2016a,b). A hierarchical robust control strategy is studied by Fusco and Ringwood (2014). Neural control (Mundon et al., 2011) and fuzzy logic control (Schoen et al., 2008a,b) are numerical simulated to maximise the WEC power capture. Witt et al. (2012) tested SMC strategy on an OWC device.

  The MPC strategies are first applied on an AWS device by Gieske (2007) and then applied on PAWEC systems by Bacelli et al. (2009); Cretel et al. (2011); Hals et al. (2011b). MPC strategies with physical constraints (displacement and PTO force limitations) are investigated by Li and Belmont (014a,b). Richter et al. (2013); Tom and Yeung (2013) extended linear MPC to deal with non-linear mooring forces. These MPC strategies assume that the future information of wave excitation force is known. Brekken (2011) implemented MPC with excitation force prediction via an AR model. MPC shows great potential to maximise WEC power harness since it can deal with constraints naturally. An overview comparison among optimal control, MPC and MPC-like algorithms for WECs can be found in Faedo et al. (2017).

Since most optimum control strategies are based on the assumption that the wave or excitation force information is predicted within a suitable period. In engineering applications, this future information can be gained via wave prediction (Fusco and Ringwood, 2010; Ge and Kerrigan, 2016) or excitation force estimation and prediction (Abdelrahman et al., 2016; Brekken, 2011). Comparison of control performance of a variety of control strategies are discussed by De la Villa Jan and Santana (2016); Hals et al. (2011a); Valério et al. (2007). Some excellent review papers on WEC optimal

control are delivered by Drew et al. (2009); Hong et al. (2014); Ringwood et al. (2014); Salter et al. (2002).

These classic control methods (reactive control and phase/amplitude control) mentioned above generally assume the PTO system is a MSD system. In this study a TPMLG is adopted as the PTO mechanism and hence the callsic control methods are extended and developed to discuss their implementations on electrical machines. For this specific PTO system, linear/non-linear W2W models are derived in Chapter 7 and Chapter 8 proposed a 3-level tracking control structure based on the development of the classic control methods. Hence control study in this work has special focus on (i) extention and development of classic control methods and their implementations and (ii) real-time control based on the proposed linear/non-linear W2W models. This part of work is detailed in Chapter 8.

2.5 Summary

This Chapter details the literature review of WEC devices, together with typical numerical modelling approaches and power maximisation control strategies. Section 2.2 gives a historical review of a wide variety of WEC concepts and devices. The most promising devices are classified into six main types, the OWCs, over-topping devices, PAs, attenuators, terminators and other novel devices. WEC hydrodynamic modelling approaches are outlined in Section 2.3 with discussion and comparison of the analytical/empirical methods, linear numerical modelling methods, non-linear extension of linear numerical methods and fully non-linear CFD methods. The review of control strategies applied on WEC systems to achieve maximum power capture is discussed in Section 2.4 where reactive control (or complex-conjugate control), phase/amplitude control and advanced control strategies are discussed and compared.

Among the various types of WEC devices described in Section 2.2, a $1/50$ cylindrical heaving PAWEC is selected in this study due to its easily recognisable advantages: (i) The PAWEC is economic in construction and installation; (ii) The PAWEC shows high survivability and reliability in an offshore environment; (iii) The PAWEC can reduce maintenance work to a small level. The details of scaling-down ratio, prototype design and construction, wave tank tests are detailed in Chapter 6.

For selected PAWEC device, a hybrid linear/non-linear numerical modelling method is adopted in this work to represent the PAWEC hydrodynamics with linear/non-linear comparative study and wave tank tests for model verification. This hybrid modelling approach can achieve a compromise between computation efficiency and accuracy. On one hand, the linear numerical modelling approach is effective but inaccurate in computation. On the other hand, non-linear calibration to linear models can improve the modelling fidelity without significantly increasing the computation burden. Hence this work handles the modelling challenges of non-linear modelling and model verification mentioned in Section 2.3, which are detailed in Chapters 3, 4 and 5.

As introduced in Section 2.4, the main challenge of WEC control is the real-time implementation problem. Hence this work extends the reactive control and phase/amplited control methods to electrical machine implementation and discusses their realisation via a TPMLG as the PTO mechanism. Based on the W2W models derived in Chapter 7, Chapter 8 proposes a 3-level tracking control structure for real-time power maximisation control of WEC devices.

Chapter 3

WEC linear modelling approach

3.1 Introduction

This Chapter discusses some fundamental principles of wave energy conversion, including the wave properties, wave-PAWEC interaction and linear modelling of the PAWEC system. Section 3.2 gives basic mathematical representations of wave properties. Section 3.3 introduces the fundamentals of wave-PAWEC interaction. Section 3.4 describes a simple linear modelling approach of the $1/50$ scale PAWEC, which is a second order system with frequency-determined parameters. Based on the linear model, the complex amplitude expression is introduced to derive the power maximisation condition in Section 3.5.

3.2 Wave properties

Although there is no mathematical theory that can give precise description of real sea waves. However, some wave theories can provide appropriate approximations to the behaviour of real sea waves. Amongst these the most notable and widely accepted one is the classical Airy's wave theory, also known as the linear wave theory (Airy, 1845). In this Section, the linear wave theory is outlined with ideal fluid and small wave height assumptions, together with the mathematical representations of both regular and irregular waves. Since this work focuses on the WEC power maximisation under

moderate sea conditions rather than the WEC survivability under extreme sea conditions, only linear wave theory is studied in the following sections and chapters.

3.2.1 Linear wave theory

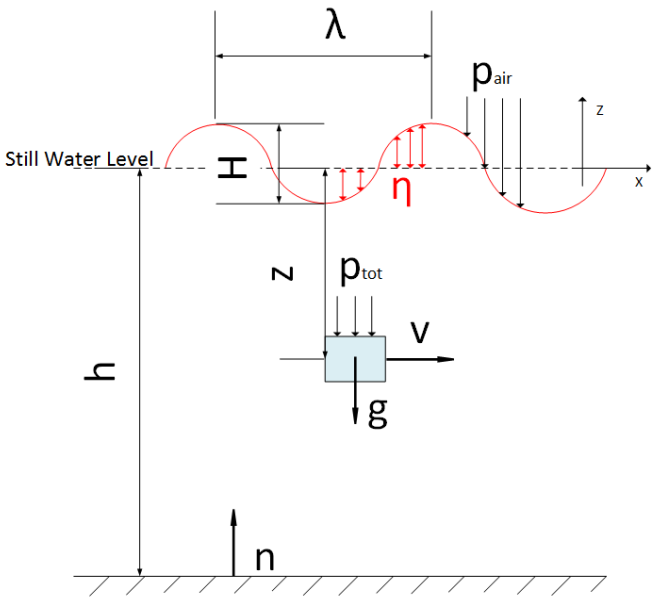

Fig. 3.1 Sketch of wave parameters.

As shown in Fig. 3.1, the motion of a small fluid element obeys two basic equations, the continuity equation and the Navier-Stokes equation. The continuity equation is given as (Falnes, 2002):

$$\frac{\partial \rho}{\partial t} + \nabla \cdot (\rho \vec{v}) = 0, \tag{3.1}$$

where $\rho(x,y,z,t)$ and $\vec{v}(x,y,z,t)$ are the fluid density and velocity (see Fig. 3.1), respectively. Generally speaking, sea water is incompressible , which means that $\rho(x,y,z,t)$ is a constant and $\frac{\partial \rho}{\partial t} = 0$. Thus, the continuity equation in Eq. (3.1) can be rewritten as:

$$\nabla \cdot \vec{v} = 0. \tag{3.2}$$

If the fluid velocity vector $\vec{v}$ satisfies the irrotational assumption, there exists a scale function $\phi(x,y,z,t)$ (an auxiliary function), called the velocity potential function. Thus $\vec{v}$ can be represented by ϕ as (Falnes, 2002):

$$\vec{v} = \nabla\phi, \tag{3.3}$$

where ∇ is the vector differential operator.

Thus, based on the incompressible and irrotational assumptions, the continuity function in Eq. (3.1) can be represented by ϕ, substituting Eq. (3.3) into Eq. (3.2):

$$\nabla^2\phi = 0, \tag{3.4}$$

where ∇^2 is the Laplace operator.

The other basic equation is the Navier-Stokes equation (Falnes, 2002), given as:

$$\frac{d\vec{v}}{dt} = \frac{\partial\vec{v}}{\partial t} + (\vec{v}\cdot\nabla)\vec{v} = -\frac{1}{\rho}\nabla p_{tot} + \nu\nabla^2\vec{v} + \vec{g}, \tag{3.5}$$

where $p_{tot}(x,y,z,t)$, ν and $\vec{g}$ represent the total pressure, kinematic viscosity coefficient and gravity vector (see Fig. 3.1), respectively. There is no analytical solution for the Navier-Stokes equation in Eq. (3.5), as a consequence of the non-linear term $\nu\nabla^2\vec{v}$. One interesting fact is that the kinematic viscosity coefficient ν of sea water is very small (order of magnitude 10^{-6}), which results in a very small viscous force relative to the gravitational and inertial forces. Thus the viscous term $\nu\nabla^2\vec{v}$ is neglected here. Therefore, to substitute Eq. (3.3) in to Eq. (3.5) gives:

$$\frac{\partial\phi}{\partial t} + \frac{(\nabla\phi)^2}{2} + \frac{p_{tot}}{\rho} + gz = \frac{p_{air}}{\rho}, \tag{3.6}$$

where $p_{air}(x,y,z,t)$, g and z are the air pressure, gravity constant and fluid particle vertical position, respectively, as shown in Fig. 3.1. This is a Bernoulli's equation which is valid for unsteady irrotational flow (Newman, 1977).

For most situations, the air pressure is a constant, approximating the standard atmospheric pressure. To apply Eq. (3.6) on the air-water surface gives the free-surface boundary condition (Falnes, 2002), given as:

$$g\eta + \left[\frac{\partial \phi}{\partial t} + \frac{(\nabla \phi)^2}{2}\right]_{z=\eta} = 0, \tag{3.7}$$

where $\eta(x,y,t)$ represents wave elevation. For most moderate sea states, wave height is relatively smaller than wave length. In this situation, the second or higher order terms in Eq. (3.7) can be neglected to linearise the free-surface boundary condition (Falnes, 2002), written as:

$$g\eta + \left[\frac{\partial \phi}{\partial t}\right]_{z=\eta} = 0, \tag{3.8}$$

The velocity of water particles can be computed either from the potential function ϕ or from the particle displacements η, so there exists an identical relation $\frac{\partial \phi}{\partial z} = v = \frac{\partial \eta}{\partial t}$. Therefore, the derivative of Eq. (3.8) is given as (Falnes, 2002):

$$\left[\frac{\partial^2 \phi}{\partial t^2} + g\frac{\partial \phi}{\partial z}\right]_{z=0} = 0. \tag{3.9}$$

This is the reason why this wave theory is so-called linear wave theory. It also indicates that the linear wave theory is only valid when wave height is much smaller than wave length.

If the fluid is assumed inviscid, the fluid particles around the wet surface move together with the solid body. Thus the solid-body boundary condition can be expressed as (Falnes, 2002):

$$\frac{\partial \phi}{\partial \vec{n}} = \vec{n} \cdot \vec{u}, \tag{3.10}$$

where $\vec{u}(x,y,z,t)$ and $\vec{n}(x,y,z,t)$ represent the solid body moving velocity and the unit normal vector on wet surface. Since the sea bed does not move $\vec{u} = 0$ m/s, the sea-bed boundary condition can be written as (Falnes, 2002):

$$\left[\frac{\partial \phi}{\partial z}\right]_{z=-h} = 0. \tag{3.11}$$

The linear wave theory is applied to solve the Laplace equation in Eq (3.4) under the free-surface and sea-bed boundary conditions in Eqs. (3.9) and (3.11), rewritten here as:

$$\nabla^2 \phi = 0, \tag{3.12}$$

$$\left[\frac{\partial^2 \phi}{\partial t^2} + g\frac{\partial \phi}{\partial z}\right]_{z=0} = 0, \tag{3.13}$$

$$\left[\frac{\partial \phi}{\partial z}\right]_{z=-h} = 0. \tag{3.14}$$

To note, the Laplace equation in Eq. (3.12) is based on the incompressible and irrotational assumptions which are generally satisfied by sea water. The free-surface condition in Eq. (3.13) is based on the assumptions of inviscid, incompressible and irrotational fluid and small wave height. General observations of the characteristics of sea waves indicate that wave height is very small compared with wave length and hence this linearisation is valid for most of the moderate sea states. The sea-bed boundary condition in Eq. (3.14) is always satisfied since the fluid velocity is almost zero near the sea bed.

The Laplace equation Eq. (3.12) can be solved in an analytical way (Falnes, 2002; Newman, 1977) or in a numerical way with BEM codes (Babarit et al., 2012). Thus the fluid velocity, pressure and wave elevation can be represented by the potential function

ϕ, given as (Falnes, 2002):

$$\vec{v}(x,y,z,t) = \nabla\phi, \tag{3.15}$$

$$p(x,y,z,t) = -\rho(\frac{\partial\phi}{\partial t} + \frac{(\nabla\phi)^2}{2}) \approx -\rho\frac{\partial\phi}{\partial t}, \tag{3.16}$$

$$\eta(x,y,t) = -\frac{1}{g}[\frac{\partial\phi}{\partial t}]_{z=0}. \tag{3.17}$$

In this thesis, linear wave theory is selected due to two main reasons. On one hand, waves under moderate sea states satisfy the idea fluid (incompressible, irrotational, inviscid) and small wave height assumptions. Thus linear wave theory provides a good approximation of real sea waves. On the other hand, the $1/50$ scale PAWEC is tested in the Hull University wave tank, whose wave-maker is designed to generate regular/irregular waves according to linear wave theory. For some extreme sea states, linear wave theory is not valid and non-linear wave theories can provide appropriate approximations of ocean waves. The second or even higher order Stokes waves are introduced by Boccotti (2000); McCormick (1981).

3.2.2 Regular waves

Regular or harmonic waves, can be expressed by several specific parameters, including wave height, period, frequency, wave number, wave length and velocity. Amongst these parameters, only the wave period T and height H can be measured directly via wave gauges or pressure transducers. The wave length λ is measurable if more advanced equipments, like satellites or radars, are applied. Other parameters can be derived from these measurable parameters mathematically. As shown in Fig. 3.1, a harmonic wave propagating towards the $+x$ direction can be expressed as:

$$\eta(x,t) = \frac{H}{2}\cos(\frac{2\pi}{T}t - \frac{2\pi}{\lambda}x + \phi_w), \tag{3.18}$$

where ϕ_w represents the initial phase of wave elevation. The wave length λ and period T describe the spatio-temporal periodicity of the propagating wave.

The temporal periodicity can be represented by the wave frequency f, which is the reciprocal of the period T, given as:

$$f = 1/T. \tag{3.19}$$

Thus, the wave angular frequency ω is given as:

$$\omega = 2\pi f = 2\pi/T. \tag{3.20}$$

The spatial periodicity can be represented by the wave number k, defined as:

$$k = 2\pi/\lambda. \tag{3.21}$$

Thus, the wave elevation can be rewritten with the angular frequency ω and the wave number k, as:

$$\eta(x,t) = \frac{H}{2}\cos(\omega t - kx + \phi_w). \tag{3.22}$$

The spatial and temporal periodicities are related to each other with the dispersion relation (McCormick, 1981), as:

$$\omega^2 = gk\tanh(kh), \tag{3.23}$$

where h is water depth as shown in Fig. 3.1. $\tanh(X)$ is the hyperbolic tangent function of X.

If the water depth tends to infinity $h \to \infty$, the hyperbolic tangent function tends to a constant value $\tanh(kh) \to 1$. Here define the deep sea when the water depth h satisfy

$\tanh(kh) \approx 1$. If the approximation error is set within 1%, the water depth should satisfy $\tanh(kh) > 0.99$. That is, the dispersion relation can be simplified as $\omega^2 = gk$ with a small error (Falnes, 2002). In this situation, the sufficient and necessary condition of $\tanh(kh) > 0.99$ is:

$$h > 0.4\lambda. \tag{3.24}$$

In this thesis, the deep sea is defined when the water depth satisfies Eq. (3.24).

Based on the deep sea assumption in Eq. (3.24), the wave length can be expressed as:

$$\lambda = 2\pi/k = \frac{gT^2}{2\pi\tanh(kh)} \approx \frac{gT^2}{2\pi}. \tag{3.25}$$

Since this thesis focuses on wave energy conversion, it is also necessary to introduce the wave-energy transport concept, which is defined as the power density per unit width of wave front (Falnes, 2002), given as:

$$J = \frac{\rho g^2 T H^2}{32\pi}. \tag{3.26}$$

3.2.3 Irregular waves

The forming process of sea waves is random, which shows irregularities in wave height, period, phase and direction. Thus real sea waves are investigated in a statistical way using so-called power spectra. Several wave spectra were proposed to represent the properties of ocean waves, including the Pierson-Moskowitz (PM) spectrum, the Joint North Sea Wave Observation Project (JONSWAP) spectrum, the Neumann spectrum, the Bretschneider/Mitsuyasu spectrum and etc. The PM spectrum (Pierson and Moskowitz, 1964) is adopted in this study due to two reasons: (i) the PM spectrum shows good accordance with fully developed sea waves and (ii) the wave-maker system can stably generate irregular waves satisfying the PM spectrum for the wave tank tests in Chapter

6. The PM spectrum is given as:

$$S(\omega) = \frac{\alpha g^2}{\omega^5} \exp\left[-\beta \left(\frac{\omega_0}{\omega}\right)^4\right], \tag{3.27}$$

where $\alpha = 0.0081$, $\beta = 0.74$ are the empirical constants to identify the PM spectrum. The $\omega_0 = g/U_{19.5}$ is related to wind speed $U_{19.5}$ which is measured at 19.5 m above sea surface. This form of spectrum is not convenient and intuitive since it is difficult to relate wave properties (such as wave height, period, wave energy transport and sea state) with the spectrum parameters directly. One modification of the PM spectrum with the significant wave height H_s and the peak frequency f_p is adopted by International Ship Structure Congress (ISSC) [1], given as:

$$S(f) = \frac{5H_s^2}{16} \frac{f_p^4}{f^5} \exp\left(-\frac{5}{4}\frac{f_p^4}{f^4}\right). \tag{3.28}$$

The significant wave height H_s is defined as the average wave height of the highest $1/3$ waves and the peak frequency f_p is the frequency point at which $S(f)$ hits its peak value (Boccotti, 2000). The significant wave height H_s can be represented by the spectral moment, given as:

$$H_s = 4\sqrt{m_0}. \tag{3.29}$$

where m_0 is the zero order spectral moment. More generally, the spectral moments are defined as:

$$m_n = \int_0^\infty f^n S(f) df, \tag{3.30}$$

where n represents the order of the spectral moment.

[1] The PM spectrum identified by significant wave height and peak frequency is also called the ISSC wave spectrum.

The energy period of the spectrum is defined as (Falnes, 2007):

$$T_e = \frac{m_{-1}}{m_0}. \tag{3.31}$$

Thus the wave energy transport in Eq. (3.26) can be expressed by the significant wave height and the energy period. To substitute $H = H_s/\sqrt{2}$ and $T = T_e$ into Eq. (3.26) gives (Falnes, 2007):

$$J = \frac{\rho g^2 T_e H_s^2}{64\pi}. \tag{3.32}$$

3.3 Wave-PAWEC interaction

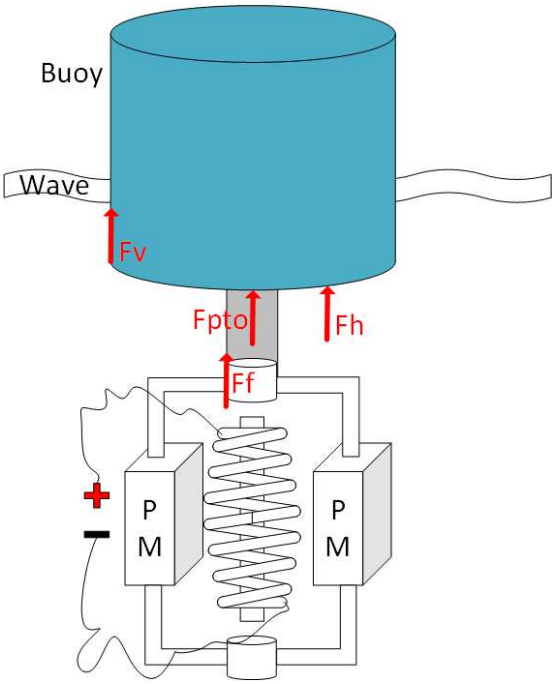

Fig. 3.2 Sketch of a semi-submerged cylindrical buoy constrained in heave mode.

As shown in Fig. 3.2, a $1/50$ scale floating cylindrical buoy moves up and down under the excitation of incident waves. Its motion obeys the Newton second law (Falnes,

2002), given as:

$$M_b\ddot{z} = F_h + F_{pto} + F_v + F_f. \tag{3.33}$$

Here $z(t)$ represents the buoy displacement in heave mode and $\ddot{z}(t)$ is the buoy acceleration in heave mode. For simplicity, only heave motion is considered in this study (other modes are constrained by a group of linear bearings). $F_v(t)$ represent the fluid viscous force due to the relative velocity between the buoy and water particles around it. $F_f(t)$ is the friction force determined by the mechanical structure. $F_{pto}(t)$ represents the PTO force, which is generally regarded as the control force. $F_h(t)$ represents the total hydrodynamic force of the wave-buoy FSI process, which is expressed as:

$$F_h = F_{hs} + F_e + F_r, \tag{3.34}$$

where $F_{hs}(t)$, $F_e(t)$ and $F_r(t)$ represent the hydrostatic, excitation and radiation forces, respectively.

The hydrostatic force F_{hs} is due to the mismatch between the buoyancy and gravity (that's why the gravitational force is not included in Eq. (3.33)) , which is given as (Falnes, 2002):

$$F_{hs} = -\rho g \pi r^2 z = -K_{hs} z, \tag{3.35}$$

where r and $K_{hs} = \rho g \pi r^2$ are the buoy radius and hydrostatic stiffness, respectively.

The incident wave and its interaction force $F_w(t)$ on the buoy can be expressed as the integration of pressure on the buoy wet surface, given as (Falnes, 2002; Newman, 1977):

$$F_w = \iint_{SW} p\vec{n}dS, \tag{3.36}$$

where SW means the wetted surface of the buoy. For linear modelling approaches, the wetted surface is generally assumed with a constant area if the WEC motion amplitude

is small. Some non-linear modelling methods(Merigaud et al., 2012; Peñalba et al., 2015; Penalba Retes et al., 2015) can handle time-varying wetted surface area.

Based on the superposition principle (Ogilvie, 1964; St Dinis and Pierson Jr, 1953), the wave-buoy interaction force can be computed via solving the diffraction and radiation problems. Thus wave excitation force F_e can be computed via solving the diffraction problem, whilst, the radiation force F_r can be calculated during the solving of the radiation problem.

The diffraction problem is to compute the scattering potential function $\phi_s(x,y,z,t)$ when the buoy is fixed at its equilibrium point and excited by incident waves (This is the principle to design the excitation tests in Section 6.6.4). The scattering potential function is the summation of the incident potential function $\phi_i(x,y,z,t)$ and the diffraction potential function $\phi_d(x,y,z,t)$, given as (Falnes, 2002):

$$\phi_s = \phi_i + \phi_d, \tag{3.37}$$

Similar to the linear wave theory, this scattering potential function $\phi_s(x,y,z,t)$ satisfies the Laplace function under the free-surface, sea-bed and solid-body boundary conditions, expressed as:

$$\nabla^2\phi_s = 0, \tag{3.38}$$

$$\left[\frac{\partial^2\phi_s}{\partial t^2} + g\frac{\partial\phi_s}{\partial z}\right]_{z=0} = 0, \tag{3.39}$$

$$\left[\frac{\partial\phi_s}{\partial z}\right]_{z=-h} = 0, \tag{3.40}$$

$$\frac{\partial\phi_s}{\partial\vec{n}} = 0. \tag{3.41}$$

To substitute the scattering potential ϕ_s into Eqs. (3.16) and (3.36), the excitation force is given as (Falnes, 2002):

$$F_e = -\rho\iint_{SW}\frac{\partial\phi_s}{\partial\vec{n}}\vec{n}dS. \tag{3.42}$$

Similarly, the radiation problem is to solve the radiation potential function $\phi_r(x,y,z,t)$ when the buoy oscillates in still water and radiates waves propagating outwards. The radiation potential function satisfies the Laplace function under the free-surface, sea-bed, solid-body and infinite boundary conditions, given as (Falnes, 2002):

$$\nabla^2\phi_r = 0, \tag{3.43}$$

$$\left[\frac{\partial^2\phi_r}{\partial t^2} + g\frac{\partial\phi_r}{\partial z}\right]_{z=0} = 0, \tag{3.44}$$

$$\left[\frac{\partial\phi_r}{\partial z}\right]_{z=-h} = 0, \tag{3.45}$$

$$\frac{\partial\phi_r}{\partial\vec{n}} = \vec{u}\cdot\vec{n}, \tag{3.46}$$

$$\left[\frac{\partial\phi_r}{\partial\vec{r}}\right]_{\vec{r}=\infty} = 0, \tag{3.47}$$

where $\vec{u}$ is the buoy velocity; $\vec{r}$ is the radiation vector outwards. Eq. (3.47) represents the far-field condition of the radiation effect. To substitute the radiation potential function ϕ_r into Eqs. (3.16) and (3.36), the radiation force is given as (Falnes, 2002):

$$F_r = -\rho\iint_{S_w}\frac{\partial\phi_r}{\partial\vec{n}}\vec{n}dS. \tag{3.48}$$

The diffraction and radiation problems can be solved by analytical or numerical methods. The analytical derivations are investigated by Falnes (2002); Newman (1977). Also, there are several numerical methods to solve the hydrodynamics of the floating buoy, the notable ones of which are the standard packages AQWA™, NEMOH, CHIL3D and etc.

3.4 Linear PAWEC modelling

3.4.1 NEMOH simulation

As mentioned above, the wave-PAWEC interaction can be transformed into a diffraction and radiation problem, which can be solved numerically. BEM is the most widely

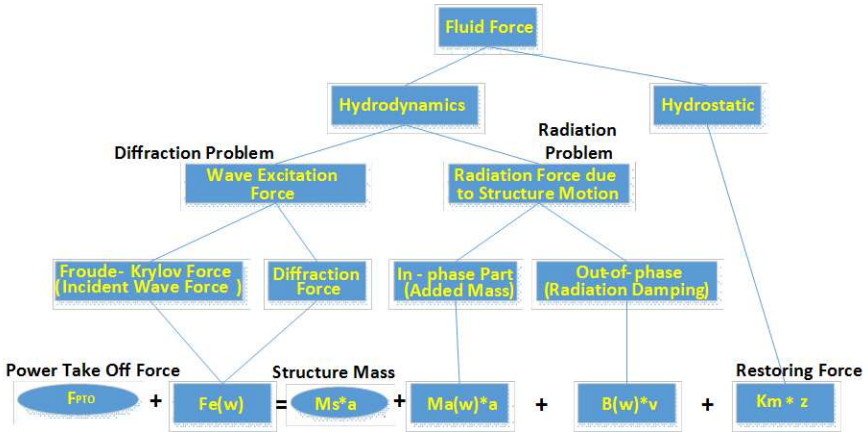

Fig. 3.3 The principle of NEMOH simulation.

used numerical approach to solve the diffraction and radiation problems in frequency-domain. The BEM codes, including NEMOH, AQWA™, WAMIT™, compute the linear hydrodynamics for offshore structures under sea wave excitations. Amongst these BEM packages, NEMOH is an open source CFD software to estimate the first order wave loads acting on offshore structures (Babarit and Delhommeau, 2015; LHEEA, 2016). It is a perfect alternative of the commercial BEM codes, like WAMIT™ and AQWA™. Thus in this study, NEMOH is selected to solve the wave-buoy interaction hydrodynamics.

As shown in Fig. 3.3, the BEM code NEMOH computes the hydrodynamic and hydrostatic forces separately. The hydrodynamic problem is separated into the diffraction and radiation problems. The former one aims to compute the wave excitation force whilst the latter one computes the radiation force due to buoy oscillation. Analytically, the radiation force can be separated into two parts: the in-phase part (radiation damping effect) and the out-of-phase part (added mass effect), given as:

$$F_r = -M_a(\omega)\ddot{z} - R_r(\omega)\dot{z}, \tag{3.49}$$

where $M_a(\omega)$ and $R_r(\omega)$ represent the added mass and radiation damping coefficient, which are determined by the structure and its motion.

NEMOH is a BEM code in the frequency-domain, which is subject to the assumptions of an ideal fluid (incompressible, irrotational and inviscid) as well as linear wave theory and the small body motion amplitude assumption. The diffraction and radiation problems are solved in small discretised sub-domains and the mesh size influences the

accuracy of computational results. Thus the result convergence due to varying mesh solutions should be checked first.

NEMOH simulation is based on the $1/50$ scale PAWEC with radius $r = 0.15$ m, draught $d = 0.28$ m and mass $M_b = 19.79$ kg. To compromise the computing time and the computation accuracy, a convergence verification of radiation damping coefficient is tested with variable mesh solutions. The radiation damping coefficient is tested with 20, 90, 270, 720 and 1320 mesh elements[2] and the results are shown in Fig. 3.4. The radiation damping coefficient tends to its final values when the mesh number is larger than 270.

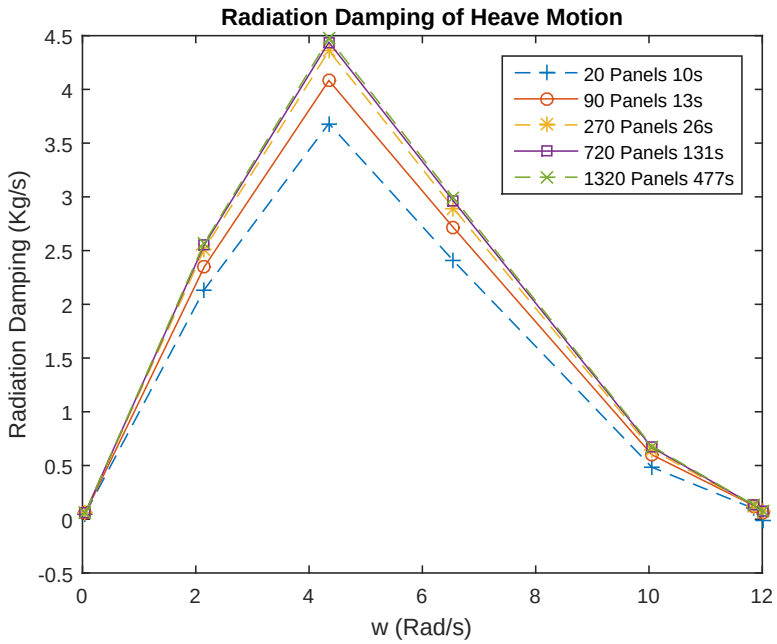

Fig. 3.4 Convergence verification of radiation damping coefficient in NEMOH.

It is clear that the computing time increases as the mesh size is refined. The results for 270, 720 and 1320 mesh elements converged to final values with computing time of 26, 131, and 477 s, respectively. The processor is an Intel Core2 Quad CPU Q8300 @ 2.50 GHz 2.50GHz with RAM 8.00 GB. The mesh of 720 elements is selected for the rest numerical simulations in NEMOH, since it provides accurate results and acceptable computational efficiency. The numerical results from NEMOH are illustrated in Figs. 3.5 and 3.6, with angular frequency $\omega = 0.05 : 0.05 : 12\ Rad/s$. Fig. 3.5 lists out the added mass and radiation damping coefficient varying with wave angular frequencies.

[2]Because of symmetry one quarter of the total number of mesh elements is used to represent the whole PAWEC device in NEMOH to improve the computational efficiency.

The excitation force FRF is given in Fig. 3.6, in formulations of amplitude and phase responses.

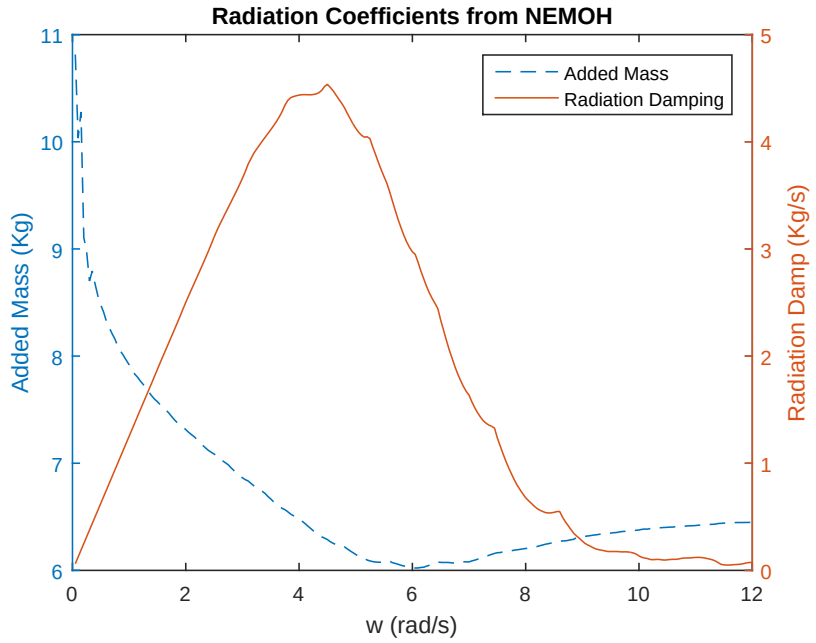

Fig. 3.5 Added mass and radiation damping coefficient from NEMOH.

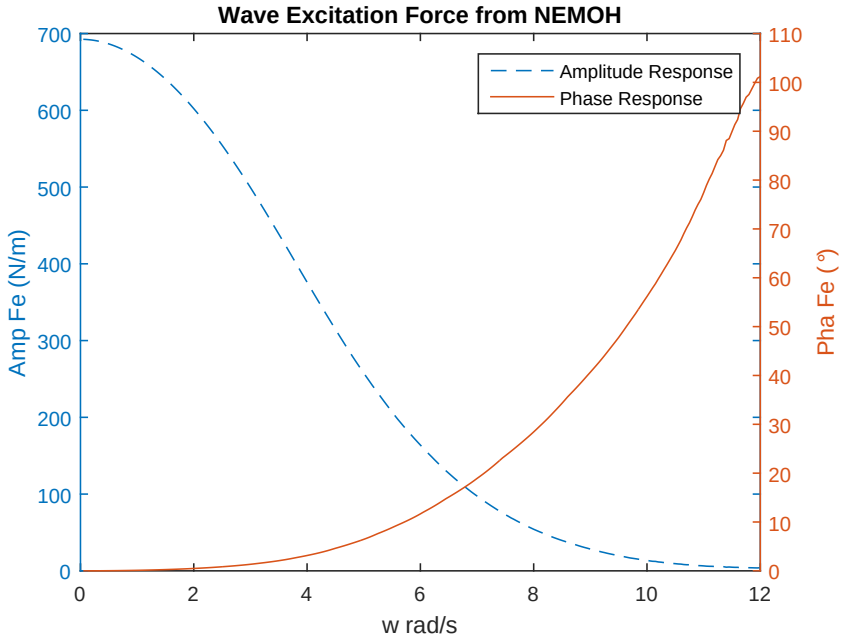

Fig. 3.6 Frequency response function of the wave excitation force from NEMOH.

3.4.2 Linear PAWEC model with frequency-determined parameters

If the viscous and friction forces are not considered, the buoy motion excited by harmonic waves in Eq. (3.33) can be rewritten as:

$$[M_b + M_a(\omega)]\ddot{z} + R_r(\omega)\dot{z} + K_{hs}z = F_e + F_{pto}. \tag{3.50}$$

A simple PTO mechanism can be simulated as a MSD system, given as:

$$F_{pto} = -[M_{pto}\ddot{z} + R_{pto}\dot{z} + K_{pto}z], \tag{3.51}$$

where M_{pto}, R_{pto} and K_{pto} represent the mass, damping coefficient and spring stiffness of the PTO mechanism. The MSD system is selected in this study due to tree main reasons: (i) The MSD is generally used by the wave energy community as the PTO mechanism and hence it is selected in this study to keep consistency with the published work. (ii) For a specific frequency, the PAWEC dynamics can be represented as a MSD system and hence the MSD system is preferred to represent the PTO mechanism for consistency. (iii) The MSD system shows its physical significance instinctively for the derivation of optimum PTO load.

Thus, Eq. (3.50) can be rewritten as:

$$F_e = M\ddot{z} + R\dot{z} + Kz, \tag{3.52}$$

where $M = M_b + M_a + M_{pto}$, $R = R_r + R_{pto}$ and $K = K_{hs} + K_{pto}$ are the total mass, damping coefficient and stiffness of the PAWEC. For a specific harmonic wave with known wave height H and angular frequency ω, the added mass M_a and radiation damping coefficient R_r are given in Fig. 3.5. The wave excitation force can be computed from its frequency-domain responses in Fig. 3.6. Alternatively, curve-fitting technique can be applied to give more convenient expressions of the radiation and excitation forces

in the frequency-domain, as:

$$M_a(\omega) = 87.01\exp\left[-\left(\frac{\omega+40.28}{26.73}\right)^2\right] \tag{3.53}$$

$$+ \; 4.716\exp\left[-\left(\frac{\omega-12.91}{7.092}\right)^2\right], \tag{3.54}$$

$$R_r(\omega) = 4.594\exp\left[-\left(\frac{\omega-4.225}{2.816}\right)^2\right], \tag{3.55}$$

$$A_{fe}(\omega) = 707\exp\left[-\left(\frac{\omega-0.2235}{4.849}\right)^2\right], \tag{3.56}$$

$$\phi_{fe}(\omega) = 3.78\exp\left[-\left(\frac{\omega-18.24}{7.129}\right)^2\right], \tag{3.57}$$

where $A_{fe}(\omega)$ and $\phi_{fe}(\omega)$ are the amplitude and phase responses of wave excitation force shown in Fig. 3.6. This curve-fitting technique is based on non-linear least-square Gaussian model and easy to apply via MATLAB® curve-fitting toolbox. Compared with other models, the Gaussian model gives very good fitting for peaks. This fitting technique is simple. However, if the wave frequency and amplitude are known, the PAWEC motion can be represented as a second-order system with frequency-determined parameters in Eqs. (3.53), (3.55), (3.56) and (3.57). This modelling approach is useful for some theoretical study of power maximisation and fits well with the swell waves. More sophisticated modelling approaches of the radiation force is given in Section 4.2 and modelling methods of the wave excitation force are described in Section 5.3. The curve-fitting results of the added mass in Eq. (3.53), the radiation damping coefficient in Eq. (3.55), the excitation amplitude and phase responses in Eqs. (3.56) and (3.57) are shown in Figs. 3.7, 3.8, 3.9 and 3.10, respectively. The dashed lines are the lower/upper 95% confidence boundaries.

As indicated in Figs. 3.7 and 3.8, the estimated radiation coefficients are very close to the NEMOH results. There are only very small errors in the very low frequency region within $\omega \in [0,1]$ rad/s. However, this region seldom contains wave energy for the scaled down PM spectrum and the buoy rarely experiences waves with such a low frequency. As illustrated in Figs. 3.9 and 3.10, the curve-fitting results of the excitation force FRF are very close to the NEMOH results within a wide range of wave frequency $\omega \in [0,12]$ rad/s. Alternatively, a goodness of fit function is defined to evaluate the

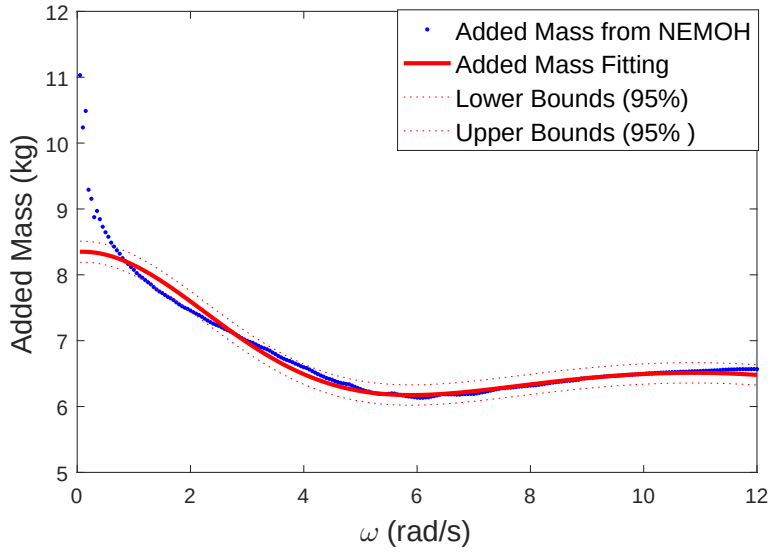

Fig. 3.7 Curve-fitting results of the added mass in Eq. (3.53).

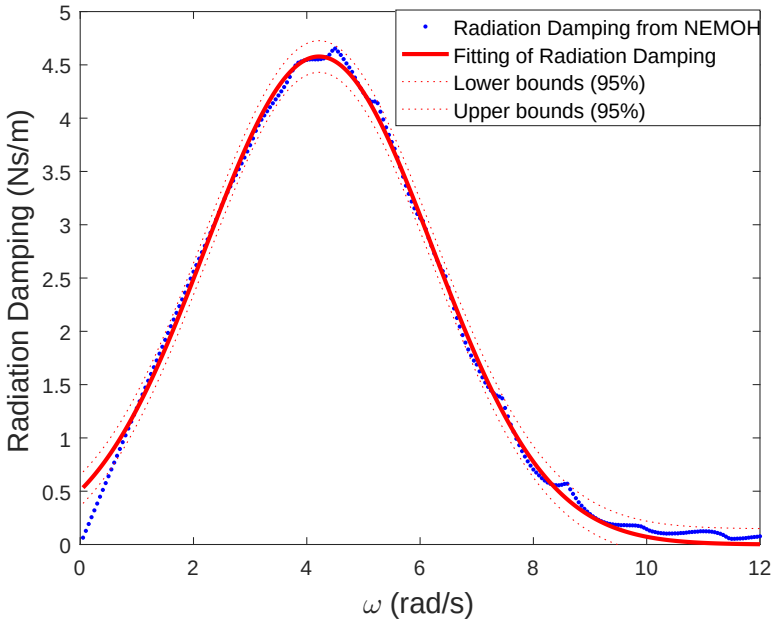

Fig. 3.8 Curve-fitting results of the radiation damping coefficient in Eq. (3.55).

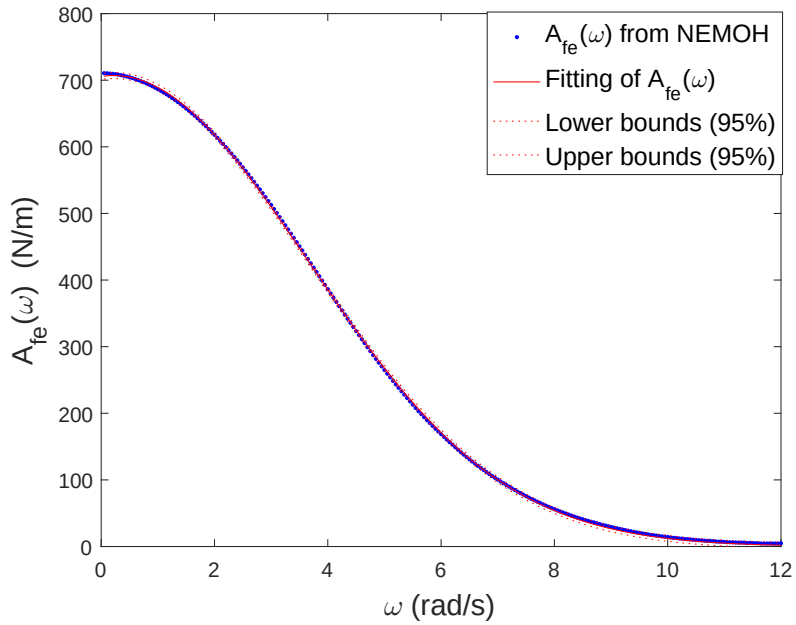

Fig. 3.9 Curve-fitting results of the amplitude response of wave excitation force in Eq. (3.56).

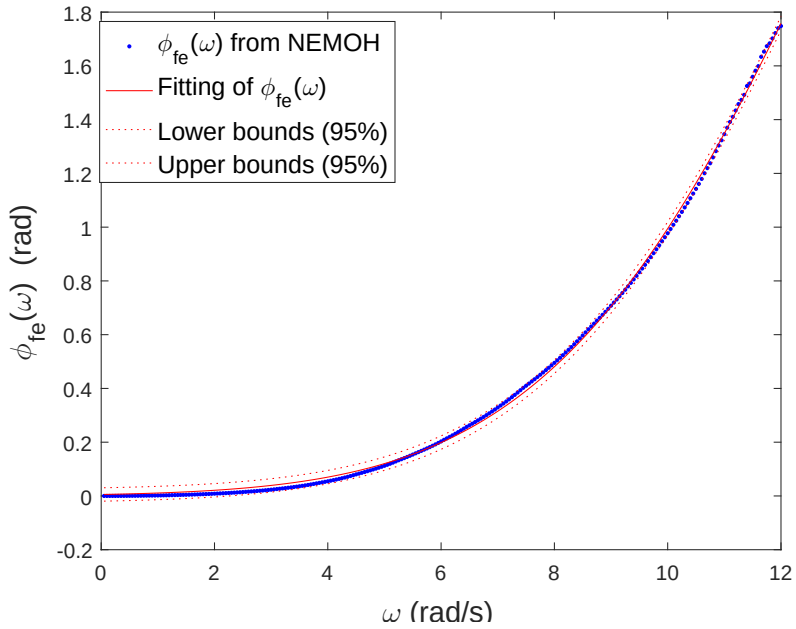

Fig. 3.10 Curve-fitting results of the phase response of wave excitation force in Eq. (3.57).

curve-fitting performance, given as:

$$G_{fit} = \frac{\Sigma_{n=1}^{N}(\tilde{X}_i - \bar{X})^2}{\Sigma_{n=1}^{N}(X_i - \bar{X})^2}, \tag{3.58}$$

where $\tilde{X}_i$, $\bar{X}$ represent the estimation and average value of the data X. N represents the length of the data X. The goodness of fit G_{fit} in Eq. (3.58) varies within $[0,1]$ in which $G_{fit} = 1$ means perfect fitting whilst $G_{fit} = 0$ indicates the worst fitting. The goodness of fit of the added mass, radiation damping, excitation amplitude and phase responses are 0.9903, 0.9979, 0.9999 and 0.9994, respectively.

Thus based on the curve-fitting results, the excitation force given in Eqs. (3.56) and (3.57), or Figs. 3.9 and 3.10 can be rewritten as:

$$F_e = \frac{H}{2} A_{fe}(\omega) \cos\left[\omega t + \phi_w + \phi_{fe}(\omega)\right]. \tag{3.59}$$

Similarly, the radiation parameters can be updated by the curve-fitting results in Eqs. (3.53) and (3.55) if the instantaneous frequency is estimated. Thus the radiation force in Eq. (3.49) can be rewritten as:

$$F_r = -\left[M_a(\omega)\ddot{z} + R_r(\omega)\dot{z}\right]. \tag{3.60}$$

In this situation, if the excitation force in Eq. (3.59) is considered as the system input and the buoy displacement is viewed as the system output, the PAWEC motion can then be represented by a second order system in Eq. (3.52) with frequency-determined parameters in Eqs. (3.59) and (3.60). To note that this simple modelling approach is valid for harmonic waves and is applicable for swell sea wave conditions.

3.5 Optimum condition for power maximisation

3.5.1 Complex amplitude expressions

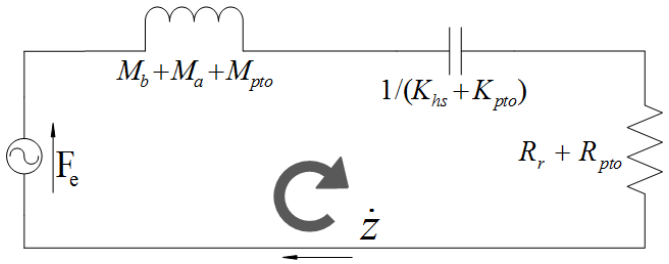

Fig. 3.11 Electromechanical analogue.

For a specific wave frequency, the PAWEC device can be represented as a second-order MSD system given in Eq. (3.52) and hence this mechanical MSD system can be considered as an analogue to a Resistance-Inductance-Capacitance (RLC) circuit as shown in Fig. 3.11. According to the study by Falnes (2002), the electric analogue approach is applicable and helpful for the deep understanding of the PAWEC system. In Fig. 3.11, wave excitation force is analogous to the driving voltage; buoy displacement is analogous to the charge on the capacitor and buoy velocity is analogous to the current in electrical circuit. In RLC circuit analysis, the complex representations of electrical voltage, current and impedance are widely adopted and show great advantage in the integral and differential operations. Therefore, the complex representations are applied in this thesis to derive the optimal power capture condition based on the maximum power transfer theorem.

In the domain of complex plane, the wave elevation can be expressed as (Falnes, 2002):

$$\eta = \frac{\hat{\eta}}{2} e^{j\omega t} + \frac{\hat{\eta}}{2} e^{-j\omega t}, \tag{3.61}$$

where $\hat{\eta} = \frac{H}{2} e^{j\phi_w}$ is the complex amplitude of wave elevation. Thus, wave excitation force in Eq. (3.59) can be rewritten as:

$$F_e = \frac{\hat{F}_e}{2} e^{j\omega t} + \frac{\hat{F}_e}{2} e^{-j\omega t}, \tag{3.62}$$

where $\hat{F}_e = A_{fe}(\omega)\hat{\eta}e^{j\phi_{fe}(\omega)}$ is the complex amplitude of wave excitation force. Due to the same principle, the radiation force can be expressed in a complex formation, as:

$$F_r = \frac{\hat{F}_r}{2}e^{j\omega t} + \frac{\hat{F}_r}{2}e^{-j\omega t}, \tag{3.63}$$

where $\hat{F}_r = -[j\omega M_a(\omega) + R_r(\omega)]\hat{v}$ is the complex amplitude of the radiation force. $\hat{v}$ is the complex amplitude of buoy velocity.

The PTO force can be expressed as:

$$F_{pto} = \frac{\hat{F}_{pto}}{2}e^{j\omega t} + \frac{\hat{F}_{pto}}{2}e^{-j\omega t}, \tag{3.64}$$

where $\hat{F}_{pto} = -(j\omega M_{pto} + R_{pto} + \frac{K_{pto}}{j\omega})\hat{v}$ is the complex amplitude of PTO force.

In a complex plane domain, the buoy displacement $z(t)$ can be written as:

$$z = \frac{\hat{z}}{2}e^{j\omega t} + \frac{\hat{z}}{2}e^{-j\omega t}, \tag{3.65}$$

where $\hat{z}$ is the complex amplitude of the buoy displacement. Therefore, the buoy motion in Eq. (3.52) can be represented in terms of complex amplitude, as:

$$\left[-M\omega^2 + K + j\omega R\right]\hat{z} = \hat{F}_e. \tag{3.66}$$

Thus the complex amplitude of buoy displacement is determined by the excitation force, buoy radiation properties and PTO mechanism, given as:

$$\hat{z} = \frac{\hat{F}_e}{-M\omega^2 + K + j\omega R}. \tag{3.67}$$

To submit $\hat{F}_e = A_{fe}(\omega)\hat{\eta}e^{j\phi_{fe}(\omega)}$ into Eq. (3.67), Response Amplitude Operation (RAO) can be given as:

$$RAO = \frac{|\hat{z}|}{H/2} = \frac{A_{fe}(\omega)}{\sqrt{[K - M\omega^2]^2 + R^2\omega^2}}. \tag{3.68}$$

Since the complex amplitude of buoy displacement is given in Eq. (3.67), the buoy velocity can be expressed in complex formulation, as:

$$v = \frac{\hat{v}}{2}e^{j\omega t} + \frac{\hat{v}}{2}e^{-j\omega t}, \tag{3.69}$$

where $\hat{v} = j\omega\hat{z}$ is the complex amplitude of buoy velocity. Alternatively, the buoy motion expressed in Eq. (3.66) can be represented by wave excitation force and buoy velocity, rewritten as:

$$\left[R + j\left(\omega M - \frac{K}{\omega}\right)\right]\hat{v} = \hat{F}_e. \tag{3.70}$$

As shown in Fig. 3.11, wave excitation force is analogous to voltage, whilst buoy velocity is analogous to current. Analogously, the mechanical impedance can be defined as the ratio between wave excitation force and buoy velocity (Falnes, 2002), given as:

$$Z = \frac{\hat{F}_e}{\hat{v}} = R + jX \tag{3.71}$$

where $X = \omega[M_b + M_a(\omega) + M_{pto}] - (K_{hs} + K_{pto})/\omega$ is the mechanical reactance and $R = R_r(\omega) + R_{pto}$ is the mechanical resistance. If $X = \omega[M_b + M_a(\omega) + M_{pto}] - (K_{hs} + K_{pto})/\omega = 0$, wave excitation force F_e is in-phase with buoy velocity v. This in-phase phenomenon is defined as *resonance* in this study, with the system natural frequency

given as (Falnes, 2002):

$$f_n = \frac{1}{2\pi}\sqrt{\frac{K}{M}}. \tag{3.72}$$

3.5.2 Optimum power conversion condition

For the direct-drive PAWEC system, wave power is captured first by the buoy during the wave-buoy interaction, named the captured power P_e in this study, given in a time-average formation as (Falnes, 2002):

$$P_e = \lim_{T\to\infty}\frac{1}{T}\int_0^T F_e v dt. \tag{3.73}$$

Here positive P_e means that the power is captured from waves to the PAWEC system.

Part of the captured power P_e is then consumed during the radiation procedure, named radiation power P_r (Falnes, 2002), given as:

$$P_r = -\lim_{T\to\infty}\frac{1}{T}\int_0^T F_r v dt. \tag{3.74}$$

Here the negative sign $-$ in Eq. (3.74) indicates that the power is consumed by the PAWEC system during the radiation process. That is, positive P_r means the power is dissipated.

The other part of the captured power is absorbed by the PTO mechanism and then converted to useful power, such as electrical power, referred to as the absorbed power P_{pto}, given as:

$$P_{pto} = -\lim_{T\to\infty}\frac{1}{T}\int_0^T F_{pto} v dt. \tag{3.75}$$

Positive P_{pto} means that the power goes out of the PAWEC system, e.g. electrical power to the grid. Similar to the mechanical impedance definition in Eq. (3.71), mechanical impedance of the PTO mechanism Z_{pto} is defined as:

$$Z_{pto} = R_{pto} + jX_{pto}, \tag{3.76}$$

where $X_{pto} = M_{pto}\omega - K_{pto}/\omega$ represents PTO mechanical reactance. Thus the complex amplitude of the PTO force can be expressed as:

$$\hat{F}_{pto} = -Z_{pto}\hat{v}. \tag{3.77}$$

Therefore, the mechanical impedance to describe the wave-buoy interaction is defined as the internal impedance Z_i (Falnes, 2002), given as:

$$Z_i = R_i + jX_i, \tag{3.78}$$

where $X_i = (M_b + M_a)\omega - K_{hs}/\omega$, $R_i = R_r$ represent internal reactance and resistance, respectively. Therefore, the PAWEC mechanical impedance are divided into the internal and PTO parts, written as:

$$Z = Z_i + Z_{pto}. \tag{3.79}$$

Also, buoy motion in Eq. (3.70) can be rewritten as:

$$(Z_i + Z_{pto})\hat{v} = \hat{F}_e. \tag{3.80}$$

Thus the optimal power conversion condition is derived from the maximum power transfer theorem, given as (Falnes, 2002):

$$Z_{pto} = Z_i^*, \tag{3.81}$$

where Z_i^* means the complex-conjugate operation of Z_i.

3.6 Summary

This Chapter discusses some fundamental theories of wave properties, wave-buoy interaction, PAWEC dynamics and power maximisation condition. Linear wave theory is detailed in Section 3.2 based on the assumptions of incompressible, irrotational and inviscid fluid and small wave height. With the incompressible and irrotational assumptions, the continuity equation in Eq. (3.1) can be simplified as a Laplace equation in Eq. (3.12). The free-surface boundary condition in Eq. (3.13) is linearised near the wave-air interface from the Navier-Stokes equation since the the wave height is assumed relative small to the wave length. The sea-bed boundary condition in Eq. (3.14) is valid since the fluid assumed inviscid. Therefore, the fluid velocity, pressure and wave elevation can be computed for the velocity potential function.

The wave-PAWEC interaction is outlined in Section 3.3 and a linear model with frequency-determined parameters is derived from BEM simulation. The BEM package NEMOH is applied to obtain the radiation and excitation parameters in frequency-domain with the results shown in Fig. 3.5 and 3.6. With a simple MSD PTO mechanism, the optimal power conversion condition is derived in Eq. (3.81) to maximise the captured power in Eq. (3.73) and the absorbed power in Eq. (3.75). To satisfy the optimal condition, reactive control and phase/amplitude control approaches are derived and simulated in Chapter 8.

The linear model derived in this Chapter is only valid for harmonic waves and applicable for the swell sea states. Although this simple model is very useful to derive the optimum condition for power maximisation, the main drawbacks are: (i) The radiation force is determined by the added mass in Eq. (3.53) and the radiation damping coefficient in Eq. (3.55), which limits the applicability of the model in irregular waves. (ii) Non-linear effects, such as the friction and viscous forces, are not considered in this model.

These non-linear effects are crucial, especially for the $1/50$ scale PAWEC. (iii) The model input is wave excitation force rather than wave elevation. For an oscillating prototype during wave tank tests, wave excitation force is not measurable. To obtain more applicable models, Chapter 4 deals with the identification of the radiation force, modelling of non-linear friction and viscous forces. Meanwhile, Chapter 5 identifies wave excitation force from wave measurements, or estimates the excitation force from the measurements of pressure, displacement and acceleration, or observes the excitation force as an unknown input from the system output (displacement).

Chapter 4

Linear and non-linear F2M modelling

4.1 Introduction

This Chapter discusses linear and non-linear F2M modelling approaches of the $1/50$ scale PAWEC. For the non-linear F2M modelling approach, the radiation force is approximated by a finite order system, the viscous force is modelled as the drag term in the Morison equation (Morison et al., 1950) and the friction force is represented by the Tustin model (Armstrong-Hélouvry et al., 1994; Tustin, 1947). Section 4.2 details the radiation force identification techniques in both the frequency- and time-domains. Based on the radiation approximations, a linear F2M model is derived to represent the PAWEC dynamics. The modelling of non-linear viscous and friction forces are discussed in Section 4.3 and their summation is defined as the lumped non-linear force. Therefore, the lumped non-linear force is substituted into the derived linear F2M model to form a non-linear F2M model. Tank tests are described in Section 4.4 to verify the lumped non-linear force model, the linear and non-linear F2M models. The numerical results are compared with the experimental data in Section 4.5.

4.2 Radiation force approximations

As illustrated in Chapter 3, the radiation force is characterised by the added mass and radiation damping coefficient in Eq. (3.60). The radiation force in Eq. (3.60) is rewritten

here, as:

$$F_r = -M_a(\omega)\ddot{z} - R_r(\omega)\dot{z}. \tag{4.1}$$

The added mass $M_a(\omega)$ and radiation damping coefficient $R_r(\omega)$ vary with wave frequency, given in Fig. 3.5 or by the curve-fitting results in Eqs. (3.53) and (3.55). This is a hybrid representation with frequency-determined parameters, which requires an external signal processing system to estimate the instantaneous frequency of incident waves. Thus the added mass $M_a(\omega)$ and radiation damping coefficient $R_r(\omega)$ can be updated with the instantaneous estimate of wave frequency $\tilde{\omega}$.

In the frequency-domain, the hybrid representation in Eq. (4.1) can be rewritten as (Falnes, 2002):

$$F_r(j\omega) = -[j\omega M_a(\omega) + R_r(\omega)]V(j\omega), \tag{4.2}$$

where $V(j\omega)$ represents buoy velocity in the frequency-domain. Alternatively, the radiation force can be expressed in the time-domain, called the Cummins equation (Cummins, 1962), as:

$$F_r = -A_\infty \dot{v} - k_r * v, \tag{4.3}$$

where A_∞ is the added mass at infinite frequency and $k_r(t)$ is the Impulse Response Function (IRF) of the radiation force, also known as the kernel function. $X * Y$ represents the convolution operation between X and Y. As a brief introduction to the convolution approximation procedure, the radiation force convolution term is defined as a subsystem $F_r^{'}(t)$, written as:

$$F_r^{'} = k_r * v = \int_0^t k_r(t-\tau)v(\tau)d\tau. \tag{4.4}$$

The relationship of the radiation coefficients between the time- and frequency-domains is derived by Ogilvie (1964) and referred to as the Ogilvie relation, given as:

$$M_a(\omega) = A_\infty - \frac{1}{\omega}\int_0^\infty k_r(t)sin(\omega t)dt, \tag{4.5}$$

$$R_r(\omega) = \int_0^\infty k_r(t)cos(\omega t)dt. \tag{4.6}$$

Thus, the FRF of the radiation subsystem $F_r^{'}(t)$ can be expressed as (Ogilvie, 1964):

$$K_r(j\omega) = j\omega\left[M_a(\omega) - A_\infty\right] + R_r(\omega). \tag{4.7}$$

Alternatively, the radiation kernel function can be represented by the radiation coefficients, as:

$$k_r = \frac{2}{\pi}\int_0^\infty R_r(\omega)cos(\omega t)d\omega, \tag{4.8}$$

$$A_\infty = \lim_{\omega\to\infty} M_a(\omega). \tag{4.9}$$

These hydrodynamic coefficients of $F_r(t)$ are computed by the BEM code NEMOH. The added mass and radiation damping coefficient in the frequency-domain are given in Fig. 3.5. The time-domain kernel function (or IRF) of the radiation force $k_r(t)$ is shown in Fig. 4.1.

The convolution operation in Eq. (4.3) is not convenient and straightforward for buoy hydrodynamic analysis and control system design. Hence, it is important to approximate the convolution term with a finite order system model. The causality of the radiation process is proved by Wehausen (1992). Thus the radiation force can be approximated by a finite order system with constant parameters via frequency- or time-domain system identification approaches. These approaches are investigated by Beirdol et al. (2007); Davidson et al. (2015); Kristiansen et al. (2005); Roessling and Ringwood (2015); Taghipour et al. (2008); Unneland et al. (2006); Valério et al. (2008). Thus these radiation force approximation approaches are mature and this Section just gives a brief description.

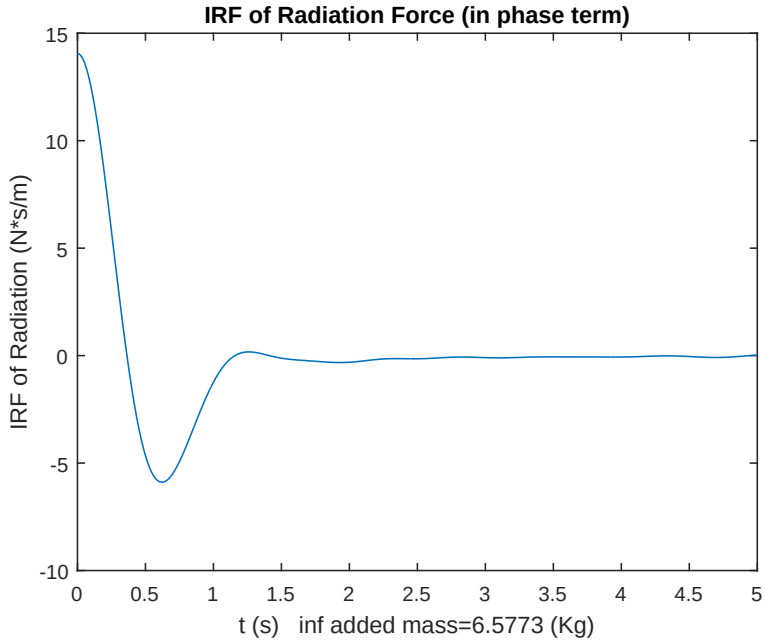

Fig. 4.1 The radiation IRF obtained from NEMOH simulation.

4.2.1 Frequency-domain identification of radiation force

The frequency-domain representation of the radiation force in Eq. (4.2) can be rewritten as:

$$F_r^{'}(j\omega) = K_r(j\omega)V(j\omega). \tag{4.10}$$

The FRF $K_r(j\omega)$ is the frequency-domain representation of $k_r(t)$, represented by its Fourier transform as:

$$K_r(j\omega) = \int_0^{\infty} k_r(\tau)e^{-j\omega\tau}d\tau. \tag{4.11}$$

Thus frequency-domain system identification technique can be applied to the FRF to approximate the convolution term, which is investigated by Perez and Fossen (2009, 2011); Roessling and Ringwood (2015); Taghipour et al. (2008); Valério et al. (2008).

In this study, MATLAB® function *invfreqs* and *tf2ss* are applied to the FRF $K_r(j\omega)$ in Eq. (4.7) or (4.11) to obtain a state-space model. Thus the convolution term can be

approximated by a state-space model, given as:

$$\dot{x}_{r,f} = A_{r,f}x_{r,f} + B_{r,f}v, \tag{4.12}$$
$$F_r^{'} = C_{r,f}x_{r,f}, \tag{4.13}$$

where $x_{r,f} \in \mathbb{R}^{n\times 1}$ is the state vector for the identified system and n is the system order number. $v(t)$ is buoy velocity. $A_{r,f} \in \mathbb{R}^{n\times n}$, $B_{r,f} \in \mathbb{R}^{n\times 1}$, $C_{r,f} \in \mathbb{R}^{1\times n}$ are the system matrices.

To determine the system order, a goodness of fit function $G_{fit,r}$ is defined with a cost-function of the Normalised Mean Square-Error (NMSE), as:

$$G_{fit,r} = 1 - \left\| \frac{x-\tilde{x}}{x-\bar{x}} \right\|_2^2, \tag{4.14}$$

where x is the original data (it can be the added mass, radiation damping or the IRF) and $\tilde{x}$ represents the approximation of x. $\|X\|_2$ is the 2-norm operation of X and $\bar{X}$ is the mean value of X. The goodness of fit tends to 1 for the perfect fitting and tends to $-\infty$ for the worst fitting.

The frequency-domain identified systems with second, third, fourth and firth order are compared with NEMOH data in Figs. 4.2 and 4.3. A third order system gives a good fitting in the frequency-domain for both the added mass ($G_{fit,r} = 0.9604$) and the radiation damping coefficient ($G_{fit,r} = 0.9858$). Therefore, $n = 3$ is selected for the frequency-domain identification of the radiation force.

4.2.2 Time-domain identification of radiation force

For control system design, a time-domain model is preferred. Finite order approximations of the radiation force in the time-domain are proposed and applied for offshore structure motion prediction by Davidson et al. (2015); Genest and Ringwood (2016b); Kristiansen et al. (2005); Roessling and Ringwood (2015); Yu and Falnes (1995).The comparative studies between the time- and frequency-domain identification approaches are discussed by Pérez and Fossen (2008); Taghipour et al. (2008). In this study, the

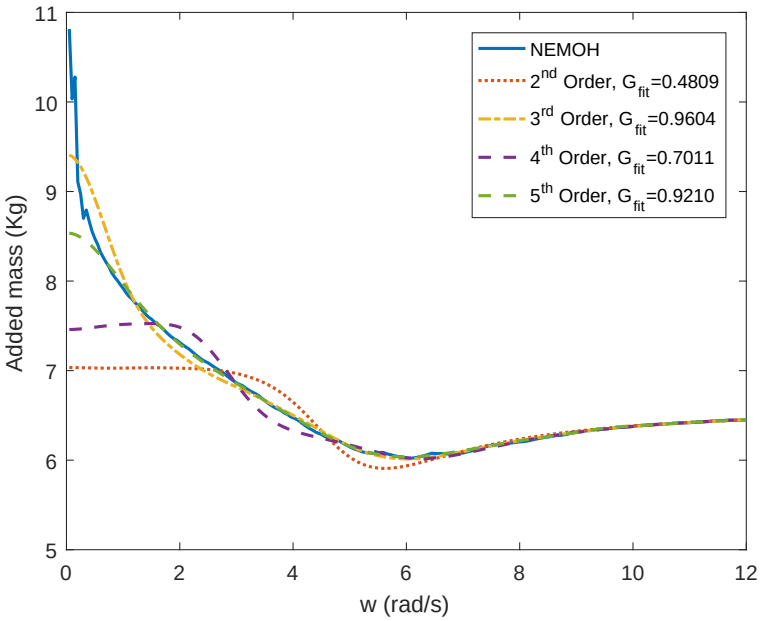

Fig. 4.2 Comparison of added mass between NEMOH and frequency-domain identified results.

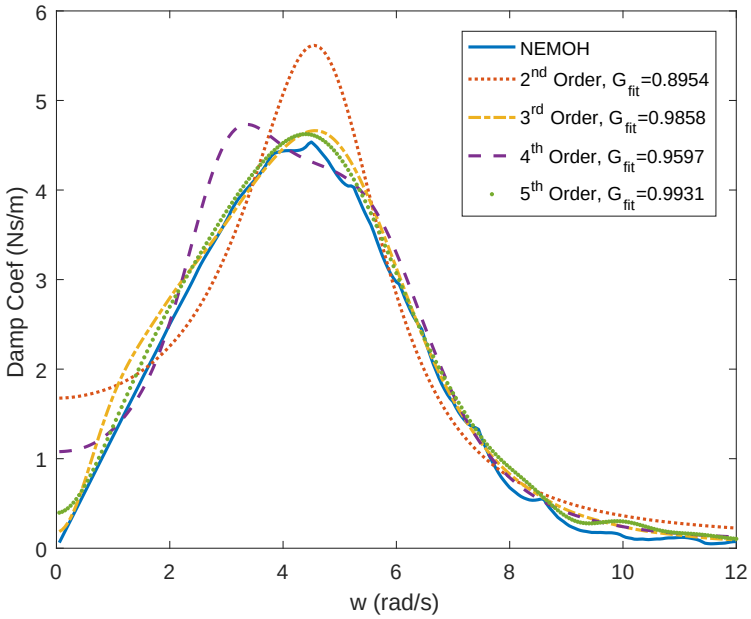

Fig. 4.3 Comparison of radiation damping coefficient between NEMOH and frequency-domain identified results.

realisation theory method is applied to identify a linear state-space model from the radiation force IRF in the time-domain.

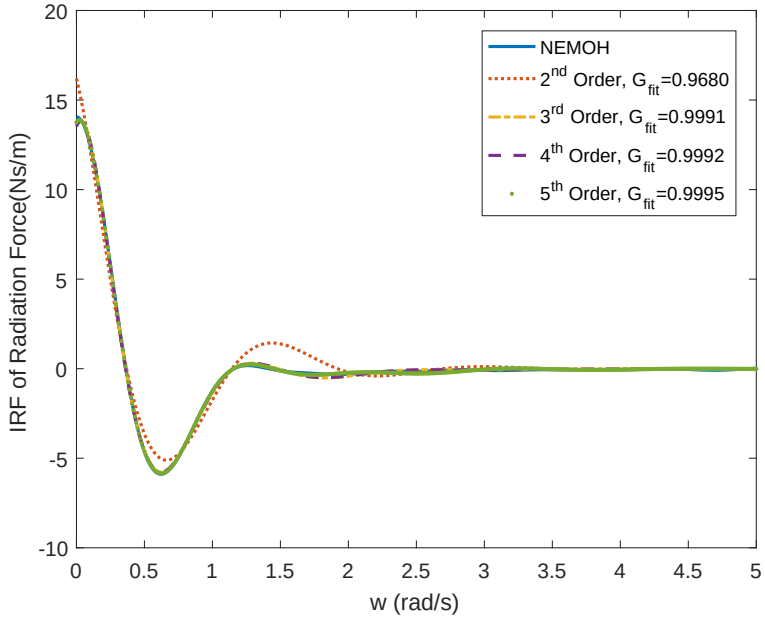

Fig. 4.4 Comparison of IRFs between NEMOH and time-domain identified results.

The IRF $k_r(t)$ in Eq. (4.4) is obtained from NEMOH simulation, shown in Fig. 4.1. The realisation theory is applied on the IRF to get a linear state-space model directly with MATLAB® function *imp2ss* (Kung, 1978) from the Robust Control Toolbox. Thus the convolution term can be approximated by:

$$\dot{x}_r = A_r x_r + B_r v, \tag{4.15}$$

$$F_r^{'} = C_r x_r, \tag{4.16}$$

where $x_r \in \mathbb{R}^{n\times 1}$ is the state vector of the identified system. $A_r \in \mathbb{R}^{n\times n}$, $B_r \in \mathbb{R}^{n\times 1}$ and $C_r \in \mathbb{R}^{1\times n}$ are the system matrices for the identified system.

The order of the initially identified system is quite high and determined by the IRF data. Model reduction is required and can be achieved by the square-root balanced model reduction method with MATLAB® function *balmar* (Safonov and Chiang, 1988). The appropriate order is determined by the goodness of fit function $G_{fit,r}$ defined in Eq. (4.14).

The IRFs of second, third and fourth order linear state-space models, determined by time-domain system identification techniques, are compared with the original IRF from NEMOH in Fig. 4.4. The goodness of fit are $0.9680, 0.9991, 0.9992$ for the second, third and fourth order systems, respectively. The IRF of the third order system matches the original IRF well and a further order increase introduces extra system complexity without improving the approximation accuracy significantly. Thus a third order system is adopted to approximate the convolution term.

Comparing the goodness of fit, the time-domain identified third order system shows slight better performance than the frequency-domain identified third order system. Therefore, a third order state-space model identified in the time-domain is adopted to approximate the convolution term in Eq. (4.3) to provide a straightforward, convenient and highly efficient mathematical model for numerical analysis and PAWEC control system design. The matrices of Eq. (4.15) and (4.16) are given as:

$$A_r = \begin{bmatrix} -3.1848 & -4.3372 & -3.1009 \\ 4.3372 & -0.0875 & -0.3882 \\ 3.1009 & -0.3882 & -2.8499 \end{bmatrix}, \tag{4.17}$$

$$B_r = \begin{bmatrix} -40.6964 & 5.9737 & 16.2722 \end{bmatrix}^\top, \tag{4.18}$$

$$C_r = \begin{bmatrix} -0.4070 & -0.0597 & -0.1627 \end{bmatrix}. \tag{4.19}$$

4.2.3 Linear force-to-motion modelling

As wave excitation force is viewed as the system input and buoy displacement is set as the system output, a linear F2M model is derived according to Eq. (3.60), as:

$$x_{f2m} = [z \;\; \dot{z} \;\; x_r]^T, \tag{4.20}$$

$$\dot{x}_{f2m} = A_{f2m}x_{f2m} + B_{f2m}F_e + B_{f2m}F_{pto}, \tag{4.21}$$

$$y_{f2m} = C_{f2m}x_{f2m}, \tag{4.22}$$

with

$$A_{f2m} = \begin{bmatrix} 0 & 1 & 0 \\ -\frac{K_{hs}}{M_t} & 0 & -\frac{C_r}{M_t} \\ 0 & B_r & A_r \end{bmatrix}, \tag{4.23}$$

$$B_{f2m} = \begin{bmatrix} 0 & -\frac{1}{M_t} & 0 \end{bmatrix}^T, \tag{4.24}$$

$$C_{f2m} = \begin{bmatrix} 1 & 0 & 0 \end{bmatrix}, \tag{4.25}$$

where $M_t = M_b + A_\infty$ represents the total mass. $x_{f2m} \in \mathbb{R}^{5\times1}$ is the F2M state vector. $A_{f2m} \in \mathbb{R}^{5\times5}$, $B_{f2m} \in \mathbb{R}^{5\times1}$ and $C_{f2m} \in \mathbb{R}^{1\times5}$ are the system matrices.

This linear F2M model is convenient and straightforward for numerical analysis of PAWEC hydrodynamics and also for the development of control systems. If the initial condition $x(0)$ and the excitation force F_e are applied to excite the linear model at time $t = 0$ s, the response can be written as:

$$z = C_{f2m} e^{A_{f2m}t} x_{f2m}(0) + \int_0^t e^{A_{f2m}(t-\tau)} B_{f2m} [F_e(\tau) + F_{pto}(\tau)] d\tau. \tag{4.26}$$

For the hydrodynamic tests, the PTO force is set $F_{pto} = 0$ N. The linear system response can be separated into two parts, the zero-input and zero-state responses, as:

- **Free-decay tests**: if $F_e = 0$ and $x_{f2m}(0) \neq 0$, the system response is called zero-input response, identified here as the *free-decay tests*, written as:

$$z = C_{f2m} e^{A_{f2m}t} x_{f2m}(0). \tag{4.27}$$

- **Forced-motion tests**: if $F_e \neq 0$ and $x_{f2m}(0) = 0$, the system response is called the zero-state response, identified here as the *forced-motion tests*, written as:

$$z = \int_0^t C_{f2m} e^{A_{f2m}(t-\tau)} B_{f2m} F_e(\tau) d\tau. \tag{4.28}$$

In this study, a series of free-decay tests are conducted in a wave tank to compare with the numerical simulations, discussed further in Section 4.4. One main drawback of this linear F2M model is that the omission of non-linear effects leads to overestimation of buoy motion, especially when the incoming wave frequency is close to the PAWEC

natural frequency. This work places special emphasis on these non-linear viscous and friction phenomena and the non-linear effects are discussed in Section 4.3.

4.3 Non-linear force-to-motion modelling

In practice, the viscous force due to fluid viscosity and mechanical friction due to relative motion cannot be ignored. In this work, the quadratic viscous force is modelled as the drag force term in the Morison equation (Morison et al., 1950), whilst the friction force is modelled as the Tustin model, a combination of the Stribeck, Coulomb and damping friction forces (Armstrong-Hélouvry et al., 1994; Tustin, 1947). The summation of the viscous and friction forces is defined as the lumped non-linear force and is the focus of this Section, leading to a more applicable non-linear F2M model for the investigation of PAWEC dynamics.

4.3.1 Modelling of viscous force

As suggested by Eidsmoen (1996); Li and Yu (2012); Ringwood et al. (2014), the viscous force $f_v(t,x)$ follows the drag force in the Morison equation (Morison et al., 1950). The initial term in the Morison equation is not discussed in the viscous force as it is included in the PAWEC hydrodynamics as the added mass phenomena. Hence, the viscous force can be expressed as:

$$f_v(t,x) = -0.5\rho C_d \pi r^2 (\dot{z}-u)|\dot{z}-u|, \tag{4.29}$$

where C_d is the viscous coefficient; $u(t)$ is the vertical velocity of water particles around the buoy. C_d is a function of the Reynolds number R_e, the Keulegan-Carpenter number K_c and the roughness number K_r (Gudmestad and Moe, 1996). As suggested in by Gudmestad and Moe (1996), the empirical value of C_d varies from 0.6 to 1.2. For small K_c value ($K_c \approx 3.67$ for the $1/50$ scale PAWEC), the appropriate range of C_d from 0.8 to 1 is commonly acceptable (Sarpkaya, 1986) and hence $C_d = 0.93$ is selected in this study on a semi-empirical basis. Alternatively, the viscous coefficient C_d can be estimated from wave tank tests (Guo et al., 2017).

4.3.2 Modelling of friction force

Several mechanical friction models are reviewed by Armstrong-Hélouvry et al. (1994). Among these, the Tustin model is expressed as a combination of the Coulomb, Stribeck and damping friction forces by Armstrong (1988); Armstrong-Hélouvry et al. (1994); Marton and Lantos (2007); Tustin (1947). As shown in Fig. 4.5, the friction force components can be divided as:

$$f_c(t,x) = -s_v F_c, \tag{4.30}$$

$$f_s(t,x) = -s_v F_s e^{-C_s|\dot{z}|}, \tag{4.31}$$

$$f_d(t,x) = -s_v C_f |\dot{z}|, \tag{4.32}$$

where $s_v = sgn(\dot{z})$ is the sign of the buoy velocity; $f_c(t,x)$ is the Coulomb friction force with its coefficient F_c; $f_s(t,x)$ is the Stribeck friction force with its coefficient F_s and shape factor C_s; $f_d(t,x)$ is the damping friction force with its coefficient C_f. The negative symbol means that the friction force always impedes the PAWEC velocity.

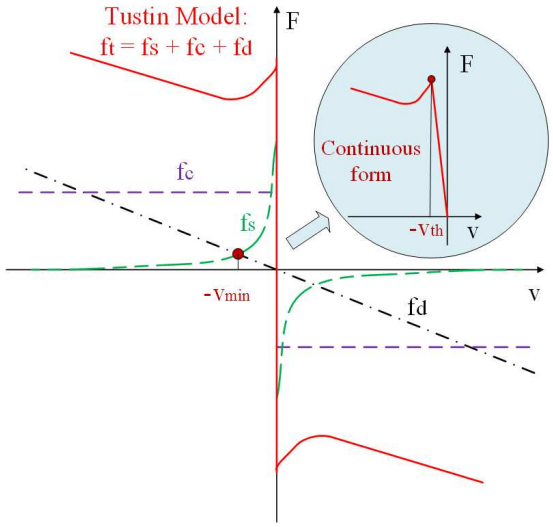

Fig. 4.5 Sketch of the Tustin model with continuous approximation (inset).

As shown in Fig. 4.5, the Tustin model is expressed as:

$$f_f(t,x) = -s_v(F_c + F_s e^{-C_s|\dot{z}|} + C_f|\dot{z}|). \tag{4.33}$$

The Stribeck shape factor can be determined by the point of intersection of the Stribeck friction force curve and the damping friction force line, given as:

$$C_s = \frac{1}{V_{min}} \ln \frac{C_f V_{min}}{F_s}, \tag{4.34}$$

where V_{min} is the velocity related to the point of intersection (also the point associated to the minimum friction in Eq. (4.33)).

A key characteristic of this model is that the friction is discontinuous at the zero-velocity point. The discontinuity may cause difficulties for numerical modelling of the friction force. The mechanical friction force can be estimated from the velocity measurement made during wave tank tests. Measurement noise is unavoidable and has a significant influence on the friction modelling, especially when the velocity is close to zero. Therefore, a velocity threshold V_{th} is applied to the Tustin model in this work to improve its continuity within the zero-velocity region. As shown in the inset in Fig. 4.5, the continuous formulation of the Tustin model can be rewritten as:

$$f_f(t,x) = \begin{cases} -s_v(F_c + F_s e^{-C_s|\dot{z}|} + C_f|\dot{z}|), & |\dot{z}| \geq V_{th}; \\ -s_v(F_c + F_s e^{-C_s V_{th}} + C_f V_{th}) \frac{|\dot{z}|}{V_{th}}, & |\dot{z}| < V_{th}. \end{cases} \tag{4.35}$$

V_{th} is always set with a very small value. For the continuous form, the Stribeck shape factor can be rewritten as:

$$C_s = \frac{1}{V_{min} - V_{th}} \ln \frac{C_f (V_{min} - \frac{V_{th} F_c}{F_s + F_c})}{F_s}. \tag{4.36}$$

In the friction model in Eq. (4.35), there are five unknown parameters (F_s, F_c, C_f, V_{th} and V_{min}) to be determined.

4.3.3 Non-linear force-to-motion modelling

In the wave tank tests, the viscous and friction forces are lumped and cannot be decoupled from each other. Therefore, a lumped non-linear force $F_{ln}(t,x)$ is defined as

a summation of the viscous force $f_v(t,x)$ and the friction force $f_f(t,x)$, given as:

$$f_{ln}(t,x) = f_v(t,x) + f_f(t,x). \tag{4.37}$$

If the lumped non-linear force is considered, Eq. (3.33) is rewritten as:

$$M\ddot{z} = F_e + F_r + F_{hs} + f_f(t,x) + f_v(t,x), \tag{4.38}$$
$$= F_e + F_r + F_{hs} + f_{ln}(t,x). \tag{4.39}$$

Thus the $1/50$ scale PAWEC hydrodynamics can be expressed as a non-linear F2M model in the state-space formulation, as:

$$\dot{x}_{f2m} = A_{f2m}x_{f2m} + B_{f2m}F_e + B_{f2m}f_{ln}(t,x) \tag{4.40}$$
$$y_{f2m} = C_{f2m}x_{f2m}, \tag{4.41}$$

The system matrices are given in Eq. (4.23), (4.24) and (4.25). The lumped non-linear force is given in Eq. (4.37). All the non-linear viscous and friction forces parameters can be observed from free-decay and free-fall tests, as discussed in Section 4.4.2.

4.4 Wave tank tests

To check the validity of the linear and non-linear F2M models, a series of free-fall and free-decay tests are conducted in the Total Environment Simulator (TES) tank (Parsons, 2016). The TES is a large world-class experiment wave tank designed for environmental studies. The wave tank can replicate through appropriate scaling a wide range of sea wave conditions (Parsons, 2016). Hence the wave tank system provides valuable experimental facility for wave energy system development. This Section only details the free-fall and free-decay tests. More information of wave tank tests is detailed in Chapter 6.

4.4.1 Free-fall tests

The mechanical friction profile can be estimated experimentally. In free-fall tests, the buoy is lifted into the air (above the water), held stable for a short period and then released suddenly. The free-fall motion fits Newton's second law and hence the mechanical friction force can be "pseudo" measured as $f_{f,m}(t)$, written as:

$$f_{f,m} = -Mg - Ma_m, \tag{4.42}$$

where $a_m(t)$ is the measured heaving acceleration. Meanwhile, the LVDT records the buoy displacement to provide "pseudo" velocity measurement $v_m(t)$ via the difference method.

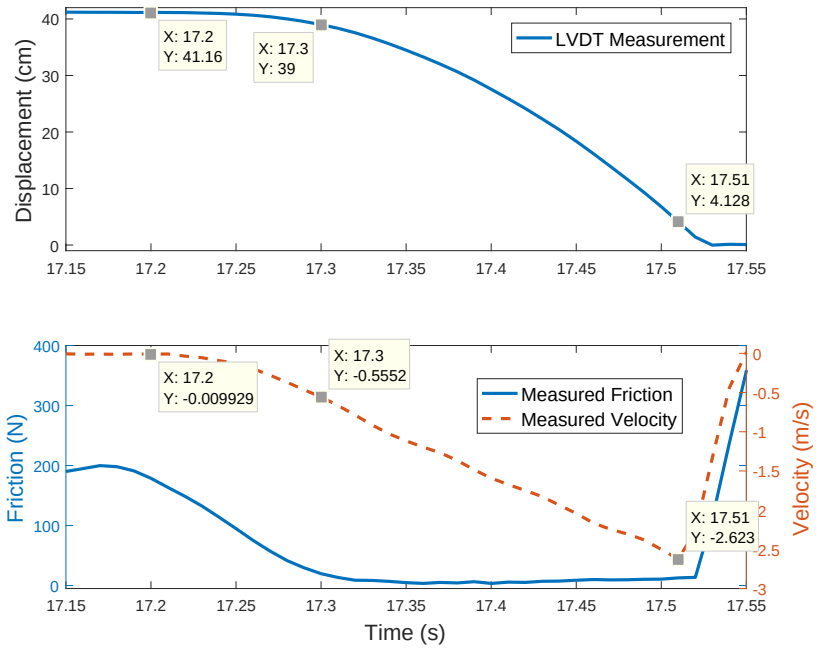

Fig. 4.6 Free-fall tests to determine the Coulomb and damping coefficients.

The free-fall test results are shown in Fig. 4.6. According to the displacement and velocity measurements, the buoy is released at $t = 17.20$ s and then experiences free acceleration until $t = 17.51$ s, within which the measured velocity increases stably. After $t = 17.51$ s, the buoy hits the wave tank gantry.

The parameters of the Coulomb and damping forces in Eq. (4.35) are obtained via linear least-squares fitting applied to the measured friction and velocity data within the time interval from $t = 17.30$ s to $t = 17.51$ s. The resulting parameters are:

$$f_{f,m} = F_c - C_f v_m = 2.6579 - 2.988 v_m. \tag{4.43}$$

Thus $F_c = 2.6579$ N and $C_f = 2.988$ Nsm^{-1} are chosen for the mechanical friction model.

4.4.2 Free-decay tests

As defined in Eq. (4.27), free-decay tests are conducted in the wave tank. The buoy is pushed down to a non-zero initial position, held stable for a short term and then released suddenly [1] During free-decay tests, the lumped non-linear force is "pseudo" measured as $f_{ln,m}(t)$, given as:

$$f_{ln,m} = Ma_m - \pi r^2 \bar{p}, \tag{4.44}$$

where $\bar{p}(t)$ is the mean value of PS1-5 measurements. It is fair to note that the measurement via Eq. (4.44) only gives a simple approximation of the lumped non-linear force. More sensors are needed to achieve measurement performance.

During a free-decay test, the buoy oscillates several times and is damped to its equilibrium point. The point where $v_m(t)$ changes its direction is defined as the *zero-crossing point*. Within the zero-crossing point vicinity, the measured velocity is close to zero and hence the fluid viscous force is small enough to be ignored. Therefore the friction parameters in Eq. (4.35), F_s and V_{min}, can be observed from the measurements of $f_{ln,m}(t)$ and $v_m(t)$. According to the comparison between the experimental data and the

[1] The free-decay tests are symmetric to lift the buoy up or push the buoy down. However, it is observed that the vertex shedding is much more sever by lifting to buoy up than pushing the buoy down. Since the non-linear effect of the vertex shedding is out of the scope of this study and hence all the free-decay tests are conducted by pushing the buoy down to a non-zero displacement.

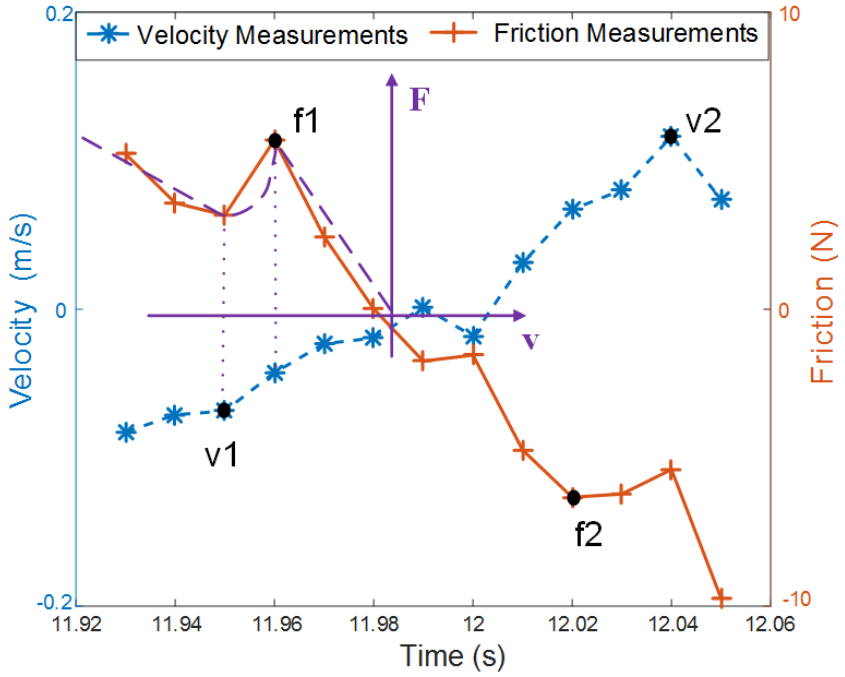

Fig. 4.7 Zero-crossing point to determine the Stribeck force parameters.

Tustin model in Fig. 4.7, the parameters F_s and V_{min} are written as:

$$F_s = (f_1 - f_2)/2 - F_c, \tag{4.45}$$

$$V_{min} = (v_2 - v_1)/2, \tag{4.46}$$

where f_1, f_2 locate the breakaway friction points and v_1 and v_2 are associated with the points where $f_d(t,x)$ intersects with $f_s(t,x)$. The average values of $F_s = 3.5574$ N and $V_{min} = 0.0838$ ms^{-1} are computed from ten zero-crossing points leading to the data in Table 4.1.

To determine the velocity threshold, the buoy is fixed to its equilibrium point. In this case the velocity is zero but the velocity measurement varies around zero due to measurement noise. In this situation, the measurement noise has a significant influence on the friction estimation. Observed from $v_m(t)$, the magnitude of the measurement noise is around 0.0375 ms^{-1}. To attenuate the influence caused by the measurement noise, the velocity threshold (see the inset in Fig. 4.5) is selected as $V_{th} = 0.038$ ms^{-1}, slightly larger than 0.0375 ms^{-1}.

Table 4.1 Parameters of the friction/viscous models in Eqs. (4.35) and (4.29).

Parameter	Unit	Value
F_s	N	5.0065
F_c	N	3.1160
f_d	$\mathrm{N}\cdot\mathrm{s}\cdot\mathrm{m}^{-1}$	2.7200
v_{th}	$\mathrm{m}\cdot\mathrm{s}^{-1}$	0.038
v_{min}	$\mathrm{m}\cdot\mathrm{s}^{-1}$	0.1056
C_d	1	0.9300

4.5 Model verification

In this Section, both the modelled and tested results of the lumped non-linear force are compared via free-decay tests. Further comparison is made by the displacement decay of the wave tank tests, as well as the linear and non-linear modelling to emphasise the importance of the non-linear viscous and friction forces and the way in which they influence the PAWEC dynamics.

4.5.1 Model verification of lumped non-linear force

The power dissipated by the mechanical friction can be decomposed according to the friction components, as:

$$P_c = |f_c(t,x)\dot{z}| = F_c|\dot{z}|, \tag{4.47}$$

$$P_s = |f_s(t,x)\dot{z}| = F_s e^{-C_s|\dot{z}|}|\dot{z}|, \tag{4.48}$$

$$P_d = |f_d(t,x)\dot{z}| = C_f|\dot{z}|^2, \tag{4.49}$$

where $P_c(t)$, $P_s(t)$ and $P_d(t)$ represent the dissipated power by the Coulomb, Stribeck and damping friction forces, respectively.

In free-decay tests, the velocity of water particles is small enough to be ignored and hence Eq. (4.29) can be rewritten as:

$$f_v(t,x) = -0.5\rho C_d \pi r^2 \dot{z}|\dot{z}|. \tag{4.50}$$

Thus the associated power dissipation $P_v(t)$ is given as:

$$P_v = |f_v(t,x)\dot{z}| = 0.5\rho C_d \pi r^2 |\dot{z}|^3. \tag{4.51}$$

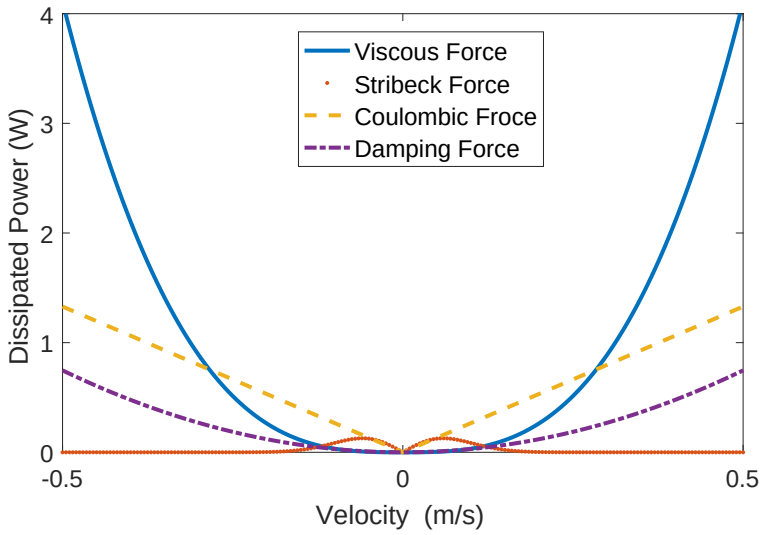

Fig. 4.8 Comparison of power dissipations by the Coulomb, Stribeck and damping friction forces and viscous force.

The comparison between these power dissipations is shown in Fig. 4.8. According to Fig. 4.8, the fluid viscous and Coulomb friction forces are important since they dissipate significant power. The damping friction force does not consume as much power as the fluid viscous and Coulomb forces but cannot be neglected when the velocity is large. When the velocity decays to a small amount, the Stribeck force is an important factor that impedes the buoy motion back on returning to the equilibrium point. Therefore, the lumped non-linear force is modelled as a combination of the fluid viscous, Coulomb, Stribeck and damping friction forces in Eq. (4.37).

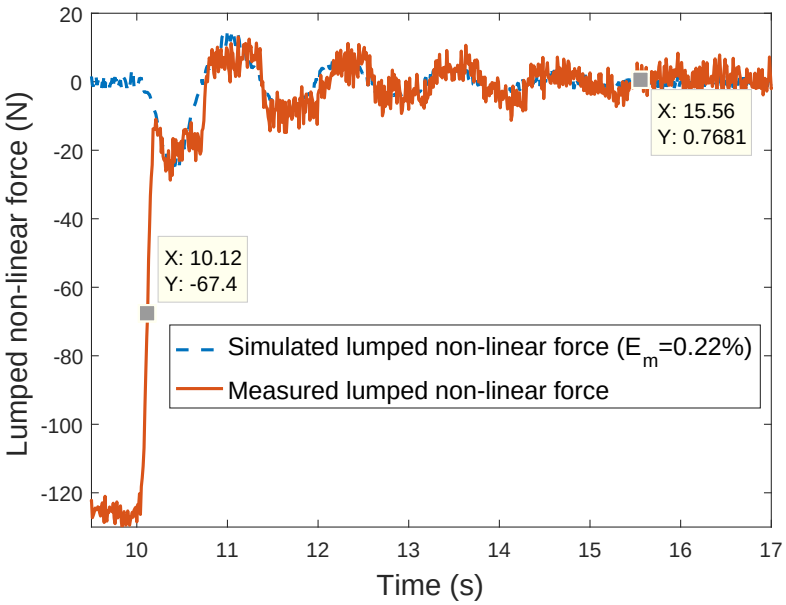

Fig. 4.9 Comparison of the lumped non-linear force between the measured and simulated data.

For a free-decay test with initial position -18cm, the measured and simulated results of the lumped non-linear force are shown in Fig. 4.9. The buoy is released at time $t_r = 10.12$ s (defined as the *releasing time* t_r) and is damped to its equilibrium point at time $t_s = 15.56$ s (defined as the *settling time* t_s). The simulation results of the lumped non-linear force fit the experimental measurements to a high degree (with a normalised modelling error $E_m = 0.22\%$).

E_m is defined as the *normalised modelling error* of the lumped non-linear force by means of the average dissipated power from the releasing time t_r to the settling time t_s, as:

$$P_{ms} = \frac{\int_{t_r}^{t_s} v_m(t) f_{lnms}(t) dt}{t_s - t_r}, \tag{4.52}$$

$$P_{md} = \frac{\int_{t_r}^{t_s} v_m(t) f_{lnmd}(t) dt}{t_s - t_r}, \tag{4.53}$$

$$E_m = \left| \frac{P_{md} - P_{ms}}{P_{ms}} \right| \cdot 100\%, \tag{4.54}$$

Table 4.2 Normalised modelling error of the lumped non-linear force.

Initial Position	E_m Eq. (4.54)	Initial Position	E_m Eq. (4.54)
−2cm	1.73%	−12cm	1.31%
−4cm	0.20%	−14cm	2.78%
−6cm	2.84%	−16cm	0.81%
−8cm	4.39%	−18cm	0.22%
−10cm	1.61%	−20cm	0.83%

where $f_{lnms}(t)$ is measured lumped non-linear force; $f_{lnmd}(t)$ is the modelled lumped non-linear force; P_{ms} and P_{md} are the average values of the measured and modelled power dissipations from t_r to t_s, respectively.

A wide range of free-decay tests are conducted to check the modelling accuracy of the lumped non-linear force. Table 4.2 shows that the mathematical model of the lumped non-linear force fits the experimental measurements with a very small error ($< 5\%$). Thus this lumped non-linear force model is accurate and useful for deriving a practical non-linear numerical solution for the buoy motion prediction.

4.5.2 Displacement response comparison

The simulation results of the linear and non-linear F2M models are compared with the experimental data shown in Fig. 4.10 with an initial displacement of -0.20 m. The linear model is defined in Eqs. (4.21) and (4.22) whilst the non-linear model considering the viscous and friction forces is expressed in Eqs. (4.40) and (4.41). All the data are normalised as referred to the initial position -0.20 m. Fig. 4.10 indicates that:

- The natural period of the linear model is about 1.215 s. For the non-linear model, the period is 1.230 s, whilst for the tank test it is 1.223 s. However, the motion decay speeds vary and depend on the dissipative factors. For the linear model, the motion decays slowly since the radiation force is the only dissipative force. Considering both the viscous and friction forces, the excursion of the non-linear model decays quickly and converges to the equilibrium point in 5 s. The

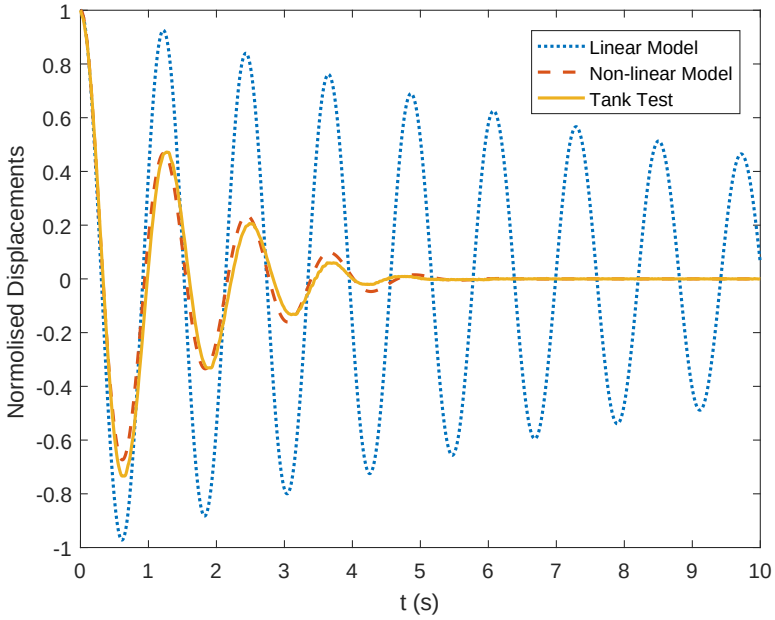

Fig. 4.10 Normalised displacement response comparison between numerical and experimental results of a free-decay test with initial displacement -0.20 m.

simulation of the non-linear model in Eqs. (4.40) and (4.41) fits the experimental data well.

- Within the first period, due to a high velocity, the viscous force is the predominant dissipative effect and damps the motion quickly. During the second and third periods, the Coulomb and damping friction forces become the major factors to consume power and impede the buoy. When the velocity becomes small in the forth period, the Coulomb and Stribeck friction forces drive the buoy back to its equilibrium point.

- The difference between the free-decay test and the non-linear model result is slight and the normalised modelling goodness for the -0.20 m free-decay situation is up to 0.9794, defined in Eq. (4.55). Thus the proposed non-linear model in Eqs. (4.40) and (4.41) provides a more accurate plant for the PAWEC motion analysis and control system design.

To evaluate the difference between the wave tank tests and the non-linear model results, a modelling goodness function MG is defined by the cost-function of the NMSE, as:

$$MG = 1 - \left\| \frac{d_{ft}(t) - d_{NM}(t)}{d_{ft}(t) - \bar{d}_{ft}(t)} \right\|_2^2, \tag{4.55}$$

where $d_{ft}(t)$ and $d_{NM}(t)$ are the displacements of wave tank test and non-linear model simulation, respectively.

Table 4.3 Modelling goodness of the non-linear model referred to the experimental data.

Initial Position	**MG**	**Initial Position**	**MG**
$-0.02\ m$	0.9582	$-0.12\ m$	0.9576
$-0.04\ m$	0.9536	$-0.14\ m$	0.9755
$-0.06\ m$	0.9578	$-0.16\ m$	0.9810
$-0.08\ m$	0.9808	$-0.18\ m$	0.9875
$-0.10\ m$	0.9808	$-0.20\ m$	0.9724

A series of free-decay tests are conducted with initial displacements varying from 0.02 to 0.20m. The simulation results of the non-linear F2M model are compared with the experimental data and shown in Table 4.3. The simulation results of the non-linear model fit well with the wave tank tests, with a modelling goodness more than 0.95. Therefore, it is concluded that the non-linear model can represent the $1/50$ scale PAWEC hydrodynamics for a wide range of the free-decay tests.

4.5.3 Energy dissipation comparison

For the -3cm, -8cm and -18cm free-decay tests, the dissipated power defined in Eqs. (4.47), (4.48),(4.49) and (4.51) are compared in Fig. 4.11, which illustrates that:

- For the -3cm free-decay test, the Coulomb friction force dissipates most power. Only a small amount power is consumed by the Stribeck, damping and viscous forces.
- For the -8cm free-decay test, the Coulomb and fluid viscous forces consume the main part of power and the rest is dissipated by the damping friction force.
- For the -18cm free-decay test, the fluid viscous force uses most of power and the rest is dissipated by the Coulomb and damping friction forces. From the viewpoint of power dissipation, the influence of the Stribeck friction force can be ignored in this test.

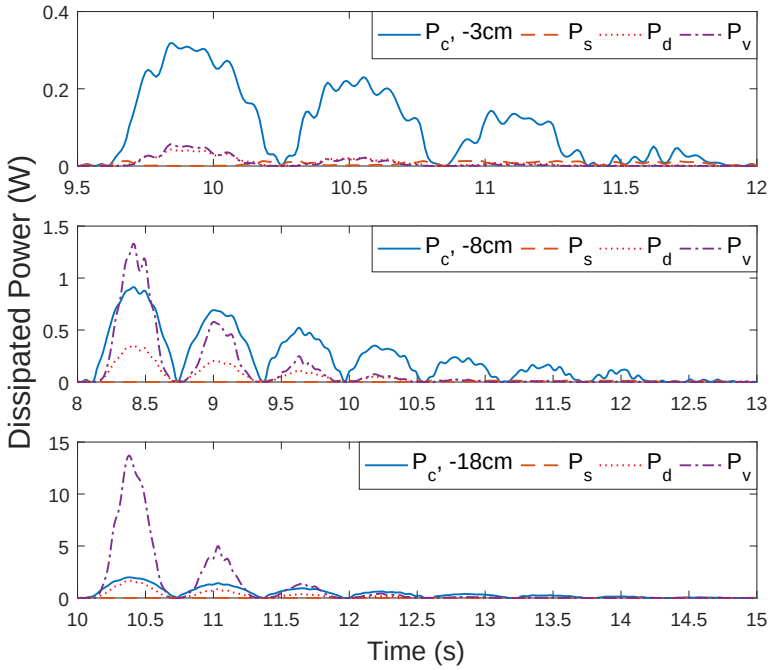

Fig. 4.11 Power dissipation comparison among the dissipative forces of free-decay tests with initial displacements of -3 cm, -8 cm and -18 cm.

- From the viewpoint of the normalised displacement response, the Stribeck friction force is important to damp the buoy back to its equilibrium point when the velocity is small. This is illustrated by Fig. 4.10.

From the viewpoint of energy conservation, all the potential energy at the initial position should be dissipated by the radiation, viscous and friction forces. For a initial displacement the z_i, the potential energy is given as:

$$E_p = \frac{1}{2} K_{hs} z_i^2. \tag{4.56}$$

The energy dissipated by the radiation force $E_r(t)$ can be represented as:

$$E_r = \int_{t_r}^{t_s} F_r(t)\dot{z}(t)dt. \tag{4.57}$$

The radiation force $F_r(t)$ is given in Eq. (4.3) and $\dot{z}(t)$ represents the buoy velocity measurement during the free-decay tests.

The energy dissipated by the Comlumbic friction ($E_c(t)$), Stribeck friction ($E_s(t)$), damping friction ($E_d(t)$), and viscous force ($E_v(t)$) are given as:

$$E_c = \int_{t_r}^{t_s} P_c dt, \tag{4.58}$$

$$E_s = \int_{t_r}^{t_s} P_s dt, \tag{4.59}$$

$$E_d = \int_{t_r}^{t_s} P_v dt, \tag{4.60}$$

$$E_v = \int_{t_r}^{t_s} P_d dt. \tag{4.61}$$

The total dissipated energy $E_t(t)$ is defined as:

$$E_t = E_r + E_c + E_s + E_d + E_v. \tag{4.62}$$

According to energy conservation theorem, the potential energy is all dissipated when the buoy is settled down to its equilibrium point, as:

$$E_t = E_p. \tag{4.63}$$

For a free-decay test with initial displacement -18 cm, the energy dissipations are given in Fig. 4.12. It is clear that:

- The total dissipated energy at the settling time is very close to the theoretical potential energy stored at the releasing time. Thus the non-linear F2M model shows high correspondence to the experimental results in term of energy dissipation.
- Among the dissipative factors, the viscous force consumes half of the total energy and the other half is dissipated by the radiation force, Coulomb and damping friction forces.
- From an energy viewpoint, the Stribeck friction is not important since it seldom dissipates energy. However, the Stribeck friciton is essential when the

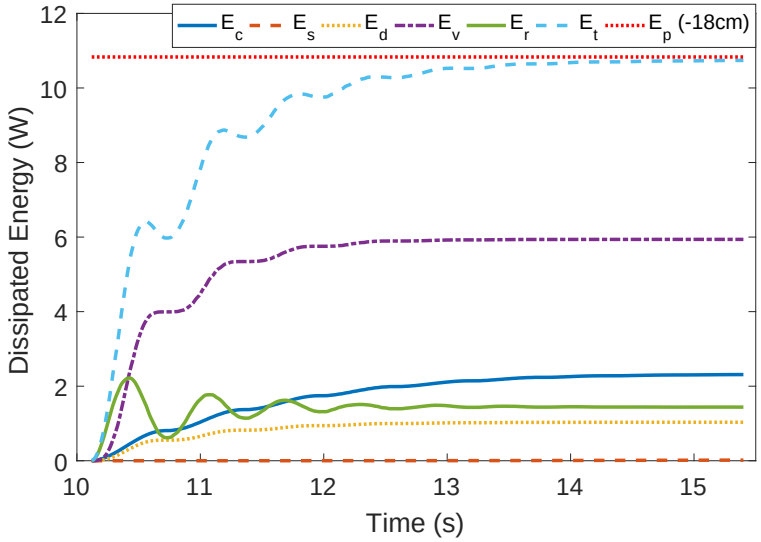

Fig. 4.12 Dissipated energy comparison among the dissipative forces.

displacement response is studied with a small initial displacement, shown in Fig. 4.10.

4.6 Summary and conclusion

4.6.1 Summary

This Chapter focuses on the hydrodynamics of the $1/50$ scale PAWEC for wave energy conversion. Linear and non-linear F2M models are proposed to represent the PAWECs hydrodynamics with the assumption that the wave excitation force is known. As a starting point, a linear model is derived from the simulation results using BEM code NEMOH in the frequency-domain, detailed in Section 4.2. The importance of the non-linear effects is investigated in Section 4.3. The non-linear viscous force is modelled as the drag force in the Morison equation and the non-linear friction force is modelled as the Tustin model. The viscous and friction forces cannot be decoupled from each other and their summation is defined as a lumped non-linear force. To study how this lumped non-linear force influences the buoy motion, non-linear F2M model considering the lumped non-linear force is compared with the linear F2M model. For model verification and parameter estimation, a series free-fall tests and free-decay tests are conducted. The

wave tank tests are detailed in Section 4.4 and the numerical and experimental data are compared in Section 4.5.

The simulation results of the non-linear F2M model fit with the experimental data to a much higher extent than the linear one. Compared with fully non-linear modelling approaches, such as CFD, the proposed non-linear F2M model can provide a convenient, straightforward and efficient model for control system design and time-saving numerical simulation. However, one main drawback of the proposed F2M models assumes that the wave excitation force is known. However, the wave excitation force cannot be measured for an oscillating device whilst the wave elevation is measurable. Hence it is useful to estimate the wave excitation force from the wave elevation and then to derive W2W models to represent the PAWEC dynamics. Therefore, Chapter 5 specially focuses on the system identification of the wave excitation force to derive linear and non-linear W2M models of the $1/50$ scale PAWEC device.

4.6.2 Conclusion

Compared with the linear modelling approaches, the non-linear F2M model considering the viscous and friction forces can provide more precise hydrodynamic representation of the PAWEC. As a summation of the viscous force and the friction force, the lumped non-linear force fits the measurement to a very high degree and the normalised modelling error of the lumped non-linear force is within 5%. Thus the modelling of the lumped non-linear force can represent the non-linear phenomena of the $1/50$ PAWEC prototype. For this small scale prototype, he friction force is relatively large and hence cannot be ignored. For a larger scale PAWEC prototype, the friction force may be not as important as it is for this PAWEC.

Comparison of PAWEC displacement responses between the numerical simulations and wave tank tests, the linear F2M model tends to overestimate the buoy motion since non-linear dissipative effects are not taken into account. The proposed non-linear F2M model provides more accurate PAWEC motion estimate considering the viscous force and friction phenomena and the model gives good agreement with the experimental data in terms of displacement response. Hence, the proposed non-linear F2M model can be considered applicable and suitable for the analysis of the $1/50$ PAWEC device dynamics and design of control systems.

From the viewpoint of the energy dissipation in Figs. 4.11 and 4.12, the non-linear effects dissipate more energy than the radiation damping effect for the $1/50$ PAWEC. When the buoy velocity is small, the friction force is relatively large and the viscous force is relatively small. The friction force may dissipate more energy than the radiation force. When the buoy velocity is large, the viscous force is relatively large and the friction force cannot be ignored in terms of energy dissipation. For the free-decay tests, it is observed that the non-linear friciton and viscous forces dissipated more energy than the radiation force and therefore these non-linearities must be considered in the power maximisation design.

Chapter 5

Excitation force approximations

5.1 Introduction

As mentioned in Chapter 4, the modelling of the excitation force is essential for the dynamic analysis and controller design of WEC systems. Some WEC modelling approaches assume that wave excitation force is accessible and known. However, the excitation force is not directly measurable for oscillating bodies. This Chapter emphasises the modelling approaches of the excitation force to provide accurate approximations for WEC control system design. Section 5.2 describes the analytical modelling approach of the excitation force in the literature. Section 5.3 details the excitation force estimation from the wave elevation, referred to as the W2EF approach. In Section 5.4, the excitation force is derived from real-time measurements of (i) WEC wetted-surface pressure, (ii) WEC acceleration and (iii) displacement, referred to as the PAD2EF method. In Section 5.5, the excitation force is observed from an UIO, referred to as the UIOEF technique. The W2EF model is integrated into linear and non-linear F2M models in Chapter 4 to deduce linear and non-linear W2M models given in Section 5.6. The experimental data are compared with the numerical results of the proposed W2EF, PAD2EF and UIOEF approaches and linear/non-linear W2M models in Section 5.7.

5.2 Analytic modelling approach

In the literature, the excitation force is generically modelled via analytical approaches. As described by Newman (1962), the excitation force is represented by the integral of the pressure acting on the wet surface of the buoy. This provides a good way to estimate the excitation force for fixed rather than oscillating offshore structures (such as a WEC device excited by the wave motion). Also, there are some empirical formula providing relatively precise estimations of the excitation force for some structures with specific shape (Greenhow and White, 1997). For irregular wave conditions, the excitation force can be computed based on the superposition principle as well as on its FRF (Babarit et al., 2012). These excitation force estimates are useful for assessing the wave energy resource, as well as the WEC dynamics and control performance. However, these analytical approximations are inappropriate for real-time power optimum control of WEC systems, since these approximations are not related to either the wave elevation or the WEC motion.

The most extensively used analytical model of the excitation force $F_e(t)$ is derived by solving the far-field velocity potential problem based on the Haskind relationship (Newman, 1962), given in an analytical representation as:

$$F_e = \frac{H}{2}\left(\frac{2\rho g^3 R(\omega)}{\omega^3}\right)^{1/2}\cos(\omega t), \tag{5.1}$$

This analytical model is adopted in a series of research works, notable of which are these studied by Greenhow and White (1997); Tedeschi et al. (2011).

For irregular waves, the excitation force can be computed based on the superposition principle and its FRF, given in a spectrum formation by Babarit et al. (2012), as:

$$F_e = \Re\left[\sum_i \sqrt{2S(\omega_i)\Delta\omega}H_e(j\omega_i)e^{j(\omega t+\phi_i)}\right], \tag{5.2}$$

where $\Delta\omega$ is the angular frequency step, ϕ_i are a set of random phases and $H_e(j\omega_i)$ are the frequency-domain responses of the excitation force. $\Re(X)$ is the real operation of X. This representation is widely used to assess the performance or yield of various WEC devices. However, the analytical representations in Eqs. (5.1) and (5.2) are

not suitable for real-time control implementation since the wave excitation force is simulated according to wave spectra as a known input for numerical studies. The following Section identifies the excitation force from the wave elevation with special focus on its real-time implementations.

5.3 W2EF modelling approach

5.3.1 Methodology

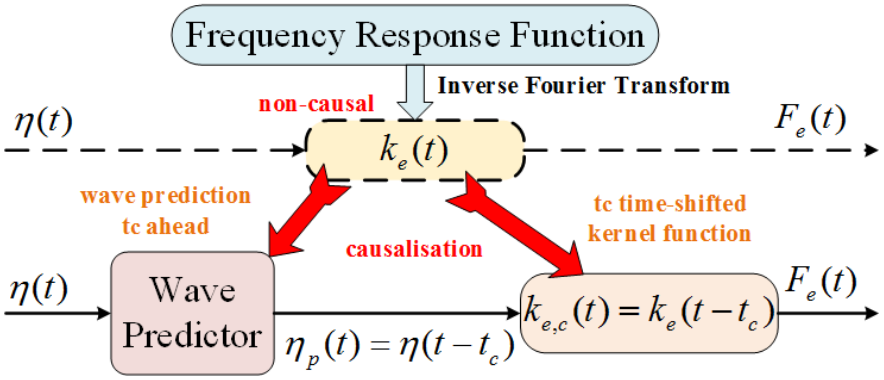

Fig. 5.1 Schematic diagram of the W2EF modelling approach.

Since the frequency-domain response of the excitation force is available in Fig. 3.6, its time-domain kernel function $k_e(t)$ can be gained by inverse Fourier transform. However, the kernel function $k_e(t)$ characterises that the W2EF process is non-causal, for $k_e(t) \neq 0$ for $t < 0$. Therefore, the dashed system in Fig. 5.1 is physically unimplementable. To overcome the non-causality, a time-shift technique is applied to the non-causal kernel function $k_e(t)$ to derive its causalised form $k_{e,c}(t)$. t_c is defined as the causalisation time (Falnes, 1995). Thus, the wave elevation prediction η_p with t_c in advance is required based on local wave elevation measurement η. The implementation of the W2EF modelling are detailed in this Section.

According to the frequency-domain response in Fig. 3.6, the excitation force can be represented as:

$$F_e(j\omega) = H_e(j\omega)A(j\omega), \tag{5.3}$$

where $H_e(j\omega)$ is the excitation force FRF. $A(j\omega)$ is the frequency-domain representation of incident wave $\eta(t)$.

Alternatively, the excitation force can be expressed in the time-domain as:

$$F_e = k_e * \eta = \int_{-\infty}^{\infty} k_e(t-\tau)\eta(\tau)d\tau, \tag{5.4}$$

where $k_e(t)$ is the excitation force IRF, which is related to its FRF $H_e(j\omega)$ as:

$$k_e = \frac{1}{2\pi}\int_{-\infty}^{\infty} H_e(j\omega)e^{j\omega t}d\omega. \tag{5.5}$$

Based on the frequency-domain response in Fig. 3.6, the kernel function $k_e(t)$ is computed according to Eq. (5.5) and shown in Fig. 5.2, in which the solid blue curve illustrates the non-causality of the W2EF process (Falnes, 1995, 2002). The $k_e(t)$ values for the $t < 0$ part are almost the same as the $t > 0$ part. Clearly, ignoring the $t < 0$ non-causal component will cause significant errors in the modelling of the excitation force.

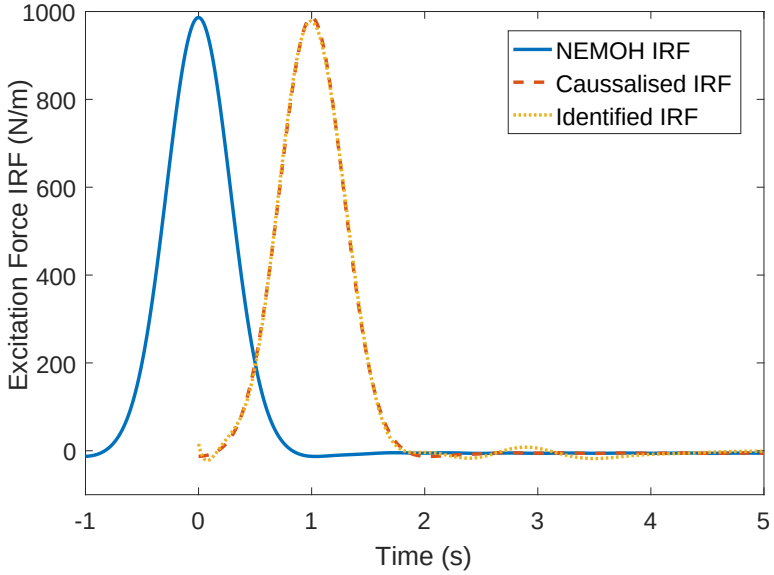

Fig. 5.2 Comparison of the excitation force IRFs.

To note that: The time-shift technique is first studied numerically by Falnes (1995); Yu and Falnes (1995) to causalise the excitation force IRF. After the time-shift, the causalised IRF is treated as a curve fitting or identification problem without further discussion of its implementation. Also, the results of the excitation force is not given by Falnes (1995); Yu and Falnes (1995). This Section emphasises the excitation force causalisation and its implementation with wave prediction in a short-term horizon. Specially, the numerical results of the excitation force is compared with the experimental data both in the frequency- and time-domains in Section 5.7.1.

As shown in Fig. 5.1, the incident wave propagates through a non-causal system characterised by $k_e(t)$ and generates the excitation force. However, this non-causal system is not implementable. Therefore, causalisation is required and can be achieved with a time-shifted kernel function $k_{e,c}(t)$ and wave prediction $\eta_p(t)$. The wave prediction horizon is the same as the causalisation time t_c.

According to the property of the convolution operation, this causalised system with wave prediction gives the same excitation force of the non-causal system, since:

$$\begin{aligned} F_e &= k_e * \eta && (5.6)\\ &= k_e(t-t_c) * \eta(t+t_c) && (5.7)\\ &= k_{e,c} * \eta_p, && (5.8) \end{aligned}$$

where

$$k_{e,c} = k_e(t-t_c), \tag{5.9}$$

$$\eta_p = \eta(t+t_c). \tag{5.10}$$

$k_{e,c}(t)$ and $\eta_p(t)$ are the causalised IRF of the excitation force and predicted wave elevation with t_c in advance, respectively. If wave excitation force prediction is required, the wave prediction horizon should be extend to cover both the caucalisation time and the excitation force prediction horizon. The algorithms to identify $k_{e,c}(t)$ and to predict $\eta_p(t)$ are detailed as following.

5.3.2 System identification of causalised kernel function

For a causalised system in Eq. (5.8), the convolution operation approximation is the same as the radiation force approximation detailed in Section 4.2.2. A slight difference is that the system order n and the causalisation time t_c should be selected carefully before the system identification. Hence, it is important to apply the goodness of fit function in Eq. (4.14) to determine the appropriate values of t_c and n.

The goodness of fit of the causalised excitation IRF relies on the causalisation time t_c and system order number n. The causalisation time is chosen as $t_c = 0.8 : 0.05 : 2$ s and the system order is selected as $n = 3 : 1 : 12$. The goodness of fit is shown in Fig. 5.3. It can be seen that:

- The goodness of fit increases as the system order n increases.
- The goodness of fit decreases as the causalisation time t_c increases.
- For $n = 6$ and $t_c = 1$ s, the goodness of fit is up to 0.9993.

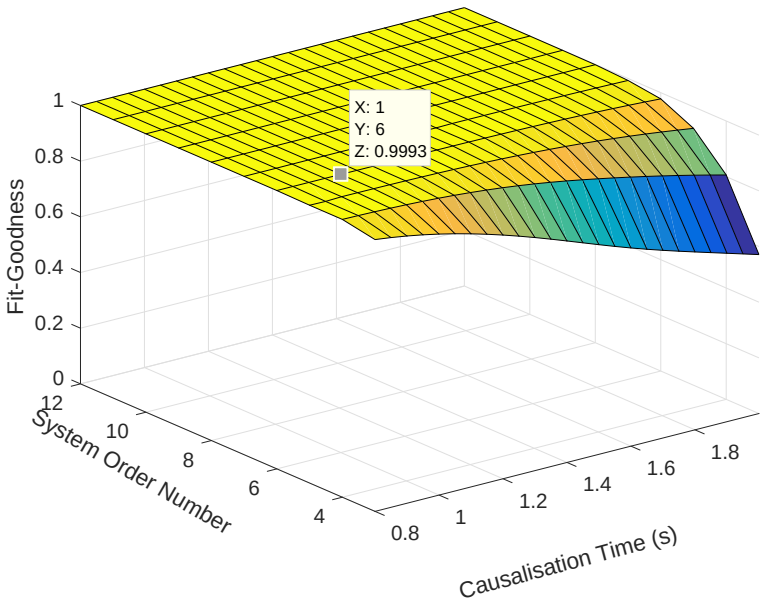

Fig. 5.3 Goodness of fit with varying causalisation time t_c and system order number n.

Therefore, a state-space system with $t_c = 1$ s and $n = 6$ is adopted to approximate the causalised kernel function $k_{e,c}(t)$ in Eq. (5.9), given as:

$$\dot{x}_e = A_e x_e + B_e \eta_p, \tag{5.11}$$

$$F_e = C_e x_e, \tag{5.12}$$

where $x_e \in \mathbb{R}^{6\times1}$ is the state vector for the excitation system. $A_e \in \mathbb{R}^{6\times6}$, $B_e \in \mathbb{R}^{6\times1}$ and $C_e \in \mathbb{R}^{1\times6}$ are the system matrices. The identified IRF is compared with the causalised IRF and the original IRF of the excitation force in Fig. 5.2. The identified system fits the causalized system with a goodness of fit of 0.9993.

The system identification method is same as the time-domain radiation IRF approximation, detailed in Section 4.2.2. This Section only introduce the W2EF method and hence the FRF of the identified system is compared with the numerical and experimental results in Section 5.7.1.

5.3.3 Wave prediction

According to Eq. (5.7), a short-term wave prediction is required to achieve the causalisation problem in Fig. 5.1. There are several approaches to provide reasonably accurate wave predication for a short-term horizon, the most notable of which are: (i) Auto-Regressive (AR) model approach (Fusco and Ringwood, 2010), (ii) Auto-Regressive Moving Average (ARMA) model approach (Ge and Kerrigan, 2016) and (iii) Fast Fourier Transform (FFT) approach (Halliday et al., 2011). The real-time implementation of wave prediction is discussed by Fischer et al. (2012). Amongst these approaches, the wave prediction via an AR model shows a high accordance to the ocean waves in the Irish sea (Fusco and Ringwood, 2010). Since the technique is mature, the AR model approach developed by Fusco and Ringwood (2010) is adopted in this study to provide a short-term wave prediction.

For harmonic waves, wave prediction is easy to obtain. For irregular waves, the PM spectrum (Pierson and Moskowitz, 1964) is applied to describe the fully developed ocean waves. In the wave tank tests, one set of irregular wave satisfies the PM spectrum with peak frequency $f_p = 0.6$ Hz and significant wave height $H_s = 0.11$ m. The wave prediction with $t_c = 1$ s via an AR model is compared with the wave measurement

and shown in Fig. 5.4. The predicted wave elevation fits the experimental data well. Therefore, the AR model is adopted as a wave predictor to provide future information for the identified system, as shown in Fig. 5.1.

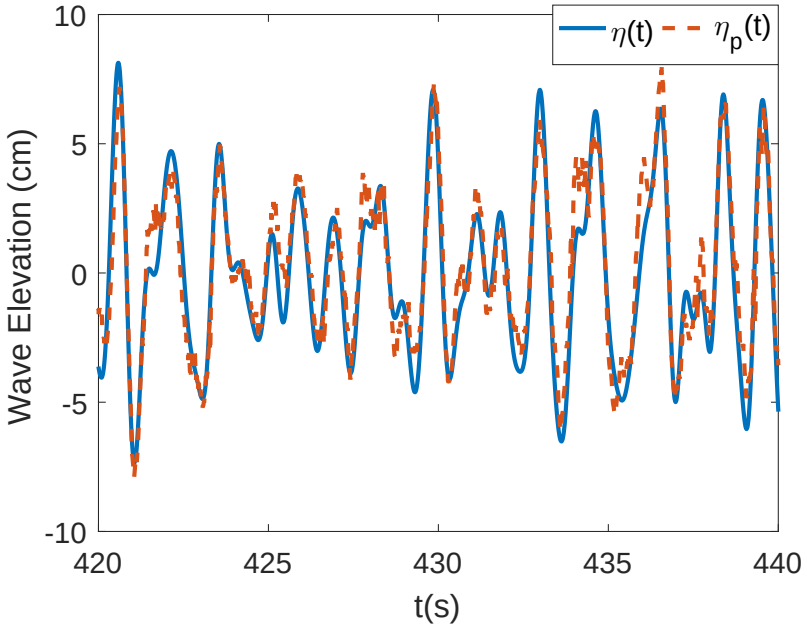

Fig. 5.4 Comparison of wave elevations between the experimental measurement and the numerical prediction with an AR model.

5.4 PAD2EF modelling approach

5.4.1 Methodology

For an oscillating PAWEC, the excitation force can be reconstructed from its sensing system. As shown in Fig. 5.5, the total wave force $F_w(t)$ acting on the structure can be estimated from the pressure sensors installed on the wet surface. The hydrostatic force defined in Eq. (3.35) can be represented by the displacement measurement. Whilst, the radiation force can be estimated from the acceleration and velocity measurements. Therefore, the excitation force can be approximated as:

$$F_e = F_w - F_{hs} - F_r. \tag{5.13}$$

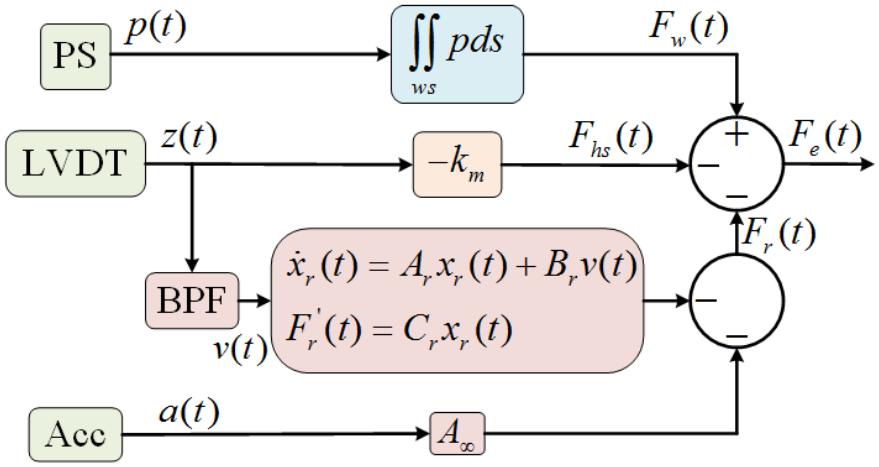

Fig. 5.5 Schematic diagram of the PAD2EF modelling approach.

The convolution term of the radiation force $F_r(t)$ in Eq. (3.48) can be approximated by a finite order system, which is detailed in Section 4.2.2.

5.4.2 Pseudo-velocity measurement

As shown in Fig. 5.5, measurements of the pressure, displacement and acceleration are accessible and implementable. However, the velocity measurement is difficult and expensive to obtain. A "pseudo-velocity" can be estimated/observed from the displacement/acceleration measurements. In the work of Abdelkhalik et al. (2016), the velocity is obtained from the first order derivative of an accurate displacement measurement (via linear variable displacement transducer) with a high sampling frequency. The drawbacks of this approach are: (i) the velocity estimation suffers from the measurement noise and (ii) the velocity estimation is always one sample period behind the real velocity (high sampling frequency is required). Alternatively, the velocity can be estimated from the acceleration measurement via accelerometer via the time integral method. However, the initial condition is required for the integral algorithm but it is not always available.

In this work, a carefully designed Band-Pass Filter (BPF) is applied to gain the velocity estimation from the displacement. Via the BPF, a smoother estimation with less phase lag can be gained, compared with the differentiation approach. A second order BPF is

given as:

$$BPF(s) = \frac{A(\omega_c)\frac{\omega_c}{Q}s}{s^2+\frac{\omega_c}{Q}s+\omega_c^2}, \tag{5.14}$$

where $A(\omega_c)$ is the amplitude response at the central frequency ω_c. Q is the quality factor. Beyond the methods mentioned above, a properly design observer can give an accurate velocity estimate. The observer design is detailed in the following Section. The comparison of pseudo-velocity measurements are illustrated in Fig. 5.6. Generally speaking, all these measure can provide accurate velocity approximations for WEC real-time control.

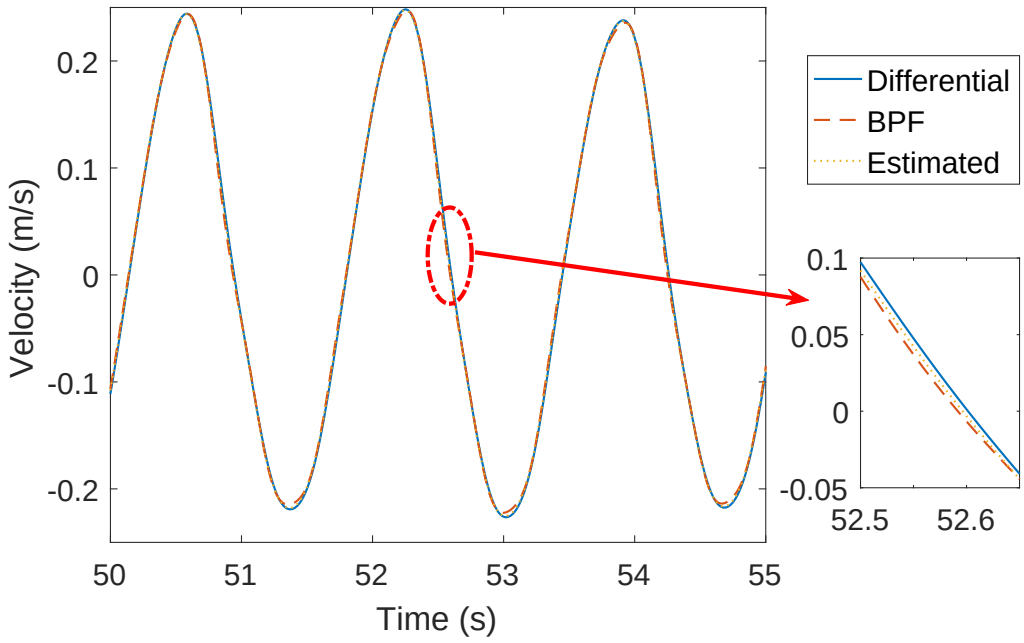

Fig. 5.6 Pseudo-velocity estimations.

Therefore, the excitation force can be estimated from the pressure measurements, acceleration and displacement, given as:

$$F_e = \iint pdS + K_{hs}z + A_\infty a + F_r^{'}. \tag{5.15}$$

The radiation subsystem $F_r^{'}(t)$ is given in Eqs. (4.15) and (4.16).

5.5 UIOEF modelling approach

5.5.1 Methodology

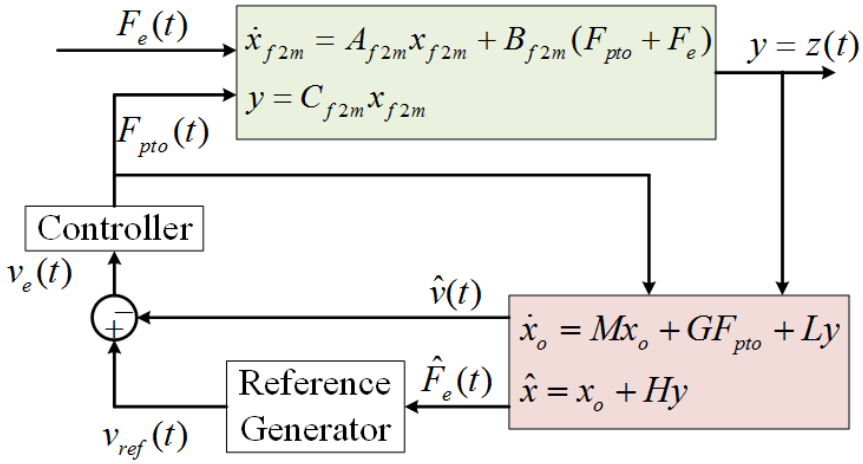

Fig. 5.7 Schematic diagram of the UIOEF modelling approach.

As the convolution term of the radiation force is approximated by a state-space model in Eqs. (4.15) and (4.16), the buoy motion under the wave excitation can be represented in a state-space form. Therefore, a carefully designed UIO can be applied to estimate the unknown excitation force. As shown in Fig. 5.7, a generic UIO is applied to estimate the excitation force and buoy velocity from the displacement measurement. The estimated excitation force is used to generate the velocity reference, whilst the estimated velocity is viewed as the velocity measurement to provide feedback for the controller. In this study, the UIO design is emphasised rather than the controller. This method is referred to as the UIOEF modelling approach. The linear F2M model is given in Eqs. (4.21) and (4.22).

5.5.2 Unknown input observer design

To estimate the unknown excitation force $F_e(t)$, it is viewed as an augmented state to the F2M system in Eqs. (4.21) and (4.22). Thus the augmented system can be written

as:

$$
\begin{aligned}
x_g &= [x_{f2m} \quad Fe]^T, && (5.16)\\
\dot{x}_g &= A_g x_g + B_g F_{pto} + D_g \dot{F}_e, && (5.17)\\
y_g &= C_g x_g, && (5.18)
\end{aligned}
$$

with

$$
\begin{aligned}
A_g &= \begin{bmatrix} A_{f2m} & B_{f2m} \\ 0 & 0 \end{bmatrix}, && (5.19)\\
B_g &= \begin{bmatrix} B_{f2m} & 0 \end{bmatrix}^T, && (5.20)\\
D_g &= \begin{bmatrix} 0 & 1 \end{bmatrix}^T, && (5.21)\\
C_g &= \begin{bmatrix} C_{f2m} & 0 \end{bmatrix}, && (5.22)
\end{aligned}
$$

where $x_g \in \mathbb{R}^{6\times1}$ is the state vector of the augmented system. $A_g \in \mathbb{R}^{6\times6}$, $B_g \in \mathbb{R}^{6\times1}$ and $C_g \in \mathbb{R}^{1\times6}$ are the system matrices.

A generic UIO form is represented by Lan and Patton (2015, 2017), in which the excitation force is treated as an unknown fault or disturbance, written as:

$$
\begin{aligned}
\dot{x}_o &= M x_o + G F_{pto} + L y_{f2m}, && (5.23)\\
\hat{x}_g &= x_o + H y_{f2m}, && (5.24)
\end{aligned}
$$

where $x_o \in \mathbb{R}^{6\times1}$ is the UIO state vector. $M \in \mathbb{R}^{6\times6}$, $G \in \mathbb{R}^{6\times1}$, $L \in \mathbb{R}^{6\times1}$ and $H \in \mathbb{R}^{6\times1}$ are the UIO system matrices.

Since the excitation force is unknown, its derivative $\dot{F}_e(t)$ in Eq. (5.17) is inaccessible and hence viewed as a disturbance. To achieve an accurate estimation of the excitation force, H_∞ technique is applied to compute the observer matrices M, G, L and H to reject the influence of $\dot{F}_e(t)$, with the MATLAB® LMI toolbox. The procedure to compute the observer matrices is studied by Lan and Patton (2017).

5.6 Wave-to-motion modelling

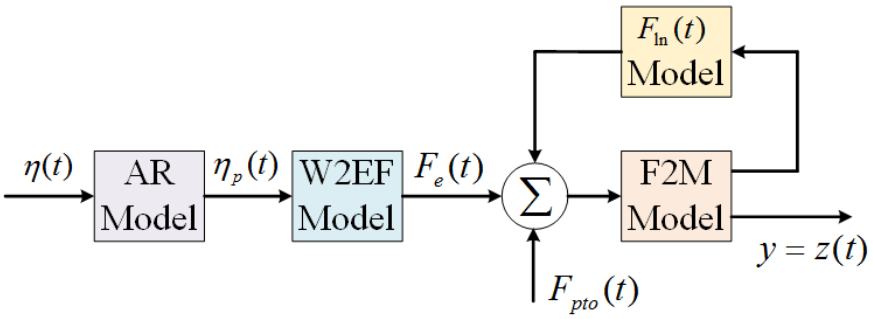

Fig. 5.8 W2M modelling approach.

As shown in Fig. 5.8, a non-linear W2M model can be derived from the W2EF, F2M and $f_{ln}(t,x)$ models, together with the wave prediction with an AR model. Thus the non-linear W2M model can be written as:

$$x_{w2m} = [x_{f2m} \quad x_e]^T, \tag{5.25}$$

$$\dot{x}_{w2m} = A_{w2m}x_{w2m} + B_{w2m}\eta_p + D_{w2m}[f_{ln}(t,x) + F_{pto}], \tag{5.26}$$

$$y_{w2m} = C_{w2m}x_{w2m}, \tag{5.27}$$

with

$$A_{w2m} = \begin{bmatrix} A_{f2m} & B_{f2m}C_e \\ 0 & A_e \end{bmatrix}, \tag{5.28}$$

$$B_{w2m} = \begin{bmatrix} 0 & B_e \end{bmatrix}^T, \tag{5.29}$$

$$D_{w2m} = \begin{bmatrix} B_{f2m} & 0 \end{bmatrix}^T, \tag{5.30}$$

$$C_{w2m} = \begin{bmatrix} C_{f2m} & 0 \end{bmatrix}. \tag{5.31}$$

where $x_{w2m} \in \mathbb{R}^{11\times 1}$ is the state vector of the W2M system. $A_{w2m} \in \mathbb{R}^{11\times 11}$, $B_{w2m} \in \mathbb{R}^{11\times 1}$, $D_{w2m} \in \mathbb{R}^{11\times 1}$ and $C_{w2m} \in \mathbb{R}^{1\times 11}$ are the system matrices.

The W2M model can be potentially used to predict the WEC system dynamics directly from existing wave records. If the displacement is measured, wave profile reconstruction can be achieved based on the observed excitation force via the UIOEF approach. If the

non-linear friction and viscous effects can be ignored and the PTO mechanism is not included, a linear W2M model can be obtained.

5.7 Results and discussion

This Section gives the results of the excitation force approximations via the W2EF, PAD2EF and UIOEF approaches. Comparisons of the excitation force approximations are made between the numerical and experimental data in terms of the excitation and forced-motion tests under regular and irregular wave conditions. The linear and non-linear W2M modelling results are compared with the forced-motion tests results as well.

5.7.1 Results of excitation tests

During the excitation tests, the buoy is excited by the incident wave but fixed to the tank gantry via G-shape clips. Therefore, the buoy cannot oscillate. Five Pressure Sensors (PSs) are installed at the base of the buoy to provide the information of the dynamic pressure acting on the PAWEC hull. Thus, the wave excitation force in heave can be represented as:

$$F_e = \iint p dS = \pi r^2 \bar{p}, \tag{5.32}$$

where $\bar{p}(t)$ represents the average value of the PSs. For the excitation tests, the excitation force is measured by the PSs via Eq. (5.32). This is a simple approximation of the excitation force and the results are accurate when the PA definition (the buoy diameter is much smaller than the wavelength) is satisfied. If the buoy diameter is greater than $1/10$ of the wavelength, more PSs are needed to provide accurate F_e measurement.

Meanwhile, five Wave Gauges (WGs) are installed to measure the wave elevation, amongst which, WG3, is situated parallel to the buoy. The measurement of WG3 represents the incident wave at the centre of the PAWEC and adopted to provide wave prediction in a short-term horizon t_c. To verify the proposed W2EF modelling approach, a series of excitation tests are conducted to compare with the numerical simulations

of Eqs. (5.11) and (5.12) under the excitation of regular and irregular waves. In the excitation tests, the measurement of the excitation force is derived from the pressure sensors according to Eq. (5.32).

Regular Wave Conditions

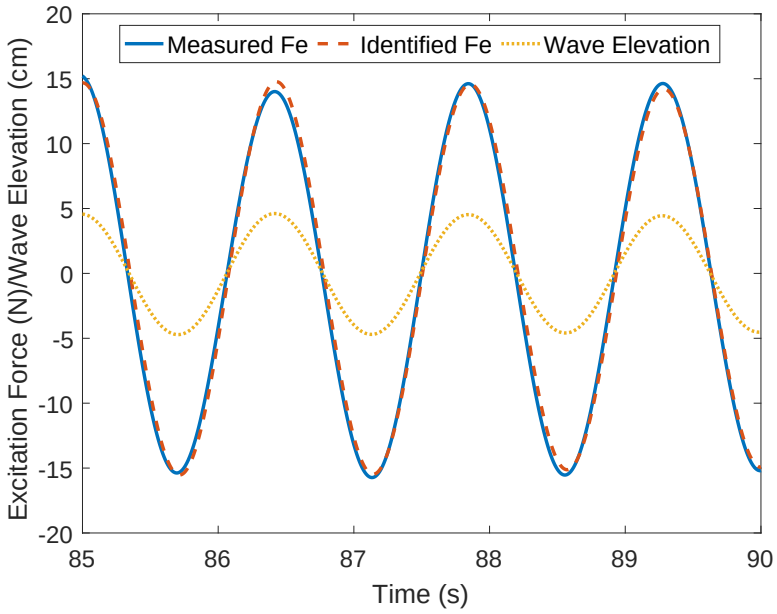

Fig. 5.9 Comparison of the excitation forces between the measurement and the estimation via the W2EF method.

Nine excitation tests are conducted under regular wave conditions with wave height $H = 0.08$ m and wave frequencies $f = 0.4 : 0.1 : 1.2$ Hz. For harmonic waves, precise wave prediction with $t_c = 1$ s is easy to achieve. Therefore, the W2EF modelling approach always provides accurate approximations of the excitation force. For the harmonic wave with frequency $f = 0.7$ Hz, the excitation force measurement in Eq. (5.32) and estimation in Eqs. (5.11) and (5.12) are compared and shown in Fig. 5.9. The estimation via W2EF method shows a high accordance to the experimental data, which indicates the validity of the W2EF method for excitation tests under regular wave conditions.

To check the fidelity further, the frequency-domain response of the excitation tests is compared with the W2EF results as well as the NEMOH computation. The amplitude and phase responses are shown in Fig. 5.10 and Fig. 5.11, respectively. The amplitude response of the W2EF method fits the NEMOH and excitation tests data to a high

degree. This is why the analytical representation of the excitation force in Eqs. (5.1) and (5.2) are widely adopted to investigate WEC dynamics.

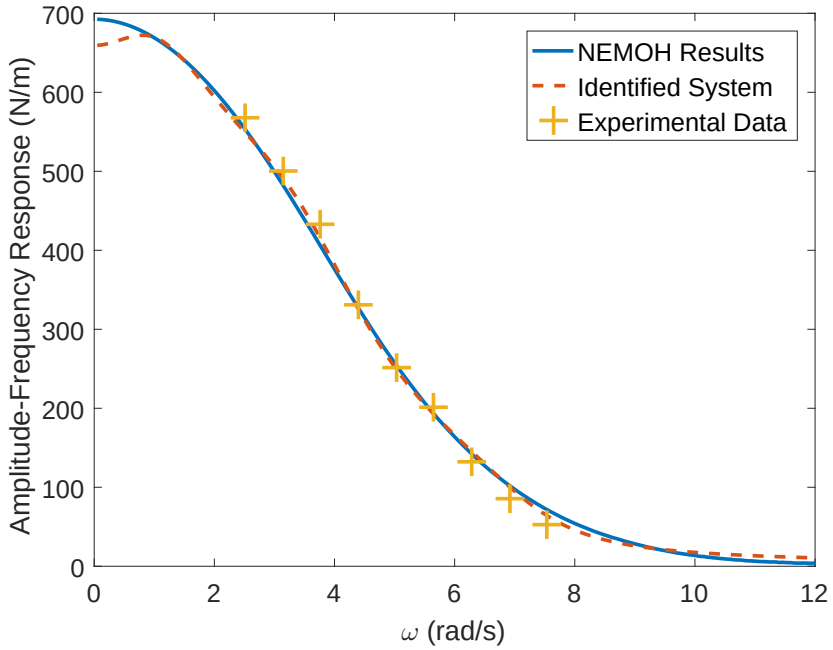

Fig. 5.10 Amplitude response comparison between the excitation tests, NEMOH computations and W2EF simulations.

Fig. 5.11 compares the experimental and numerical phase responses from the incident wave $\eta(t)$ to the excitation force $F_e(t)$ in Eq. (5.6). The phase response is not considered in the analytical representations in Eqs. (5.1) and (5.2). Therefore they are not suitable for some real time control strategies, since the phase information is essential for the phase control. Good accordance of the phase response means that the W2EF modelling approach with kernel function causalisation and wave prediction in Eq. (5.8) gives almost the same system description in Eq. (5.6).

Irregular Wave Conditions

Irregular waves characterised by the PM spectrum are adopted in the excitation tests. For a PM spectrum wave with peak frequency $f_p = 0.6$ Hz and significant wave height $H_s = 0.11$ m, the excitation force comparison is given in Fig. 5.12. The estimated excitation force via the W2EF method shows a good accordance to the experimental data for most of the time. The estimation only varies a bit from the measurement when

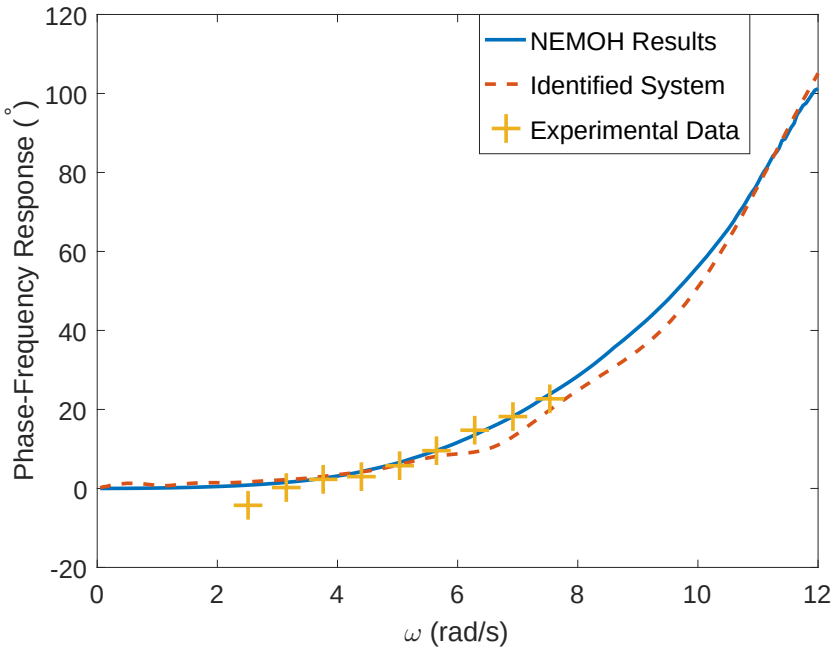

Fig. 5.11 Phase response comparison between the excitation tests, NEMOH computations and W2EF simulations.

the wave elevation is small. However, this part is not important from the viewpoint of power maximisation and displacement restriction. To compare the wave elevation and the excitation force, it is very interesting to find that the high-frequency irregularity of the wave elevation does not influence the excitation force. The reason is that the W2EF process itself is a "natural" low pass filter. The estimation error of the excitation force influence on control performance is studied by Fusco and Ringwood (2011a).

5.7.2 Results of forced-motion tests

During the forced-motion tests, the PAWEC is forced to oscillate from zero-initial condition under the excitation of incident waves. In this situation, the measurements from the pressure sensors represent the total wave force rather than the excitation force, given as:

$$F_w = \iint p dS = \pi r^2 \bar{p}. \tag{5.33}$$

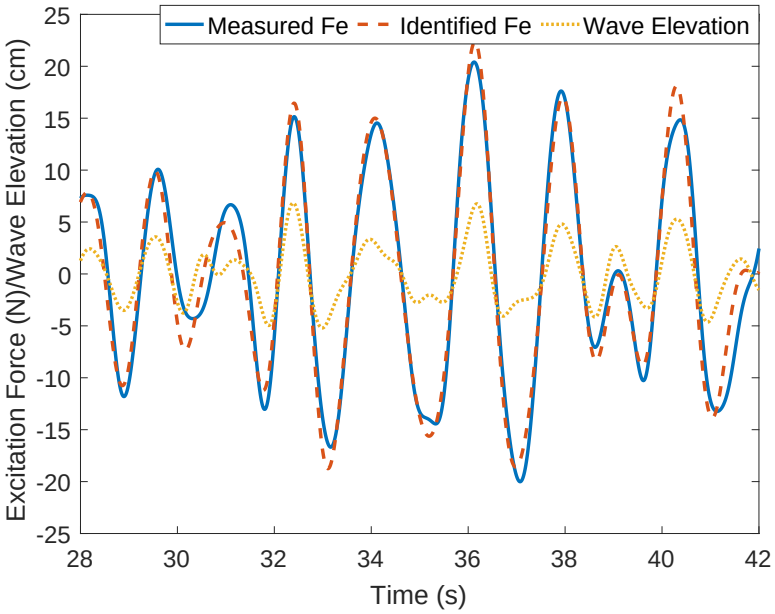

Fig. 5.12 Comparison of the excitation force between the excitation tests and the W2EF modelling under the irregular wave conditions.

Meanwhile, the buoy acceleration and displacement are measured by an accelerometer and an LVDT, respectively. Therefore, the excitation force can be estimated via the PAD2EF approach in Eq. (5.15). Also, the wave elevation measurements are accessible. Thus the W2EF method can be applied to WG3 measurement to approximate the excitation force according to Eqs. (5.11) and (5.12). Since the displacement measurement is accessible, the UIOEF approach in Eqs. (5.23) and (5.24) can be applied to estimate the excitation force.

For an oscillating PAWEC in forced-motion tests, the W2EF approach in Section 5.3, PAD2EF method in Section 5.4 and UIOEF technique in Section 5.5 are applied to estimate the wave excitation force. The approximations of the excitation force via the W2EF, PAD2EF and UIOEF approaches are compared with each other. All the data of the wave elevation, pressure, displacement and acceleration are collected from the forced-motion tests via LABVIEW™. The details of the wave tank tests are given in Chapter 6.

In the forced-motion tests, the excitation force is not measurable since the pressure sensors give the total wave force $F_w(t)$ in Eqs. (5.13) and (5.33). Therefore, it is very hard to say which method is better.

Regular Wave Conditions

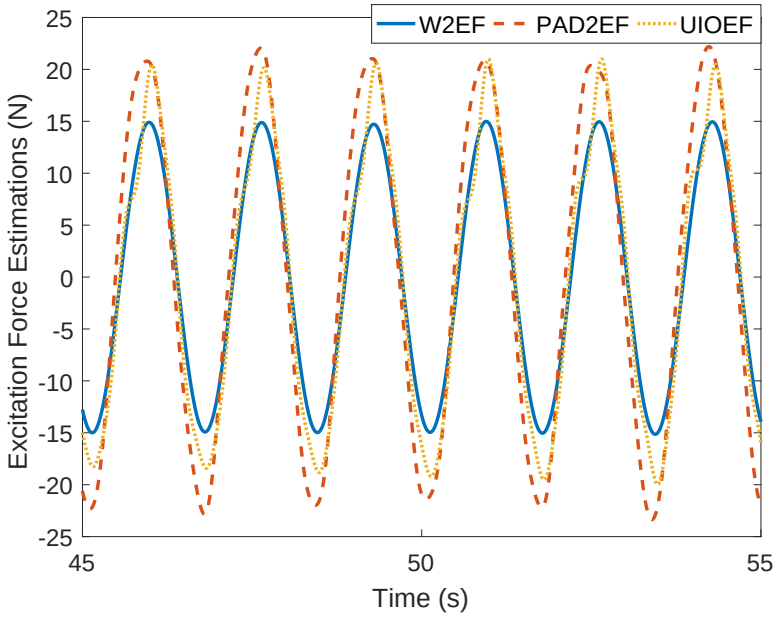

Fig. 5.13 Comparison of the excitation force approximations in a forced-motion test under regular wave.

For a regular wave with frequency $f = 0.60$ Hz and height $H = 0.08$ m, the excitation force approximations via the W2EF, PAD2EF and UIOEF approaches are compared in Fig. 5.13. All these three approximations show a good accordance to each other in terms of phase. It is very difficult to say which of the results in Fig. 5.13 is the accurate one since the wave excitation force is not directly measurable for an oscillating WEC. However, the amplitude of the W2EF estimation is smaller than the PAD2EF and UIOEF approximations. The reason for this is that the measurement of WG3 is attenuated by the radiated wave due to the interference phenomenon and this phenomenon is observed during the wave tank tests. Hence, the W2EF method may provide better approximation of the excitation force if the radiated wave is compensated.

Irregular Wave Conditions

For a PM spectrum wave with peak frequency $f_p = 0.4$ Hz and significant height $H_s = 0.24$ m, the comparison of the excitation force approximations between the W2EF, PAD2EF and UIOEF approaches is given in Fig. 5.14. Since the excitation force can not be measured directly, it is very hard to say which method is better. Via the comparison

in Fig. 5.14, it is found that: (i) all these three methods give good estimations of the excitation force when the wave (or excitation force) is large; (ii) when the wave is small or changes rapidly, the estimations given by the PAD2EF and UIOEF approaches are more variable, compared with the W2EF estimation; (iii) generally speaking, the excitation force magnitude given by the W2EF method is smaller than the ones provided by the PAD2EF and UIOEF approaches, since the WG3 measurement is attenuated by the radiated wave.

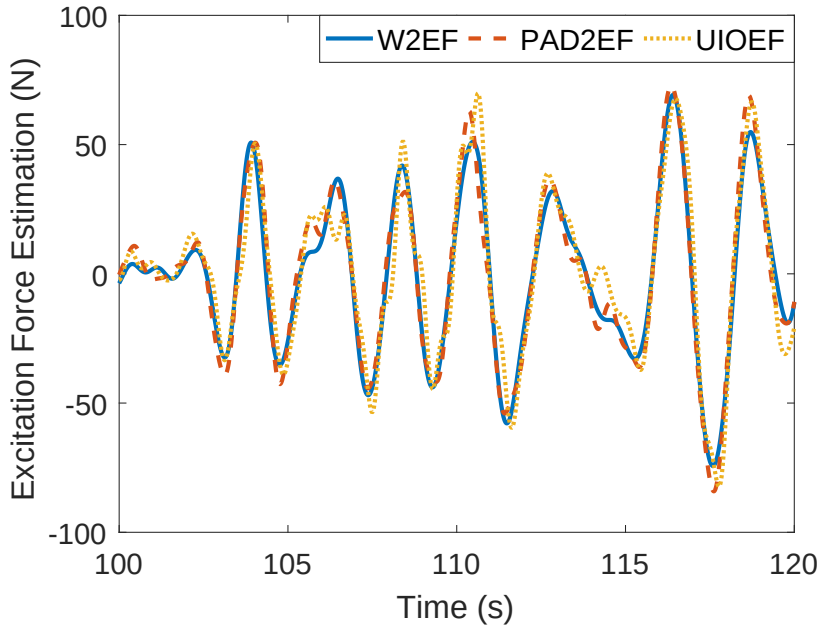

Fig. 5.14 Comparison of the excitation force approximations in a forced-motion test under irregular wave.

A comparison of these methods are made as follows:

- The W2EF modelling approach requires the wave elevation measurement only. The W2EF approach shows advantages in easy implementation and good tolerance to the mechanical friction and fluid viscous forces. However, the W2EF approach is subjected to linear wave theory and small radiated wave. Additionally, accurate wave prediction is compulsory to overcome the non-causality of the W2EF process.
- The PAD2EF modelling method requires the measurements of pressure, acceleration and displacement. Hence it is complex to implement. However, for the offshore WEC devices, it is difficult to measure the wave elevation but it is quite easy to measure the pressure, acceleration and displacement. From this viewpoint,

the PAD2EF approach is more applicable than the W2EF method. The PAD2EF estimation is affected by the fluid viscous force but not the mechanical friction force and radiated wave. Another advantage is that the PAD2EF estimation is reasonably accurate for non-linear wave conditions.

- The UIOEF modelling approach only requires the displacement measurement. Thus it is easy to implement. Also, the UIOEF estimation does not suffer from the radiated wave but is influenced by the mechanical friction and fluid viscous forces. Also, the UIOEF method can be applied under non-linear wave conditions.

5.7.3 Results of W2M modelling

Regular Wave Conditions

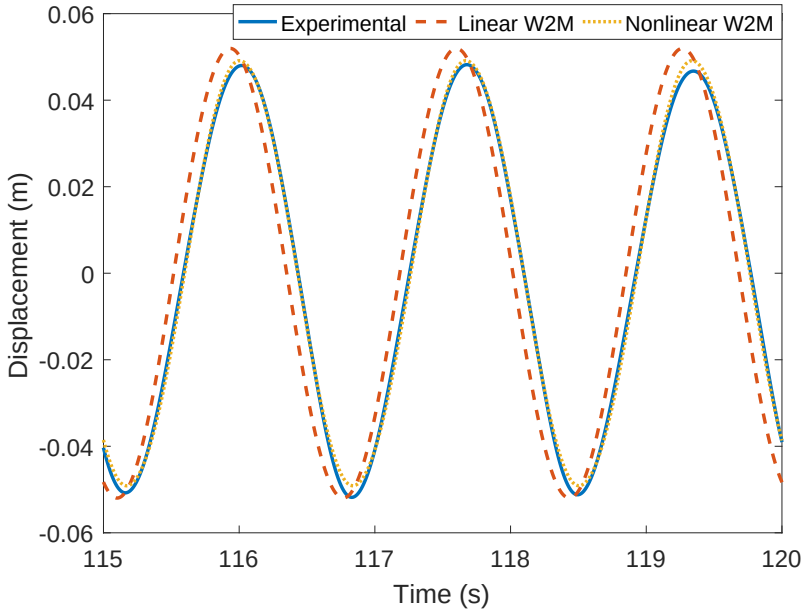

Fig. 5.15 Comparison of the displacement between the linear, non-linear W2M models and forced-motion tests.

For a regular wave with frequency $f = 0.6$ Hz and height $H = 0.08$ m, the displacement responses of the linear and non-linear W2M models are compared with the experimental results of the forced-motion tests and shown in Fig. 5.15. It is shown that the numerical result of the non-linear W2M model fits the experimental data much better than the linear W2M model in terms of the amplitude and phase responses.

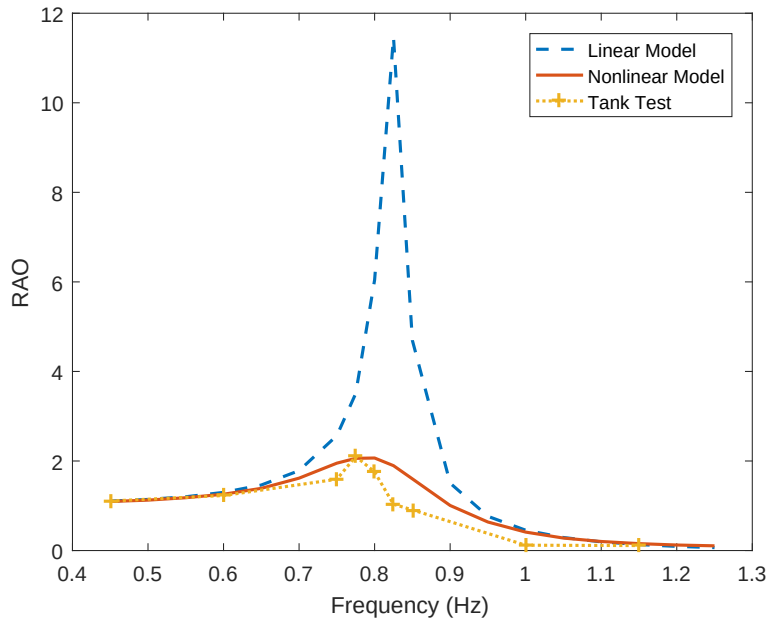

Fig. 5.16 Comparison of the RAOs between the linear, non-linear simulations and forced-motion tests.

A series of forced-motion tests are conducted in the wave tank and compared with the numerical simulations of the linear and non-linear W2M models. The RAOs of the linear and non-linear W2M are compared with the experimental data and shown in Fig. 5.16[1], which indicates:

- For the linear W2M model, the maximal RAO is about 11.77 when the wave frequency approximates 0.822 Hz (natural frequency in free-decay tests in Section 4.5.2). For the non-linear W2M model, the maximal RAO (about 2.13) occurs at the frequency 0.781 Hz. The RAO of the tank tests reaches its peak 2.10 at the frequency 0.775 Hz. The non-linear model shows better correspondence with the forced-motion tests.

- For the low (0.4–0.7 Hz) and high (above 0.9 Hz) frequency waves, the linear and non-linear W2M models share the same properties with the wave tank tests. However, when the wave frequency is within the resonant region (0.7–0.9 Hz), the linear W2M model overestimates the RAO to an unrealistic value (11.77),

[1]The definition of RAO is given in Eq. (3.68) for the linear model. For the non-linear model, the RAO concept is applied here as well to keep consistence of other publications in the community of hydrodynamics. In this situation, the RAO is defined as the amplitude ratio between the input and the output. For the PAWEC results in Fig. 5.16, RAO is defined as the amplitude ratio between the wave elevation and the buoy displacement.

which means the buoy is threw into the air. The non-linear W2M model gives an maximal RAO (2.13) close to the experimental result (2.10).

- For the 1/50 scale buoy, the pitching motion affects the heaving motion significantly within the frequency arrange of 0.85–1 Hz and thus the RAOs of the tank tests decrease rapidly within this area.

Irregular Wave Conditions

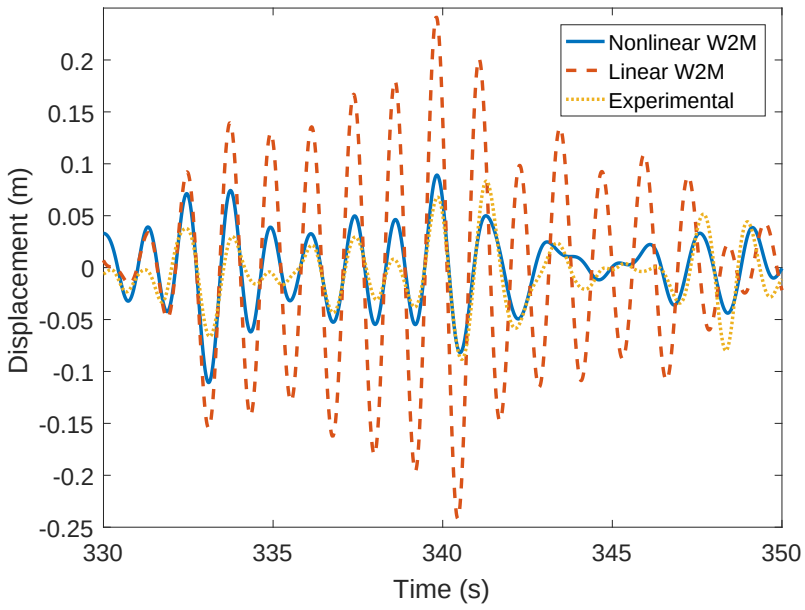

Fig. 5.17 Displacement comparison among the linear/non-linear W2M simulations and experimental data of a forced-motion test under irregular wave.

For a PM spectrum wave with peak frequency $f_p = 0.6$ Hz and significant height $H_s = 0.11$ m, the displacement responses of the linear and non-linear W2M models are compared with the forced-motion tests in Fig. 5.17. The linear W2M model overestimates the displacement of the PAWEC, whilst the non-linear W2M model gives a relatively close approximation of the displacement response.

5.7.4 Parameters of numerical simulation

The system matrices of the W2EF system in Eqs. (5.11) and (5.12) are:

$$A_e = \begin{bmatrix} -0.234 & 1.818 & 0.530 & -0.554 & -0.314 & -0.054 \\ -1.818 & -0.900 & -3.043 & 1.082 & 0.861 & 0.130 \\ 0.530 & 3.044 & -1.798 & 4.233 & 1.553 & 0.306 \\ 0.554 & 1.082 & -4.233 & -2.688 & -5.096 & -0.480 \\ -0.314 & -0.861 & 1.553 & 5.096 & -3.590 & -3.064 \\ 0.054 & 0.130 & -0.306 & -0.480 & 3.064 & -0.157 \end{bmatrix}, \quad (5.34)$$

$$B_e = \begin{bmatrix} 164.34 & 251.36 & -236.52 & -175.67 & 114.01 & -18.71 \end{bmatrix}^T, \quad (5.35)$$

$$C_e = \begin{bmatrix} 1.6434 & -2.5136 & -2.3652 & 1.7567 & 1.1401 & 0.1871. \end{bmatrix}. \quad (5.36)$$

The parameters of the BPF in Eq. (5.14) are: $\omega_c = 8\pi$ rad/s, $A(\omega_c) = 2433$ and $Q = 100$.

The system matrices of the UIO in Eqs. (5.23) and (5.23) are:

$$M = \begin{bmatrix} -0.57 & 9.01 & 0 & 0 & 0 & 0 \\ -27.09 & -39.1 & 0.02 & 0.02 & 0.01 & 0.04 \\ -3.24 & -0.13 & -3.18 & -4.34 & -3.1 & 0 \\ -0.95 & 0.43 & 4.34 & -0.09 & -0.39 & 0 \\ 0.2 & -1.62 & 3.10 & -0.39 & -2.85 & 0 \\ -32856 & -242450 & 0 & 0 & 0 & 0 \end{bmatrix}, \quad (5.37)$$

$$G = \begin{bmatrix} 0 & 0.0379 & 0 & 0 & 0 & 0 \end{bmatrix}^T, \quad (5.38)$$

$$L = \begin{bmatrix} 357.52 & 7881.9 & 73.80 & -158.04 & -244.25 & -9183200 \end{bmatrix}^T, \quad (5.39)$$

$$H = \begin{bmatrix} -8.01 & 39.1 & -40.57 & 5.55 & 17.89 & 242450 \end{bmatrix}^T. \quad (5.40)$$

The observer gains vary significantly and hence the UIO is sensitive to the measurement noise. This is due to the system property of the augmented system in Eqs. (5.17) and (5.18). The displacement varies slowly with the magnitude of 10^{-2} whilst the excitation force changes rapidly with the magnitude of 10. Therefore, the augmented system

suffers from a stiffness problem. To attenuate the influence on the UIO performance of the measurements noise, a low pass filter is applied to smooth the displacement measurement.

5.8 Summary and conclusion

5.8.1 Summary

This Chapter focuses on the modelling of the excitation force and the model verification via wave tank tests. The excitation force can be approximated with reasonable accuracy from the measurements of wave elevation, pressure, acceleration and displacement. Therefore, the W2EF, PAD2EF and UIOEF modelling approaches are proposed, simulated and tested. The experimental data show a high correspondence with the estimations from the W2EF, PAD2EF and UIOEF methods. This part of work is detailed in Sections 5.1, 5.5 and 5.7.

Linear and non-linear W2M models are derived based on the W2EF, linear and non-linear F2M models. The experimental data of the forced-motion tests indicate that the linear W2M model overestimates the PAWEC motion and the non-linear W2M model gives a more realistic estimation of the PAWEC motion and fits much better with the experimental data compared with the linear model. This part is detailed in Section 5.6.

A wide variety of excitation and forced-motion tests are conducted in a wave tank to verify the proposed excitation force approximation approaches. The experimental data collected from the excitation tests fit with the W2EF model numerical results to a high degree in the time- and frequency-domains under both regular and irregular wave conditions. For the forced-motion tests, all the W2EF, PAD2EF and UIOEF modelling approaches are applied to estimate the excitation force and their estimates are in close agreement with each other. The numerical/experimental data comparison is discussed in Section 5.7. Hence, it can be concluded that the proposed excitation force approximation approaches may be useful for the performance assessment and real-time power maximisation control of WEC systems. In Chapter 8, the W2EF method is applied to estimate wave excitation force for reference generation.

5.8.2 Conclusion

Based on the comparison among the W2EF, PAD2EF and UIOEF approaches, the application scenarios are concluded as:

- The W2EF approach in Eqs. (5.11) and (5.12) gives reasonably accurate estimation of the excitation force based on the conditions: (i) the incident wave is linear; (ii) the radiated wave due to the PAWEC motion is small compared to the incident wave; (iii) wave elevation measurement and precise prediction are accessible.
- The PAD2EF approach in Eq. (5.15) can provide good estimation of the excitation force if the conditions are satisifed: (i) the measurements of pressure, acceleration and displacement are available and (ii) the fluid viscous force is small enough to be neglected.
- The UIOEF strategy in Eqs. (5.23) and (5.24) only depends on the displacement measurement and can provide precise estimation of the excitation force and the velocity. But the mechanical friction and fluid viscous forces can not be decoupled from the excitation force estimation.
- The UIOEF method shows great potential for the real-time power maximisation control since the measurement system is so simple and the UIO technology is flexible to apply. For off-shore application, the PAD2EF method may be more practical than the W2EF approach. The PAD2EF sensing system seems more complex than the W2EF sensing system. However, the real-time wave elevation measurement is very difficult to achieve whilst the press, displacement and acceleration are easy to measure.

Based on the W2EF modelling, the derived non-linear W2M model can provide more precise prediction of the PAWEC dynamics than the linear one. From the frequency-domain RAO scanning in Fig. 5.16, it is clear that the linear W2M model overestimates the PAWEC displacement response within the resonance frequency area, whilst the non-linear modelling results fit well with the forced-motion tests. For the time-domain tests under irregular wave conditions shown in Fig. 5.17, the non-linear simulation results are much more close to the experimental data than the linear W2M modelling. This results are expected since it is concluded that the non-linear viscous and friction forces have huge impact on the PAWEC dynamics and energy dissipation in Chapter 4.

Chapter 6

PAWEC design and wave tank tests

6.1 Introduction

This Chapter discuses the mechanical and electrical design of the scaled down PAWEC and its wave tank tests. Section 6.2 details the procedure to scale down the PAWEC for wave tank tests according to the Froude analysis. Section 6.3 gives the details of the mechanical design of the scaled down PAWEC and its sketch solution in SOLIDWORKS®. Section 6.4 describes the sensing system design and the calibration procedure, whilst Section 6.5 details the DAQ hardware and its GUI design in LABVIEW™. Section 6.6 illustrates the wave tank dimension, wave-maker properties and the configuration of the free-fall, free-decay, excitation and forced-motion tests.

6.2 Scaling problem

This Section discusses why the Frounde number is selected as the scaling principle and how the modal and prototype parameters are selected. The details are given as follows.

6.2.1 Froude number

The design sea state is characterised by the PM spectrum with peak frequency $f_p = 0.095$ Hz and significant wave height $H_s = 4.3$ m, which is typical for the north sea.

The design parameters related to this PM spectrum are called the *modal parameters*. Thus the modal wave height H_m, modal period T_m and modal wavelength λ_m are given as:

$$H_m = H_s, \tag{6.1}$$

$$T_m = T_e, \tag{6.2}$$

$$\lambda_m = \frac{gT_m^2}{2\pi}. \tag{6.3}$$

The significant wave height H_s and energy period T_e are defined in Eqs. (3.29) and (3.31), respectively. Here modal wavelength λ_m is related to the modal period T_m and given in Eq. (6.3) to determine the PAWEC diameter by satisfying the PA definition in Section 2.2.1. Therefore, the modal velocity is given as:

$$v_m = \frac{\pi H_m}{T_m}. \tag{6.4}$$

According to the PM spectrum specifications $H_s = 4.3$ m and $f_p = 0.095$ Hz, the modal parameters are $H_m = 4.3$ m, $T_m = 9.1201$ s, $\lambda_m = 129.86$ m, $v_m = 1.4812$ m/s.

The choice of the buoy radius should satisfy: (i) the point absorber definition (see Section 2.2) and (ii) good power capture performance. According to the definition of PAWEC by Budal and Falnes (1975b), the horizontal extent of a point absorber is much smaller than one wave length. According to the shape optimisation study by Goggins and Finnegan (2014), PAWEC devices with radius varying within 5–10 m have good power capture performance for the case study of the Atlantic marine energy test site for a specific wave spectrum. The wave spectrum selected in this study is represented by the PM spectrum with $H_m = 4.3$ m and $f_p = 0.095$ Hz which is close to the spectrum detailed in Goggins and Finnegan (2014). Therefore the modal radius is selected as $r_m = 7.5$ m to satisfy the PA definition and the optimal radius range.

The selection of the draft should satisfy: (i) good power capture performance and (ii) avoiding over-topping and submerging phenomena. The influence of the draft-radius ratio on the PAWEC performance is investigated by Goggins and Finnegan (2014) and it is concluded that good performance can be achieved when the ratio is around 2. Therefore, in this study the draft-radius ratio is selected as 1.86. Thus the modal draft is set as $d_m = 14$ m and the modal heigh is set as $b_m = 2d_m = 28$ m.

Since all the modal parameters are specified, the scaling problem can be solved by similarity analysis. According to the study by Newman (1977), the orders of magnitude of the initial, gravitational and viscous forces should be estimated and compared before the scaling down procedure. These forces are characterised by the physical length $l_m = 2r_m$, water density ρ, gravity constant g, modal velocity v_m and viscosity coefficient μ. Thus the orders of magnitude of the initial force F_i, gravitational force F_g and viscous force F_v are given in Table 6.1.

Table 6.1 Orders of magnitude of the inertial, gravitational and viscous forces.

Force	**Order of Magnitude**	**Value**
Inertial Force	$\rho v_m^2 l^2$	10^5
Gravitational Force	$\rho g l^3$	10^7
Viscous Force	$\mu v_m l$	10^{-2}

From the comparison made in Table 6.1, it is clear that the inertial and gravitational forces govern the PAWEC dynamics rather than the viscous force. Compared to the inertial and gravitational forces, the viscous force can be ignored. Therefore the Froude number FN (the ratio between the inertial and gravitational forces) is applied to scale down the PAWEC model rather than the Reynolds number (the ratio between the inertial and viscous forces), given as:

$$FN = \sqrt{\frac{\rho v_m^2 l^2}{\rho g l^3}} = \frac{v_m}{\sqrt{gl}}. \tag{6.5}$$

To note: The dynamic viscosity of water is selected at the temperature 20° as $\mu = 1.002$ mPa$\cdot$s. In the real situation, the water satisfies the Newton fluid conditions. However, when we discuss the surface wave based on linear wave theory, the viscosity of water is omitted since it is small compared with the gravitational force. When we discuss the buoy-wave interaction, the viscous force is ignored if the relative velocity between the PAWEC and the water particles is small. However, if resonance occurs, the relative velocity is large and thus the viscous force cannot be ignored. This part of the work is detailed in Chapter 4.

6.2.2 Scale ratio

The scale down ratio between the PAWEC model in real sea and the small prototype for wave tank tests is determined by the modal parameters and the wave tank dimensions. Here define the geometric scaling ratio $S_{r,l}$ as;

$$S_{r,l} = \frac{r_p}{r_m}, \tag{6.6}$$

where the subscript l means "length"; subscript p means "prototype" which is the scaled down prototype for wave tank tests; and subscript m means "modal" which is the full-scale PAWEC model in the real sea.

According to the Froude number FN in Eq. (6.5), the scale ratios for time, velocity, force, power, power density and mass are given as:

$$S_{r,t} = S_{r,l}^{0.5}, \tag{6.7}$$
$$S_{r,v} = S_{r,l}^{0.5}, \tag{6.8}$$
$$S_{r,f} = S_{r,l}^{3}, \tag{6.9}$$
$$S_{r,p} = S_{r,l}^{3.5}, \tag{6.10}$$
$$S_{r,pd} = S_{r,l}^{2.5}, \tag{6.11}$$
$$S_{r,m} = S_{r,l}^{3}. \tag{6.12}$$

The wave tank in the University of Hull is 13 m in length, 6 m in width and 2 m in height (with water depth 0.9 m). Up to eight pistons can be selected to generate regular/irregular waves. The wave-maker can generate stable waves with frequencies $f = 0.4 : 0.1 : 1.2$ Hz and height around $H = 0.1$ m. For this application the geometric ratio is selected as $S_{r,l} = 1/50$, to satisfy: (i) the wave-maker capacity (both the wave frequency and height) and (ii) deep water assumption in Eq. (3.24).

Therefore, the time ratio is $S_{r,t} = 1/7.0711$. The modal sea state represented by a PM spectrum with peak frequency $f_p = 0.095$ Hz and significant wave height $H_s = 4.3$ m can be scaled down to its $1/50$ spectrum (according to the Froude number) featured by the peak frequency $f_p = 0.0952 \times 7.0711 = 0.67$ Hz and significant wave height $H_s = 4.3/50 = 0.086$ m. Therefore, the wave conditions in the wave tank tests are

configured with wave frequencies as $f = 0.4 : 0.1 : 1.2$ Hz and wave height $H = 0.08$ m for regular waves. For irregular waves, the peak frequencies of the PM spectra are selected as $f_p = 0.4 : 0.2 : 1$ Hz.

6.2.3 Design parameters

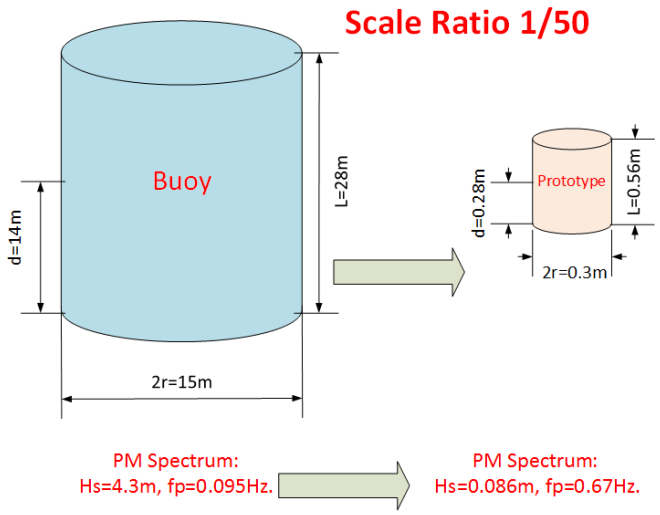

Fig. 6.1 Scaling down sketch of the experimental buoy.

Since the scale down ratio in length is selected as $S_{r,l} = 1/50$, other scaling down ratios can be computed according to Eqs. (6.7)–(6.12). Some critical parameters of the scaled down prototype are given in Table 6.2 and Fig. 6.1. These parameters are used for the PAWEC system design.

Table 6.2 Design parameters of the scaled down prototype.

Parameters	**Scale Ratio**	**Modal Value**	**Prototype Value**
PAWEC Radius	$1/50$	7.5 m	0.15 m
PAWEC Draft	$1/50$	14 m	0.28 m
PAWEC Mass	$1/(1.25 \times 10^5)$	2.4740×10^6 kg	19.792 kg
Peak Frequency	$7.0711/1$	0.095 Hz	0.67 Hz
Significant Height	$1/50$	4.3 m	0.086 m
Power Transport	$1/(1.7678 \times 10^4)$	8.2292×10^4 W/m	4.6673 W/m

6.3 Mechanical design

This Section discusses the sketch of the PAWEC mechanical system and its installation with the sensing system and the wave tank gantry. The details are given as follows.

6.3.1 Buoy design and sketch

A Computer Aided Design (CAD) software, SOLIDWORKS®, is adopted in this study to design the PAWEC mechanical system according to the prototype parameters in Table 6.2. The impression view of the PAWEC is shown in Fig. 6.2 with $r = 0.15$ m, $b = 2d = 0.56$ m. The total mass is designed as 10 kg for the PAWEC mechanism and the left amount of mass (9.79 kg) is reserved for the PTO mechanism. For the hydrodynamic tests without PTO mechanism, the buoy weight can be balanced by ballasts.

As shown in Fig. 6.2, the buoy is separated into the bottom, side and top components in the design. All the design details are given in Appendix A. For the WEC bottom component (or base), there are five open holes designed for the installation of pressure sensors, as shown in Fig. 6.3, for the purpose of measuring the dynamic pressure acting on the wet surface.

There is an open hole in the top component (see Fig. 6.4) with a lid (Appendix A). The radius is 0.06 m to give enough space to install the pressure sensors. Also, the gravity and buoyancy centres can be easily balanced with ballasts through this hole. The top, side and bottom components are welded together with water-proof tight level. With the concern of anti-corrosion, the material is stainless steel 316. All the details of the mechanical design are given in Appendix A.

6.3.2 Connection joints

The buoy system is guided by a polished circular rod through two linear bearings. The linear bearings are fixed to the wave tank gantry via aluminium profiles, as shown in Fig. 6.5. The linear bearings, made by NSK Ltd with series number LMF20UU403, can reduce the mechanical friction to a small amount if they are appropriately lubricated.

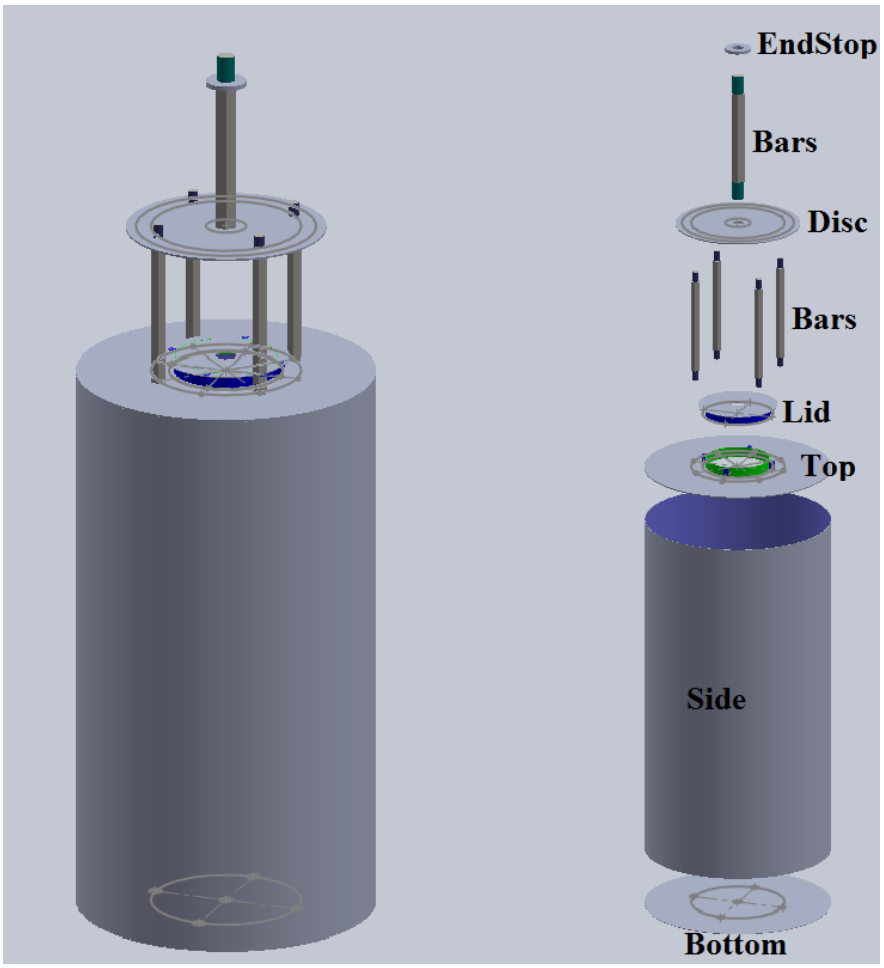

Fig. 6.2 Impression view of the 1/50 scaled PAWEC in SOLIDWORKS®.

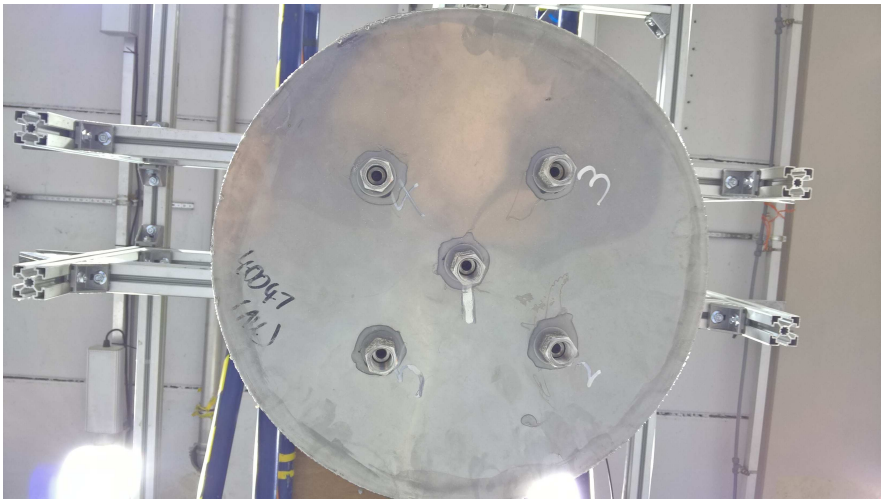

Fig. 6.3 Five pressure sensors installed at the bottom of the buoy.

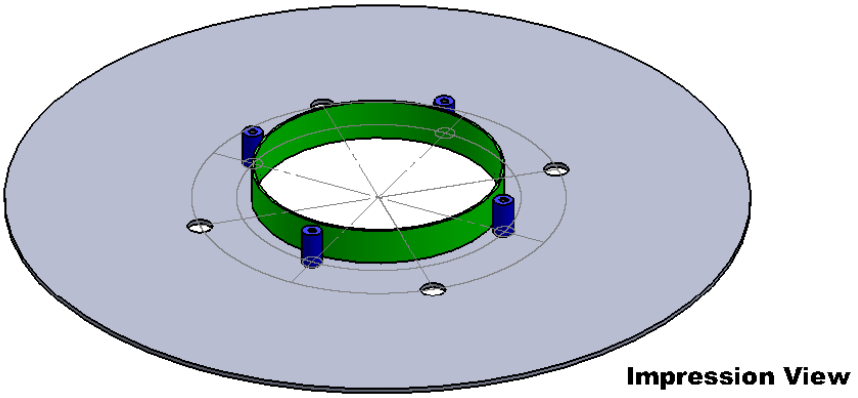

Fig. 6.4 Impression view of the top component in SOLIDWORKS®.

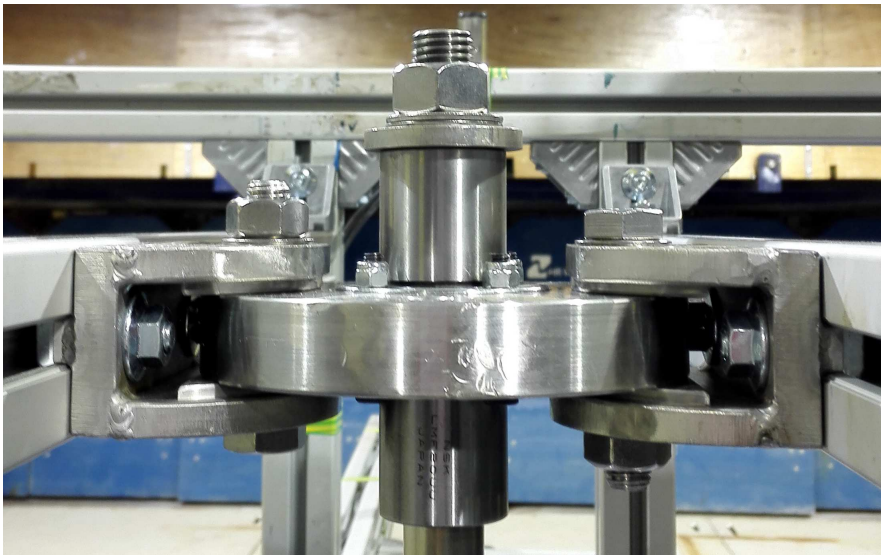

Fig. 6.5 Linear bearings and their connection to the wave tank gantry.

The housing of the LVDT is fixed to the wave tank gantry while the core is rigidly connected to the buoy via a rod-end terminal, as shown in Fig. 6.6. For good displacement measurement, the LVDT is installed as close as possible to the buoy. The rod-end bearing terminal is selected for friction reduction.

Fig. 6.6 The connection of the LVDT to the PAWEC and wave tank gantry.

To note: Great help came from Mr. Stuart Butterick for the mechanical system design and manufacture. All the design details can be found in Appendix A.

6.4 Electrical design

This Section discusses the electrical design of the sensing subsystem, the power supply and interface circuits. The details are given as follows.

6.4.1 Sensing subsystem

The sensing subsystem compromises the pressure sensors, LVDT, accelerometer and wave gauges, detailed as follows.

Pressure sensors

Five pressure sensors are installed at the bottom of the PAWEC and named as PS1-5. To choose the pressure sensors, some critical specifications should be satisfied, including the power supply, output range and measurement range. For the tanks tests, the maximal water depth is 1 m and hence the maximum pressure is about 0.1 bar. The measurement range of the pressure sensors should cover this range. The power supply is shared by all sensors. Therefore, the pressure sensors are selected with production number 3300R01B0G01B manufactured by the Gems Sensors & Controls Manufacturing Ltd. According to the data-sheet (GemsSensors, 2015), some key specifications are given as:

- Supply voltage: $8-30$ V_{dc}.
- Output voltage: $0-5$ V_{dc}.
- Measurement range: $0-1$ bar.
- Temperature compensated.

The enclosure level is International Protection rate 65 (IP65) which is not water-proof and hence sealing design is required. The sealing is achieved by O-rings and silicone rubber (DOW CORNING 3140 RTV COATING) and shown in Fig. 6.7. The sealing performance is tested with the buoy submerged in water for 24 hours before wave tank tests.

For the purpose of signal synchronisation, a submersible level/depth transmitter is needed and numbered PS6. The requirements of PS6 is all most the same as PS1-5. However, a good water-proof performance is required since it is submerged all the time. The pressure sensor from Applied Measurements Ltd with series number Pi9942-6mWG-A4AAV-10-000 satisfies the application scenario and is selected in this study. The PS6 satisfies the IP68 level and hence has good water-proof property. Other specifications of PS6 are similar to the PS1-5 and thus are not given here.

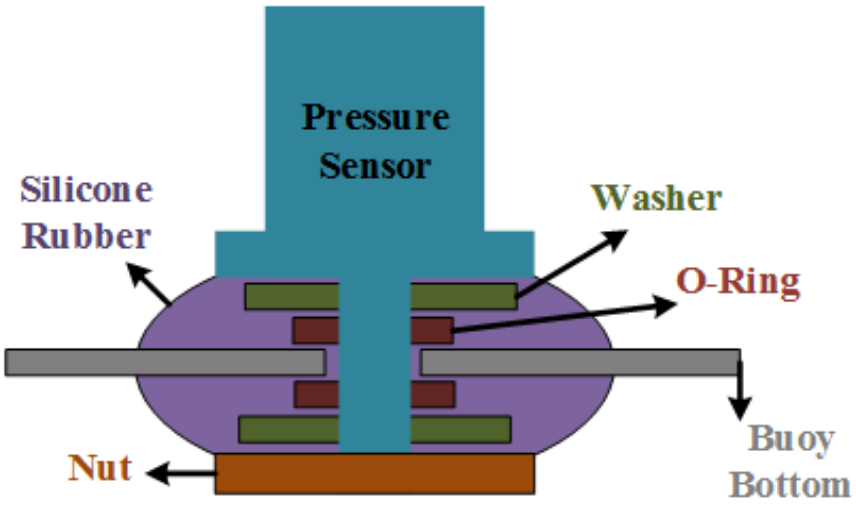

Fig. 6.7 The sealing of the pressure sensors.

Since the accuracy of the pressure sensors relies on the temperature and application environment, daily calibration is required and discussed in Section 6.5.2.

Displacement sensor

To select the displacement sensor, its power supply should be compatible with the pressure sensors and its output voltage should meet the DAQ system input range. For the wave tank test, the wave height is set as $H = 0.08$ m and the buoy displacement is within ± 0.2 m. Therefore, the displacement sensor is selected from Applied Measurements Ltd with series number AML/IEU+/-200mm-ROR-02-000. Some key specifications are given as:

- Supply voltage: $10 - 24$ V_{dc}.
- Output voltage: $0 - 5$ V_{dc}.
- Measurement range: ± 200 mm.

The measurement accuracy is influenced by the application environment and hence daily calibration is required and discussed in Section 6.5.2.

Acceleration sensor

According to the wave conditions and the PAWEC responding properties, the PAWEC acceleration is within $\pm 2\ \mathrm{m \cdot s^{-2}}$. Thus a 3-axis accelerometer from the Analog Devices Corporation with series number ADXL327 is selected in this study. The accelerometer is fixed to the top of the buoy and sealed by the silicone rubber for the purposes of water-proof and electrostatic protection. The accelerometer ADXL327 is very sensitive to the static electricity and any touch without antistatic treatment is not allowed. Some key specifications are given as:

- Supply voltage: $1.8 - 3.6\ \mathrm{V_{dc}}$.
- Output voltage: $0 - 3\ \mathrm{V_{dc}}$.
- Measurement range: $\pm 19.62\ \mathrm{m \cdot s^{-2}}$.
- Excellent temperature stability.

Other specifications can be found from the data-sheet (AnalogDevices, 2009). Since the accelerometer characterises excellent temperature stability, it is calibrated once before installation rather than daily calibration. The calibration procedure is given in Section 6.5.2.

Wave gauges

The wave elevation is measured by five wave gauges, as shown in Fig. 6.8. These wave gauges are integrated with the wave tank system. The wave gauges were bought from the HR Wallingford Ltd with product number HRIA-1014. The wave gauges are monitored by a wave probe monitor with production number HRWG-0091. The monitor provides power supply and measurement filtering for the wave gauges and sockets for wave tank DAQ subsystem. The wave tank DAQ subsystem was manufactured by the Measurement Computing Ltd with product number USB-1608FS (MeasurementComputing, 2014). The wave gauges are of resistive type and hence their accuracy replies a lot on the fluid temperature and application environment. Therefore daily calibration is necessary and detailed in Section 6.5.2.

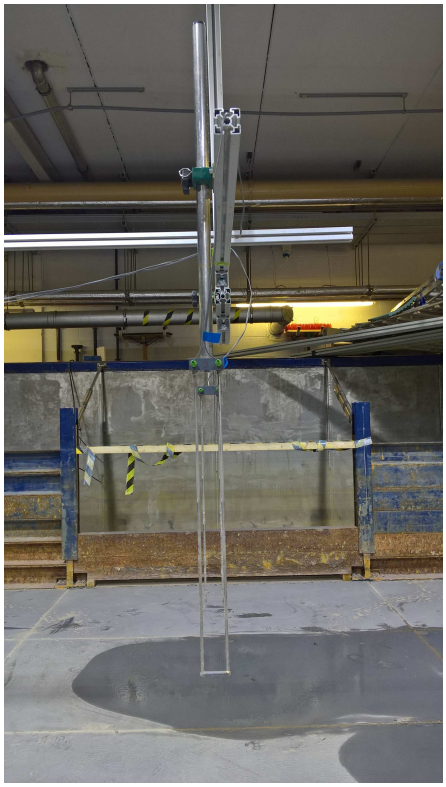

Fig. 6.8 Wave gauge installation for wave tank tests.

6.4.2 Power supply and circuits sketch

The pressure sensors, LVDT and accelerometer are powered by a triple DC power supply with series number HM7042-5. However, the ripples of the power supply is up to 200 mV in peak-to-peak value. Observed from the sensors' outputs, the power supply ripples have a significant influence on the measurement accuracy, especially on the accuracy of the pressure sensors and accelerometer. Therefore voltage stabilisation is necessary and DC regulators are applied to attenuate the ripples for the purpose of smoothing the power supply.

To stabilise the power supply, a DC-DC converter, LM2733Y from the Texas Instruments Corporation, is applied to provide smooth power supply (12 V with ripple within 20 mV) for the pressure sensors and LVDT. Another DC-DC converter, TPS63030EVM-417 from the same company, is applied to provide precise power supply (3.3 V with ripple within 10 mV) for the accelerometer. The power supply and interface circuits are designed and sketched in the ALTIUM DESIGNER™, detailed in Appendix B.

To note: Half of the circuits assembling work is done by my colleague Mr. Mustafa Abdelrahman. Great help came from Mr. David Wright and Ms. Joanna Arnett for the requisition of electrical chips.

6.5 Data acquisition and signal processing

This Section discusses the DAQ hardware selection and its collaborative software coded in LABVIEW™ with details as follows.

6.5.1 Data acquisition hardware

The PAWEC DAQ subsystem comprises the DAQ card and its corresponding software. The DAQ card should provide enough Analogue-Digital Converter (ADC) channels and be compatible with all the sensors' outputs. Also, at least on digital output port is required to trigger the wave tank DAQ subsystem. The DAQ card USB-6210 from the National Instruments Corporation satisfies all the requirements and hence is selected in this study. Its corresponding GUI is coded in the LABVIEW™. Some key specifications of the USB-6210 are given as:

- Analog input: 8 differential or 16 single analog inputs at 16 bits resolution, up to 400 kS/s sampling rate.
- Measurement range: programmable ± 10 V, ± 5 V, ± 1 V, ± 0.2 V with absolute accuracy $\pm 91.6\ \mu$V, $\pm 47.2\ \mu$V, $\pm 10.4\ \mu$V, $\pm 4.8\ \mu$V, respectively.
- Digital I/O: 4 digital input and 4 digital output, useful to generate trigger signals.
- USB bus powered.
- Frequency generator and timers are available.

All the details can be found in the USB-6210 data-sheet (NationalInstruments, 2009).

6.5.2 LABVIEW™ programming

This Section discusses the LABVIEW™ GUIs coded for sensor calibration, data collection and monitoring. The details are given as follows.

Calibration GUI

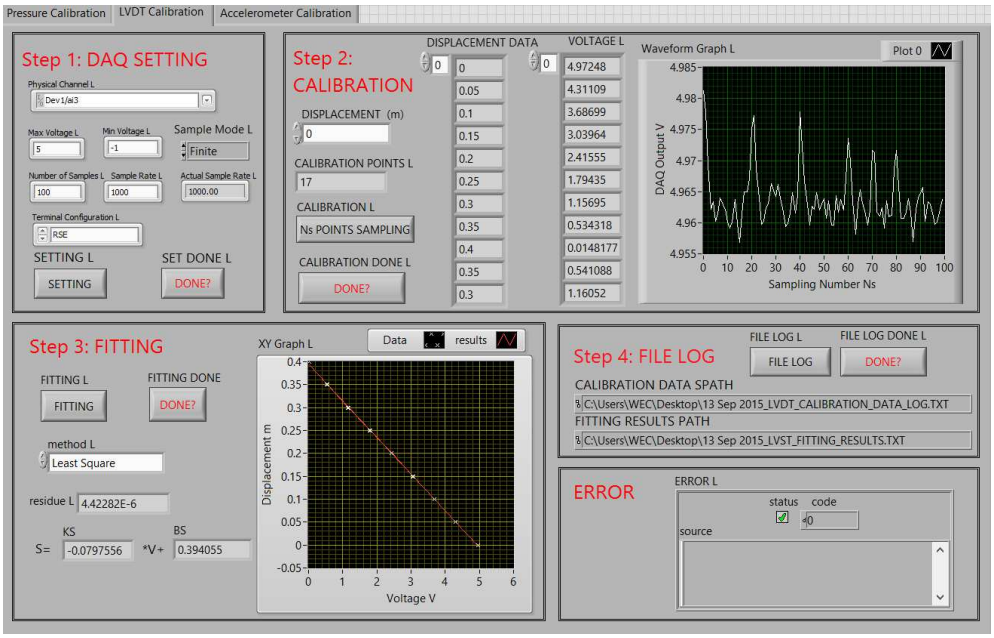

Fig. 6.9 Calibration procedure and results of the LVDT.

A DAQ GUI is developed in LABVIEW™ to calibrate the pressure sensors, LVDT and accelerometer, correspondence with the DAQ card USB-6210. The calibration procedure of the LVDT is given in Fig. 6.9. The calibration procedure of the LVDT is given as:

- Step 1: Set the DAQ card configuration according to the LVDT specifications. 100 samples are collected at each calibration point and their mean value represents the voltage output. Go to Step 2 after the DAQ setting.
- Step 2: Set the displacement of the LVDT to a series of constant value (to say ± 0.2, ± 0.15, ± 0.1, ± 0.05 and ± 0 m), and then collect the voltage outputs. All the 100 samples for each calibration point are shown in the waveform graph. If the ripples exceed 30 mV, repeat Step 2. If the ripples are small, go to Step 3.

- Step 3: Set the collected voltage as the independent variable and the displacement as the dependent variable. Linear least square fitting is applied to calibrate the relationship between the displacement and voltage and the fitting results are shown in an XY Graph window. If the fitting is not as good as expected, repeat Step 2 and 3. If the fitting is good with a small residue, go to Step 4.
- Step 4: Save all the collected data and fitting results for the wave tank tests.

The calibration procedures of the wave gauges and pressure sensors are the same as the LVDT calibration and hence omitted here. To note that the calibration of the wave gauges is conducted with the wave tank DAQ subsystem, following the same procedure above.

The calibration principle of the accelerometer is different from the LVDT on Step 2, since a constant acceleration is difficult to set. Therefore a 3-point calibration method is applied here to make use of the gravity constant. As shown in Fig. 6.10, the accelerometer is laid horizontally with its top side upwards. In this situation, the collected voltage is corresponding to $-g$ for the acceleration of the vertical direction a_z. Similarly, the voltages for $0g$ and $+g$ of the vertical acceleration can be obtained to put the accelerometer vertical and the bottom side upwards, respectively.

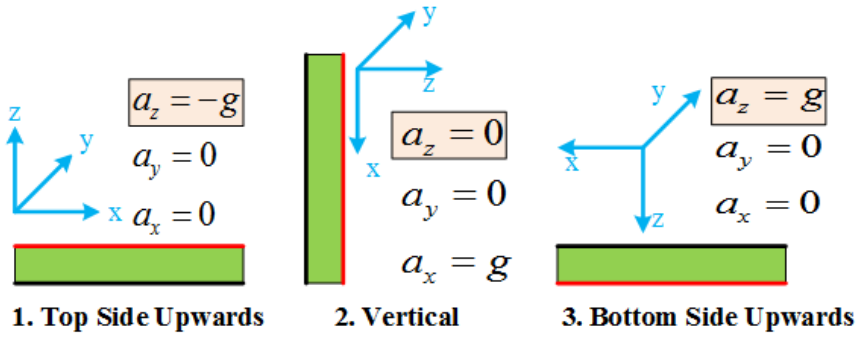

Fig. 6.10 Calibration procedure of the accelerometer.

All the pressure sensors, LVDT and wave gauges are calibrated everyday before wave tank tests and the accelerometer is calibrated once before the tank tests. According to the calibration methods mentioned above, Table 6.3 gives the calibration results on July 4^{th}, 2016.

Table 6.3 Calibration results on July 4th, 2016.

Sensor Number	Units	Slope	Intercept
PS1	Pa	1.9592×10^4	-2.8134×10^3
PS2	Pa	1.9485×10^4	-2.5755×10^3
PS3	Pa	1.9689×10^4	-2.5666×10^3
PS4	Pa	1.9850×10^4	-2.7828×10^3
PS5	Pa	2.1229×10^4	-2.8356×10^3
PS6	Pa	1.1811×10^4	-3.4835×10^3
Acc-z	$m \cdot s^2$	-21.3989	28.0160
LVDT	cm	7.8884	-20.2699
WG1	cm	3.5989	-0.0802
WG2	cm	3.8415	-0.7869
WG3	cm	3.3056	-0.0988
WG4	cm	3.3922	-0.2516
WG5	cm	2.6903	-0.3274

Data acquisition and monitoring GUI

As shown in Fig. 6.11, the data acquisition GUI contains following various functions: data acquisition, sensor outputs monitoring, physical signals monitoring, real-time file log and spectrum analysis.

The ADC channels are set as single mode with the range of 0-5 V. For the file log, the TDMS file format is selected for quick response. The sampling frequency is set as 100 Hz, which is the maximal sampling frequency of the wave tank DAQ software. The P0.0 port of the USB-6210 is configured as the digital output to trigger the wave tank DAQ subsystem with a rising edge.

To note: Half of the programming work of the DAQ GUI is done by my colleague Mr. Mustafa Abdelrahman. Special help came from Dr. Antony Wilkinson for the orgnisation of the LABVIEW™ training course from the National Instruments Cooperation.

Fig. 6.11 Data acquisition GUI coded in LABVIEW™.

6.5.3 Signal processing

Since there are two DAQ subsystems, one from the PAWEC system and the other from the wave tank system[1]. The former one triggers the latter one. Therefore, the synchronisation between these two DAQ subsystems is of critical importance. PS6 is installed in line with WG1 and perpendicular to the wave direction. The synchronisation is achieved via the waveform matching between the measurements of PS6 and WG1 and shown in Fig. 6.12. In Fig. 6.12, the phase of the PS6 measurement fits the WG1 measurement well and hence this method can provide a good synchronisation performance.

From the comparison in Fig. 6.12, the wave elevation measurement from PS6 is smaller than the one from WG1 in terms of the magnitude. The reason is that the pressure sensors gives the measurement of the dynamic pressure rather than the static one.

[1]The wave tank system has its own power supply, sensing, filtering and DAQ subsystems. The PAWEC sensing and DAQ subsystems are not allowed to be connected to the wave tank system in case there are any conflicts causing damage to the wave tank system. Hence, there are two DAQ subsystems and the synchronisation problem raises up due to the difference between these two DAQ subsystems. For the purpose of synchronising the two DAQ subsystems, PS6 is installed in line with WG1 and the wave tank DAQ subsystem is triggered by the PAWEC DAQ subsystem.

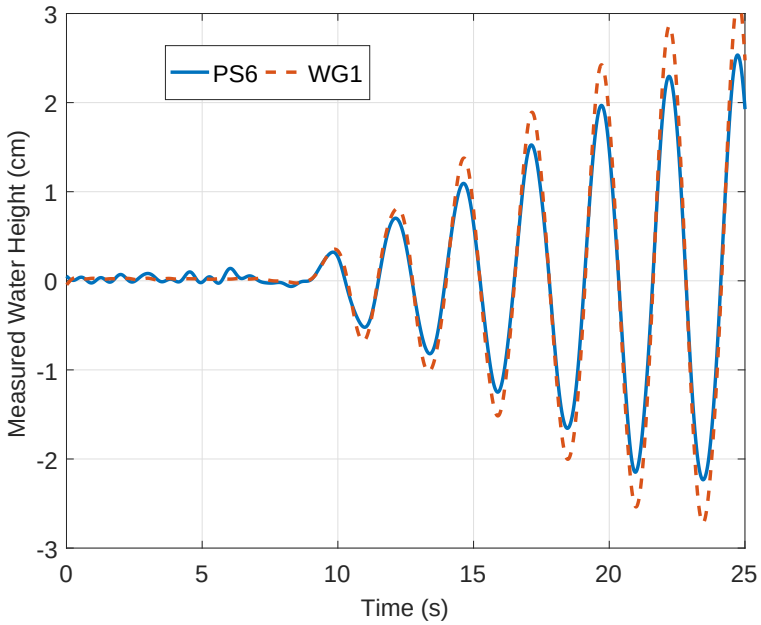

Fig. 6.12 Synchronisation of the two DAQ subsystems.

According to the Bernoulli equation, the dynamic pressure is smaller than the static one. Therefore the wave elevation estimated from the pressure sensor is smaller than the wave gauge measurements. The phase information is more important than the amplitude information for the purpose of synchronisation. As shown in Fig. 6.12, the PS6 measurement keeps in phase with the WG1 measurement and thus the synchronisation is achieved.

Low pass filters are applied to attenuate the measurement noise. An Infinite Impulse Response (IIR) type low pass filter is applied as softer filter in MATLAB®, with function *designfilt*. The low pass filter is configured with cut-off frequency $f_c = 5$ Hz, order number $n = 10$. As shown in Fig. 6.13, the low pass filter can attenuate the measurement noise to a very small amount. This measurement is collected from PS2 and given in a formation of water head.

As mentioned in Section 5.4.2 The band pass filter is adopted to provide "pseudo-velocity" or soft measurement from the physical displacement measurement. The details are given as follows.

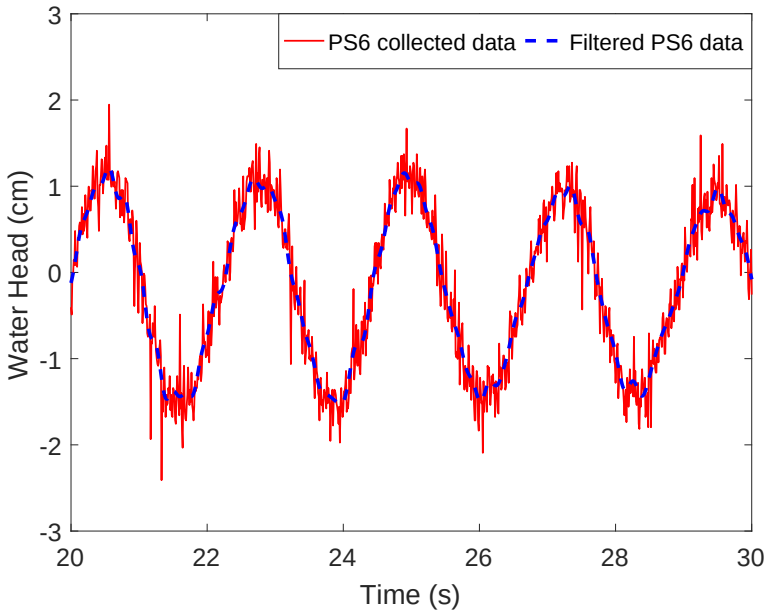

Fig. 6.13 Comparison of the pressure measurements between the filtered and unfiltered data from PS2.

6.6 Wave tank tests

This Section discusses the wave tank dimensions, wave-maker properties and the procedures of various wave tank tests, including the free-fall, excitation, free-decay and forced-motion tests.

6.6.1 Wave tank properties

Wave tank dimensions

As shown in Fig. 6.14, the wave tank is 13 m in length, 6 m in width and 2 m in height (with water depth 0.9 m). Up to 8 pistons can be selected moving forwards and backwards to generate waves from the right side propagating to the left. In this wave tank, regular and irregular waves can be generated.

The $1/50$ scale PAWEC is installed in the centred area of the wave tank. Five WGs are mounted to measure the water elevation in real-time, with two wave gauges in the up-stream (WG1 & WG2), one wave gauge (WG3) in line with the buoy and two wave gauges (WG4 & WG5) in the down-stream. Five pressure sensors (PS1-5) are installed

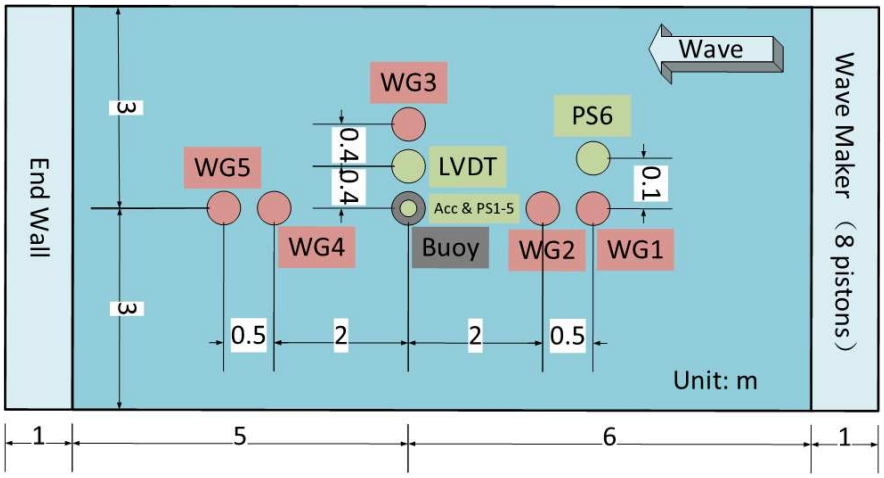

Fig. 6.14 Sketch of the wave tank, the installation of the 1/50 scale prototype and the configuration of the sensing subsystem.

at the bottom of the buoy to measure the dynamic pressure of buoy-wave interaction and one pressure sensor (PS6) is fixed at the same position as WG1 for synchronisation. To investigate the buoy motion, an LVDT is connected to the buoy rigidly to measure the displacement and a 3-axis Accelerometer (Acc) is mounted at the top of the buoy to measure the acceleration of the buoy. All the sensing signals are collected via a DAQ subsystem connected with a GUI coded in LABVIEW™. The sampling frequency is 100 Hz.

Wave-maker and wave generation

The wave-maker consists of eight individual paddles which can move forwards and backwards to generate regular and irregular waves. According to the data-sheet of the wave-maker system (Beresford, 2003), some key specifications are given as:

- Paddle width: 0.75 m.
- Paddle stroke: 0.6 m.
- Paddle velocity: 0.87 ms^{-1}.
- Paddle force: 1.3 kN.
- Paddle nominal power: 1.0 kW.
- Force feedback available for wave-maker calibration.

More details can be found from the data-sheet (Beresford, 2003).

The wave generation theory of the wave-maker is based on the superposition principle (Ogilvie, 1964; St Dinis and Pierson Jr, 1953). Thus the irregular waves can be viewed as a summation of a group of harmonic waves. Each of the harmonic waves is represented by appropriate amplitude $a(n)$, frequency $f(n)$ and initial phase $\phi(n)$. The amplitude $a(n)$ and frequency $f(n)$ should be sampled from the PM spectrum and the initial phase $\phi(n)$ obeys the uniform distribution within $[0, 2\pi]$. The PM spectrum is divided in to N_s strips from the starting frequency f_1 (about $f_p/2$) to the end frequency f_2 (about $3f_p$). Thus the boundary frequency of each strip is given as:

$$f_b(n) = f_s + n\frac{f_1 - f_2}{N_s}, \tag{6.13}$$

where $n = 0, 1, 2 \cdots N_s$.

According to the definition of the wave spectrum, the amplitude and frequency can be expressed by the spectrum, given as:

$$a(n) = \sqrt{2\int_{f_b(n)}^{f_b(n+1)} S(f)df}, \tag{6.14}$$

$$f(n) = \frac{\int_{f_b(n)}^{f_b(n+1)} fS(f)df}{\int_{f_b(n)}^{f_b(n+1)} S(f)df}. \tag{6.15}$$

Thus the irregular wave can be written as the summation of the N_s harmonic waves, as:

$$\eta = \Sigma_{n=1}^{N_s} a(n)\cos\left[2\pi f(n)t + \phi(n)\right], \tag{6.16}$$

where the wave measure point is set at the point $(x, y) = (0, 0)$.

For a PM spectrum identified by the significant height $H_s = 0.2482$ m and the peak frequency $f_p = 0.4$ Hz, the numerical wave elevation at $x = 0$ m is shown in Fig. 6.15. The wave height and period vary significantly and these characteristic parameters can be computed in a statistical way. The zero-crossing detection technique is applied here to determine the up-crossing and down-crossing zeros, which are marked as '+' in Fig.

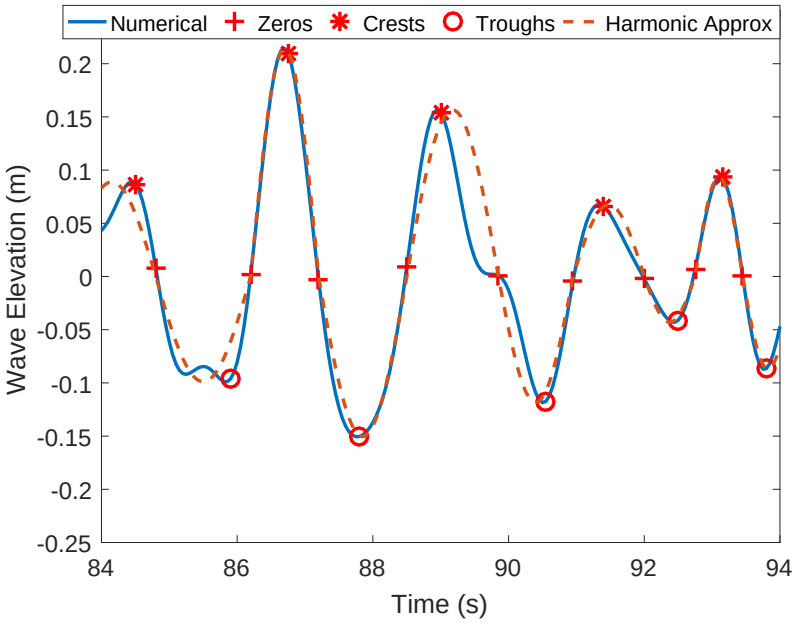

Fig. 6.15 Wave elevation and its harmonic approximation of numerical simulation according to Eq. (6.16).

6.15. The maximum point between a up-crossing and down-crossing points is defined as the wave crest, marked as '*' as shown in Fig . 6.15. Within the up-crossing and down crossing points, the wave can be approximated well with a harmonic wave, as:

$$\tilde{\eta} = \frac{H}{2} sin(\frac{\pi}{t_{dc} - t_{uc}} t - \frac{\pi t_{dc}}{t_{dc} - t_{uc}}), \tag{6.17}$$

where the H, t_{dc} and t_{uc} represent the local wave height, the down-crossing and up-crossing time instants, respectively. Similarly, the other half-wave can be approximated by the wave trough, down-crossing and up-crossing zeros. As shown in Fig. 6.15, this half-harmonic-wave method gives a very close approximation to the real wave, which indicates that the real wave can be specified by instant magnitude and frequency. This also indicates that the estimation of instantaneous magnitude and frequency can be useful to generate reference signal for power maximisation control and this part of work is detailed in Section 8.4.1.

To generate irregular waves in the wave tank system, the significant wave height is set as $H_s = 0.2482$ m and peak frequency is set as $f_p = 0.4$ m in the wave-maker software. The collected data from the wave gauges are similar to the numerical simulation in Eq.

(6.16) and shown in Fig. 6.16. Thus the significant wave height for the experimental wave elevation can be computed via the zero-crossing method.

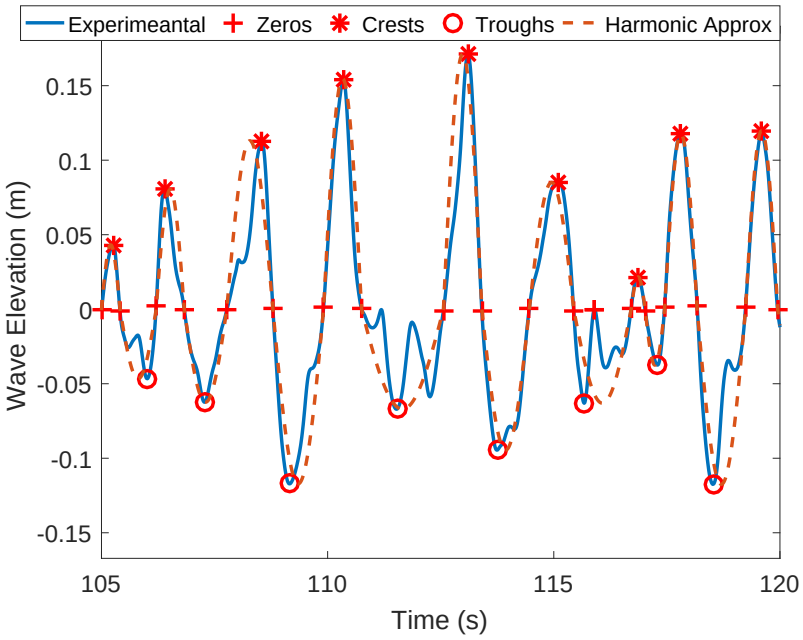

Fig. 6.16 Wave elevation collected from the wave tank tests (WG2) and its harmonic approximation.

For the numerical wave elevation simulated in MATLAB®, the conditions are $N_s = 50$, $f_1 = 0.2$ Hz, , $f_2 = 1.2$ Hz and $\Delta f = 0.02$ Hz. The numerical simulation corresponding to the irregular wave satisfies the same PM spectrum for the wave tank tests and is represented by the summation of N_s harmonic waves in Eq. (6.16). A large N_s gives better fitting to the theoretical PM spectrum and introduces more computation. Hence, $N_s = 50$ is selected to make sure that the estimated spectrum from the numerical simulation is close to the theoretical PM spectrum, shown in Fig. 6.17. To keep consistent with the wave tank tests data acquisition, the sampling frequency is 100 Hz and the time span analysed is about 300 s for both the numerical and experimental configurations.

To verify that the time series of wave elevation satisfy the PM spectrum defined in Eq. (3.28), spectrum analysis is applied on the wave elevation in Fig. 6.15. The spectrum analysis results are compared with the theoretical PM spectrum in Fig. 6.17. The estimated spectra of the numerical wave elevation and the experimental data are very close to the theoretical curve. Thus the wave elevation generated by the wave-maker satisfies the stationariness and the ergodicity of the PM spectrum in Eq (3.28).

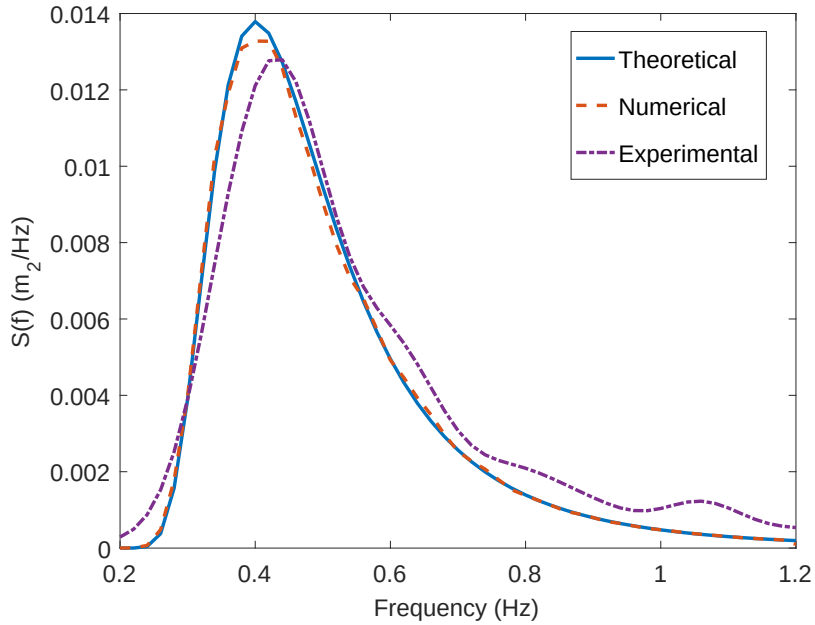

Fig. 6.17 Spectrum verification of the numerical and experimental wave elevations via the PM spectrum comparison among the theoretical PM spectrum in Eq. (3.27) and estimated spectrum from numerical wave elevation in Eq. (6.16) and the experimental data of collected from WG2.

Another way to valid the wave elevation data is to computer the wave significant height in a statistic way. The significant height computed by the zero-crossing detection technique is about $H_s = 0.2433$ m for the numerical simulation and $H_s = 0.2569$ m for the wave tank tests, which is close to the configured value of $H_s = 0.2482$ m or the spectral moment representation in Eq. (3.29), $H_s = 0.2463$ m. Therefore, the wave elevation in Eq. (6.16) can satisfy the PM spectrum properties well and is suitable to represent fully developed sea waves as testing data.

6.6.2 Free-fall test procedure

The mechanical friction originates from the translation between the connecting rod and the linear bearing. In the wave tank tests, the friction cannot be neglected, compared with the amplitude of the wave force (the wave height is small in the wave tank tests). Thus the friction profile must be estimated experimentally. As shown in Fig. 6.18, simple tests, the *free-fall tests*, can be applied to lift the buoy into the air, hold it stable for a short period and then release it suddenly. The collected data from the LVDT and

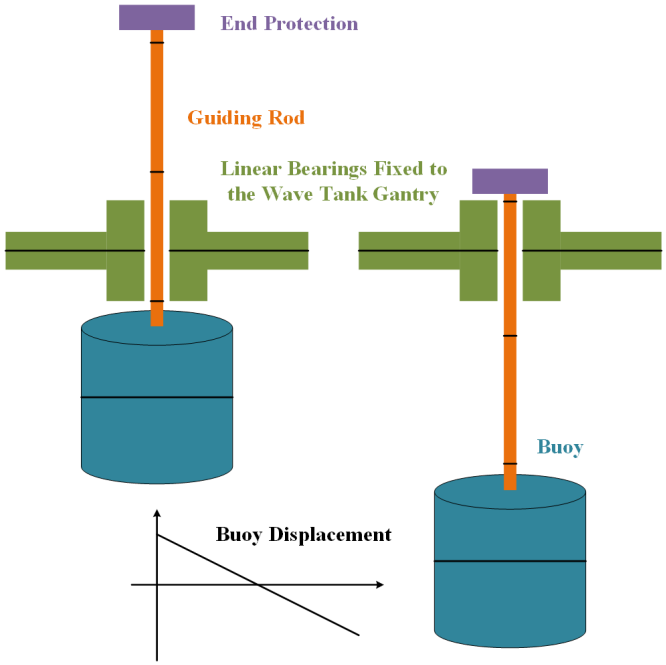

Fig. 6.18 Diagrammatic sketch of the free-fall tests.

accelerometer can be used to identify the friction parameters, which are detailed in Sections 4.4.1 and 4.5.1.

6.6.3 Free-decay test procedure

As defined in Eq. (4.27) and shown in Fig. 6.19, *free-decay tests* are applied in the wave tank to identify the friction parameters and to verify linear/non-linear F2M models. The buoy is pushed down to a non-zero initial position, held stable for a while and then released. Pressure sensors are installed at the bottom of the buoy to record the pressure variation in order to represent the buoy-wave interaction. The buoy velocity can be derived either from the derivative of the LVDT signal or the integral of the accelerometer signal with certain suitable initial values. The viscous force is due to the relative velocity between the buoy and nearby water particles. However the velocities of nearby water particles are small enough to be neglected in the free-decay tests. The friction force originates from the translation between the buoy guiding rod and the linear bearing. Also, the linear bearing constrains the buoy motion to be in heave only. Recall that, the viscous force and friction cannot be decoupled and their superposition is referred to as a lumped non-linear force in Eq. (4.37). The results of the free-decay tests are detailed in Sections 4.4.2 and 4.5.2.

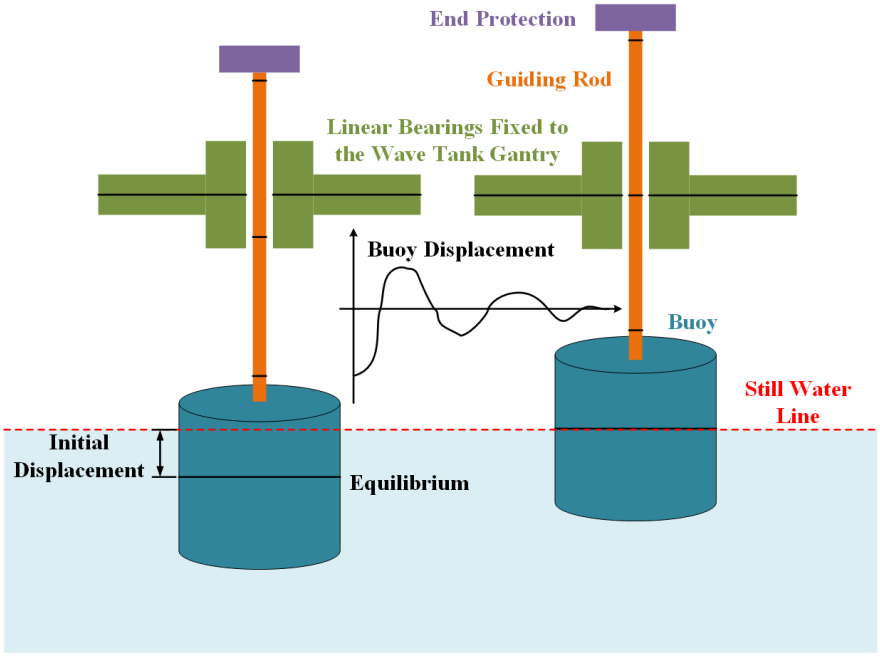

Fig. 6.19 Diagrammatic sketch of the free-decay tests.

6.6.4 Excitation test procedure

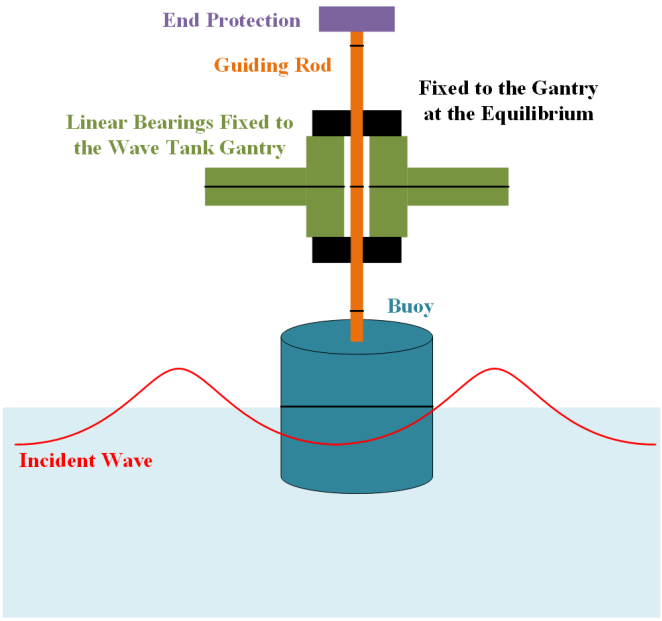

Fig. 6.20 Diagrammatic sketch of the excitation tests.

As shown in Fig. 6.20, for *excitation tests*, the buoy is fixed to the wave tank gantry via G-shap clips and excited by incident waves. Therefore, the buoy cannot oscillate. The five pressure sensors installed at the bottom of the buoy provide the information of the

dynamic pressure acting on the PAWEC hull. Thus, the wave excitation force in heave can be represented by pressure measurements.

Meanwhile, five wave gauges are installed to measure the wave elevation, amongst which, WG3, is in line with the buoy and perpendicular to the wave incoming direction. The measurement of WG3 represents the incident wave at the centred of the PAWEC and adopted to provide wave prediction in a short-term horizon t_c. To verify the proposed W2EF modelling approach, a series of excitation tests are conducted to compare with the numerical simulations of Eqs. (5.11) and (5.12) under the excitation of regular and irregular waves. In the excitation tests, the measurement of the excitation force is derived from the pressure sensors according to Eq. (5.32). The results of the excitation tests are given in Section 5.7.1.

6.6.5 Forced-motion test procedure

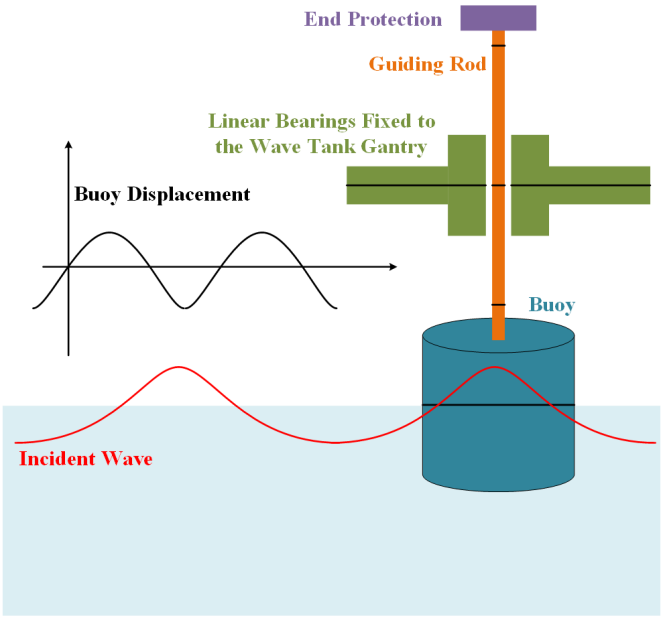

Fig. 6.21 Diagrammatic sketch of the forced-motion tests.

As shown in Fig. 6.21, during the *forced-motion tests*[2], the PAWEC is forced to oscillate from zero-initial condition under the excitation of incident waves. In this situation, the measurements from pressure sensors represent the total wave force rather than the excitation force.

[2]It is also called "free-motion" test in some publications. Here "forced-motion" test is preferred since the PAWEC is forced to oscillate under the excitation of incident waves.

Meanwhile, the buoy acceleration and displacement are measured by an accelerometer and an LVDT, respectively. Therefore, the excitation force can be estimated via the PAD2EF approach in Eq. (5.15). Also, the wave elevation measurements are accessible. Thus the W2EF method can be applied to WG3 measurement to approximate the excitation force according to Eqs. (5.11) and (5.12). Since the displacement measurement is accessible, the UIOEF approach in Eqs. (5.23) and (5.24) can be applied to estimate the excitation force.

For an oscillating PAWEC in forced-motion tests, the W2EF approach in Section 5.3, PAD2EF method in Section 5.4 and UIOEF technique in Section 5.5 are applied to estimate the wave excitation force. The approximations of the excitation force via the W2EF, PAD2EF and UIOEF approaches are compared with each other. All the data of the wave elevation, pressure, displacement and acceleration are collected from the forced-motion tests via LABVIEW™.

In the forced-motion tests, the excitation force is not measurable since the pressure sensors give the total wave force $F_w(t)$ in Eqs. (5.13) and (5.33). Therefore, it is very hard to say which method is better. The excitation force estimate from the forced-motion tests via W2EF, PAD2EF and UIOEF approaches are given in Section 5.7.2 and the verification of linear/non-linear W2M models is detailed in Section 5.7.3.

To note: The first round of wave tank tests were conducted from September 18$^{\text{th}}$ to 25$^{\text{th}}$, 2015, with great help from my colleagues Mr. Jiangling Lan and Mr. Mustafa Abdelrahman under the guidance of Mr Brendan Murphy, Dr Stuart McLelland, Professor Dan Parsons of the School of Geography, Environment & Earth Sciences (GEES) for the management and service of the Hull University wave tank. The experimental data collected in this round are affected a lot by the cogging force of the generator and the friction force of the mechanical structure. This experiences are useful to improve the PAWEC system design for the second round tests.

To note: Thus for the second round tests from June 23$^{\text{rd}}$ to July 14$^{\text{th}}$, 2016, the generator was removed to decouple the cogging force and two linear bearings were applied to reduce the friction. The experimental data collected from this round are detailed and compared with the numerical results in Chapter 4 and 5, to verify the non-linear lumped force in Eq. (4.37), non-linear F2M model in Eqs. (4.40) and (4.41), W2EF model in Eqs. (5.11) and (5.12) and the non-linear W2M model in Eqs. (5.26) and (5.27). Also, the experimental data are applied to verify the PAD2EF method in Eq. (5.13) and UIOEF approach in Eqs. (5.23) and (5.24). For the second round wave tank tests,

great help came from my colleagues Ms Siya Jin and Mr. Mustafa Abdelrahman and great wave tank service and management of Mr Brendan Murphy, Dr Stuart McLelland, Professor Dan Parsons.

6.7 Summary and Conclusion

6.7.1 Summary

This Chapter details the scaling problem and the design of the scaled down PAWEC system. After the comparison of the magnitude orders between the gravitational, inertial and viscous forces, the Froude number is selected as the scaling principle. The scale ratio is selected as $1/50$ with consideration of the modal wave condition and wave tank dimensions. This part of work is detailed in Section 6.2. Based on the scaled down PAWEC specifications, the mechanical design is sketched in SOLIDWORKS® and manufactured in Hull University mechnical workshop. The mechanical design details are given in Section 6.3. To collect the experimental data, a sensing system with hardware is designed in ALTIUM DESIGNER™ and cooperative DAQ GUI is coded in LABVIEW™. The part of work is illustrated in Sections 6.4 and 6.5. A wide variety of wave tank tests are conducted to verify the mathematical modelling of buoy-wave interaction in Chapters 4 and 5, including the free-fall, excitation, free-decay, forced-motion tests under both regular and irregular wave conditions, described in Section 6.6.

All the experimental data are applied to verify the numerical models derived in Chapters 4 and 5. As concluded in Chapter 4, the free-fall and free-decay tests are conducted to estimate the unknown parameters in the friction and viscous models and to verify the F2M models. The non-linear F2M modelling shows a high accordance to the free-decay tests in terms of the normalised displacement and energy dissipation. The experimental data of the excitation tests are applied to verify the W2EF modelling approach whilst the forced-motion tests are applied to validate the PAD2EF, UIOEF and W2M modelling approaches. The experimental data are compared with the numerical results in Chapter 5. Hence the experimental results are not discussed in this Chapter.

6.7.2 Conclusion

During the wave tank tests, it is observed that some non-linear effects influence the PAWEC dynamics significantly. Hence, there are some tips or advices to improve the experimental results for the next campaign of wave tank tests, as:

- For the experiments in 2015, the permanent magnet linear generator is connected with the PAWEC and unexpected latching is often observed. The main cause is the cogging force of the generator which mainly determined by the displacement. Hence cogging force reduction is very important. For the $1/50$ PAWEC, it will be much better if the amplitude of the cogging force is smaller than 1 N (since the amplitude of the excitation force is about 20 N).
- It will be very useful to install strain gauges between the buoy and the TPMLG to measure the PTO force. This measurement is helpful to understand how the PTO subsystem couples with the buoy system and to investigate the force constraints.
- As mentioned in Section 5.4.2, the PAWEC velocity is pseudo-measured. Hence it is important to install a linear variable velocity transmitter to provide precise velocity information to verify the pseudo-velocity measurement and to provide feedback signal for velocity tracking control.
- It is observed that the non-linear hydrodynamics, like viscosity, shedding vertex, are several for the flat-bottom buoy. CFD simulation indicates that the buoy with a semi-sphere bottom can reduce these non-linearities. Hence it is important to optimise the buoy shape for next campaign of wave tank tests.
- Since the PAWEC dimension is small, the mechanical friction force is relatively large. Hence it is critical to reduce the friction force to a small amount. It is a good idea to apply self-lubricating linear bearings to replace the linear bearings.
- It is found that the DAQ system coded in LABVIEW™ introduces time delay about 1 s. Hence it is not suitable for real-time control implementation. Embedded system based on DSP or FPGA chips has great potential to implement the real-time power maximisation control for the PAWEC.

Chapter 7

TPMLG modelling

7.1 Introduction

As the wave-buoy interaction is modelled and verified in the previous Chapters, this Chapter deals with the modelling of a TPMLG that can be used as a PTO mechanism. The physical simulation of the TPMLG is studied in MAXWELL™ due to three reasons: (i) The failure of tank tests in September 2016 is due to huge cogging force existing the TPMLG which causes unexpected latching to the PAWEC dynamics. Thus cogging force reduction via TPMLG optimisation is required. (ii) Published TPMLG mathematical models vary from each other. In some publications, the pole pair number is required to derive the TPMLG *dq-axis* models (Cheema et al., 2012; Cheema and Fletcher, 2013; Faiz et al., 2011; Mohammadpour and Parsa, 2011). However, some electromagnet experts exclude the pole pair number during the TPMLG modelling (Colli et al., 2005; DelliColli et al., 2006; Zhu and Cho, 2007). Thus it is necessary to understand the physical significance behind the TPMLG models. Via MAXWELL™ simulations it is clear that the pole pair number is not involved in the *dq-axis* models since it is replaced by the pole pitch. (iii) It is also important to know the TPMLG limits or constraints in terms of voltage, current, PTO force and power via physical simulation in MAXWELL™.

Hence, to provide suitable background Section 7.2 compares a variety of PTO systems and their application scenarios. In Section 7.3, an initial TPMLG design is given based on (i) the 1/50 scale PAWEC system described in Section 6.3 together with (ii) the wave conditions for wave tank tests given in Section 6.6.1. FEM simulation is applied to

optimise the TPMLG design to satisfy the design specifications and to achieve cogging force reduction, as detailed in Section 7.4. Based on the optimised design, a *dq-axis* model of the TPMLG is derived in Section 7.5. The coupling between the TPMLG and the buoy is discussed in Section 7.6 and linear/non-linear W2W models are proposed for control system design of the 1/50 PAWEC prototype.

7.2 Reivew of power take-off systems

A PTO system is a critical component for any WEC device, which should be weighted among cost, reliability, efficiency and control complexity. For most WEC applications, the PTO system is acting as control actuator as well as PTO mechanism. PTO systems currently in development include: (i) air turbines, (ii) water turbines, (iii) hydraulic pumps/motors, (iv) direct-drive systems and (v) other novel PTO systems, such as dielectric elastomer generators.

The air turbines are suitable for OWC devices, independently of whether or not they are shoreline based or floating structures. The commonly used air turbines are (i) the Wells turbine, (ii) the Denniss-Auld turbine and (iii) the impulse turbine (López et al., 2013), as shown in Fig. 7.1.

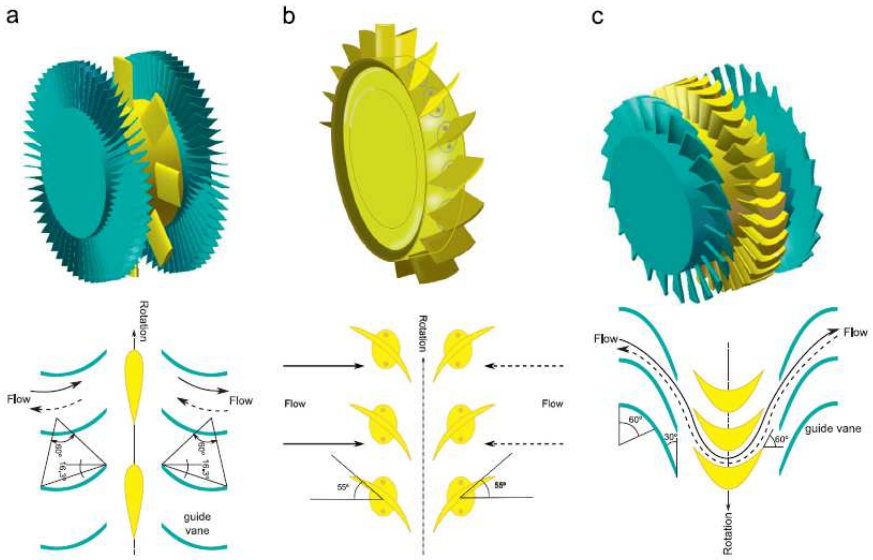

Fig. 7.1 The Wells, the Denniss-Auld and the impulse turbines (López et al., 2013) are applied as PTO mechanisms for OWC devices. Conventional rotating generators are driven by these turbines to produce electricity.

The water turbines are applicable for the over-topping type WEC devices, e.g. the Wave Dragon, the TAPCHAN. There are three sub-types, including (i) the Pelton turbine, (ii) the Kaplan turbine and (iii) the Francis turbine (López et al., 2013), as shown in Fig. 7.2. Since the air/water turbines are not applicable for the 1/50 PAWEC, the details are not given here but can be found in Drew et al. (2009); López et al. (2013). This study only compares the hydraulic, direct-drive and elastomer PTO systems.

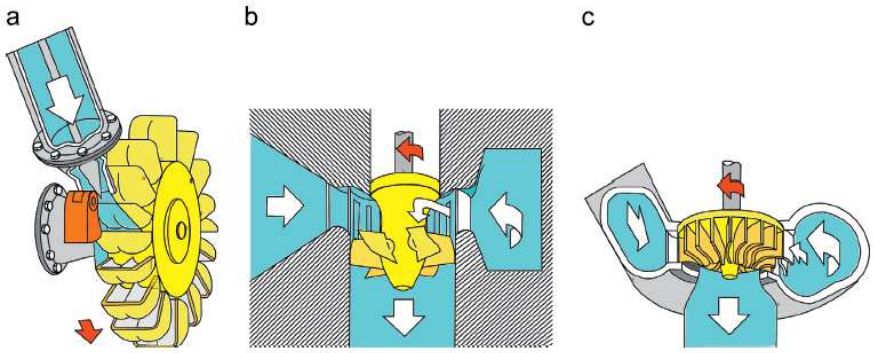

Fig. 7.2 Water turbines for the over-topping devices, including the Pelton, Kaplan and Francis turbines (López et al., 2013).

7.2.1 Hydraulic PTO systems

The hydraulic PTO systems are the most mature and applicable technique for WEC devices. As shown in Fig. 7.3, there are two types of hydraulic PTO systems, one with variable pressure and the other with constant pressure (Costello et al., 2011). Generally speaking, a hydraulic PTO system comprises hydraulic rams, pipes, regulating valves, accumulators, hydraulic pumps/motors and rotating generators. The main advantages are: (i) The hydraulic technology is very mature and widely applied on industrial applications (Bard and Kracht, 2013). Thus all the hydraulic components are available in the market and the experience of hydraulic system O&M is portable for WEC applications. (ii) Hydraulic systems can provide a huge force for a low speed application and this feature fits well with the wave energy application scenarios within which the wave speed is quite low but the wave force is huge (Falcão, 2010; Polinder et al., 2005b). This also explains why the hydraulic PTO systems are preferred in the WEC community. (iii) Hydraulic PTO systems can be feasibly used for a wide variety of WEC systems and show great potential for multi-motion WEC devices. Other PTOs are not as flexible as the hydraulic PTOs for multi-DoF WEC devices (Lin et al., 2015).

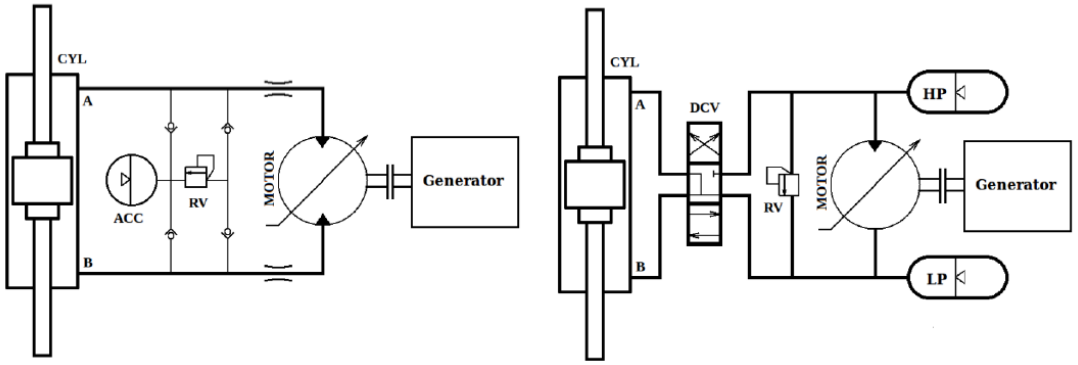

Fig. 7.3 Hydraulic PTO systems with the variable pressure type on the left and the constant pressure type on the right (Costello et al., 2011).

Although the advantages of the hydraulic PTO systems are quite obvious, their application on WEC systems are still constrained by some drawbacks: (i) The overall efficiency is lower compared with other PTO systems, due to the friction/viscous loss of the hydraulic system and several energy conversion steps (Henderson, 2006). (ii) Regular maintenance is required and hence the maintenance fee will be expensive, especially for offshore applications. As reported by Bard and Kracht (2013), the hydraulic oil needs to be replaced after some thousand hours of operation. That is, the oil should be refilled once or twice per year. (iii) Pollution risk comes up due to the use of hydraulic oil and hence there is a very difficult challenge of how to most effectively seal the system (Drew et al., 2009). Maintenance schedules for these sealed systems are very expensive since the seals have to be broke simply to achieve the work for the schedule.

Hydraulic PTO systems also act as the actuators and provide a way for control implementation. On one hand, some control strategies, e.g. latching, declutching and bang-bang control approaches, can be easily achieved by hydraulic PTO systems (Falcão, 2008, 2010). On the other hand, the hydraulic PTO features also limit the control strategies in the discrete-time domain (Bard and Kracht, 2013). More smooth control performance requires more hydraulic rams and accumulators, which increases the PTO system complexity immediately.

7.2.2 Direct-drive PTO systems

The direct-drive PTO systems are successfully applied on wind turbines and some experience can be transformed to the wave energy harvesting. The Permanent Magnet Linear Generator (PMLG) concept is proposed by Omholt (1978) to produce electrical

power from sea waves. A PMLG, as shown in Fig. 7.5, is designed and tested by Hodgins et al. (2012); Mueller and Baker (2002); Mueller et al. (2008); Polinder et al. (2004); Prado and Polinder (2011) as the PTO mechanism for a AWS device tested in Portugal (De Sousa Prado et al., 2006; Polinder et al., 2005a). A variety of PMLGs are compared by Mueller et al. (2007); Polinder et al. (2005b); Rhinefrank et al. (2012).

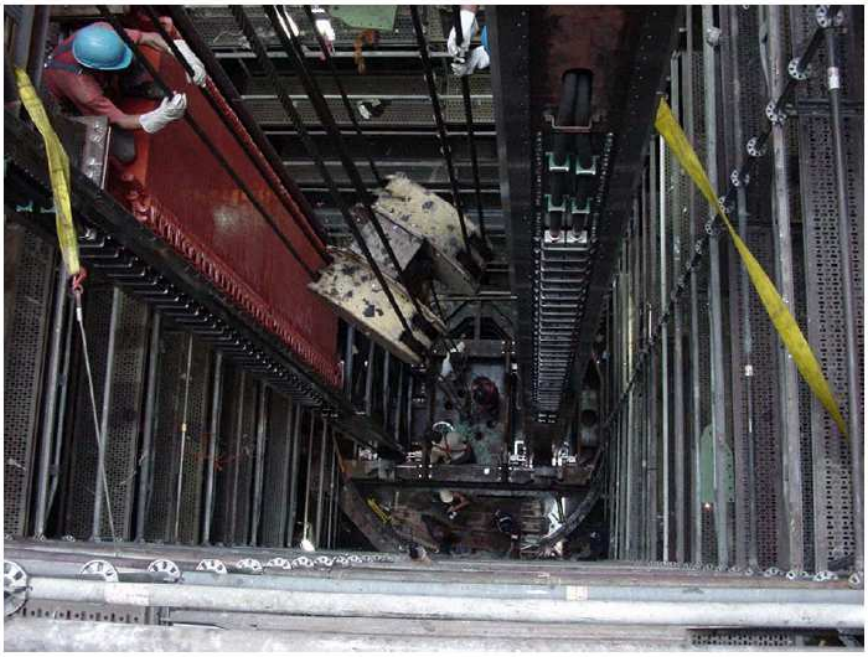

Fig. 7.4 Direct-drive PTO system for the AWS device (Prado and Polinder, 2011).

Compared with the hydraulic PTO systems, the main advantages of the direct-drive PTO systems are: (i) The direct-drive technology provides a high overall efficiency since only a few energy conversion steps are involved (Falcão, 2010; Mueller et al., 2007). (ii) The reliability is expected to be high since the direct-derive PTO system compromises less components. (iii) There is a low requirement for maintenance work due to its simple topological structure. For the PMLG, only the bearings need lubrication and there is no other maintenance work required (Bard and Kracht, 2013). (iv) The direct-drive PTO system is feasible to control via electrical approaches. Control strategies developed for the electricity industry are portable for the control design of the direct-drive PTO systems (Leijon et al., 2006). (v) Direct-drive PTO systems can operate reliably even when they operate at over rated power. For wave energy applications, the peak power can be up to 10 times of the average power (Genest et al., 2014; Sjolte et al., 2012). The PMLG shows a stable performance even when it is overrated.

For direct-drive PTO systems, the main drawbacks are: (i) The power/force density is low and thus a huge volume and weight are required to achieve certain rated power levels (Falcão, 2010; López et al., 2013). (ii) The manufacturing cost is relatively high, compared with the hydraulic PTO systems, due to the high cost of the permanent magnets (Polinder et al., 2005b). Up to the present time, due to the development of permanent magnet materials, the force density has increased and the permanent magnets cost has decreased a lot (Polinder et al., 2004). However, the direct-drive PTO systems is not comparable with the hydraulic PTO systems in terms of force density and construction cost. Meanwhile, the direct-drive technology shows great potential to achieve LCoE via reducing maintenance cost and increasing overall efficiency.

Alternatively, a rotating machine with gear box can be applied as a PTO system to convert the reciprocation motion into rotation and to drive a conventional rotating machine (Rhinefrank et al., 2012; Tedeschi et al., 2011). As shown in Fig. 7.5, the application of the gear box increases the rotation speed but at the same time increases the system complexity and decreases the system reliability. However, it is not always good to increase the rotation speed. For harmonic wave conditions, the WEC velocity is represented by a sine wave. Even with the assistance of the gear box, the rotation speed is also represented as a sine wave. Hence, the rotational machine is required to achieve high efficiency over a very wide range of rotor speed. Thus regular maintenance is required and hence the rotating machine with gear box structure is not discussed further in this study.

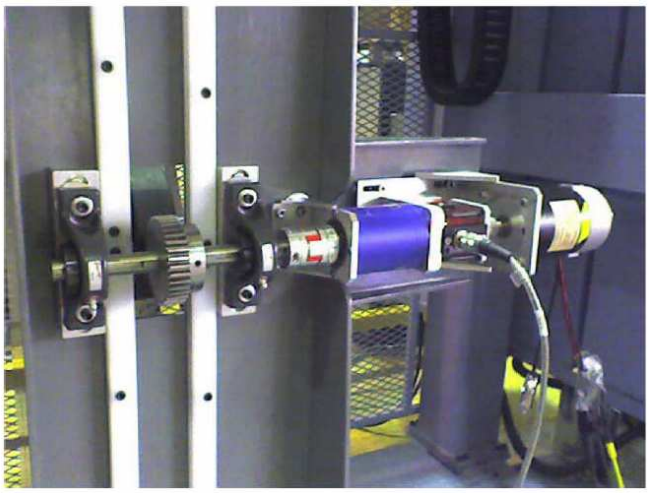

Fig. 7.5 PTO system with a gear box and rotating machine (Rhinefrank et al., 2012).

For the PAWEC using a PMLG as the PTO mechanism, the rotor angular speed can be amplified by reducing the pole pitch. Even though, the low speed problem still exists since the PAWEC speed is observed as a "periodic" signal and crosses zero-speed twice in one period. Additionally, the reducing of the pole pitch may cause some difficulties in the manufacture of PMLGs.

Permanent magnetic generations are generally applied for wind turbines and some of the technologies may be portable for this PAWEC design. However, there is an obvious difference between the wine turbine and PAWEC PTO systems. The rotor speed of wind turbines is always of uni-direction, whilst the rotor speed of WEC devices is of bi-direction. Intermediate systems like hydraulic pumps/motors can regulate the reciprocating PAWEC motion into uni-directional and stable rotation for electricity generation. At the same time, the drawbacks of the intermediate systems are introduced, such as the drawbacks of the hydraulic PTO discussed in Section 7.2.1.

7.2.3 Elastomer PTO systems

More recently, novel materials are applied for WEC applications. A material called dielectric elastomer, or electroactive polymer artificial muscle, is applied as PTO mechanism, called Dielectric Elastomer Generator (DEG), for some WEC devices. As shown in Fig. 7.6, the DEGs have been designed and tested for a heaving PAWEC device by Chiba et al. (2010) and for a shoreline OWC device by Vertechy et al. (2013). The main advantages are: (i) The DEG is electrically controllable. This provides an easy way to control the WEC operating partly as a generator and partly as an actuator. (ii) The efficiency of the DEG is relatively high. Its theoretical efficiency is up to $80-90\%$ (Pelrine et al., 2000) and the tested efficiency have been achieved $70-75\%$ (Chiba et al., 2010). Additionally, the efficiency is not sensitive to frequency and thus the DEG can overcome the wave frequency irregularity. (iii) The material is flexible and environment-friendly. Thus, the material and manufacture costs are low (Papini et al., 2013).

The main drawbacks are: (i) The DEG technology is immature and more tests are required before it is suitable for commercial development. (ii) High electrical fields are required and this may cause a problem for device coating and sealing (Vertechy et al., 2013). (iii) For a certain rated power, the DEG volume makes this form of PTO much

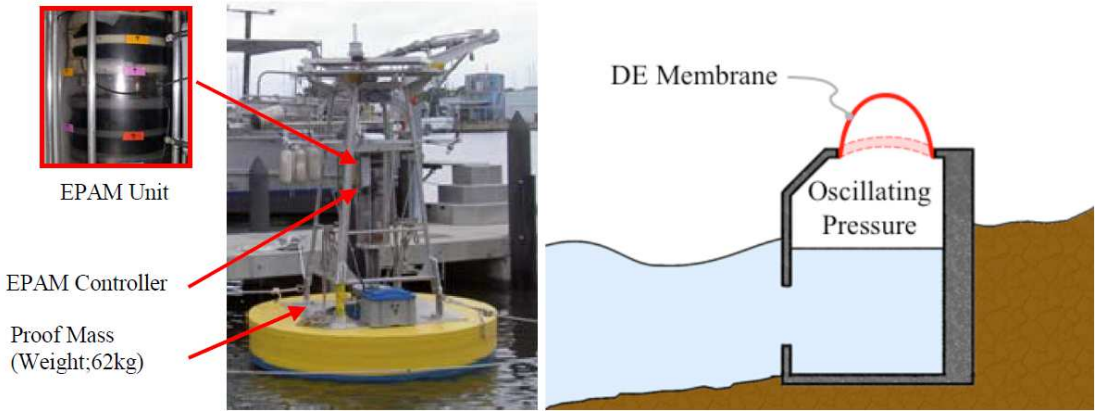

Fig. 7.6 DEGs applied as PTO systems for the PA and OWC types WEC devices (Chiba et al., 2010; Vertechy et al., 2013).

larger when compared with other PTO systems (Papini et al., 2013). This in turn may increase the complexity of a WEC geometric design.

7.3 TPMLG geometric design

Compared with the PTO systems mentioned above, the direct-drive PTO systems shows a great potential for the heaving PAWEC device. As mentioned by Mueller et al. (2007); Polinder et al. (2004), the linear generator can overcome some of the disadvantages. With the development of the material for the permanent magnet manufacture, the Neodymium-Iron-Boron (NdFeB) permanent magnets can provide a low cost solution to achieve high force/power density. However, the generator physical size and mass reduction are still challenging.

Compared with other types of linear generators detailed in Hodgins et al. (2012); Huang et al. (2011); Polinder et al. (2004), a TPMLG can provide a higher force/power density and a lower attractive force. Thus the TPMLG is selected in this study. The following Sections deal with the design, modelling and optimisation of the TPMLG for the 1/50 scale PAWEC prototype.

7.3.1 Rated power

As discussed in Section 6.2.2, the wave conditions for the wave tank tests are: (i) $f = 0.4 : 0.1 : 1.2$ Hz and wave height $H = 0.08$ m are selected for regular waves. (ii) For irregular waves, the peak frequencies of the PM spectra are selected as $f_p = 0.4 : 0.2 : 1$ Hz.

For regular waves, one possible test condition is $f = 0.4$ Hz and $H = 0.10$ m [1]. Thus the power transport can be computed according to Eq. (3.26). As described by Falnes (2002), for a single DoF devices, the theoretical efficiency is 50%. Thus the maximum absorbed power $P_{m,a}$ is given as:

$$P_{m,a} = Jr. \tag{7.1}$$

For irregular waves, the significant wave height, energy period and energy transport can be computed according to Eqs. (3.29), (3.31) and (3.32), respectively. Thus the maximum average power can be computed according to Eq. (7.1). For a wide range of wave conditions, the maximum absorbed power is given in Table 7.1.

Table 7.1 Maximum average absorbed power under regular/irregular waves.

f **(Hz)**	H **(m)**	J **(W/m)**	$P_{m,a}$ **(W)**	f_p **(Hz)**	H_s **(m)**	J **(W/m)**	$P_{m,a}$ **(W)**
0.4	0.1	23.93	3.59	0.4	0.25	63.87	9.58
1.2	0.1	7.98	1.20	0.6	0.11	8.36	1.25
0.4	0.08	15.32	2.30	0.8	0.06	1.96	0.29
1.2	0.08	5.11	0.77	1.0	0.04	0.64	0.10

To satisfy all the harmonic wave and irregular wave conditions of $f_P = 0.6$ Hz and $f_P = 0.8$ Hz, the rated power of the TPMLG is selected as $P_{tpmlg,r} = 9$ W. It is selected smaller than the irregular wave condition of $f_P = 0.4$ Hz. This wave condition is reserved for the extreme wave condition tests.

[1] $H = 0.10$ m is used here rather than $H = 0.08$ m, since this wave height $H = 0.10$ m is available in the Hull University wave tank for wave tank tests in the future.

As shown in Fig. 5.17, the Root-Mean Square (RMS) value of the buoy velocity is around 0.24 m/s. Therefore, the rated velocity is selected as $v_r = 0.24$ m/s. As shown in Fig. 5.16, the RAO during the wave tanks tests can reach 2.13. Therefore, the stroke should be larger than 0.2 m. For irregular waves, the wave height may be significantly larger than its significant height and thus the stroke is limited to 0.4 m.

7.3.2 Initial geometric parameters

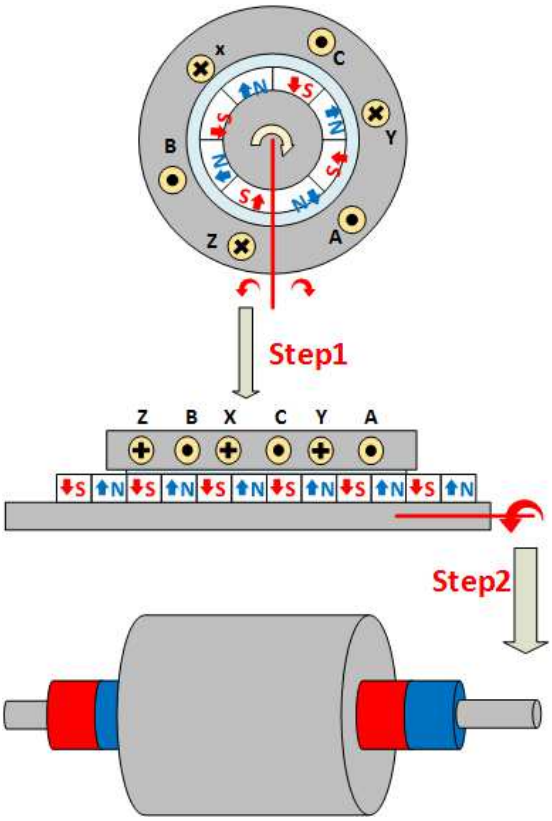

Fig. 7.7 Comparison of the working principles between the PMSM and TPMLG.

A three-phase TPMLG is designed initially in this Section with its parameters determined analytically. To satisfy the rated power, the rated phase voltage and current are selected as $E_{rms} = 6$ V and $I_{rms} = 0.5$ A. The TPMLG is a special topological structure of conventional Permanent Magnet Synchronous Machine (PMSM), as shown in Fig. 7.7. A PMSM can be modified into a TPMLG within two steps. The first step is to cut the PMSM through its radial direction and lay it on a horizontal plane. In this case, the PMSM is transformed to a flat linear motor/generator. The second step is to rotate the flat linear generator around the longitudinal direction of the iron core. What emerges from this is a TPMLG. From this viewpoint, most design and optimisation techniques

developed for the PMSMs are portable for the TPMLG design. Based on this concept, an 8-pole and 9-slot TPMLG is plotted in Fig. 7.8.

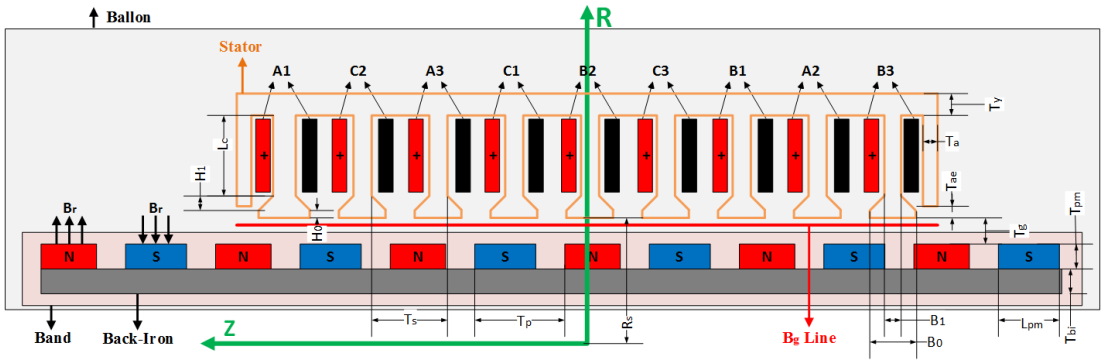

Fig. 7.8 TPMLG geometric structure.

The synchronising frequency $f_{s,g}$ is determined by the pole pitch τ_p and the rated velocity v_r, given as:

$$f_{s,g} = \frac{v_r}{2\tau_p}. \tag{7.2}$$

The slot pitch relies on the pole pitch τ_p, slot number N_s and pole number N_p, given as:

$$\tau_s = \tau_p \frac{N_p}{N_s}. \tag{7.3}$$

The pole pitch is set as $\tau_p = 18$ mm. The pole and slot numbers are selected as $N_p = 8$ and $N_s = 9$ to maximise their least common multiple in order to reduce the cogging force (Wang et al., 2003b). Therefore, the slot pitch is selected as $\tau_s = 16$ mm and hence the synchronising frequency is $f_{s,g} = 6.67$ Hz. To note, these parameters are not independent from each other and the selection procedure has to consider material accessibility, manufacture and system performance. In this Section, these design parameters are roughly selected half-empirically and half-analytically and are then set as the initial design parameters for numerical FEM simulations.

To calculate the air gap flux density, the materials for the magnets and iron core are selected as the standards NdFeB35 and B50A470. The NDFeB35 and B50A470

properties are given in Appendix C. Thus the residual flux density is $B_r = 1.2$ T. If the flux leakage is ignored, the flux density in the air gap B_g is given as (Krishnan, 2010):

$$B_g = B_r \frac{T_{pm}}{T_{pm} + T_g}, \tag{7.4}$$

where T_{pm} and T_g are the thickness of the permanent magnets and air gap, respectively. Thus the magnetic flux on one tooth can be expressed as:

$$\phi_t = B_g S_c, \tag{7.5}$$
$$S_c = 2\pi R_s W_c, \tag{7.6}$$

where S_c is the area of the tooth crown, R_s is the internal radius of the stator and W_c is the width of the tooth crown.

The RMS value of the induced EMF, E_{rms}, is given as (Krishnan, 2010):

$$E_{rms} = 4.44 f_{s,g} \phi_t K_w N, \tag{7.7}$$

where K_w is the winding factor, which is selected as $K_w = 0.83$ for the winding approach in Fig. 7.8. Therefore, the winding turn number N for each tooth is given as:

$$N = \frac{1}{3} \frac{E_{rms}}{4.44 f_{s,g} K_w \phi_t}. \tag{7.8}$$

To satisfy the rated power 9 W, the RMS value is set as $E_{rms} = 6$ V and the rated current is set as $I_{rms} = 0.5$ A. In this situation, $T_{pm} = 4$ mm, $T_g = 2$ mm and $W_c = 12$ mm are selected as the initial design. Thus, $B_g = 0.8$ T, $\phi_t = 0.0015$ Wb and $N = 60$.

For a rated load of $R_l = 11\ \Omega$, the generator resistance per phase should be configured as $R_p \leq 1\ \Omega$. To achieve this, the slot should be designed compatible with the winding

wire, to satisfy the limitations of the phase resistance and slot space, given as:

$$R_p = 2\pi 6N\rho_{awg}(R_s + \frac{L_c}{2}) \leq 1, \tag{7.9}$$

$$K_c = \frac{2NA_{awg}}{(\tau_s - W_t)L_c} \leq 0.8, \tag{7.10}$$

where W_t is the width of a tooth and K_c is the coil space factor ($K_c = 0.8$ is selected empirically). ρ_{awg} and A_{awg} are the resistivity and area of the AWG wires. The electrical properties of AWG wires are given in Appendix C. $L_c = 25$ mm, $W_t = 4$ mm, $R_s = 25$ mm and AWG15 wire are selected, which satisfy Eqs. (7.9) and (7.10). Thus the phase resistance is $R_p = 0.9\ \Omega$.

For the TPMLG topological design in Fig. 7.8, all the initial design parameters are given in Table 7.2.

Table 7.2 TPMLG initial design parameters.

Para	Value	Unit	Para	Value	Unit
τ_p	18	mm	τ_s	16	mm
W_c	12	mm	W_t	4	mm
T_{pm}	4	mm	W_{pm}	14	mm
H_0	2	mm	H_1	2	mm
R_s	25	mm	L_s	25	mm
T_y	4	mm	T_{bi}	4	mm
T_a	5	mm	T_{ae}	0	mm
τ_g	2	mm	N	60	N/A
L_{bi}	720	mm	V_r	0.24	m/s

7.4 Finite element analysis of TPMLG

The TPMLG is simulated and analysed in the MAXWELL™ package which is used as a common tool to solve the Maxwell equations. Based on the initial design in Table 7.2, this Section introduces the MAWELL™ package and the TPMLG simulation and optimisation is conducted in MAWELL™.

7.4.1 Basic equations in MAXWELL™

The differential form of Maxwell's equations are given as (Griffiths, 1999):

$$\nabla \times H_m = J_e + \frac{\partial D}{\partial t}, \tag{7.11}$$

$$\nabla \times E = -\frac{\partial B}{\partial t}, \tag{7.12}$$

$$\nabla \cdot B = 0, \tag{7.13}$$

$$\nabla \cdot D = \rho_e. \tag{7.14}$$

H_m is the magnetic field intensity. J_e is the conduction current density. D is the electric displacement. E is the electric field. B is the magnetic flux density. ρ_e is the charge density. Eqs. (7.11)-(7.14) describe Ampere's law, Faraday's law of induction, Gauss's law for magnetism and Gauss's law for electricity, respectively.

The constitutive equations of electromagnetism are given as (Griffiths, 1999):

$$D = \varepsilon E, \tag{7.15}$$

$$B = \mu H_m, \tag{7.16}$$

$$J_e = \sigma E, \tag{7.17}$$

where ε is the permittivity of the material; μ is the permeability of the material; σ is the conductivity of the material.

If the magnetic potential function A_m and the electrical potential function ϕ_m are applied here, the magnetic flux density and the electric field can be rewritten as (Maxwell, 2016):

$$B = \nabla \times A_m, \tag{7.18}$$

$$E = -\nabla \phi_m - \frac{\partial A_m}{\partial t}. \tag{7.19}$$

The potential functions can be solved via a FEM variational principle, detailed in Maxwell (2016). For static simulations, The magnetic vector potential function A_m can

be solved in the field equation as:

$$J_{dc} = \nabla \times (\frac{1}{\mu_r \mu_0} \nabla \times A_m), \tag{7.20}$$

where μ_r is the relative permeability of material and μ_0 is the permeability of free space. J_{dc} is the DC current density field.

For transient simulations, the magnetic equation is expressed as:

$$\nabla \times \nu \nabla \times A_m = J_s - \sigma \frac{\partial A_m}{\partial t} - \sigma \nabla \phi_m + \nabla \times H_c + \sigma v \times \nabla \times A_m, \tag{7.21}$$

where H_c is the permanent magnet coercivity; J_s is the source current density; v is the velocity of the moving part; ν is the reluctance. Eqs. (7.20) and (7.21) are derived from the Maxwell equations in Eqs. (7.11)-(7.14) with the back-iron, permanent magnets, air-balloon and vacuum boundary conditions. The procedure is almost the same as the derivation of the linear wave theory in Section 3.2.1. Thus the derivation of Eqs. (7.20) and (7.21) are not detailed here but can be found in Maxwell (2016). Since the potential functions are solved by MAXWELL™ other parameters can be obtained via post-processing according to Eqs. (7.15)-(7.19).

7.4.2 Convergence verification

The convergence verification in the MAXWELL™ simulation is tested according to six mesh solutions shown in Table 7.3. The induced voltages of phase A are compared among four mesh solutions and shown in Fig. 7.9. It is clear that the induced voltage converges to the stable value for the 2^{nd} mesh solution. Meanwhile, the convergence test result of the cogging force is illustrated in Fig. 7.10 and the 5^{th} mesh method gives a stable cogging force approximation which is very close to its static result. In this study, the static simulation of the cogging force is viewed as theoretical value as the static solver in the MAXWELL™ only gives the result of the converged evaluations. As shown in Fig. 7.10, the maximum cogging force is up to 10 N. However, the maximum wave excitation force for wave tank tests in Fig. 5.12 is about 20 N. The cogging force is relatively large compared to the wave excitation force and may cause unexpected

latching of the PAWEC motion. Hence, cogging force reduction is important to smooth the PAWEC motion. This part of work is detailed in Section 7.4.3.

Table 7.3 TPMLG mesh convergence verification with $t = 0 : 0.005 : 0.3\ s$ and $v = 0.24\ m/s$.

Mesh Code	**Mesh NO**	**Elapsed Time (Minutes)**	**Voltage Convergence**	**Force Convergence**
1	1170	7	N	N
2	2762	10	Y	N
3	5235	13	Y	N
4	15731	24	Y	N
5	76514	162	Y	Y
6	237203	623	Y	Y
Static	22560	205	N/A	Theoretical

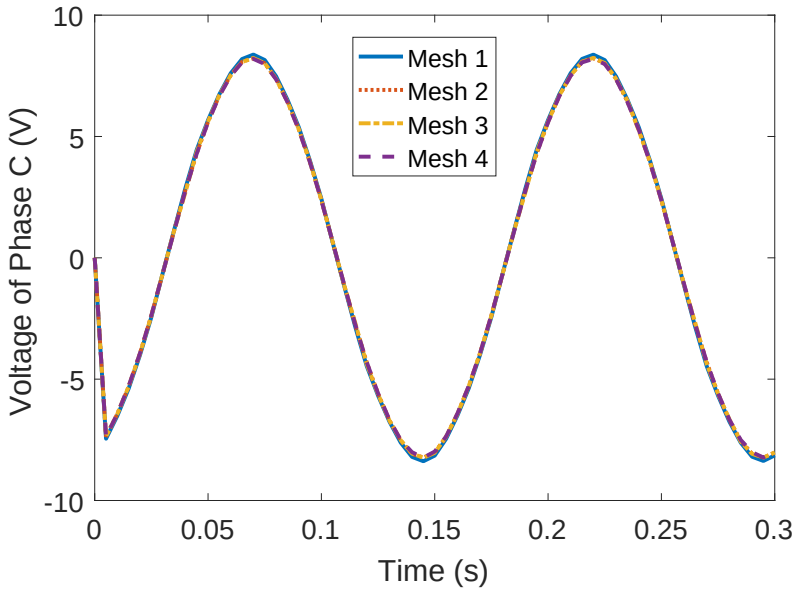

Fig. 7.9 Convergence tests of phase A induced voltages.

To simulate the electrical performance of the TPMLG, the 2^{nd} mesh method can provide acceptable accuracy and computing time. For the cogging reduction analysis, the 5^{th} mesh method is adopted here to gain a more precise solution, even though a long computing time is required. If both the voltage and cogging force analysis are applied, only the 5^{th} mesh approach can be used. Thus the following simulations in MAXWELL™ are computed with the 5^{th} mesh approach.

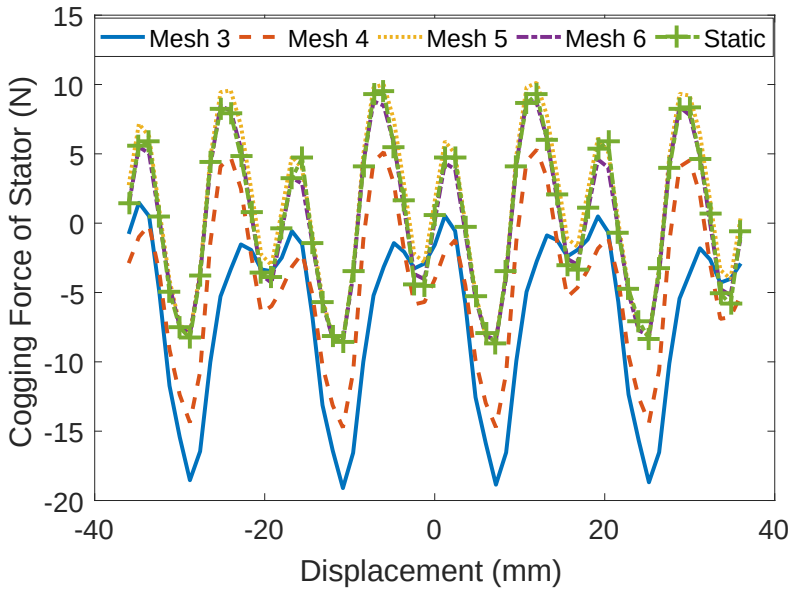

Fig. 7.10 Convergence tests of the cogging forces.

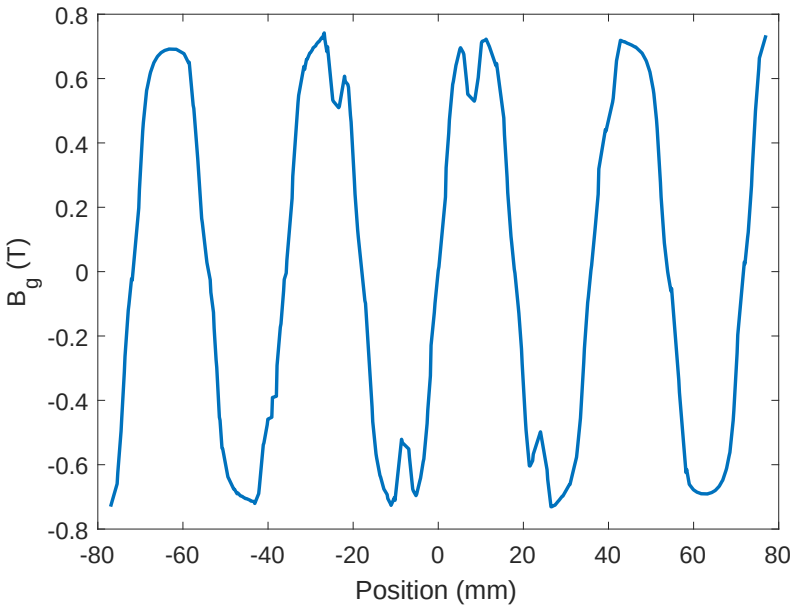

Fig. 7.11 Magnet flux density distribution in the air gap for the initial design in Table 7.2.

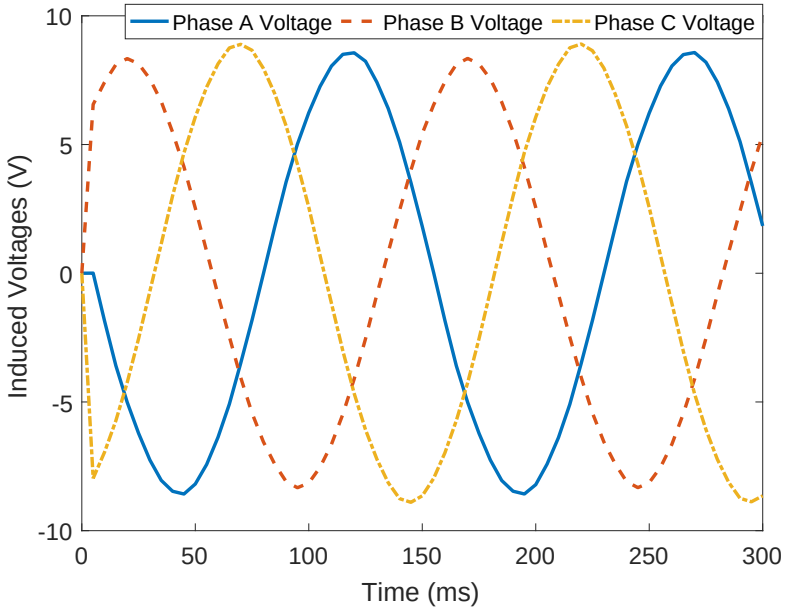

Fig. 7.12 Induced phase voltages for the initial design in Table 7.2.

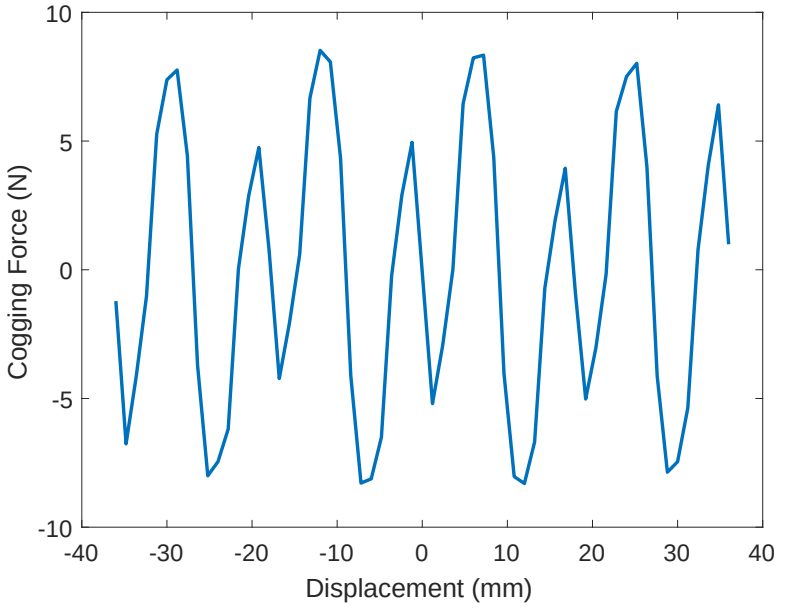

Fig. 7.13 Cogging force for the initial design in Table 7.2.

Based on the initial design in Table 7.2 and the 5^{th} mesh solution, FEM simulations are conducted in the MAXWELL™ package. The magnet flux density in the air gap is shown in Fig. 7.11. Its maximum value is $B_{g,m} = 0.75$ T, which is slightly smaller than 0.8 T (analytical value according to Eq. (7.4)) due to the flux leakage. Therefore, it is required to increase the number of winding turns slightly from $N = 60$ to $N = 65$ to achieve the rated induced phase voltage. The induced voltages of each phase are shown in Fig. 7.12 and $E_{rms} = 6$ V is achieved. Meanwhile, the cogging force simulated in the MAXWELL™ is given in Fig. 7.13. The Peak-to-Peak Value (VPP) of the cogging force is up to $F_{cog,vpp} = 19$ N, which is quite large for wave tank tests and hence cogging force reduction is required[2] and detailed in the following Sections.

7.4.3 Cogging force reduction and design optimisation

For conventional PMSMs, an electromagnetic torque exists even when there is no current excitation. This torque is defined as the cogging torque or detend torque (Krishnan, 2010; Yang et al., 2009), which rises up from the interaction between the rotor permanent magnets and the stator teeth. Since the working principle of the TPMLG is the same as the PMSM, a cogging force can be defined to represent the variation of co-energy in the TPMLG when the translator moves, given as:

$$F_{cog} = \frac{\partial W_c}{\partial z}. \tag{7.22}$$

W_c is the co-energy mainly existing in the air gap and permanent magnets (Krishnan, 2010; Yang et al., 2009), expressed as:

$$W_c \approx W_{c,ag} + W_{c,pm} = \frac{1}{2\mu_0}\int_V B^2 dV, \tag{7.23}$$

where V represents the integral volume. As shown in Fig. 7.14, most electromagnetic energy is stored in the permanent magnets and the air gap. When the translator moves, the energy distribution changes and thus the cogging force can be computed in the FEM simulation according to Eq. (7.22).

[2] A series of tank tests were conducted in September 2016 and it was found out that the cogging force of the TPMLG was as the same magnitude as the wave excitation force and caused unexpected latching/stucking of the PAWEC motion. Thus the cogging force reduction is very important.

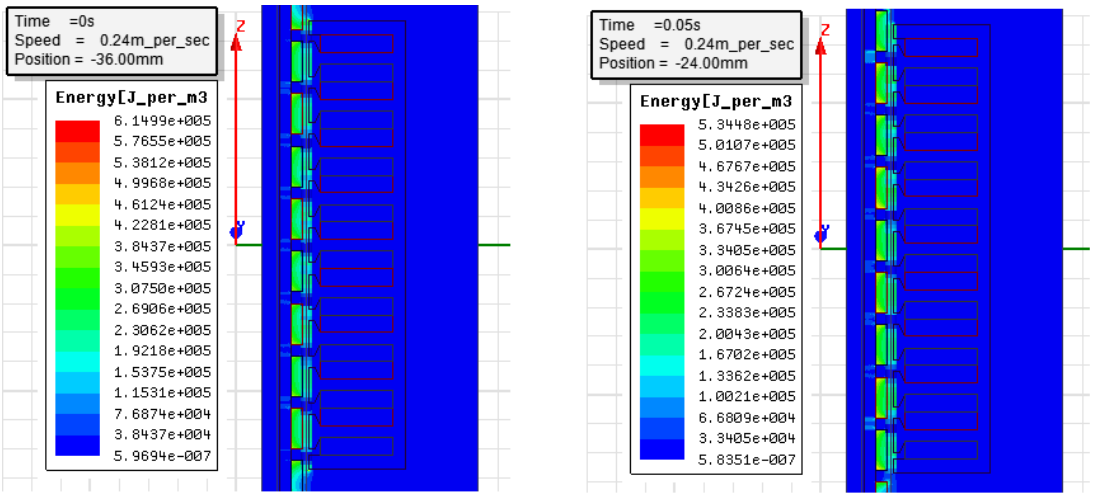

Fig. 7.14 Co-energy distribution of the TPMLG.

The most direct way to reduce the cogging force is to modify the geometric parameters of the PM and the air gap. However, the optimisation of the air gap is not discussed in the study. The main reason is that the air gap is constrained by the shear stress density, magnet flux density amplitude, maximum stator current, heat dissipation and manufacture accuracy. Hence it is difficult to select an optimal air gap to achieve a proper compromise among these constrains. Hypothetically, a smaller air gap can give higher shear stress density and better performance. However, the air gap cannot be smaller than a certain value. Otherwise the amplitude of the magnet flux density in the air gap will be huge and may cause saturation in the back iron or the stators core. The saturation will cause huge iron loses. Additionally, the air gap can not be too small due to manufacture accuracy. Hence the amplitude of the air gap flux density is selected around 1 T (Polinder et al., 2007). In this study, the air gap is selected from 1.5 to2.5 mm for (i) limiting the amplitude of the magnet flux density in the air gap around 0.8 T, (ii) preserving enough space for heat dissipation and (iii) considering manufacture accuracy.

For a PMSM, the cogging torque mainly comes from the attracting or repelling forces between the permanent magnets and the stator teeth. For a TPMLG, the cogging force comes from the stator teeth, as well as the stator end edges. The stator's end edge shape influence on the cogging force is defined as the *end effect*, which is studied analytically, numerically and experimentally by Inoue and Sato (2000); Wang et al. (2003a, 2005). As concluded by Inoue and Sato (2000); Wang et al. (2005), the end effect can be attenuated to a small amount with appropriate design of the stator length and end edge shapes. For the cogging force reduction of the TPMLG due to the stator

teeth, the approaches are the same as the PMSMs, including pole/slot number matching, permanent magnet shape optimisation, pole-shoe shape optimisation and etc. (Krishnan, 2010; Yang et al., 2009). The cogging force reduction in the TPMLG is investigated using the MAXWELL™ software package with its embedded parametric analyser.

Pole-shoe parametric analysis

As shown in Fig. 7.8, the pole-shoe shape relies on the design parameters of L_c, W_t, W_c, H_0 and H_1. The cogging force VPP decreases with the increase of L_c from $25-35$ mm, as shown in Fig. 7.15. The RMS value of the induced phase voltage keeps stable with $E_{rms} \geq 6$ V. Considering the stator size and winding space, $L_c = 27$ mm is selected for the next step parametric analysis and 26 mm $\leq L_c \leq$ 30 mm is selected for the design optimisation.

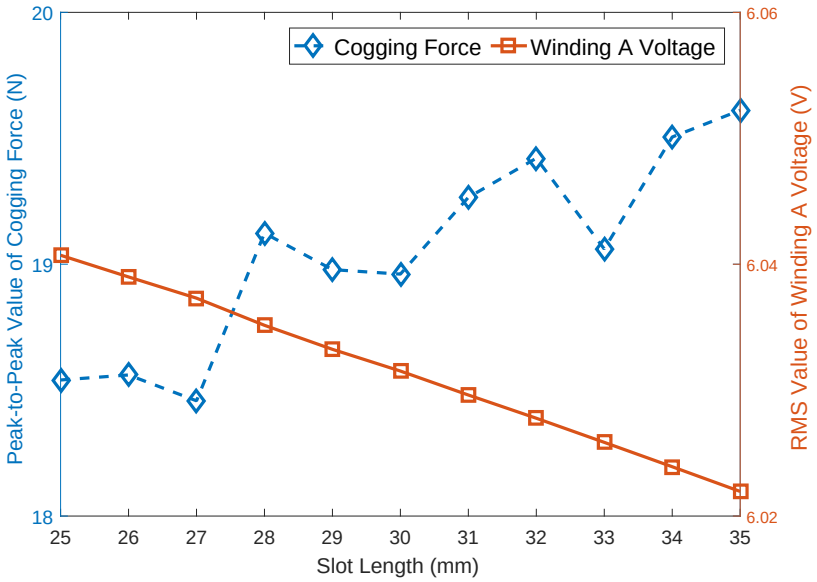

Fig. 7.15 Cogging force reduction via pole-shoe parametric analysis of L_c.

Fig. 7.16a indicates that the cogging force decreases as W_c and W_t increases. However, the phase voltage increases at the same time, as shown in Fig. 7.16b. Thus there is a trade-off between the cogging force and the induced phase voltage. For this study, $W_c = 13$ mm and $W_t = 4$ mm are selected for the next step parametric analysis. 12 mm $\leq W_c \leq$ 14 mm and 3 mm $\leq W_t \leq 5$ mm are selected for the design optimisation.

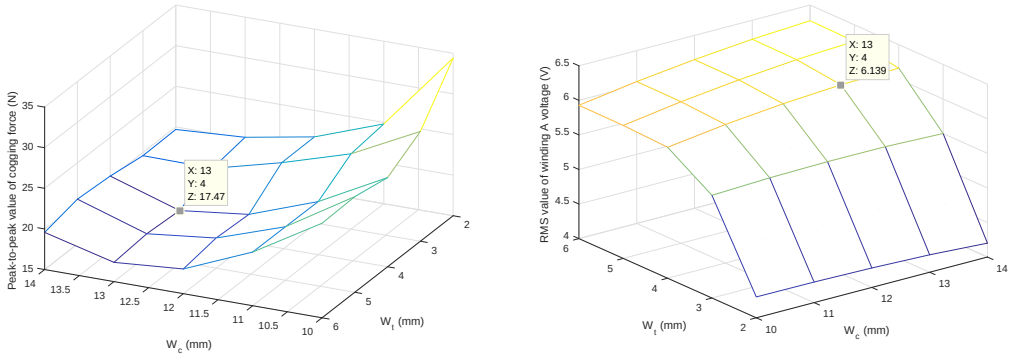

(a) $F_{cog,vpp}$ (b) $V_{a,rms}$

Fig. 7.16 Pole-shoe parametric analysis of W_t and W_c.

For the pole-shoe parametric analysis of H_0 and H_1, the results are shown in Fig. 7.17. To make a compromise between the cogging force and the induced voltage, $H_0 = 3.5$ mm and $H_1 = 2$ mm are selected for the next step parametric analysis. 1 mm $\leq H_0 \leq 4$ mm and 1 mm $\leq H_1 \leq 4$ mm are selected for the design optimisation.

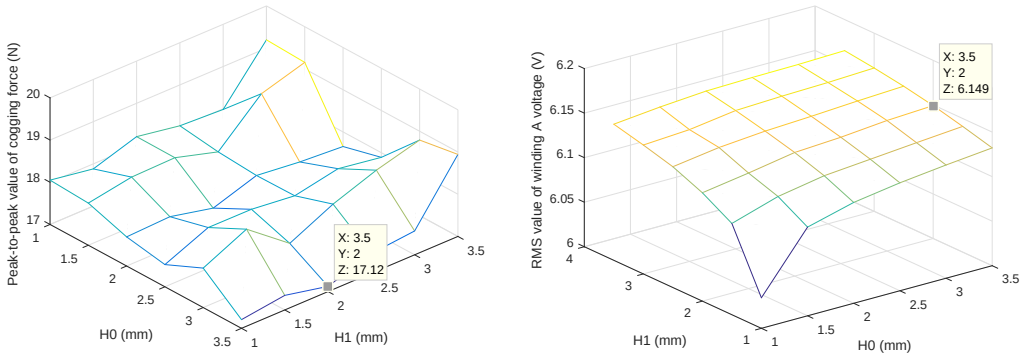

(a) $F_{cog,vpp}$ (b) $V_{a,rms}$

Fig. 7.17 Pole-shoe parametric analysis of H_0 and H_1.

Comparing Fig. 7.15 with Fig. 7.17a, the cogging force VPP is reduced from 19 N to 17 N. From this viewpoint, the pole-shoe shape is not the main factor influencing the cogging force. This is expected since most of the electromagnetic energy is stored in the permanent magnets and air gap (see Fig. 7.14). The change on pole-shoe shape can only affect the cogging force indirectly via changing the magnet flux density within the air gap. However, the inappropriate design of the pole-shoe may cause large cogging force and this is illustrated in Fig. 7.16a. The maximum cogging force VPP can reach 34 N.

Permanent magnet shape parametric analysis

Since the permanent magnets are the main material storing most of the electromagnetic energy, the permanent magnet shape can severely influence the cogging force, especially for conventional PMSMs. As described by Faiz et al. (2010); Krishnan (2010); Yang et al. (2009), varying the permanent magnets length can achieve cogging force/torque reduction. In the study, the influence of the permanent magnets thickness T_{pm} and length L_{pm} on the cogging force and the induced phase voltage are studied via FEM simulation. As shown in Fig. 7.18, there are some certain value sets of T_{pm} and L_{pm} can give a small cogging force. Thus $T_{pm} = 5$ mm and $L_{pm} = 13$ mm are selected for the next step parametric analysis. 4 mm $\leq T_{pm} \leq$ 6 mm and 12 mm $\leq L_{pm} \leq$ 18 mm are selected for the design optimisation.

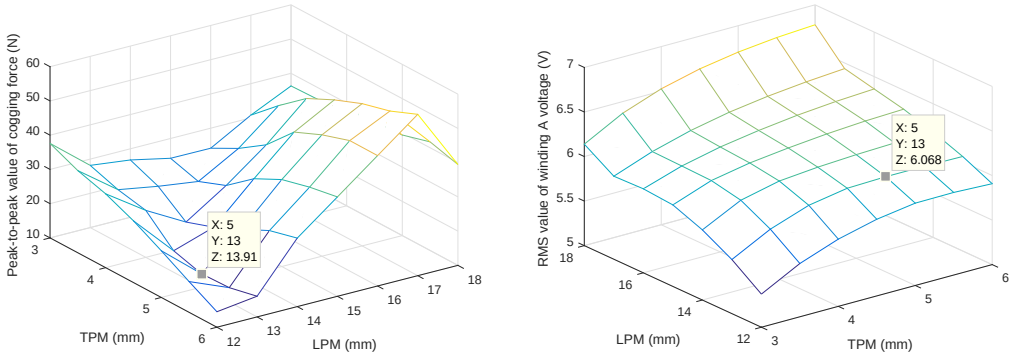

(a) $F_{cog,vpp}$ (b) $V_{a,rms}$

Fig. 7.18 Permanent magnet parametric analysis of T_{pm} and L_{pm}.

Comparing Figs. 7.15, 7.17a and 7.18a, the cogging force VPP is reduced from 19 N to 17 N via pole-shoe parametric analysis and to 14 N via permanent magnet parametric analysis. Additionally, Fig. 7.18a illustrates that inappropriate design of permanent magnets shape may introduce large cogging force with a maximum VPP of 48 N.

End-effect attenuation

As concluded by Inoue and Sato (2000), the end effect is the total detent force arising at both side edges of the stator core. The experimental and numerical results by Inoue and Sato (2000); Wang et al. (2005) show that the end effect can be attenuated to a small amount via optimising the stator length and smoothing the edge surface. Due to

similar principles, an auxiliary tooth method is investigated by Liu et al. (2013) and this method is adopted in this study to attenuate the TPMLG end effect. As shown in Fig. 7.8, two auxiliary teeth are added to both ends of the stator core. The FEM simulation results of T_a and T_{ae} parametric analysis are given in Fig. 7.19. Compromising between the cogging force and induced phase voltage, $T_a = 5$ mm and $T_{ae} = 1$ mm are selected for the next step parametric analysis. 4 mm $\leq T_a \leq$ 6 mm and 0.5 mm $\leq T_{ae} \leq$ 3 mm are selected for the design optimisation.

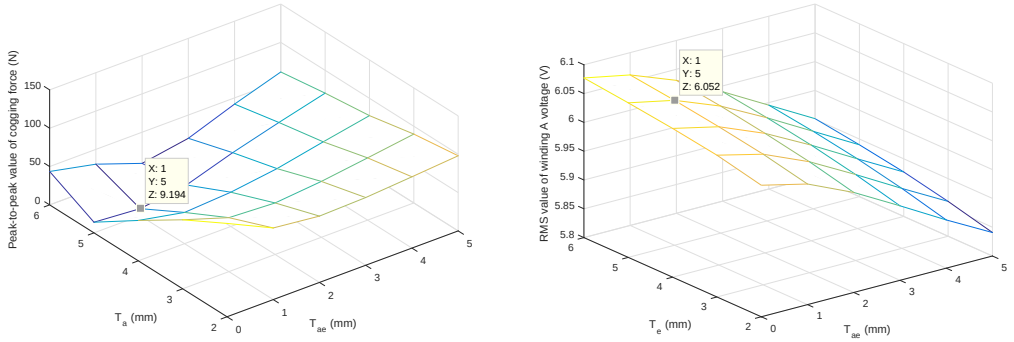

(a) $F_{cog,vpp}$ (b) $V_{a,rms}$

Fig. 7.19 Auxiliary teeth parametric analysis of T_a and T_{ae}.

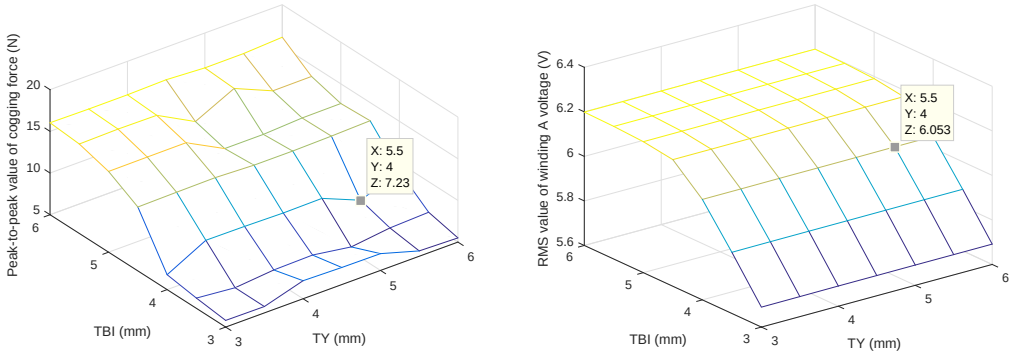

(a) $F_{cog,vpp}$ (b) $V_{a,rms}$

Fig. 7.20 Back-iron/yoke parametric analysis of T_{bi} and T_y.

The parametric analysis results of the back-iron thickness T_{bi} and yoke thickness T_y are shown in Fig. 7.20. $T_{bi} = 4$ mm and $T_y = 5.5$ mm are selected for the next step parametric analysis. 3 mm $\leq T_{bi} \leq$ 5.5 mm and 4 mm $\leq T_y \leq$ 6 mm are selected for the design optimisation.

Comparing Figs. 7.15, 7.17a, 7.18a and 7.20a, the cogging force VPP is reduced from 19 N to 17 N via pole-shoe parametric analysis, then to 14 N via permanent magnet parametric analysis and 7 N via end effect attenuation. It should be noted that Fig. 7.19a also illustrates that the end effect influences the cogging force most of all, compared with the pole-shoe and permanent magnets shape. Hence, a bad design of the stator length and end edge surface may lead to a huge resulting cogging force, whose VPP exceeds 100 N.

Design optimisation

As described above, the cogging force VPP can be reduced from 19 N to 7 N via parametric analysis. However, it is still large, compared with the wave excitation force during the wave tank tests (see Section. 6.2.2). For instance, the excitation force magnitude is about 20 N for the regular wave of $f = 0.6$ Hz and $H = 0.10$ m. A cogging force with a magnitude of 3.5 N can not be ignored and may cause huge ripples on PAWEC dynamics. Some unexpected latching may happen during wave tank tests. Thus, a further reduction of the cogging force is required.

During the parametric analysis of the pole-shoe, permanent magnet and stator shapes, these design parameters are investigated in a step by step way. Further cogging force reduction can be achieved to optimise all the parameters simultaneously. Thus the embedded optimisation solver in MAXWELL™ is adopted in this study to optimise the TPMLG design to achieve (i) $F_{cog,vpp} \leq 2$ N and (ii) $E_{rms} \geq 6$ V. Therefore, a cost function C_{tpmlg} is given as:

$$C_{tpmlg} = |F_{cog,vpp} - 2| + |E_{rms} - 6|. \tag{7.24}$$

The initial values for the design optimisation are configured according to the parametric analysis results and given in Table 7.4. Based on the optimisation setting in Table 7.4, the cost-function varying against the optimisation evaluations is shown in Fig. 7.21. The 120^{th} optimisation evaluation is adopted in this study and the final design is given in Table 7.4.

For the optimised design, the FEM simulation results are given in Figs. 7.22 and 7.23. It is clear that the parametric analysis and design optimisation can keep the induced phase

Table 7.4 TPMLG parameters for the design optimisation.

Paras	**initial (mm)**	**Min (mm)**	**Max (mm)**	**optimised (mm)**
L_c	27	26	30	27.56
W_c	13	12	14	13.58
W_t	4	3	5	3.63
H_0	3.5	1	4	3.46
H_1	2	1	4	5.52
T_{pm}	5	4	6	4.64
L_{pm}	13	12	18	14.98
T_a	5	4	6	5.45
T_{ae}	1	0.5	3	1.90
T_{bi}	4	3	5.5	3.37
T_y	5.5	4	6	5.81
τ_g	2	1.5	2.5	2.12
N	65	60	75	68

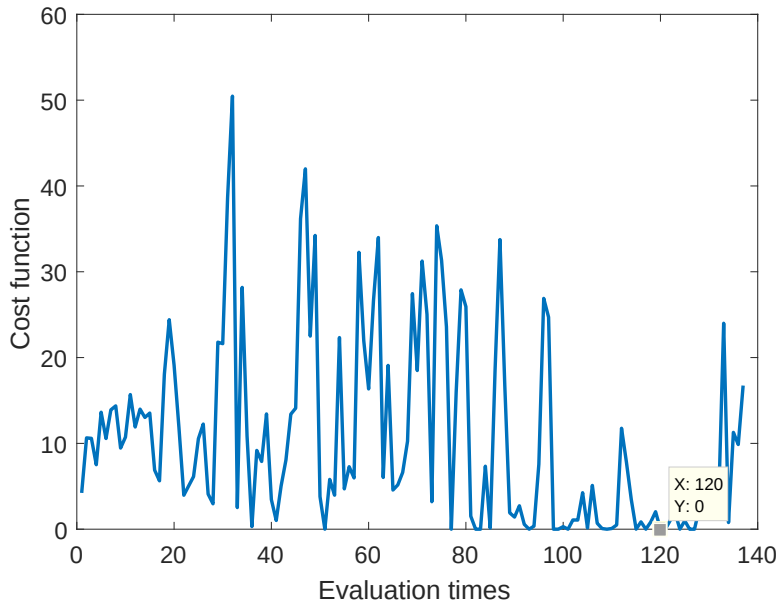

Fig. 7.21 Cost function varies against the optimisation evaluations.

voltage satisfying the design specifications and can reduce the cogging force to a small amount simultaneously. In Fig. 7.23, the cogging force is reduced to $F_{cog,vpp} = 1.5$ N, which is small enough to be ignored during the wave tank tests.

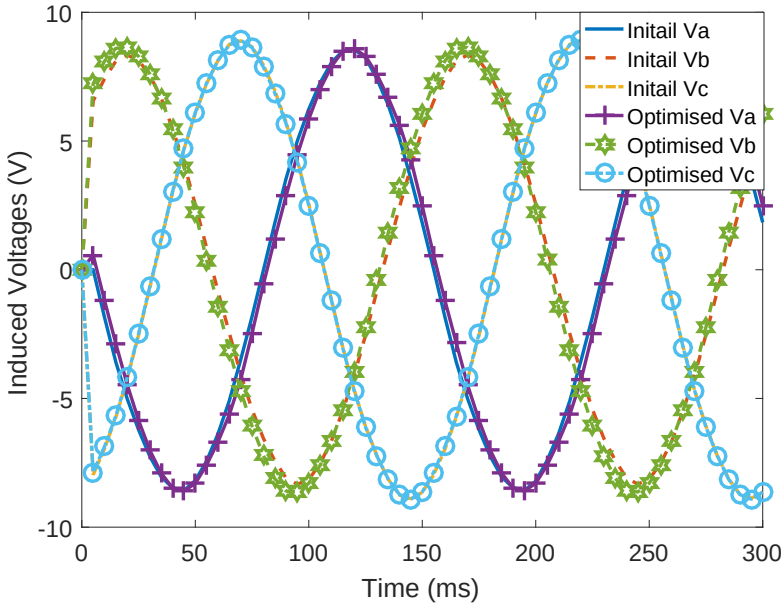

Fig. 7.22 Comparison of the induced phase voltages between the initial and optimised designs.

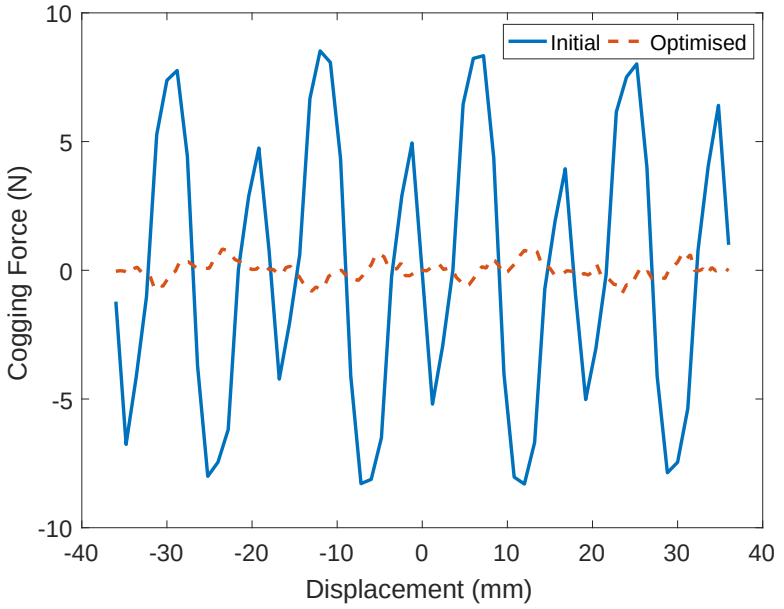

Fig. 7.23 Comparison of the cogging force between the initial and optimised designs.

For the cogging force, it is a function of the position and can be expressed as a summation of harmonic forces. From this the optimised cogging force can be represented as:

$$F_{cog,fit} = \Sigma_{i=1}^{n} a_i \sin(b_i z + c_i), \tag{7.25}$$

where n is the order number and a_i, b_i and c_i are the unknown parameters to be determined by curve-fitting techniques. The MATLAB® function *fit* is applied here to obtain the unknown parameters, as shown in Table 7.5. The cogging force for the FEM simulation is compared with its fitted result in Fig. 7.24. $n = 6$ is selected in this study based on the spatial FFT analysis.

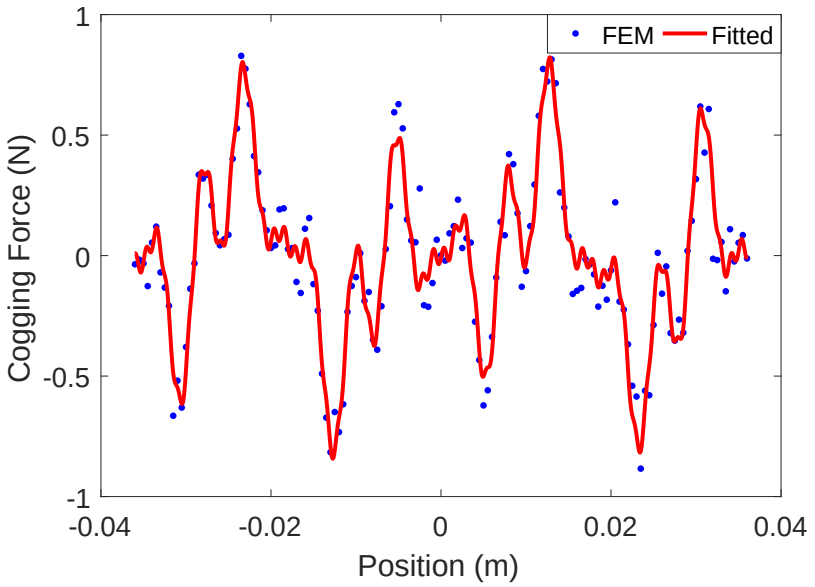

Fig. 7.24 Cogging force and its fitted formulation of the optimised design.

Table 7.5 Parameters for cogging force fitting.

i	a	b	c	i	a	b	c
1	0.3027	350.2	3.119	4	0.1763	185.7	0.01218
2	0.2137	1052	-0.04885	5	0.1221	688	-0.01472
3	0.1762	1400	3.134	6	0.03702	5023	-0.1966

7.5 TPMLG mathematical representation

7.5.1 State-space model of TPMLG

As described in Fig. 7.7, the TPMLG is a special topological structure of conventional PMSMs. Hence, the TPMLG mathematical model is the same as the PMSMs, given in the *dq-axis* as (DelliColli et al., 2006; Krishnan, 2010; Kundur et al., 1994):

$$U_d = -R_s I_d - L_d \dot{I}_d + \omega_e I_q L_q, \tag{7.26}$$

$$U_q = -R_s I_q - L_q \dot{I}_q - \omega_e (I_d L_d - \phi_{pm}), \tag{7.27}$$

where U_d, U_q, I_d, I_q are the voltages and currents for the *d-axis* and *q-axis*. ϕ_{pm} is the flux linkage constant referred to permanent magnets and ω_e is the electrical angular velocity. R_s, L_d and L_q are synchronous resistance, *d-axis* inductance and *q-axis* armature inductances, respectively. The model described by Eqs. (7.26) and (7.27) is for generator rather than motor. The difference lays in the definition of *dq-axis* current directions, which are shown in Fig. 7.25

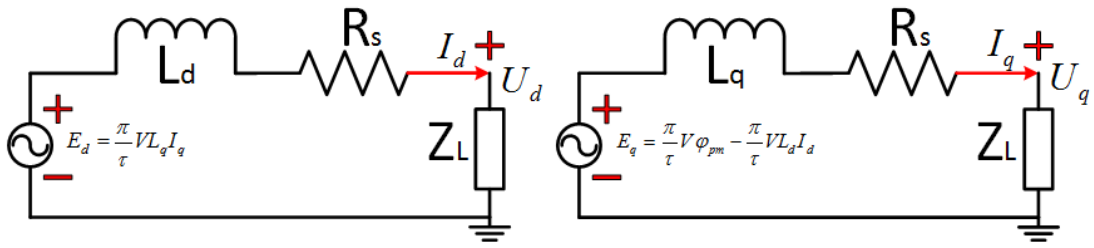

Fig. 7.25 Sketch of the TPMLG *dq-axis* model.

The electrical angular velocity and PTO force (Colli et al., 2006; DelliColli et al., 2006) are given:

$$\omega_e = \frac{\pi}{\tau_p} v, \tag{7.28}$$

$$F_{pto} = \frac{3\pi}{2\tau_p} [I_q (I_d L_d - \phi_{pm}) - I_d I_q L_q]. \tag{7.29}$$

For a TPMLG, the *d-axis* current is controlled as $I_{d,ref} = 0$ A for maximizing the force-to-current ratio. Thus the PTO force can be rewritten as:

$$F_{pto} = -\frac{3\pi}{2\tau_p}\phi_{pm}I_q. \tag{7.30}$$

The power captured by the generator is expressed as:

$$P_g = -F_{pto}v = -\frac{3\pi}{2\tau_p}\phi_{pm}I_q v. \tag{7.31}$$

Here define:

$$K_e = \frac{\pi}{\tau_p}\phi_{pm}, \tag{7.32}$$

$$K_f = \frac{3\pi}{2\tau_p}\phi_{pm}, \tag{7.33}$$

$$K_{pm} = \frac{\pi}{\tau_p}, \tag{7.34}$$

as the back-electromotive-force (back-EMF) and thrust force coefficients and the permanent magnet 'wave number', respectively.

It is assumed that the TPMLG translator mass is included in the buoy mechanical dynamics. The vertical buoy motion drives the generator which reacts with a bi-directionally coupled PTO force to the mechanical system. All the parameters in Eqs. (7.26) and (7.27) can be obtained with the FEM simulation in MAXWELL™. Thus the specified TPMLG design parameters are given in Table 7.6.

7.5.2 Design specifications

To "verify" the mathematical TPMLG model in Eqs. (7.26) and (7.27), FEM simulations in MAXWELL™ are compared with the PMSM simulations in MATLAB®. For a constant buoy velocity $v_r = 0.24$ m/s, the comparison results are given in Fig. 7.26.

Table 7.6 TPMLG electromagnetism parameters

Contents	**Units**	**Values**
Force Constant (K_f)	N ·A	54.4019
Back EMF Constant (K_e)	V · s · m $^{-1}$	36.2679
Pole Pitch (τ)	mm	18
Flux Linkage Constant (ϕ_{pm})	Wb · m	0.2078
D-axis Inductance (L_d)	mH	32.78
Q-axis Inductance (L_q)	mH	35.47
Synchronous Resistance (R_s)	Ω	1.04

For a harmonic wave condition of $f = 0.6$ Hz, the buoy velocity is selected as $v_r(t) = 0.34\sin(1.2\pi t)$ m/s and the comparison results are given in Fig. 7.27. For both the constant and variable velocity situation, the mathematical TPMLG model in Eqs. (7.26) and (7.27) gives the same results as the FEM simulation. Thus this model is used to represent the PTO mechanism for the PAWEC modelling and control.

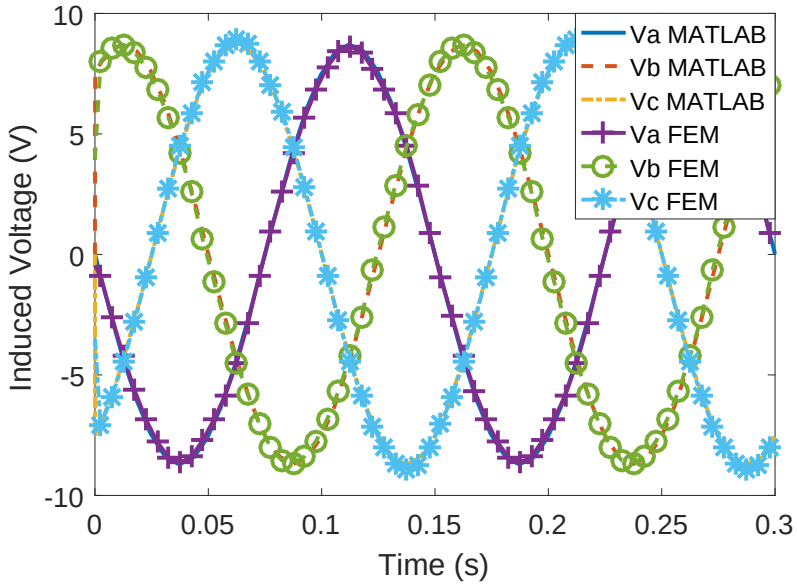

Fig. 7.26 Comparison of the induced phase voltages between the MAXWELL™and MATLAB® simulations for $v_r = 0.24$ m/s.

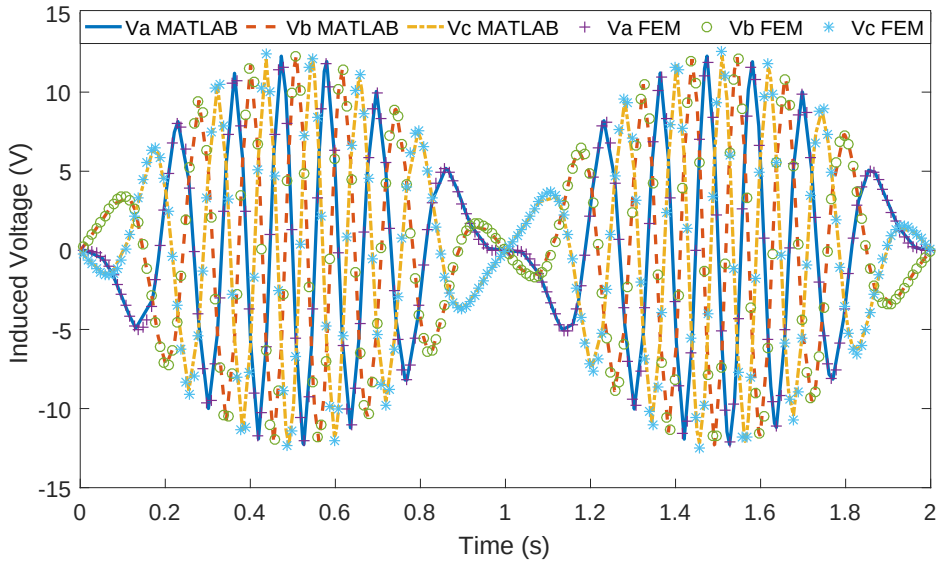

Fig. 7.27 Comparison of the induced phase voltages between the MAXWELL™and MATLAB® simulations for $v_r = 0.34\sin(\pi t)$ m/s

7.6 Wave-to-wire modelling

Eqs. (7.26) and (7.27) can be rewritten as:

$$\dot{I}_d = -\frac{R_s}{L_d}I_d - \frac{1}{L_d}U_d + \frac{\pi L_q}{\tau L_d}vI_q, \tag{7.35}$$

$$\dot{I}_q = +\frac{\pi\phi_{pm}}{\tau L_q}v - \frac{R_s}{L_q}I_q - \frac{1}{L_q}U_q - \frac{\pi L_d}{\tau L_q}vI_d. \tag{7.36}$$

Substituting Eqs. (7.32) and (7.34) into Eqs. (7.35) and (7.36) gives:

$$\dot{I}_d = -\frac{R_s}{L_d}I_d - \frac{1}{L_d}U_d + \frac{L_q}{L_d}K_{pm}vI_q, \tag{7.37}$$

$$\dot{I}_q = +\frac{1}{L_q}K_e v - \frac{R_s}{L_q}I_q - \frac{1}{L_q}U_q - \frac{L_d}{L_q}K_{pm}vI_d. \tag{7.38}$$

To couple the PTO model in Eqs. (7.37) and (7.38) with the W2M model in Eqs. (5.26) and (5.26), a W2W model can be written as:

$$x_{w2w} = [I_d \;\; I_q \;\; x_{w2m}]^T, \tag{7.39}$$

$$\dot{x}_{w2w} = A_{w2w}x_{w2w} + B_{w2w,c}U + B_{w2w,uc}\eta_p + F_{nl}(t, x_{w2w}), \tag{7.40}$$

$$y_{w2w} = C_{w2w}x_{w2w}, \tag{7.41}$$

with

$$A_{w2w} = \begin{bmatrix} -\frac{R_s}{L_d} & 0 & 0 \\ 0 & -\frac{R_s}{L_q} & A_{v,w2w} \\ 0 & K_f D_{w2m} & A_{w2m} \end{bmatrix}, \tag{7.42}$$

$$B_{w2w,c} = \begin{bmatrix} -\frac{1}{L_d} & 0 \\ 0 & -\frac{1}{L_q} \\ 0 & 0 \end{bmatrix}, \tag{7.43}$$

$$B_{w2w,uc} = \begin{bmatrix} 0 & 0 & B_{w2m} \end{bmatrix}^T, \tag{7.44}$$

$$F_{nl}(t, x_{w2w}) = \begin{bmatrix} \frac{L_q}{L_d} K_{pm} \dot{z} I_q \\ -\frac{L_d}{L_q} K_{pm} \dot{z} I_d \\ D_{w2m} F_{ln} + \frac{3}{2} K_{pm}(L_d - L_q) D_{w2m} I_d I_q \end{bmatrix}, \tag{7.45}$$

$$C_{w2w} = \begin{bmatrix} I_4 & 0_{4\times(n_r+n_e)} \end{bmatrix}, \tag{7.46}$$

$$A_{v,w2w} = \begin{bmatrix} 0 & \frac{K_e}{L_q} & 0_{4\times(n_r+n_e)} \end{bmatrix}. \tag{7.47}$$

$U = [U_d \;\; U_q]^T$ represents the control input.

This W2W model looks very complex. However, its concept is very clear. As shown in Fig. 7.28, the W2W model is a combination of the non-linear F2M model in Chapter 4, the W2EF model detailed in Chapter 5 and the PTO model derived in this Chapter. The wave tank verification of the F2M, W2EF and W2M models are given in Chapter 6. The PTO model is obtained from the FEM simulation in MAXWELL™ and numerically verified by comparing with the PMSM model in MATLAB®. Therefore, this W2W model is useful for control system design, which will be discussed in Chapter 8.

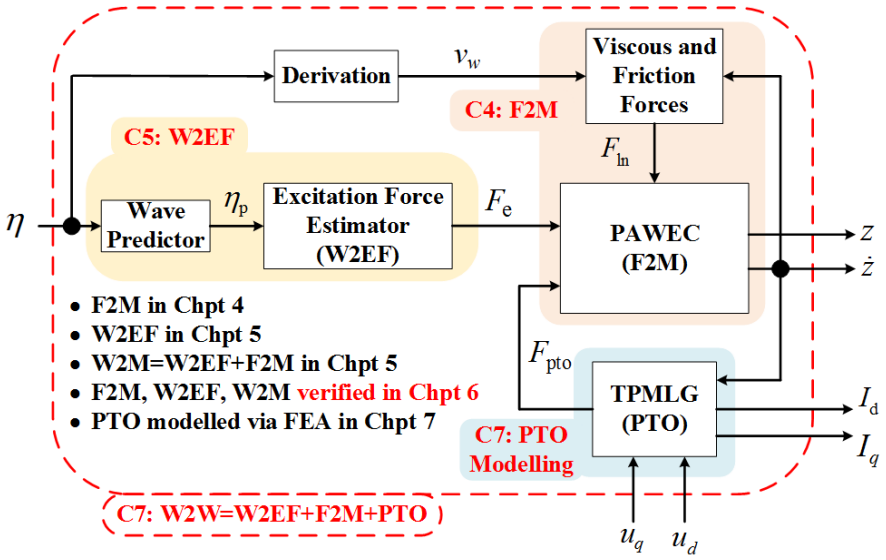

Fig. 7.28 W2W modelling approach.

7.7 Summary and conclusion

7.7.1 Summary

This Chapter begins with the comparison of a variety of PTO systems and the TPMLG is selected as a direct-drive PTO mechanism in this study. The TPMLG design specifications are computed based on the $1/50$ scale PAWEC prototype and wave conditions that can be generated in the Hull University tank system. To gain a full understanding of the TPMLG working principle, FEM simulation is conducted in MAXWELL™ for the purpose of design optimisation, as well as cogging force reduction and parameter determination. Based on the FEM simulation results, a *dq-axis* model of the TPMLG is derived and given in Eqs (7.37) and (7.38). The TPMLG model simulated in MATLAB® shows the same properties of the FEM simulation and thus this TPMLG model is adopted as the PTO model for energy harvesting and control system design.

Coupling the derived PTO model with the non-linear F2M model in Chapter 4 and the W2EF model detailed in Chapter 5, a non-linear W2W model is derived in this Chapter and given in Eqs. (7.40) and (7.41). Thus, optimal control strategies are investigated in Chapter 8 based on the proposed W2W model.

7.7.2 Conclusion

Since the TPMLG is selected as the PTO mechanism in this study, it is critical to list out some special properties of the TPMLG:

- From the viewpoint of working principle, the TPMLG is totally the same as the rotational PMSM. As described in Eqs. (7.26) and (7.27) the TPMLG mathematical model is the same as the PMSM model. The main difference bewteen the TPMLG and rotational PMSM exists in the topological structure and this leads to two special properties: (i) End protection is required for the TPMLG. (ii) The cogging force is relative larger for the TPMLG since the end effect has a large influence on the magnet field distribution.

- Inappropriate design of the TPMLG may result in large cogging force and cogging force reduction can be achieved via parametric analysis and design optimisation. Numerical simulation via FEA shows that the cogging force can be reduced to a small amount without reducing the EMF. As shown in Fig. 7.23, the amplitude of the cogging force is reduced from 8 N to 0.75 N via design optimisation. Whilst there is no obvious difference of the induced voltages bewteen the initial and optimised designs.

- Since some control methods try to control the TPMLG partly working as a generator and partly working as a motor. It is important to identify the power flow clearly via specifying the directions of the *dq-axis* voltages and currents. For the TPMLG model, the current/voltage direction definitions are illustrated in Fig. 7.25. This may be useful to investigate how the power is consumed or converted.

- Conventional generator works in a constant speed and hence the generator model can be treated as a linear model. When the PAWEC oscillation drives the TPMLG to generate electricity, the velocity oscillates periodically. Hence the TPMLG model in Eqs. (7.37) and (7.38). This problem is similar with variable speed wind turbine control and can be linearised via *dq-axis* current decoupling (see Fig. 8.17).

Chapter 8

Power maximisation control

8.1 Introduction

Based on the modelling of wave-buoy interaction in Chapters 3, 4 and 5 and the TPMLG modelling in Chapter 7, this Chapter discusses the power maximisation control strategies of the 1/50 PAWEC device. Section 8.2 describes the reactive control strategies applied on the derived linear F2M PAWEC model via both mechanical and electrical tuning approaches. Mechanical tuning approaches are difficult to implement since under some wave conditions negative stiffness spring is needed. However, based on electromechanical analogue the electrical tuning can be implemented via power electronics. Phase control by latching is investigated in Section 8.3 based on linear and non-linear F2M models. The non-linear fiction and viscous effects on the latching control performance is outlined as well. Further, a W2W tracking control design is proposed and studied with linear and non-linear W2W models in Section 8.4.

8.2 Development of reactive control strategy

This Section outlines the optimal conditions of reactive control based on harmonic waves and linear F2M model. The implementation methods are discussed via both mechanical and electrical tuning approaches.

8.2.1 Reactive control principle

The absorbed power P_{pto} in Eq. (3.75) can be represented in a complex formulation (Falnes, 2002), given as:

$$P_{pto} = \frac{1}{2}\Re(-\hat{F}_{pto}\hat{v}^*) = \frac{1}{2}\frac{R_{pto}|\hat{F}_e|^2}{[R_i+R_{pto}]^2+[X_i+X_{pto}]^2}. \tag{8.1}$$

To maximise the absorbed power, the PTO impedance is tuned to its optimum value (see Eq. (3.81)), as:

$$Z_{pto} = Z_i^*. \tag{8.2}$$

Thus this optimum control approach is so-called complex-conjugate control (Nebel, 1992). Alternatively, the PTO impedance is tuned to match the internal impedance (from the viewpoint of maximum power transfer theorem), as:

$$X_{pto} = -X_i, \tag{8.3}$$

$$R_{pto} = R_i. \tag{8.4}$$

The reactance matching procedure of Eq. (8.3) is to tune the PTO reactance to balance the reactance of the wave-buoy interaction and by doing so minimise the phase shift between the PAWEC velocity and wave excitation force. Whilst, the resistance matching in Eq. (8.4) can maximise the PTO active power. The reactive power is minimised first via the reactance tuning and then the PTO active power is maximised via the resistance matching. Thus, this power maximisation approach is also called reactive control (Salter, 1979).

For well-tuned PTO reactance and resistance in Eqs. (8.3) and (8.4), the optimal absorbed power is given as:

$$P_{pto} = \frac{|\hat{F}_e|^2}{8R_i}. \tag{8.5}$$

It is important to note that the reactance compensation/matching concept also means that there is some power transferred from the PTO mechanism to the wave-buoy interaction during part of the oscillation cycle. That is, a generator has to work as a motor during part of the oscillating cycle, which may be not applicable for some specific PTO mechanisms. In this situation, a sub-optimum control approach, called passive load control can be applied to improve wave power capture. The optimal passive load is given as:

$$R_{pto} = \sqrt{R_i^2 + X_i^2}. \tag{8.6}$$

8.2.2 Mechanical tuning approaches

To achieve the reactive control conditions in Eqs. (8.3) and (8.4), an ideal PTO mechanism can be modelled as a MSD system. To recall that the PTO mechanism is simulated as the MSD system to keep consistency to the previous definition in Section 3.4.2. Also the MSD system is preferred by other researchers and this study tries to implement control methods via electrical actuator (the TPMLG). Hence, one main issue of this Section is to discuss the advantage and disadvantages of the mechanical and electrical implementations. The PTO force can be expressed as (see Eq. (3.51)):

$$F_{pto} = -(M_{pto}\ddot{z} + R_{pto}\dot{z} + K_{pto}z), \tag{8.7}$$

Here we assume these parameters can be tuned to arbitrary values to satisfy the optimum conditions in Eqs. (8.3) and (8.4).

Mechanical resistance tuning approach

For some PTO systems, bi-direction power flow is not allowed and only the resistive parameter can be optimised. The optimal mechanical resistance is given in Eq. (8.6). Therefore, the captured power can be expressed as:

$$P_{pto} = (\int_0^{T_s} R_{pto}\dot{z}^2)/T_s, \tag{8.8}$$

where T_s represents the simulation time. The power capture efficiency η_c is defined by capture width (Evans, 1981), given as:

$$\eta_c = \frac{P_{pto}}{P_w}, \tag{8.9}$$

$$P_w = 2Jr, \tag{8.10}$$

where P_w is the wave power passing through the device. Based on the second order linear F2M model in Eq. (3.50), the results of the mechanical resistance tuning approach is given in Fig. 8.1. It is clear that the efficiency can be up to 1 when resonance occurs at $f = 0.8$ Hz. However, the power capture efficiency is quite low when the wave frequency is away from the resonance region. This also indicates the importance of impedance matching.

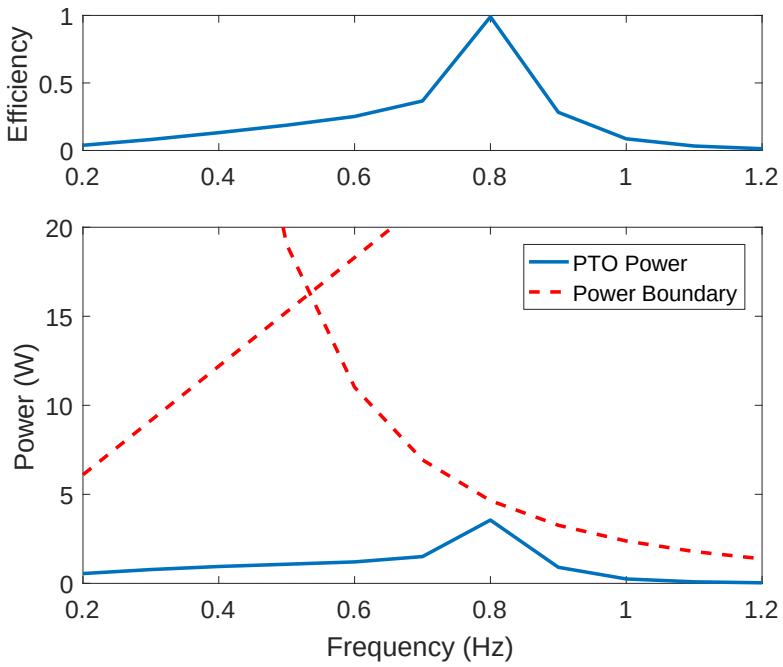

Fig. 8.1 Reactive control performance via mechanical resistance tuning.

Fig. 8.1 also lists out two power boundaries. The one decreasing with the frequency is computed according to the theoretical maximum capture width (Falnes and Hals, 2012), given as:

$$P_{a,max} = Jd_{c,max}. \tag{8.11}$$

where $d_{c,max}$ is maximum capture width defined by Evans (1976). For a heaving PAWEC, the maximum caputure width can be expressed as (Falnes and Hals, 2012):

$$d_{c,max} = \frac{\lambda}{2\pi}. \tag{8.12}$$

The other boundary increasing with the wave frequency is the so-called Budal's upper power bound which takes into account the displacement constraints (Falnes and Hals, 2012), given as:

$$P_{b,max} = \frac{\pi^2 r^2 \rho g H d}{4T}. \tag{8.13}$$

Mechanical impedance tuning approach

Since the wave frequency cannot be controlled, the PTO impedance can be controlled to tune the PAWEC natural frequency equalling to the incident wave frequency $f_n = f$. Thus the PAWEC natural frequency in Eq. (3.72) matches the wave frequency, given as:

$$\frac{K}{M} = 4\pi^2 f^2. \tag{8.14}$$

$K = K_{hs} + K_{pto}$ and $M = M_b + M_{pto} + M_a$ are the total stiffness and mass of the PAWEC system, respectively. Therefore, resonance can be achieved by tuning the PTO parameters M_{pto}, R_{pto} and K_{pto}. For any given harmonic wave conditions, a suitable selection of the PTO parameters can satisfy the optimal conditions in Eqs. (8.4) and (8.4). The power capture and efficiency of the mechanical impedance tuning approach is given in Fig. 8.2. Compared with the mechanical resistance tuning approach in Fig. 8.1, the energy conversion efficiency can reach a very high level over the low frequency region if the mechanical impedance tuning is applied. However, this is not realistic since the absorbed power is larger than the power boundary when the wave frequency is low ($f \leq 0.55$ Hz). The unrealistic high efficiency indicates that the PAWEC can absorb energy from the waves even when it is thrown into the air. This conflicts with

the physical process of wave-PAWEC interaction and thus the PAWEC displacement constraints must be taken into account to get a more accurate efficiency prediction.

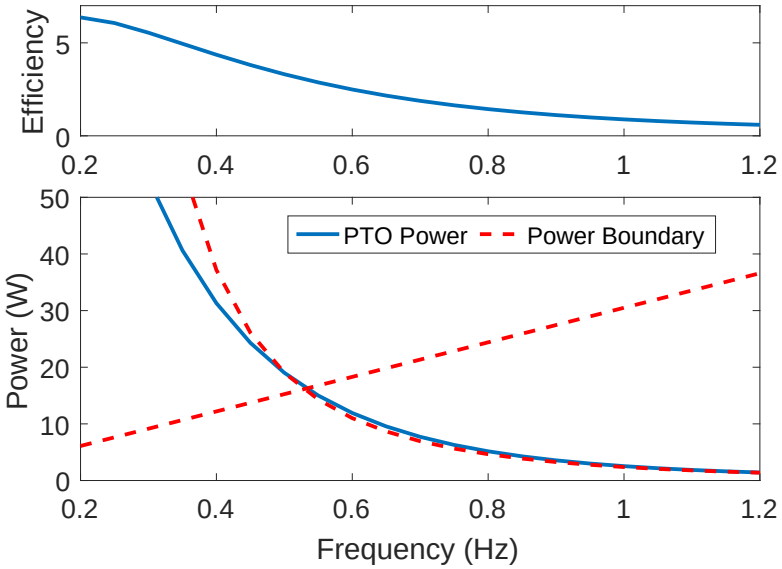

Fig. 8.2 Reactive control performance via mechanical impedance tuning.

Handling physical constraints via mechanical impedance tuning

At low frequencies ($\omega < \omega_0$), the mechanical resistance is small, compared with the hydro-stiffness and mass. The displacement response amplitude operator is large if resonance is achieved. Thus physical constraints should take precedence over power maximisation control. For a very large wave, a heavy mechanical load and a small reference should be applied to reduce the motion and to enhance the sustainability. Assume there is an optimal mechanical impedance to achieve resonance, thus a real parameter defined as the *Force-to-Velocity Ratio* (FVR), is given as:

$$R_{fv} = \frac{F_e}{v}. \tag{8.15}$$

By limiting the buoy displacement within $\pm L_z$, this ratio is given as:

$$R_{fv} \geq \frac{|F_e|}{|v|} \geq \frac{|F_e|}{\omega L_z}, \tag{8.16}$$

where $|F_e|$ and $|v|$ represents the amplitudes of the excitation force and buoy velocity, respectively. For irregular waves, this ratio is determined by the low probability of large waves.

At high frequencies ($\omega > \omega_0$), the excitation force decreases rapidly and hence the damping coefficient is relatively large. The FVR can be chosen as:

$$R_{fv} = 2R_r. \tag{8.17}$$

Summarising, the FVR can be expressed as:

$$R_{fv} = max(\frac{|F_e|}{\omega L_z}, 2R_r). \tag{8.18}$$

For a real application, the PAWEC stroke must be controlled within its physical range and this can be realised by increasing the PTO damping coefficient. For a given displacement limit $\pm L_z$ ($L_z = 0.28$ m for the 1/50 PAWEC), the PTO damping coefficient can be modified as:

$$R_{pto} = R_{fv} - R_r. \tag{8.19}$$

Thus the physical constraints can be handled to select the PTO parameters according to Eqs. (8.4) and (8.19). As shown in Fig. 8.3, the catapulted power as well as the efficiency decrease to more realistic values if displacement constraints are considered. The efficiency band width is larger than the mechanical resistance tuning approach.

According to Figs. 8.2 and 8.3, reactive control via mechanical impedance tuning approaches shows good performance for power maximisation as well as displacement

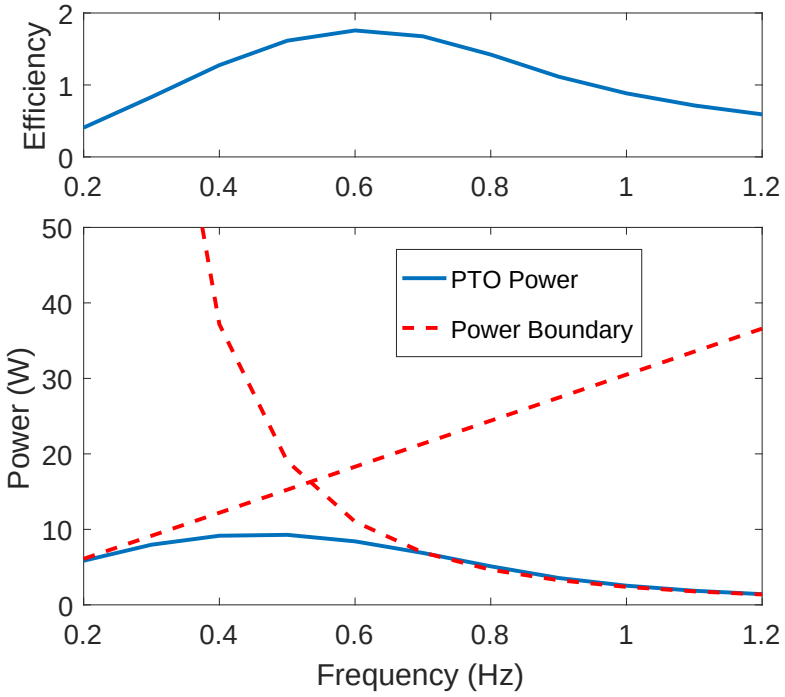

Fig. 8.3 Reactive control performance via mechanical impedance tuning considering displacement constraints.

constriction. This is based on harmonic wave excitation and linear F2M model described in Chapter 3. However, this reactive control is very difficult to implement with a mechanical MSD system since the optimal PTO mass or stiffness may be unrealistic under some wave conditions.

Difficulties in mechanical impedance tuning implementations

For the 1/50 PAWEC, mass tuning may add too much mass on the buoy and then the gravitational force may exceed the buoyancy force. Also, low frequency waves require a "negative spring" to achieve resonance. Thus, for a specified PAWEC control application, the mass or/and stiffness tuning may require a mechanical PTO system which may be difficult to achieve in practice.

Difficulties of Mass Tuning Approach: One potential control strategy is to tune the PAWEC system mass to adjust the natural frequency, e.g. pumping water in to or out of the buoy. If a mechanically controllable mass $M_{m,c}$ is considered, Eq. (8.14) can be

rewritten as:

$$\frac{K}{M+M_{m,c}} = 4\pi^2 f^2. \tag{8.20}$$

Thus the controllable mass $M_{m,c}$ is given as:

$$M_{m,c} = \frac{K}{4\pi^2 f^2} - M. \tag{8.21}$$

Here define $S_m = dM_{m,c}/df$ as the mass sensitivity function, expressed as:

$$S_m = -\frac{K}{2\pi^2}\frac{1}{f^3} = \frac{\rho g r^2}{2\pi}\frac{1}{f^3}. \tag{8.22}$$

For theoretical derivation, the mass tuning approach can achieve resonance and power maximisation. However, for a specific implementation of the 1/50 scale PAWEC, it is crucial to check the property of $M_{m,c}$ for wide range of wave frequencies. In this study, the applicability of this mass tuning is investigated based on the $1/50$ scale prototype. The PTO stiffness is set as $K_{pto} = 0$ N/m, $M = \rho\pi r^2 d$, thus $K = K_{hs} = \rho g \pi r^2$. The added mass is given in Eq. (3.53). Thus, the controllable mass and its sensitivity function are shown in Figs. 8.4a and 8.4b, respectively.

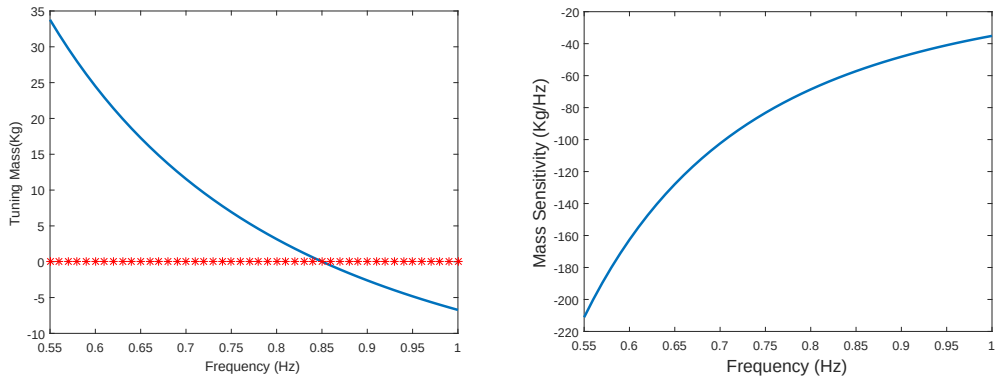

(a) Required amount of controllable mass. (b) Sensitivity function of controllable mass.

Fig. 8.4 Mass tuning approach.

Fig. 8.4a shows that the for low frequency waves (lower than 0.83 Hz), a positive mass is required to reduce the natural frequency whilst a negative mass is needed to increase the natural frequency for high frequency waves (higher than 0.83 Hz). As shown in Fig. 8.4b, $M_{m,c}$ is very sensitive to frequency changes within the frequency range $f \in [0.55, 0.65]$ Hz. For instance, if the wave frequency drops from $f = 0.6$ Hz to $f = 0.55$ Hz, the controllable mass should be decreased from $M_{m,c} = 33.77$ kg to $M_{m,c} = 26.17$ kg. Thus, the changed mass amount $dM_{m,c} = 7.60$ kg is relatively large compared with the PAWEC total mass $M = 19.79$ kg, corresponding to a small frequency variation of $df = 0.05$ Hz. Also, to pump such a large amount of water into or out of the buoy is energy-consuming in this circumstance.

Also, the controllable mass will add weight to the buoy system, which may cause the PAWEC to sink. The average density of the buoy ρ_a is computed over the whole volume $V_b = 2\pi r^2 d$, expressed as:

$$\rho_a = \frac{M_{m,c} + M}{2\pi r^2 d}. \tag{8.23}$$

The average density ρ_a varies with wave frequency, as shown in Fig. 8.5. When the wave frequency is smaller than 0.63 Hz, the average density is larger than the water density $\rho = 1000$ kg/m^3 which means the buoy cannot keep floating but sinks to the sea bed. For the situation $f = 0.83$ Hz, the average density is about $\rho = 500$ kg/m^3, which indicates the buoy is semi-submerged. Due to these two reasons, the mass tuning approach may not be suitable to apply directly on the 1/50 scale PAWEC.

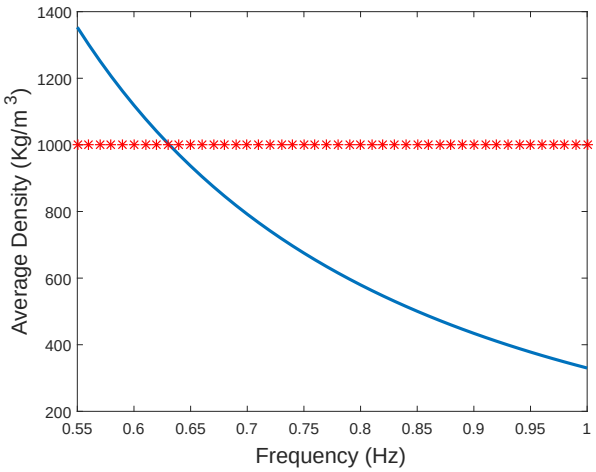

Fig. 8.5 Average density of the PAWEC with tuned mass.

There are several papers discussed the mass tuning approach in the literature, the most notable of which are due to Fu and Lecchini-Visintini (2016); Korde (1999); Piscopo et al. (2016). According to the simulation conditions of Korde (1999); Piscopo et al. (2016), the average density of the floating structure is almost the same as the water density, which means that the buoy may sink if the mass tuning approach is applied. The paper by Fu and Lecchini-Visintini (2016) even shows that negative mass or spring stiffness is required to achieve power maximisation. Thus the results in Figs. 8.4a, 8.4b and 8.5 show good accordance with the published work. Therefore, it is useful to check the mass sensitivity and buoy average density before the implementation of a mass tuning approach on a specific device.

Difficulty in Stiffness Tuning: Another potential approach is to tune the PTO spring stiffness K_{pto} to adjust the PAWEC natural frequency. According to Eq. (8.14), the optimum PTO stiffness $K_{m,c}$ is given as:

$$K_{m,c} = 4\pi^2 f^2 M - K_{hs}. \tag{8.24}$$

For the 1/50 scale PAWEC, the optimum PTO stiffness $K_{m,c}$ is shown in Fig. 8.6. For low frequency waves (lower than 0.83 Hz), the optimum PTO stiffness is negative which is not realistic for a real spring. Currently, a negative spring technique (so-called *WaveSpring*) is reported by a Swedish company Corpower Ocean (CorpowerOcean, 2017). However, this negative spring technique is still immature to apply.

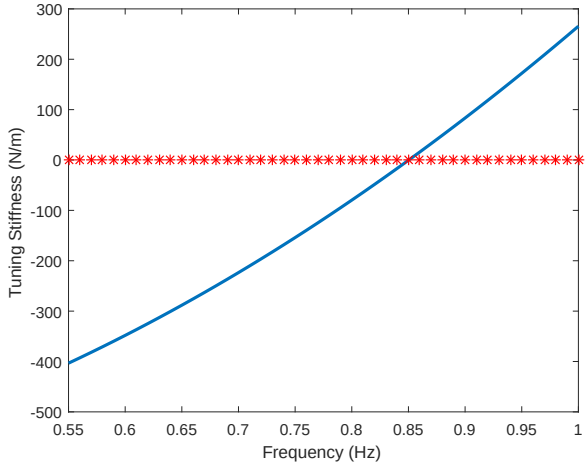

Fig. 8.6 Required stiffness to achieve resonance via mechanical impedance tuning.

8.2.3 Electrical tuning approaches

As mentioned above, the mechanical tuning approach may fail due to unrealistic requirements on huge mass amount or negative spring. However, the impedance tuning can be achieved by electrical tuning approaches actuating on the generator. As shown in Fig. 3.2, the buoy is rigidly connected to a TPMLG as the PTO mechanism. According to the electro-mechanical analogue in Fig. 3.11, the mechanical mass and stiffness are analogous to the electrical inductance and capacitance, respectively. Thus, the mass/spring tuning approaches in Eq. (8.21) or (8.24) can be achieved by tuning the inductance or capacitance of the TPMLG load. Also, the PTO damping coefficient matching can be achieved by tuning the TPMLG resistive load.

Assume the load of the generator is $Z_e = R_e + jX_e = R_e + j(\omega L_e - 1/\omega C_e)$, where R_e, X_e, L_e and C_e are the electrical resistance, reactance, inductance and capacitance, respectively. The complex amplitude of PTO force in Eq. (7.30) can be represented by the electrical parameters, as:

$$\hat{F}_{pto} = -\frac{K_e K_f}{Z_e}\hat{v}. \tag{8.25}$$

The complex amplitude of the PTO force is expressed with mechanical impedance in Eq. (3.77) and also represented by electrical impedance in Eq. (8.25). Eq. (3.77) indicates how the TPMLG influences the buoy dynamics and Eq. (8.25) represents how the buoy motion drives the TPMLG. Therefore, they are equal to each other and the electrical and mechanical impedances are related as:

$$Z_{pto} = \frac{K_e K_f}{Z_e}. \tag{8.26}$$

More general, the mechanical impedance defined in Eq. (3.71) can be converted to or from the electrical impedance. The mechanical equivalent of the electrical impedance Z_{e2m} is defined here as:

$$Z_{e2m} = \frac{K_e K_f}{Z_e} = \frac{K_e K_f}{R_e + jX_e}. \tag{8.27}$$

Alternatively, the electrical equivalent of the mechanical impedance Z_{m2e} is defined here as:

$$Z_{m2e} = \frac{K_e K_f}{R_i + jX_i}. \tag{8.28}$$

Therefore, the electro-mechanical analogue qualitatively shown in Fig. 3.11 can be expressed quantitatively as shown in Fig. 8.7. To relate the variables with their physical meanings, Eq. (8.26) is rewritten as:

$$R_{pto} + j\left(M_{pto}\omega - \frac{K_{pto}}{\omega}\right) = \frac{K_e K_f}{R_e + j(L_e\omega - 1/\omega C_e)}. \tag{8.29}$$

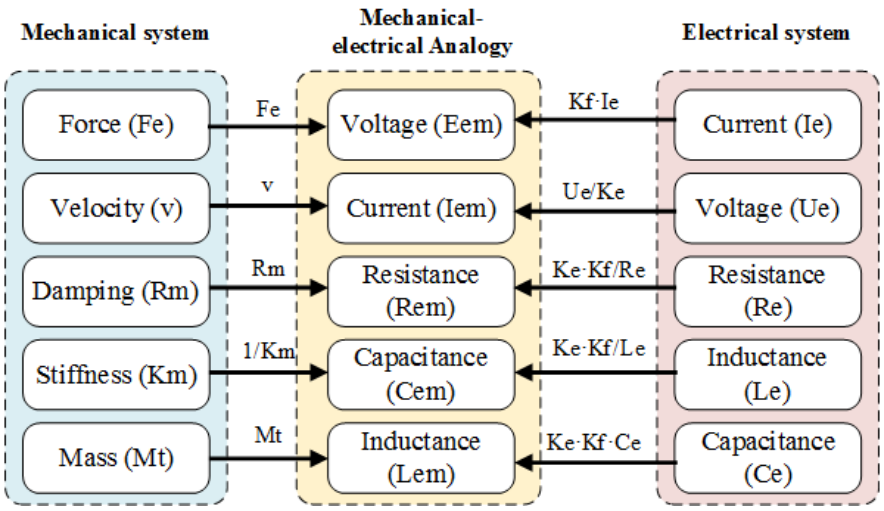

Fig. 8.7 Relationship of parameters in the electro-mechanical analogue.

Thus, the mass tuning approach in Eq. (8.21) can be achieved by tuning the electrical capacitance, as:

$$M_{m,c} = K_e K_f C_e. \tag{8.30}$$

The electrical capacitor C_e acts as a "virtual mass", which can tune the PTO impedance like mechanical mass without adding mass to the PAWEC system. Similarly, the stiffness

tuning approach in Eq. (8.24) can be achieved by tuning the electrical inductance, as:

$$K_{m,c} = \frac{L_e}{K_e K_f}. \tag{8.31}$$

The electrical inductor L_e acts as a spring. As illustrated in Fig. 8.6, a "negative" spring is required for low frequency waves. This cannot be achieved by a "negative" inductor by can be equivalently achieved by a capacitor.

For power maximisation, the mass/capacitance and stiffness/inductance tuning can only satisfy the optimum phase condition to optimise the power capture from wave to the PAWEC motion. The optimum amplitude condition to maximise the power transfer from PAWEC motion to PTO system can be achieved by the resistance tuning mechanically or electrically, as:

$$R_{pto} = \frac{K_e K_f}{R_e} = R_r. \tag{8.32}$$

Compared with the mechanical tuning approaches in Section 8.2.2, the electrical tuning approaches are more applicable. The RLC tuning can satisfy both optimum phase and amplitude conditions without real mass, spring or damper applied on the WEC system. Thus the buoyancy-gravity mismatch and negative spring problems can be avoided. Meanwhile, the RLC tuning can be easily implemented via the Flexible Alternating Current Transmission Systems (FACTS) technology used in smart grid techniques.

Electrical resistance tuning approach

If a resistive load is applied to the TPMLG and only the resistance can be tuned, the optimal resistance can be computed according to Eqs. (8.6) and (8.32), expressed as:

$$R_e = \frac{K_e K_f}{\sqrt{R_i^2 + X_i^2}}. \tag{8.33}$$

The electrical resistance tuning performance is shown in Fig. 8.8, which give almost the same performance as the mechanical resistance tuning approach in Fig. 8.1.

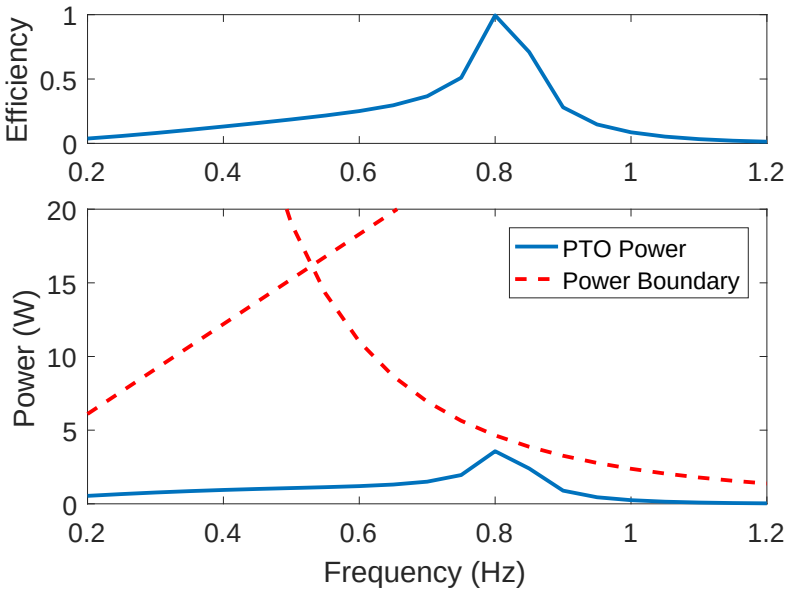

Fig. 8.8 Electrical resistance tuning performance.

Electrical impedance tuning approach

To maximise the converted power via electrical impedance tuning, the optimal electrical impedance should match with the PAWEC mechanical impedance, given as:

$$Z_m = Z_{e2m}^*, \tag{8.34}$$

where Z_{e2m}^* denotes the complex conjugate of Z_{e2m}.

To substituting $Z_e = R_e + jX_e$ into Eqs. (8.27) and (8.34), the TPMLG load can be expressed as:

$$R_e = \frac{K_e K_f R_i}{R_i^2 + X_i^2}, \tag{8.35}$$

$$X_e = \frac{K_e K_f X_i}{R_i^2 + X_i^2}. \tag{8.36}$$

At low frequencies $\omega < \omega_0$, $X_i = M_t\omega - K_{hs}/\omega < 0$ indicates a negative X_e or RC circuits, alternatively a damper and mass unit as mechanical load (see Fig. 8.7). Hence, it is reasonable to represent the PTO system as a mass-damper rather than spring-damper system under low frequency conditions. For frequencies close to the natural frequency $\omega \approx \omega_0$, a pure electrical resistance or a pure mechanical damper are required to satisfy the resonance conditions. At high frequencies $\omega > \omega_0$, $X_i = M_t\omega - K_{hs}/\omega > 0$ indicates an RL load. The PTO system can be modelled as a spring-damper system.

The performance of the electrical impedance tuning approach is given in Fig. 8.9. The captured power and efficiency are the same as the mechanical impedance tuning approach in Fig. 8.2. The efficiency is unrealistically high in the low frequency region, since the displacement constraints are not considered.

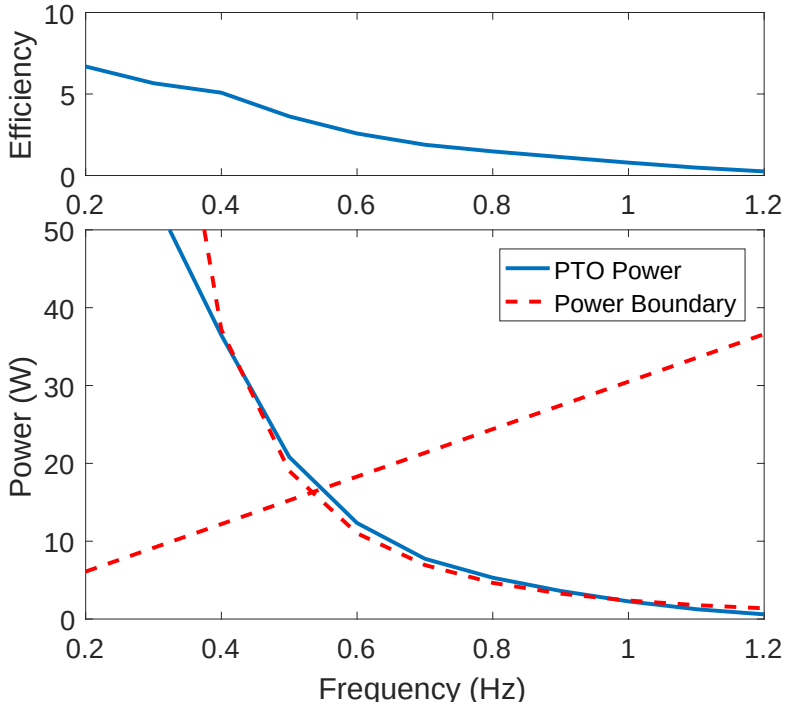

Fig. 8.9 Electrical impedance tuning performance.

Handling physical constraints via electrical tuning

To handle the displacement constraints, Eq. (8.34) can be rewritten as:

$$R_{e2m} = R_{fv} - R_i, \tag{8.37}$$

$$X_{e2m} = -X_i. \tag{8.38}$$

The optimal electrical load can then be expressed as:

$$R_e = \frac{K_e K_f (R_{fv} - R_i)}{(R_{fv} - R_i)^2 + X_i^2}, \tag{8.39}$$

$$X_e = \frac{K_e K_f X_i}{(R_{fv} - R_i)^2 + X_i^2}. \tag{8.40}$$

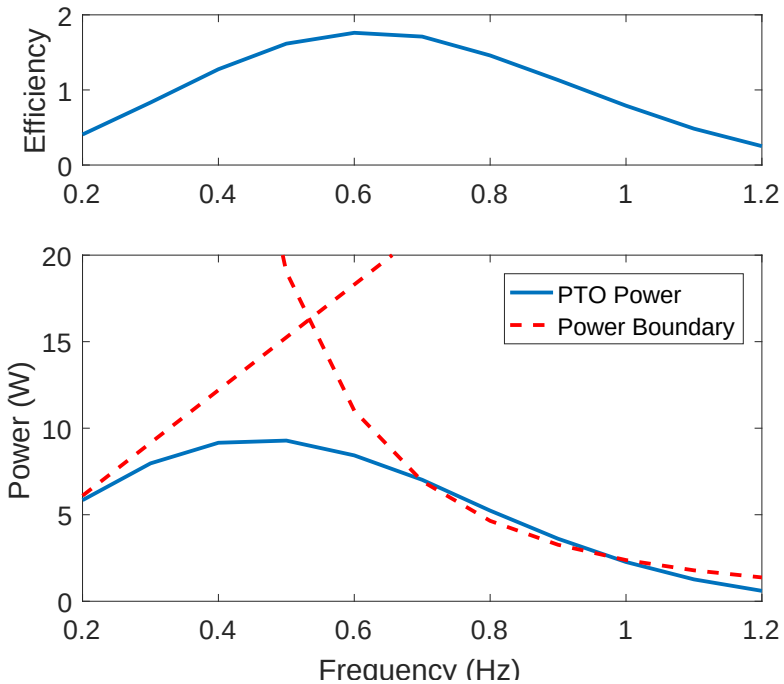

Fig. 8.10 Electrical impedance tuning performance considering the displacement constraints.

As shown in Fig. 8.10, the electrical impedance tuning approach including stroke constraints shows the same results of the mechanical impedance tuning approach with displacement constraints in Fig. 8.3.

As pointed out above, the electrical tuning approaches can achieve almost the same performance of the mechanical tuning and provide an applicable way towards physical implementation. The derivation of TPMLG PTO force in Eqs. (7.30) and (8.25) is based on $I_{d,ref} = 0$ A. Thus an external power supply is required to compensate the *d-axis* induced voltage (see Fig. 7.25). Another problem for the electrical load tuning is that huge values of capacitance or inductance are required for low or high frequency waves. These huge capacitances or inductances cannot be achieved in a passive way but can be achieved if the TPMLG is connected to the grid in a suitable way.

Another physical constraint is the PTO force or ultimately the current limitation in the TPMLG. To recall that the wire applied in the TPMLG design is AWG15, detailed in Section 7.3.2. Hence the maximum working current for AWG15 indicates the current/force constraints. According to Appendix C, the maximum working current for AWG15 is about 4.7 A. According to Eq. (7.30), the PTO force constraint should be 255.69 N. Additionally, a larger PTO load is selected to constrain the buoy displacement which indicates that the TPMLG voltage is constrained as well as the current and force. However, only the displacement constraints are considered in this study. It is possible to consider both the displacement and PTO force constraints via advanced control technologies, such as the MPC, which is beyond the scope of this study.

8.3 Development of phase control by latching

This Section outlines the phase control principle based on harmonic waves. Optimal phase is achieved by electrical latching implemented on the TPMLG modelled in Chapter 7 rather than a hydraulic PTO mechanism. Also, the influence of the non-linear fluid viscous and mechanical friction forces on the latching performance is studied numerically in this Section.

8.3.1 Phase control principle

According to the energy conversion principle, the captured power P_e is divided into the radiation power P_r and the absorbed power P_{pto}. Thus the absorbed power can be represented as:

$$P_{pto} = P_e - P_r. \tag{8.41}$$

The captured power P_e in Eq. (3.73) is rewritten in its complex formulation as:

$$P_e = \frac{1}{2}\Re(-\hat{F}_e\hat{v}^*) = \frac{1}{2}|\hat{F}_e||\hat{v}|cos(\phi_v - \phi_e). \tag{8.42}$$

Similarly, the radiation power P_r in Eq. (3.74) is rewritten as:

$$P_r = \frac{1}{2}\Re(-\hat{F}_r\hat{v}^*) = \frac{1}{2}R_i|\hat{v}|^2. \tag{8.43}$$

Therefore, Eq. (8.41) is rewritten as:

$$P_{pto} = P_e - P_r = \frac{1}{2}|\hat{F}_e||\hat{v}|cos(\phi_v - \phi_e) - \frac{1}{2}R_i|\hat{v}|^2. \tag{8.44}$$

The maximum absorbed power in Eq. (8.44) is a quadratic optimisation problem. The power maximisation happens when $\partial P_{pto}/\partial|\hat{v}| = 0$. Thus the optimum velocity amplitude is given as (Falnes, 2002):

$$|\hat{v}|_{opt} = \frac{|\hat{F}_e|}{2R_i}cos(\phi_v - \phi_e). \tag{8.45}$$

The optimum buoy velocity in Eq. (8.45) can be achieved when the optimum phase and amplitude conditions are satisfied, given as (Falnes, 2002):

$$1 = \cos(\phi_v - \phi_e), \tag{8.46}$$

$$|\hat{v}_{opt}| = \frac{|\hat{F}_e|}{2R_i}. \tag{8.47}$$

Therefore, power the maximisation approaches which satisfy the optimum phase and amplitude conditions are called "phase and amplitude control".

Theoretically speaking, the optimum phase and amplitude conditions in Eq. (8.46) and (8.47) show high correspondence with the reactive control conditions in Eq. (8.3) and (8.4). The reactance compensation in Eq. (8.4) can achieve the optimum phase condition in Eq. (8.46), aiming to keep the buoy velocity in phase with the wave excitation force to maximise the captured power. This is the resonance theory proposed by Budal and Falnes (1975b); Evans (1976); French (1979); Mei (1976); Salter (1979). The optimum PTO damping coefficient required by the resistance matching condition in Eq. (8.4) and the optimum amplitude condition in Eq. (8.47) are the same, $R_{pto} = R_r$, which aims to maximise the absorber power through the maximum power transfer theorem. Although the optimum conditions are the same in reactive control and phase/amplitude control, their derivation procedures are different, which indicates that their implementations may vary.

For engineering applications, the phase/amplitude control approach is difficult to implement. A suboptimal strategy, called latching control, is proposed by Falnes and Budal (1978) to latch the buoy when its velocity vanishes and to release it after an optimum time interval. This time interval is optimised to achieve maximum power capture width with a short-term prediction of wave excitation force. The maximisation of the absorbed power is achieved with a pure damper with optimum passive load in Eq. (8.6). The frequency ω in Eq. (8.6) should be replaced by the PAWEC natural frequency in Eq. (3.72).

Phase control by latching shows great advantage on various WEC systems if two conditions are satisfied: (i) the wave frequency is smaller than the device natural frequency; and (ii) the wave excitation force can be predicted accurately more than a quarter of wave period. To extend the application scope, Babarit et al. (2009) proposed latched-operating-declutched control with implementation on hydraulic PTO systems

and Lopes et al. (2009) tested non-prediction latching control on a two-body point absorber with assistance of pressure sensors.

It is notable that both the reactive and phase/amplitude control approaches are derived based on harmonic waves but can be extended to irregular wave situations. The buoy dynamics in Eq. (3.80) can be replaced by its Fourier transform, and the captured power in Eq. (3.73) and absorbed power in Eq. (3.75) can be replaced by its frequency-domain energy functions according to Parseval's theorem.

8.3.2 Electrical latching

To investigate the non-linear effects on control performance, a non-predictive latching strategy (Sheng et al., 2015) is applied to the linear and non-linear models. The PTO is simply simulated as a pure damper R_{pto} during the unlatching intervals and as a huge damper R_{latch} during the latching intervals. Thus the captured power is the same as Eq. (8.8). For harmonic waves, the latching time interval t_l is given as (Sheng et al., 2015):

$$t_l = 0.5(T_w - T_n), \tag{8.48}$$

where T_w and T_n are the wave period and the PAWEC natural period. Latching control can be easily realised via hydraulic PTO systems. Meanwhile, according to the relationship between mechanical and electrical impedance, the mechanical damping can be achieved by the TPMLG load switching. Therefore, it is possible to achieve latching control electrically.

For a mechanical latching control implementation, the PTO force can be expressed as:

$$F_{pto} = \begin{cases} -R_{pto}v & released, \\ -R_{latch}v & latched. \end{cases} \tag{8.49}$$

Alternatively, this latching control strategy also can be implemented via the TPMLG according to the electromechanical analogue in Eq. (8.32). Thus the PTO force via

electrical latching can be rewritten as:

$$F_{pto} = \begin{cases} -\frac{K_e K_f}{R_{e,pto}} v & released, \\ -\frac{K_e K_f}{R_{e,latch}} v & latched. \end{cases} \tag{8.50}$$

Based on the linear F2M model in Eqs. (4.21) and (4.22), the comparison between the mechanical and electrical latching implementations is given in Fig. 8.11. It is clear that the electrical latching can give the same performance as the mechanical latching implementation in terms of the PAWEC displacement, velocity and captured energy. For the linear F2M model the natural frequency is $f_n = 0.82$ Hz and the wave condition for Fig. 8.11 is $f = 0.56$ Hz and $H = 0.1$ m. Thus the latching time interval is computed according to Eq. (8.48). The PTO damping coefficients are selected as $R_{pto} = 4.55$ Nsm^{-1} when the PAWEC is released and $R_{latch} = 2000$ Nsm^{-1} when the PAWEC is latched. Thus, for the electrical latching implementation, the resistive loads of the TPMLG are selected as $R_{e,pto} = \frac{K_e K_f}{R_{pto}} = 433.64\ \Omega$ for releasing intervals and $R_{e,latch} = \frac{K_e K_f}{R_{latch}} = 0.99\ \Omega$ ($R_s = 1.04 \approx 0.99\ \Omega$) for latching intervals.

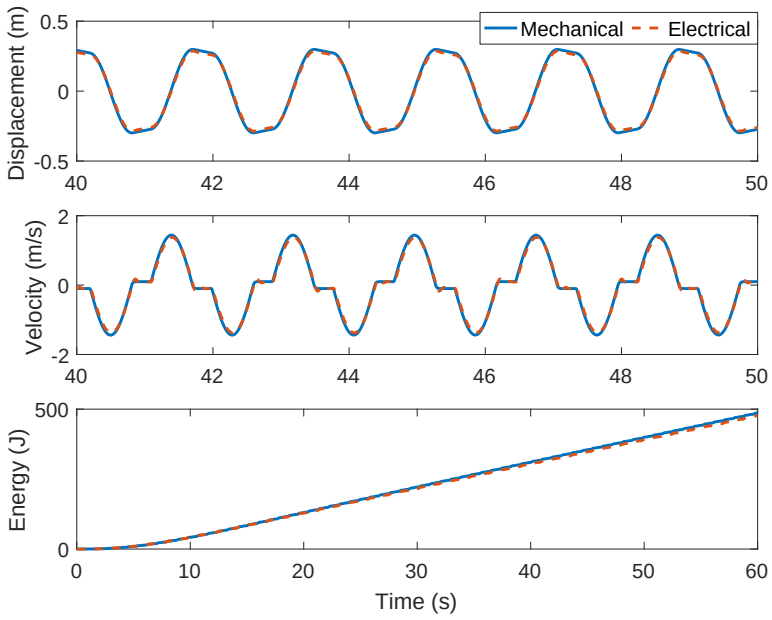

Fig. 8.11 Control performance comparison between the mechanical and electrical latching implementations in terms of displacement, velocity and captured energy.

Since the resistive load is very low ($R_{e,latch} = 0.99\ \Omega$), it is important to check whether the TPMLG is overloaded during the latching intervals. Fig. 8.12 gives the evaluations of the *dq-axis* currents. The peak value of I_q is about 4.5 A. Recall that the AWG15 wire is selected for coil winding. As shown in Fig. C.3, the maximum working current of AWG15 is 4.7 A in RMS value and the fusing current is up to 160 A. From this point of view, the TPMLG is not in risk during the latching intervals. Further more, the electrical power is low during the latching intervals since small velocity induces small voltage. To note, $I_{d,ref} = 0$ A is applied and the voltage ripples at the latching or releasing instants can be attenuated via by-pass capacitors.

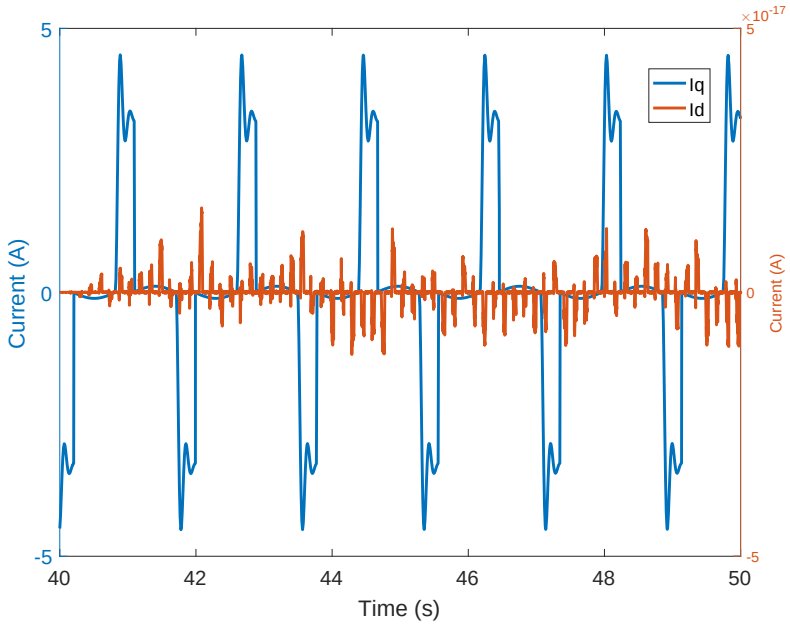

Fig. 8.12 *Dq-axis* currents evaluations for the electrical latching implementation.

8.3.3 Non-linear effects on electrical latching performance

As described in Section 5.7.3, the non-linear fluid viscous and friction forces have significant influence on the PAWEC dynamics. It is important to investigate how these non-linear factors affect the latching control performance.

When considering the non-linear friction force, the linear F2M model in Eqs. (4.21) and (4.22) becomes a non-linear F2M model *NLM1*:

$$\dot{x}_{f2m} = A_{f2m}x_{f2m} + B_{f2m}F_e + B_{f2m}F_{pto} + B_{f2m}f_f(t,x), \tag{8.51}$$
$$y_{f2m} = C_{f2m}x_{f2m}. \tag{8.52}$$

The system matrices are given in Eqs. (4.23)-(4.25). The friction force $f_f(t,x)$ is given in Eq. (4.35). The PTO force F_{pto} is given in Eq. (8.50).

Another non-linear F2M model *NLM2* involves the viscous force is given as:

$$\dot{x}_{f2m} = A_{f2m}x_{f2m} + B_{f2m}F_e + B_{f2m}F_{pto} + B_{f2m}f_v(t,x), \tag{8.53}$$
$$y_{f2m} = C_{f2m}x_{f2m}. \tag{8.54}$$

The fluid viscous force $f_v(t,x)$ is given in Eq. (4.29).

In the wave tank tests, the viscous and friction forces are lumped and cannot be decoupled from each other. Therefore, a non-linear F2M model *NLM3* considering the lumped non-linear force is given as:

$$\dot{x}_{f2m} = A_{f2m}x_{f2m} + B_{f2m}F_e + B_{f2m}F_{pto} + B_{f2m}f_{ln}(t,x), \tag{8.55}$$
$$y_{f2m} = C_{f2m}x_{f2m}. \tag{8.56}$$

The lumped non-linear force $f_{ln}(t,x)$ is given in Eq. (4.37).

The R_{pto} is optimised at a specified frequency when the RAO reaches its peak value in Fig. 5.16. For the linear model, the damping coefficient is optimised at the natural frequency 0.82 Hz. Thus $R_{pto} = 4.55$ Nsm^{-1} is selected, which is the same as the radiation damping coefficient given by NEMOH. For the non-linear models, the constant damping coefficients are selected as $R_{pto} = 7.72$ Nsm^{-1} at the frequency of 0.82 Hz for NLM1, $R_{pto} = 21.25$ Nsm^{-1} at the frequency of 0.79 Hz for NLM2 and $R_{pto} = 21.32$ Nsm^{-1} at the frequency of 0.78 Hz for NLM3. $R_{latch} = 2000$ Nsm^{-1} is fixed as a constant.

The power conversion efficiency comparison based on linear and non-linear models is shown in Fig. 8.13. The maximum efficiency of the linear model by latching control is up to 180% whilst the maximum efficiencies of the non-linear models by latching control are 98%, 55% and 38% for NLM1, NLM2 and NLM3, respectively. As reported by Evans (1976); Falnes (2002), the theoretical efficiency for a heaving floating buoy is 50%. According to Fig. 8.13 the efficiency of the linear model by latching is up to 4 times of the theoretical value 50%. The main reason is that the linear model is based on the assumption that the body motion amplitude is small. When the resonance is achieved by latching control the PAWEC motion becomes much larger and the viscous force cannot be ignored any more. In this situation, the linear modelling method is not valid any more. That is, the linear modelling method overestimates the PAWEC motion amplitude as well as the converted power. Therefore, the linear model with latching control cannot predict the power productivity accurately, whilst the NLM3 that takes account of both the viscous and friction forces can damp the power capture to a realistic level around 40% (close to the theoretical value 50%).

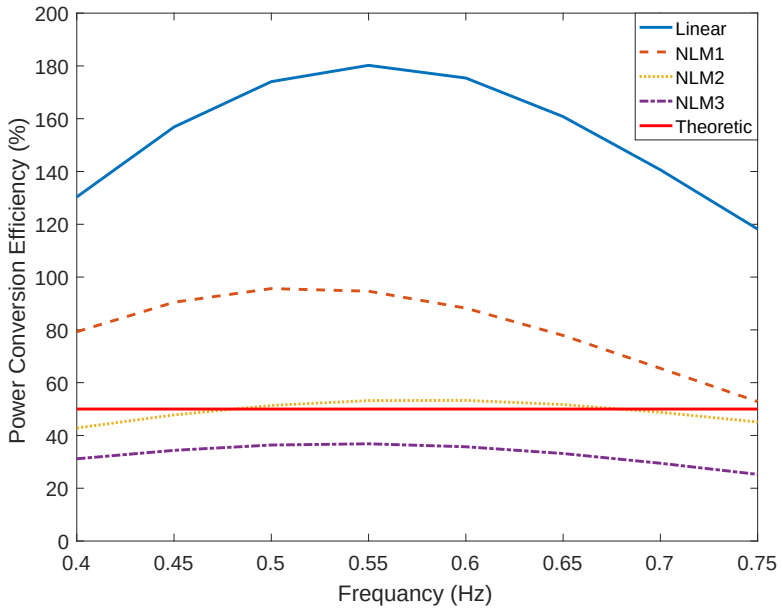

Fig. 8.13 Comparison of power conversion efficiencies between the linear and non-linear models by electrical latching.

The displacement comparison between linear and non-linear models by latching control is shown in Fig. 8.14 with testing wave of 0.56 Hz in frequency and 0.1 m in height. The buoy displacement of the linear model exceeds the displacement constraints which means the buoy is either thrown right out of the water or totally submerged under the

quiescent water level. Thus an additional end protection is required. However, this is not the case when both the viscous and friction forces are considered in NLM3. The displacement excursion of NLM3 is about twice the wave height but much smaller than the physical constraints. Extra consideration to bound the buoy motion is not necessary for moderate waves if both the friction and viscous forces are considered.

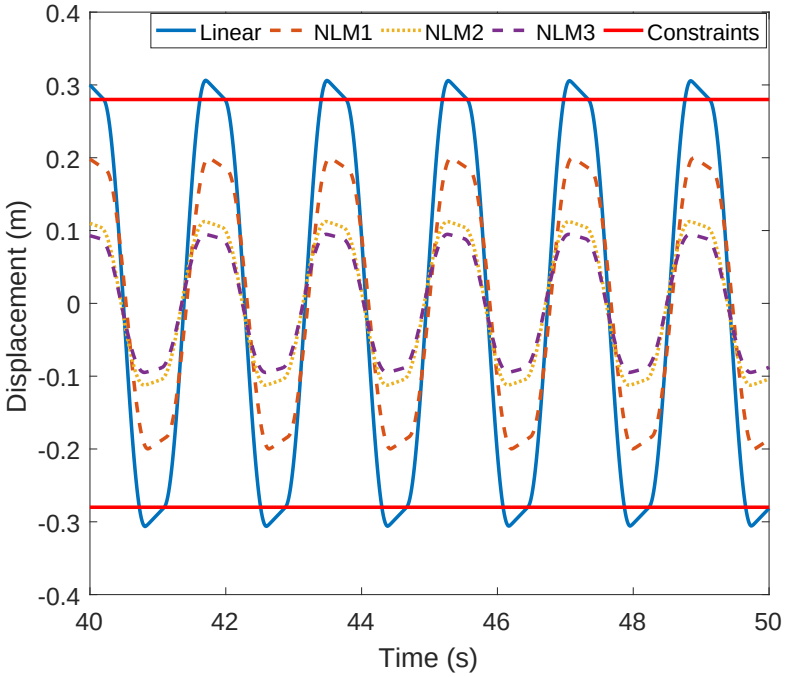

Fig. 8.14 Comparison of the buoy displacements between the linear and non-linear models by electrical latching. The constraints are selected as 0.28 m, which is half of the buoy height.

8.4 W2W tracking control structure

This Section proposes a reference tracking control strategy based on linear and non-linear W2W model derived in Section 7.6. The control structure is given in Fig. 8.15. The excitation force estimation approaches are described in Section 5.3. This Section discusses a three-level tacking control strategy for the 1/50 PAWEC power maximisation considering the displacement constraints. The following paragraphs describe the reference generation, tracking control and simulation results.

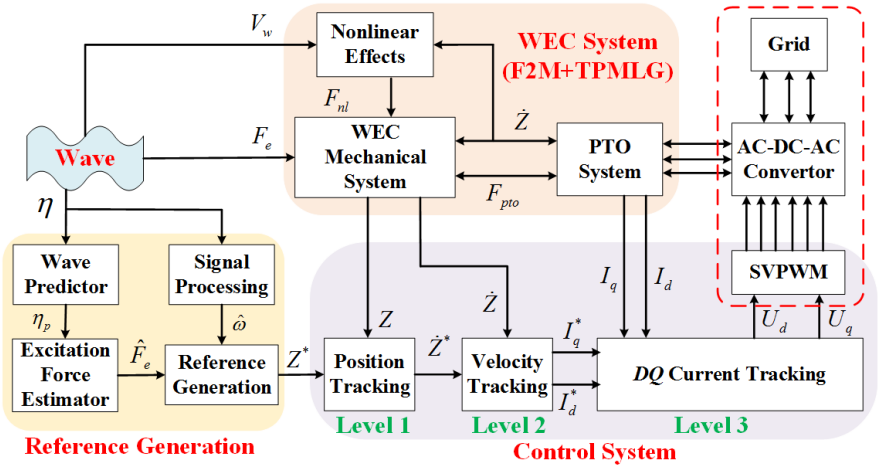

Fig. 8.15 A W2W tracking control structure.

According to Fig. 8.15, the displacement reference is obtained from the estimates of the excitation force and the wave frequency, detailed in Section 8.4.1. This displacement reference is passed to the first level controller which deals with the displacement tracking and hence gives the velocity reference for the second level controller. The second level controller forces the buoy velocity to track the velocity reference for power maximisation and generates the *dq-axis* current references for the third level controller. The third level controller only deals with the voltage regulation in the *dq-axis*. One potential implementation approach is to control the AC/DC/AC converters/inverters. However, this part of work will not be discussed in this study since it is quite mature for grid connection. Some notable papers are given by Boström et al. (2009); Ekström et al. (2015); Leijon et al. (2006).

In Fig. 8.15, the first level tracking loop is selected as the displacement tracking rather than velocity tracking. The main reasons are: (i) Displacement constraints can be handled with an appropriate displacement reference. Thus the PAWEC motion can be detuned under extreme wave conditions to improve survivability. The velocity tracking may result in a higher efficiency than the displacement tracking. However, this study gives the priority to the survivability via setting the displacement tracking as the outer loop. (ii) If only the velocity tracking is applied, the buoy displacement cannot be controlled to oscillate around the equilibrium point since the displacement response is very sensitivity to the initial conditions. For instance, if the initial displacement is zero and the velocity reference follows $\sin(\omega t)$, the PAWEC displacement will oscillate around a displacement bias rather than its equilibrium point.

8.4.1 Reference generation

If the non-linear viscous and friction forces are not considered, a linear W2W model can be marked as *W2WLM* and written as:

$$\dot{x}_{w2w} = A_{w2w}x_{w2w} + B_{w2w,c}U + B_{w2w,uc}\eta_p, \tag{8.57}$$

$$y_{w2w} = C_{w2w}x_{w2w}. \tag{8.58}$$

The system matrices are given in Eqs. (7.42)-(7.46). In this linear W2W model, the radiation force is the only dissipative factor and thus the displacement reference should be generated according to the radiation damping coefficient and the PAWEC stroke limits. The references can be derived as:

$$v_{ref} = \frac{F_e}{R_{fv}}, \tag{8.59}$$

$$z_{ref} = \frac{v_{ref}}{\omega}e^{-j\frac{\pi}{2}}. \tag{8.60}$$

R_{fv} is given in Eq. (8.18). For this linear model, the damping coefficient is optimised at the natural frequency 0.82 Hz. Thus $R_r = 4.55$ Nsm^{-1} is selected.

If the mechanical friction force is considered, a non-linear W2W model, marked as *W2WNLM1* can be written as:

$$\dot{x}_{w2w} = A_{w2w}x_{w2w} + B_{w2w,c}U + B_{w2w,uc}\eta_p + D_{w2m}f_f(t,x), \tag{8.61}$$

$$y_{w2w} = C_{w2w}x_{w2w}. \tag{8.62}$$

The friction force $f_f(t,x)$ is given in Eq. (4.35). In W2WNLM1, both the radiation and friction forces dissipate energy and thus the FVR is rewritten as:

$$R_{fv} = max(\frac{|F_e|}{\omega L_z}, 2(R_r + R_f)), \tag{8.63}$$

where R_f represents the equivalent damping coefficient of the friction force. For this non-linear model, $R_r + R_f = 7.72$ Nsm^{-1} is optimised at the frequency of 0.82 Hz according to Fig. 5.16.

If the fluid viscous force is considered, a non-linear W2W model, marked as *W2WNLM2* can be written as:

$$\dot{x}_{w2w} = A_{w2w}x_{w2w} + B_{w2w,c}U + B_{w2w,uc}\eta_p + D_{w2m}f_v(t,x), \tag{8.64}$$

$$y_{w2w} = C_{w2w}x_{w2w}. \tag{8.65}$$

The friction force $f_v(t,x)$ is given in Eq. (4.35). In W2WNLM2, both the radiation and viscous forces dissipate energy and thus the FVR is rewritten as:

$$R_{fv} = max(\frac{|F_e|}{\omega L_z}, 2(R_r + R_v)), \tag{8.66}$$

where R_v represents the equivalent damping coefficient of the fluid viscous force. $R_r + R_v = 21.25$ Nsm^{-1} is optimised at the frequency of 0.79 Hz according to Fig. 5.16.

If both the friction and viscous forces are considered, a non-linear W2W model, marked as *W2WNLM3* can be written as:

$$\dot{x}_{w2w} = A_{w2w}x_{w2w} + B_{w2w,c}U + B_{w2w,uc}\eta_p(t) + D_{w2m}f_{ln}(t,x), \tag{8.67}$$

$$y_{w2w} = C_{w2w}x_{w2w}. \tag{8.68}$$

$f_{ln}(t,x)$ is the summation of the friction and viscous forces, given in Eq. (4.35). In W2WNLM3, radiation, friction and viscosity phenomena dissipate energy and thus the FVR is modified as:

$$R_{fv} = max(\frac{|F_e|}{\omega L_z}, 2(R_r + R_f + R_v)). \tag{8.69}$$

$R_r + R_f + R_v = 21.32$ Nsm^{-1} is optimised at the frequency of 0.78 Hz according to Fig. 5.16.

As illustrated in Fig. 8.15, signal processing is required to estimate the incoming wave excitation characteristic parameters. These estimates are used to: (i) update the PAWEC radiation damping coefficient, (ii) compute the optimal FVR and (iii) generate reference signal. Instantaneous frequency and amplitude estimates are obtained using Teager's energy operation (TEO) Maragos et al. (1993). Compared with estimation via either the fast Fourier transform or the Hilbert transform approaches, the TEO method offers good accuracy with rapid computation.

As shown in Fig. 8.16, the TEO method can provide accurate estimates of the Instantaneous Magnitude (IM) and Instantaneous Frequency (IF). The excitation force is simulated according to the PM spectrum in Eq. (3.28) ($Hs = 0.25$ m, $f_p = 0.40$ Hz) and W2EF model in Eqs. (5.11) and (5.12). Therefore, the TEO method is adopted in this study to provide IM and IF estimates for reference generation.

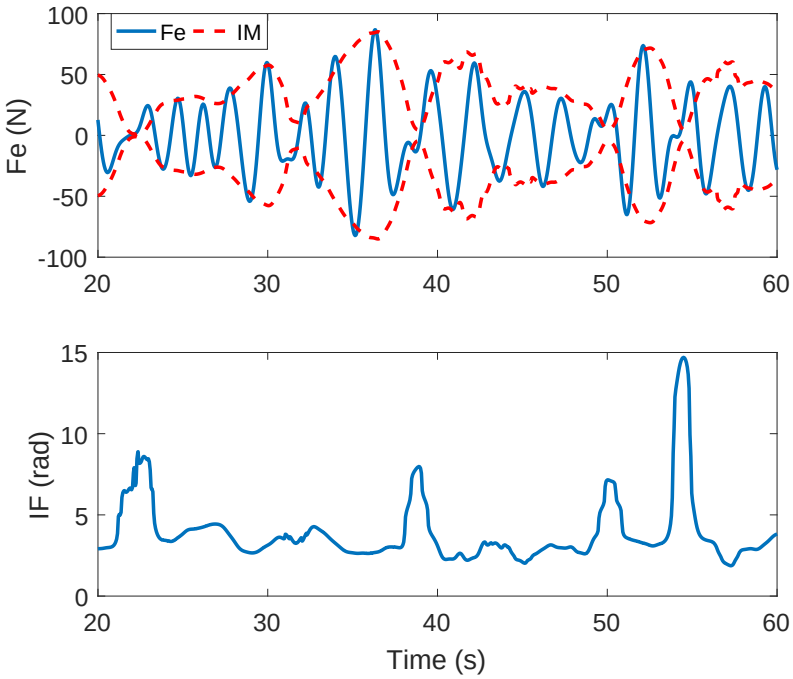

Fig. 8.16 Real-time estimates of wave excitation force instantaneous magnitude and frequency via the TEO method.

8.4.2 Tracking control

Three PI controllers are applied here to achieve the position, velocity and current tracking with parameters:

- $P_z = 128$, $I_z = 20$ for position tracking.
- $P_v = 220$, $I_v = 42$ for velocity tracking.
- $P_i = 300$, $I_i = 75$ for *dq-axis* current tracking.

For the current tracking loop, the reference of the *d-axis* current is set to $I_{d,ref} = 0$ A (i) to maximise the force-to-current ratio and (ii) to compensate the non-linear terms $\frac{3\pi}{2\tau_p} I_q(I_d(L_d - L_q)$ in Eq. (7.29) and $\frac{3}{2}K_{pm}(L_d - L_q)D_{w2m}I_dI_q$ in Eq. (7.45). As illustrated in Eqs. (7.37), (7.38) and (7.45), the non-linear terms $\frac{L_q}{L_d}K_{pm}\dot{z}I_q$ and $\frac{L_d}{L_q}K_{pm}\dot{z}I_d$ can influence the W2W modelling severely. These non-linear terms can be compensated via *dq-axis* decoupling. The *dq-axis* decoupling method developed by Pena et al. (1996); Schauder and Mehta (1993) is applied in this study to compensate the non-linear terms related to I_d and I_q.

The *dq-axis* TPMLG model in Eqs. (7.26) and (7.27) can be rewritten as their Laplace transform, as:

$$I_d = \frac{-Ud + \omega_e I_q L_q}{R_s + L_d s}, \tag{8.70}$$

$$I_q = \frac{-Uq - \omega_e I_d L_d + \omega_e \phi_{pm}}{R_s + L_d s}. \tag{8.71}$$

Thus the I_d and I_q decoupling can be achieved as illustrated in Fig. 8.17.

8.4.3 Results and discussion

The proposed W2W tracking control strategy is applied on the W2WLM, W2WNLM1, W2WNLM2 and W2WNLM3 under regular and irregular wave conditions.

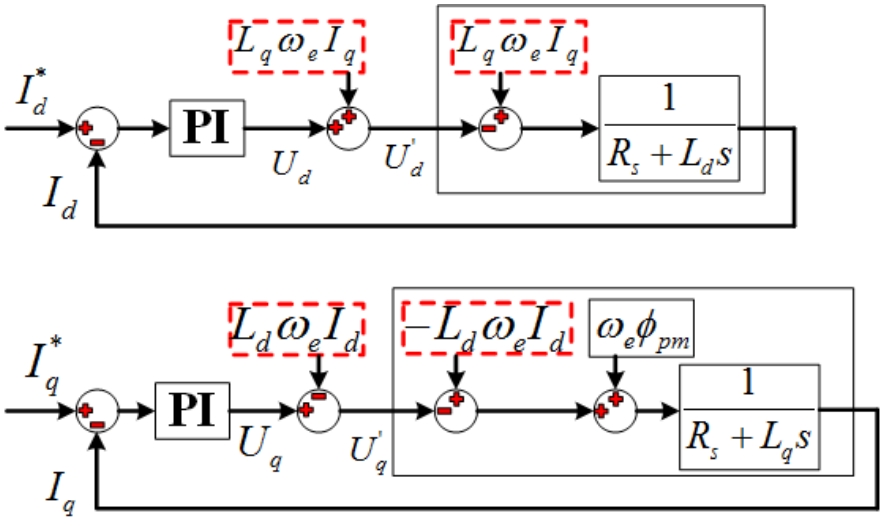

Fig. 8.17 Decoupling of *dq-axis* currents.

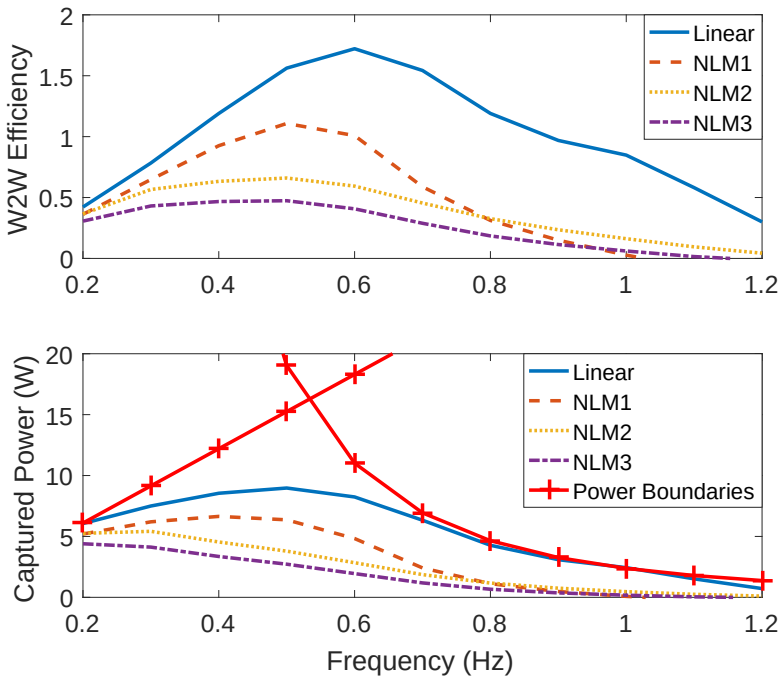

Fig. 8.18 W2W tracking control performance based on linear/non-linear W2W models under regular wave conditions.

Regular wave conditions

The W2W efficiency and captured power of the W2W tracking control strategy are shown in Fig. 8.18. The wave height is $H = 0.05$ m. Fig. 8.18 indicates that:

- The maximum efficiencies are 172%, 111%, 66% and 47% for the W2WLM, W2WNLM1, W2WNLM2 and W2WNLM3, respectively. The conclusion (as before, see Fig. 8.13) is that the linear modelling approach overestimates the captured power.
- Within the low frequency part ($f \leq 0.4$ Hz), the efficiency is low for all modelling methods due to the displacement constraints. Within the frequency range of 0.4-0.8 Hz, the proposed tracking control can achieve a high efficiency. For high frequency waves ($f \geq 0.8$ Hz), the captured power is low since the wave excitation force is small and most energy is dissipated by the friction force.
- Comparing the latching control performance in Fig. 8.13, the proposed W2W tracking control can increase the overall efficiency by 10% within the frequency range of 0.4-0.8 Hz.

Irregular wave conditions

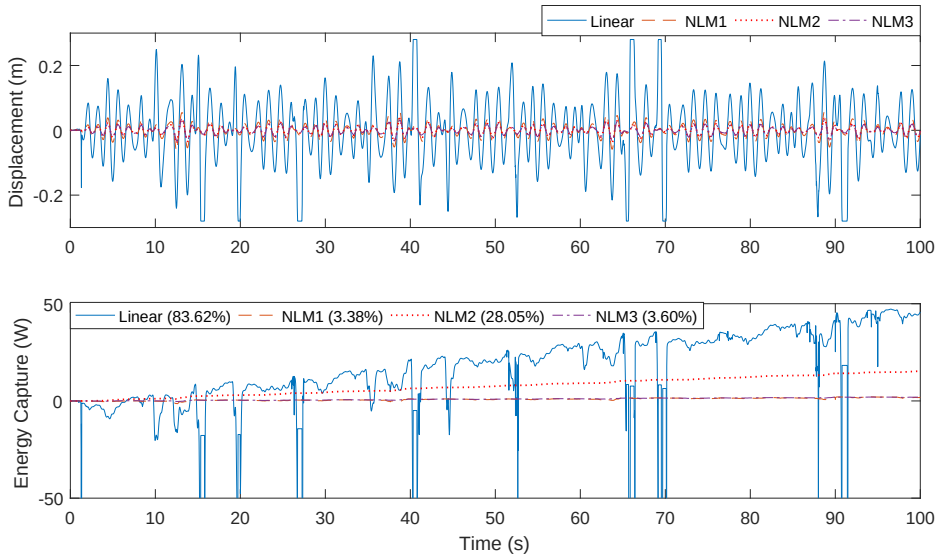

Fig. 8.19 W2W tracking control performance based on linear/non-linear W2W models under irregular wave condition of $H_s = 0.06$ m and $f_p = 0.80$ Hz.

For the irregular wave of $H_s = 0.06$ m and $f_p = 0.80$ Hz, the simulation results of the PAWEC displacement and absorbed energy are given in Fig. 8.19. It is clear that the linear model overestimates the buoy motion as well as the captured power under this wave condition. Since the wave is small and hence the wave excitation force is small. In this situation, the non-linear friction impedes the PAWEC motion and thus the overall efficiencies are low for W2WNLM1 and W2WNLM3. This shows a good correspondence to the power dissipation results of the -3 cm free-decay test in Fig. 4.11.

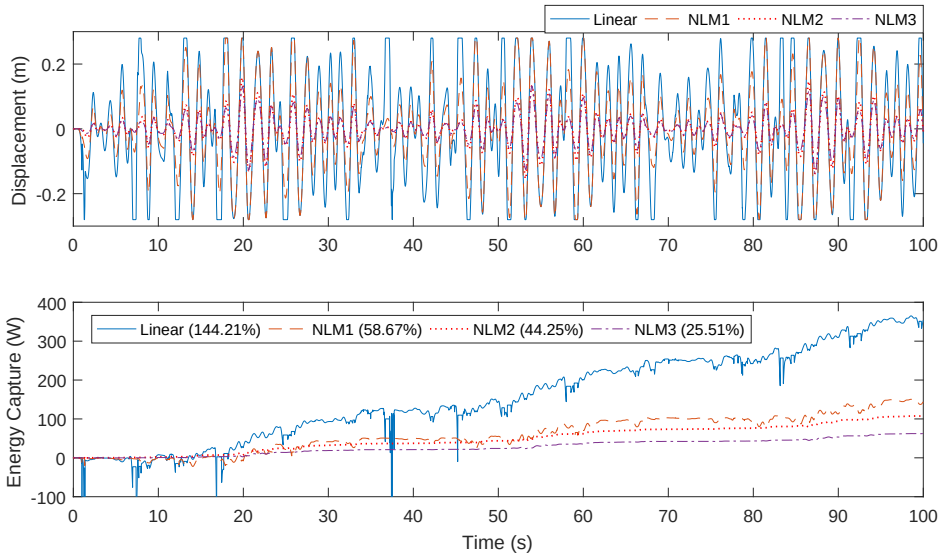

Fig. 8.20 W2W tracking control performance based on linear/non-linear W2W models under irregular wave condition of $H_s = 0.11$ m and $f_p = 0.60$ Hz.

For the irregular wave of $H_s = 0.11$ m and $f_p = 0.60$ Hz, the simulation results of the PAWEC displacement and absorbed energy are given in Fig. 8.20. This wave condition is close to the designed modal spectrum and hence the overall efficiencies are higher, up to 144.21%, 58.67%, 44.25%, 25.51% for the W2WLM, W2WNLM1, W2WNLM2 and W2WNLM3. Under this wave condition, the non-linear friction force together with the non-linear viscous force dissipates most of the energy and hence the overall efficiencies for the non-linear models are low. From the viewpoint of PAWEC displacement, end protection is required for W2WLM rather than the non-linear models.

For the irregular wave of $H_s = 0.25$ m and $f_p = 0.40$ Hz, the simulation results of the PAWEC displacement and captured energy are given in Fig. 8.21. This wave condition is more severe than the design modal spectrum and hence the overall efficiencies cannot reach very high values, around 66.79%, 57.86%, 31.66%, 26.40% for the W2WLM, W2WNLM1, W2WNLM2 and W2WNLM3. Under this wave condition, the non-

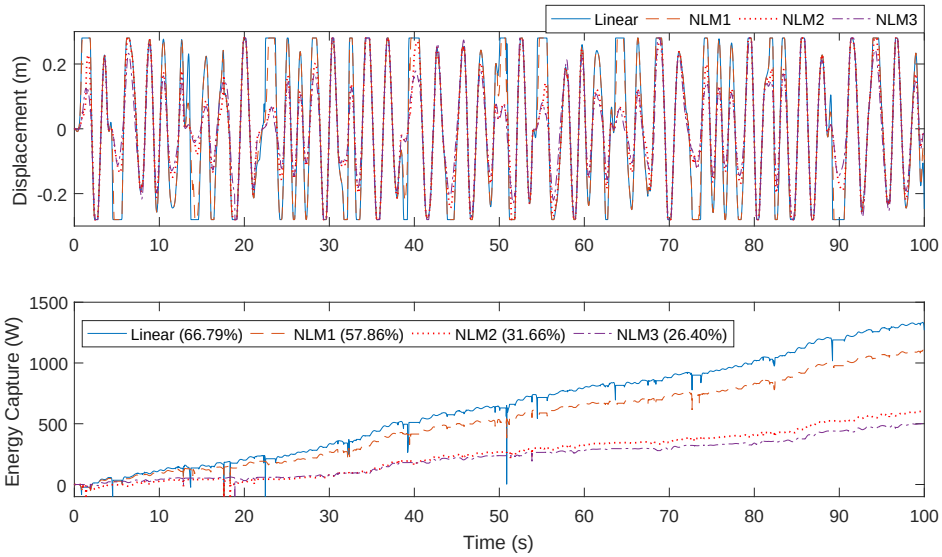

Fig. 8.21 W2W tracking control performance based on linear/non-linear W2W models under irregular wave condition of $H_s = 0.25$ m and $f_p = 0.40$ Hz.

linear viscous force dissipates more energy than the friction force. From the viewpoint of PAWEC displacement, end protection is required for W2WLM and W2WNLM1. However, the simulated displacement responses of W2WNLM2 and W2WNLM3 seldom reach their displacement constraints.

To note that the absorber energy curve for the W2WLM model has huge ripples when the PAWEC displacement hits the constraints. However, if the non-linear viscous and friction forces are considered, the non-linear W2WNLM3 gives very smooth absorbed energy curve.

8.5 Summary and conclusion

8.5.1 Summary

This Chapter discusses power maximisation control strategies based on the $1/50$ PAWEC prototype. The reactive control strategy is outlined in Section 8.2, based on the linear F2M model described in Chapter 3. The implementation approaches of the reactive control are discussed and compared between an ideal MSD mechanical PTO mechanism and an electrical PTO system (the TPMLG simulated in Chapter 7). The

electrical reactive control shows almost the same performance as the ideal mechanical PTO system and is more feasible to implement via power electronics.

Section 8.3 evaluates the phase control by latching based on the linear and non-linear F2M models in Chapter 4. For all the linear and non-linear F2M models, phase control by latching can improve the overall efficiency and can handle the displacement constraints with appropriate TPMLG resistive loads. Through a comparison between the linear and non-linear models, it is concluded that the linear model always over-predicts the PAWEC motion and power productivity. The non-linear models that account for friction and viscous forces give more accurate predictions of PAWEC motion and power capture width.

Based on linear and non-linear W2W models, a three-level tracking control strategy is proposed and evaluated in Section 8.4. Compared with the reactive control and latching control strategies, the proposed tracking control can give a slightly higher overall efficiency for harmonic waves and more flexibility in dealing with displacement constraints. Also, this tracking control structure can be extended to include operation under irregular wave conditions and is certainly implementable with suitable power electronics.

8.5.2 Conclusion

The main conclusions of this Chapter are:

- Conventional power maximisation control methods of WEC devices, including reactive control and phase/amplitude control, have special focus on MSD PTO mechanism. Few publications discussed the control implementation with electrical machines. This Chapter illustrated that the electrical implementation can achieve the same performance as the mechanical implementation and can provide more flexibility.

- The electro-mechanical relationship is derived and illustrated in Fig. 8.7. The precondition is that the *d-axis* current is controlled around zero. Under this condition, the electrical implementation can achieve power maximisation control with physical constraints. However, the power electronics to achieve bi-direction power flow are expensive.

- The comparison study of control performance between the linear and non-linear W2W models illustrates that the linear model overestimate the power production and the non-linear effects have a large influence on the controlled power output and the PAWEC dynamics. When resonance is achieved by control, the linear W2W model always exaggerates the PAWEC motion and converted power. Meanwhile, the non-linear modelling approach considering both the viscous and friction forces can provide more practical prediction of the PAWEC dynamics and power productivity. This conclusion is consistent with the numerical/experimental data illustrated in Chapters 4 and 5.

Chapter 9

Conclusion and future work

9.1 Summary

This Section summarises the work achieved in previous chapters. Chapter 1 starts with the global utilisation of wave energy and current technical challenges. The aim, objectives and structure of this thesis are given in Chapter 1. Chapter 2 gives a brief literature review of WEC systems, modelling approaches and control strategies with special focus on the PA type devices.

Chapter 3 details some fundamentals of wave properties, wave-WEC interaction and linear modelling approaches of the 1/50 PAWEC. Based on the assumptions of ideal fluid, linear wave theory and small body motion, a linear F2M model with frequency-determined parameters is obtained via BEM simulation (NEMOH). This linear model is the starting point to derive the power maximisation conditions.

Chapter 4 focuses on the non-linear F2M modelling of the $1/50$ scale PAWEC with a special focus on the non-linear viscous and friction effects. Based on the BEM results in Chapter 3, a 5^{th} state-space model with constant coefficients is studied with the convolution term of the radiation force approximated by a third order system via time- and frequency-domain system identification methods. To gain more accurate model, the fluid viscous force is modelled as the drag term in the Morison equation and the mechanical friction is modelled as the Tustin model. Hence, a non-linear F2M model representing the wave-PAWEC interaction is derived and verified by free-decay tests. The numerical data of the derived non-linear F2M model shows a very high agreement

with the experimental data in terms of power dissipation and displacement response. The errors are within 5% for a wide range of free-decay tests.

Chapter 5 only deals with the wave excitation force estimation. Three methods are investigated numerically and experimentally, including the W2EF, PAD2EF and UIOEF approaches. The W2EF method is verified by excitation tests and the other two are verified by forced-motion tests under regular and irregular wave conditions. Thus the application scenarios, advantages and disadvantages of the W2EF, PAD2EF and UIOEF are discussed via the comparison between the numerical and experimental results. Further more, the W2EF model is combined with the linear and non-linear F2M models (developed in Chapter 4) to form linear and non-linear W2M models. Both the numerical and experimental data show that the linear modelling approaches usually exaggerate the PAWEC motion and that the non-linear F2M and W2M models can give more accurate PAWEC dynamic prediction which is close to the experimental data.

Chapter 6 deals with the 1/50 PAWEC system design and procedures of wave tank tests. The PAWEC mechanical and electrical designs are given with details of the hardware and software designs. The procedures to conduct the free-fall, free-decay, forced-motion and excitation tests are also described. The experimental data are used to verify the non-linear force and F2M models in Section 4.3, excitation force estimation approaches in Sections 5.3, 5.4 and 5.5, non-linear W2M model in Section 5.6. These verified models are combined with the TPMLG model obtained in Chapter 7 to form F2W or W2W models as control plants in Chapter 8.

Chapter 7 details the design, simulation, optimisation and modelling of a TPMLG as the PTO mechanism for the 1/50 PAWEC. Initial geometric design of the TPMLG is derived half-analytically and half-empirically based on the 1/50 scale PAWEC and wave conditions of wave tank tests. A TPMLG is subject to the cogging force severely and thus parametric analysis and design optimisation are applied in the FEM software MAXWELL™. The design optimisation can reduce the cogging force from $F_{cog,vpp} =$ 19 N to $F_{cog,vpp} = 1.5$ N. Based on the WAXWELL™ simulation results, a *dq-axis* model is derived to represent the TPMLG electro-mechanical properties. To combine the TPMLG model with the non-linear W2M model proposed in Section 5.6, a non-linear W2W model is derived in Section 7.6 for control system design in Chapter 8.

Chapter 8 discusses power maximisation control strategies applied on the 1/50 scale PAWEC and their implementation approaches based on the TPMLG simulated in Chapter 7. The reactive control principle is outlined based on harmonic wave assumption

and simulated based on the linear F2W model in Section 8.2. Phase control by latching is investigated and implemented based on linear and non-linear F2W models in Section 8.3. The non-linear model considering with the viscous and friction forces can give more accurate displacement response and overall energy conversion efficiency. A W2W tracking control structure is proposed in Section 8.4 which includes displacement reference generation system and a three-level tracking control system. The outer control loop deals with the displacement tracking to handle the displacement constraints and then the second control loop forces the PAWEC velocity to keep in phase with the excitation force. The inner loop deals with the *dq-axis* currents regulation and can be implemented via power electronics.

9.2 Contribution

Based on the achievements mentioned above, the main contributions are:

- **Modelling and Verification of Non-linear F2M model:** A non-linear F2M model is proposed, simulated and verified considering the non-linear viscous and friction forces. The viscous force is modelled as the drag term in the Morison equation and the friction force is simulated as the Tustin model with the parameters identified via free-fall and free-decay tests. A wide range of free-decay tests are conducted to verify the proposed non-linear F2M model. The numerical results show a high correspondence to the experimental data in terms of both the displacement responses and the energy dissipations. This part of work is detailed in Chapter 4.

- **Modelling and Verification of Excitation Force Estimation Approaches:** Three excitation force estimation approaches are proposed in this study, including the W2EF, PAD2EF and UIOEF approaches. A wide variety of excitation tests are conducted to verify the W2EF method under regular and irregular wave conditions. Comparison study between these three approaches are investigated numerically and experimentally (forced-motion tests) to conclude the application scenarios, advantages and disadvantages of the W2EF, PAD2EF and UIOEF approaches. Further more, a non-linear W2M model is proposed, simulated and verified via forced-motion tank tests. This part of work is described in Chapter 5.

- **W2W Tracking Control Strategy:** A W2W trancking control strategy is proposed and simulated based on linear and non-linear W2W models. The W2W models are derived as a combination of the W2EF, F2M and TPMLG models. The tracking control structure includes three-level tracking controllers with (i) the outer control loop dealing with position reference tracking to handle displacement constraints, (ii) the second level control loop achieving velocity reference tracking for power maximisation and (iii) the inner control loop regulating the *dq-axis* currents for electrical implementation. The simulation results indicate the feasibility and utility of the W2W control strategy.

9.3 Conclusion

The main conclusions of this study are:

- Both the numerical and experimental results indicate that non-linear viscous and friction effects have significant influence on the PAWEC dynamics and non-linear modelling approach considering both the non-linearities can provide more precise dynamic modelling and prediction of the PAWEC. For the free-decay tests (F2M modelling), the friction force dominates the PAWEC displacement response when the PAWEC velocity is small. Whilst, the viscous force dominates the PAWEC dynamics when the velocity is larger. In terms of energy dissipation, the non-linear friction and viscous forces dissipated more energy than the radiation force and hence it is concluded that these non-linearities should be considered in the PAWEC power maximisation control. Otherwise the power capture width will be overestimated.

  For the forced-motion tests (W2M modelling), linear modelling approaches exaggerate the RAO up to five times within the resonance frequency arrange. The overestimation of the PAWEC motion therefore exaggerates the power productivity and loses modelling fidelity. Meanwhile, the non-linear modelling approach considering both the friction and viscous effects provides a RAO response almost the same as the experimental results. Time-domain displacement responses under regular/irregular wave conditions also illustrate that the non-linear modelling approach can provide much more accurate PAWEC dynamics than the linear one.

- The wave excitation force can be identified from the wave elevation, approximated from a appropriately designed sensing system or/and estimated via an properly

designed OUI. The wave excitation force modelling approaches can be used to achieve W2M/W2W modelling and to generate external reference signal for some advanced control strategies, such as the MPC. Although the wave excitation force cannot be measured directly for an oscillating WEC device, it can be approximated/estimated by the W2EF, PAD2EF and UIOEF methods proposed and verified in this work. Numerical and experimental comparative studies among these three methods indicate that the UOIEF method has great potential to provide external reference for real-time control implementation since this method is easy and flexible. The PAD2EF approach may be more practical than the W2EF method as the wave elevation measurement is difficult to obtain in off-shore environment. However, the W2EF method can provide more accurate approximation of the wave excitation force under moderate sea states than the other two.

- Non-linear friction and viscous forces can critically influence the performance of PAWEC power maximisation control strategies. When the control or PTO force is coupled, the PAWEC operates close to the resonance and hence the PAWEC displacement and velocity are large. In this situation the end protect is required to prevent the PAWEC hitting its displacement constraints. At the same time, the relative velocity between the PAWEC and the water particles are large and hence the viscous force becomes large and cannot be ignored any more. That is, hydrodynamic non-linearities will be magnified by a well designed controller and this hydrodynamic-control coupling problem should be taken into account. According to the numerical results in Chapter 8, linear modelling approaches have a strict requirement of end protection by the control systems and always over-predict the energy conversion efficiency due to the failure in the modelling of non-linear hydrodynamics. For the non-linear W2W model considering the friction and viscous forces, the displacement constraints can be easily handled by the control system since the non-linear effects dissipate most of the energy. The overall energy conversion efficiency is more practical and close to the theoretical value, although it is much smaller than the linear W2W modelling situation.

9.4 Future work

Based on the wave tank tests experiences and PAWEC modelling and simulation studies, some work is planned for the future. The main topics are:

- **PAWEC Co-design:** According to wave tank test results and numerical control performance, it is important to consider the PAWEC co-design to improve the PAWEC performance, overall energy conversion efficiency and survivability. One evidence is that the maximum overall efficiency can be realised at wave frequency $f = 0.55$ Hz via latching control or W2W tracking control applied on the non-linear W2W model, whilst the PAWEC is designed according to the modal frequency $f_m = 0.67$ Hz. Thus control effect on the PAWEC hydrodynamics should be taken into account at the very beginning of the PAWEC system design. Another experience gained from the wave tank tests is that the viscous force has significant influence on the wave-PAWEC interaction and dissipates lots of energy. The viscosity will become more significant when resonance is achieved by optimal control strategies.

  On one hand, control performance depends on the PAWEC hydrodynamics which are specified by the geometric design. On the other hand, geometric design/optimisation is sensitive to the applied control strategy. Hence, the PAWEC co-design must consider both the geometric optimisation and control system design synchronously. Some preliminary work has been by Davidson et al. (2017); Garcia-Rosa and Ringwood (2016); Giorgi and Ringwood (2016) to investigate the hydrodynamic-control coupling problem for the co-design concept. The work by Garcia-Rosa et al. (2015) also indicates that physical constraints, such as the constraints of displacement and PTO force, can critically affect the geometric optimisation and control performance. Summing up the co-design concept requires a compromise among the geometric optimisation, control system design, physical constraints, components cost and availability and is very difficult to converge to a specific design procedure.

- **Advanced Control Strategies:** Chapter 8 discusses the classic reactive control and phase control by latching and their implementations on the 1/50 PAWEC. Further a W2W tracking control is proposed and simulated to handle displacement constraints and to achieve power maximisation. However, only PI controllers are applied to achieve the position, velocity and *dq-axis* current tracking and advanced control strategies are required to improve the control performance. Some advanced control methods, such as MPC, the pseudo-spectrum control, show great potential to maximise the converted power based on the proposed W2W models. Since the excitation force can be obtained to via the W2EF method, MPC can ideally handle the power maximisation problem under physical constraints (both the displacement and PTO force constraints). However, as

addressed in this study non-linear friction and viscous forces critically affect the PAWEC dynamics and control performance, it is necessary to develop a non-linear MPC to involving these non-linearities. The non-linear MPC is expensive in computation and its real-time implementation will be a challenging problem.

Additionally, the reference generation is critically important to achieve bi-direction power flow. Inappropriate reference may force the TPMLG work as a motor only rather than partly as a generator and partly as a motor. Meanwhile this bi-direction power flow may lead to high power rating due to the reactive power is commissary to achieve optimal control. However, the reactive power can be alleviated by proper co-design to configure the PAWEC natural frequency close to the prevailing wave frequency. Passive control methods can avoid this bi-direction power flow but cannot achieve optimal control. The implementation of passive control methods will be easy and cost saving. Conversely, active control approaches can achieve WEC power maximisation under a wide range of sea states (Abraham and Kerrigan, 2013) but is expensive to implement due to the bi-direction power flow and high power overrating call for pricey back-to-back power converters (Ekström et al., 2015).

- **W2W Model Verification:** As described in Chapters 4, 5 and 6, only the wave-PAWEC dynamics are verified via tank tests. The TPMLG model and W2W tracking control are studied numerically. Verification of the W2W model and experimental evaluation of the proposed control strategy are required.

References

Abdelkhalik, O., Zou, S., Bacelli, G., Robinett, R. D., Wilson, D. G., and Coe, R. G. (2016). Estimation of excitation force on wave energy converters using pressure measurements for feedback control. In *OCEANS 2016 MTS/IEEE Monterey*, pages 1–6. IEEE.

Abdelrahman, M., Patton, R., Guo, B., and Lan, J. (2016). Estimation of wave excitation force for wave energy converters. In *2016 3rd Conference on Control and Fault-Tolerant Systems (SysTol)*, pages 654–659. IEEE.

Abraham, E. and Kerrigan, E. C. (2013). Optimal active control and optimization of a wave energy converter. *IEEE Transactions on Sustainable Energy*, 4(2):324–332.

Agamloh, E. B., Wallace, A. K., and Von Jouanne, A. (2008). Application of fluid–structure interaction simulation of an ocean wave energy extraction device. *Renewable Energy*, 33(4):748–757.

Airy, G. B. (1845). Tides and waves. *Encyclopedia Metropolitan*, 5:241–396.

Alcorn, R. and O'Sullivan, D. (2013). *Electrical design for ocean wave and tidal energy systems*, volume 17. IET.

AnalogDevices (2009). *Small, Low Power, 3-axis +/-2g Accelerometer ADXL327*. Analog Devices Ltd, One Technology Way, P.O. Box 9106, Norwood, MA 02062-9160, U.S.A., 0 edition. Revision 0: Initial Version.

Armstrong, B. (1988). Friction: Experimental determination, modeling and compensation. In *Robotics and Automation, 1988. Proceedings., 1988 IEEE International Conference on*, pages 1422–1427. IEEE.

Armstrong-Hélouvry, B., Dupont, P., and De Wit, C. C. (1994). A survey of models, analysis tools and compensation methods for the control of machines with friction. *Automatica*, 30(7):1083–1138.

Babarit, A. and Clément, A. H. (2006). Optimal latching control of a wave energy device in regular and irregular waves. *Applied Ocean Research*, 28(2):77–91.

Babarit, A. and Delhommeau, G. (2015). Theoretical and numerical aspects of the open source bem solver nemoh. In *11th European Wave and Tidal Energy Conference (EWTEC2015)*, pages 1–12.

Babarit, A., Duclos, G., and Clément, A. H. (2004). Comparison of latching control strategies for a heaving wave energy device in random sea. *Applied Ocean Research*, 26(5):227–238.

Babarit, A., Guglielmi, M., and Clément, A. H. (2009). Declutching control of a wave energy converter. *Ocean Eng.*, 36(12):1015–1024.

Babarit, A., Hals, J., Muliawan, M., Kurniawan, A., Moan, T., and Krokstad, J. (2012). Numerical benchmarking study of a selection of wave energy converters. *Renew. Energy*, 41:44–63.

Bacelli, G., Gilloteaux, J.-C., and Ringwood, J. (2009). A predictive controller for a heaving buoy producing potable water. In *European Control Conference (ECC)*, pages 3755–3760. IEEE.

Baghaei, A. (2010). The technology and the maui wave energy project. Available from http://www.ct-si.org/events/APCE/sld/pdf/32.pdf (accessed on 29 July 2016).

Bailey, H., Ortiz, J. P., Robertson, B., Buckham, B. J., Nicoll, and S, R. (2014). A methodology for wave-to-wire wec simulations. In *Marine Energy Technology Symposium*, pages 1–15. METS.

Bard, J. and Kracht, P. (2013). Linear generator systems for wave energy converters. Technical Report D3.2, Department of Civil Engineering, Aalborg University.

Beirao, P., Mendes, M., Valério, D., and Da Costa, J. S. (2007). Control of the archimedes wave swing using neural networks. In *Proc. 7th European Wave Tidal Energy Conf*, pages 1–10.

Beirdol, P., Valério, D., and Da Costa, J. S. (2007). Linear model identification of the archimedes wave swing. In *2007 International Conference on Power Engineering, Energy and Electrical Drives*, pages 660–665. IEEE.

Beresford, P. J. (2003). *HR Wavemaker Wave Generation Control Program User Mannual*. HR Wallingford Ltd, Howvery Park, Wallingford, Oxfordshire, OX10 8BA, U.K., 5 edition. Report IT 453.

Bhinder, M. A., Babarit, A., Gentaz, L., and Ferrant, P. (2015). Potential time domain model with viscous correction and cfd analysis of a generic surging floating wave energy converter. *International Journal of Marine Energy*, 10:70–96.

Boake, C. B., Whittaker, T. J., Folley, M., and Ellen, H. (2002). Overview and initial operational experience of the limpet wave energy plant. In *The Twelfth International Offshore and Polar Engineering Conference*, pages 1–9. International Society of Offshore and Polar Engineers.

Boccotti, P. (2000). *Wave mechanics for ocean engineering*, volume 64. Elsevier.

Boström, C., Lejerskog, E., Stålberg, M., Thorburn, K., and Leijon, M. (2009). Experimental results of rectification and filtration from an offshore wave energy system. *Renewable Energy*, 34(5):1381–1387.

Brekken, T. K. (2011). On model predictive control for a point absorber wave energy converter. In *PowerTech, 2011 IEEE Trondheim*, pages 1–8. IEEE.

Bricker, J. D., Esteban, M., Takagi, H., and Roeber, V. (2017). Economic feasibility of tidal stream and wave power in post-fukushima japan. *Renewable Energy*, 114:32–45.

Brito-Melo, A., Neuman, F., and Sarmento, A. (2008). Full-scale data assessment in owc pico plant. *International Journal of Offshore and Polar Engineering*, 18(01):27–34.

Budal, K. and Falnes, J. (1975a). Power generation from ocean waves using a resonant oscillating system. *Marine Science Communication*, 1:269–288.

Budal, K. and Falnes, J. (1975b). A resonant point absorber of ocean-wave power. *Nature*, 256:478.

Budal, K. and Falnes, J. (1977). Optimum operation of improved wave-power converter. *Mar. Sci. Commun.;(United States)*, 3(2).

Budal, K., Falnes, J., Hals, T., Iversen, L., and Onshus, T. (1981). Model experiment with a phase controlled point absorber. In *Proceedings of Second International Symposium on Wave and Tidal Energy*, pages 191–206.

Cameron, L., Doherty, R., Henry, A., Doherty, K., Van't Hoff, J., Kaye, D., Naylor, D., Bourdier, S., and Whittaker, T. (2010). Design of the next generation of the oyster wave energy converter. In *3rd international conference on ocean energy*, volume 6, pages 1–12.

Carbon-Trust (2011). The potential for cost reduction—insights from the carbon trust marine energy accelerator. Technical Report CTC797, Carbon Trust, London, UK.

Cheema, M., Fletcher, J., Rahman, M., and Xiao, D. (2012). Modified direct thrust control of linear permanent magnet motors with sensorless speed estimation. In *IECON 2012-38th Annual Conference on IEEE Industrial Electronics Society*, pages 1908–1914. IEEE.

Cheema, M. and Fletcher, J. E. (2013). Sensorless vector control of linear permanent magnet synchronous motor. In *ECCE Asia Downunder (ECCE Asia), 2013 IEEE*, pages 1098–1104. IEEE.

Chiba, S., Waki, M., Masuda, K., and Ikoma, T. (2010). Current status and future prospects of electric generators using electroactive polymer artificial muscle. In *OCEANS 2010 IEEE-Sydney*, pages 1–5. IEEE.

Clément, A. and Babarit, A. (2012). Discrete control of resonant wave energy devices. *Phil. Trans. R. Soc. A*, 370(1959):288–314.

Clément, A., McCullen, P., Falcão, A., Fiorentino, A., Gardner, F., Hammarlund, K., Lemonis, G., Lewis, T., Nielsen, K., and Petroncini, S. (2002). Wave energy in europe: current status and perspectives. *Renew. Sust. Energ. Rev.*, 6(5):405–431.

COER (2017). Centre for ocean energy research. Available from http://www.eeng.nuim.ie/coer/ (accessed on 24 May 2017).

Colli, V. D., Cancelliere, P., Marignetti, F., Stefano, R. D., and Scarano, M. (2006). A tubular-generator drive for wave energy conversion. *IEEE Trans. Ind. Electron.*, 53(4):1152–1159.

Colli, V. D., Di Stefano, R., and Scarano, M. (2005). A tubular generator for marine energy direct drive applications. In *Electric Machines and Drives, 2005 IEEE International Conference on*, pages 1473–1478. IEEE.

CorpowerOcean (2017). Wavespring technology. Available from http://www.corpowerocean.com/corpower-technology/wave-spring-technology/ (accessed on 29 May 2017).

Costello, R., Ringwood, J., and Weber, J. (2011). Comparison of two alternative hydraulic pto concepts for wave energy conversion. In *Proceedings of the 9th European wave and tidal energy conference (EWTEC)*, pages 1–10.

Cretel, J. A., Lightbody, G., Thomas, G. P., and Lewis, A. W. (2011). Maximisation of energy capture by a wave-energy point absorber using model predictive control. *IFAC Proceedings Volumes*, 44(1):3714–3721.

Cruz, J. (2007). *Ocean wave energy: current status and future prespectives*. Springer Science & Business Media.

Cummins, W. (1962). The impulse response function and ship motions. Technical report, DTIC Document.

Da Costa, J. S., Beirao, P., and Valério, D. (2007). Internal model control applied to the archimedes wave swing. In *International Conference on Control Systems and Computer Science*, pages 1–10.

Davidson, J., Genest, R., and Ringwood, J. (2017). Adaptive control of a wave energy converter simulated in a numerical wave tank. In *12th European wave and tidal energy conference, Cork*, pages 1–10.

Davidson, J., Giorgi, S., and Ringwood, J. V. (2015). Linear parametric hydrodynamic models for ocean wave energy converters identified from numerical wave tank experiments. *Ocean Engineering*, 103:31–39.

Davidson, J., Giorgi, S., and Ringwood, J. V. (2016). Identification of wave energy device models from numerical wave tank data—part 1: Numerical wave tank identification tests. *IEEE Transactions on Sustainable Energy*, 7(3):1012–1019.

De Koker, K., Crevecoeur, G., Meersman, B., Vantorre, M., and Vandevelde, L. (2016a). A power take-off and control strategy in a test wave energy converter for a moderate wave climate. In *International Conference on Renewable Energies and Power Quality (ICREPQ'16)*, pages 1–6. European Association for the Development of Renewable Energies, Environment and Power Quality (EA4EPQ).

De Koker, K. L., Crevecoeur, G., Meersman, B., Vantorre, M., and Vandevelde, L. (2016b). Energy storage system for off-grid testing of a wave energy converter. In *Energy Conference (ENERGYCON), 2016 IEEE International*, pages 1–5. IEEE.

De la Villa Jan, A. and Santana, A. G. (2016). Improvements in the reactive control and latching control strategies under maximum excursion constraints using short-time forecast. *IEEE Transactions on Sustainable Energy*, 7(1):427–435.

De Sousa Prado, M. G., Gardner, F., Damen, M., and Polinder, H. (2006). Modelling and test results of the archimedes wave swing. *Proceedings of the Institution of Mechanical Engineers, Part A: Journal of Power and Energy*, 220(8):855–868.

DECC (2013). Electricity generation costs 2013. Technical report, Technical Report for Department of Energy & Climate Change.

DelliColli, V., Cancelliere, P., Marignetti, F., DiStefano, R., and Scarano, M. (2006). A tubular-generator drive for wave energy conversion. *IEEE Transactions on Industrial Electronics*, 53(4):1152–1159.

Drew, B., Plummer, A., and Sahinkaya, M. N. (2009). A review of wave energy converter technology. *Proceedings of the Institution of Mechanical Engineers, Part A: Journal of Power and Energy*, 223(8):887–902.

Durand, M., Babarit, A., Pettinotti, B., Quillard, O., Toularastel, J., and Clément, A. (2007). Experimental validation of the performances of the searev wave energy converter with real time latching control. In *Proceedings of the 7th European Wave and Tidal Energy Conference (EWTEC), Porto, Portugal*, volume 1113, pages 1–8.

Edwards, K. and Mekhiche, M. (2013). Ocean testing of a wave-capturing powerbuoy. In *Marine Energy Technology Symposium, Washington, DC*.

Eidsmoen, H. (1995). Hydrodynamic parameters for a two-body axisymmetric system. *Applied Ocean Research*, 17(2):103–115.

Eidsmoen, H. (1996). Simulation of a slack-moored heaving-buoy wave-energy converter with phase control. Technical report, Division of Physics, NTNU, Trondheim, Norway.

Ekström, R., Ekergård, B., and Leijon, M. (2015). Electrical damping of linear generators for wave energy converters—a review. *Renewable and Sustainable Energy Reviews*, 42:116–128.

EMEC (2016). The european marine energy centre. Available from http://www.emec.org.uk/ (accessed on 4 August 2016).

EPSRC (2015). Supergen marine challenge 3 - research on marine energy development. Available from https://www.epsrc.ac.uk/funding/calls/supergenmarinechallenge3/ (accessed on 4 August 2016).

Eriksson, M. (2007). *Modelling and experimental verification of direct drive wave energy conversion: Buoy-generator dynamics*. PhD thesis, Acta Universitatis Upsaliensis.

Evans, D. (1976). A theory for wave-power absorption by oscillating bodies. *J. Fluid Mech*, 77(1):1–25.

Evans, D. (1981). Power from water waves. *Annual review of Fluid mechanics*, 13(1):157–187.

Evans, D. and de O Falcao, A. (1985). Hydrodynamics of ocean wave-energy utilization. Technical report, Springer-Verlag New York, Inc., New York, NY.

FaBTest (2016). Fabtest - a nursery site for marine renewable energy devices. Available from http://www.fabtest.com/ (accessed on 4 August 2016).

Faedo, N., Olaya, S., and Ringwood, J. V. (2017). Optimal control, mpc and mpc-like algorithms for wave energy systems: An overview. *IFAC Journal of Systems and Control*, 1:37–56.

Faiz, J., Ebrahimi-Salari, M., and Shahgholian, G. (2010). Reduction of cogging force in linear permanent-magnet generators. *IEEE Transactions on Magnetics*, 46(1):135–140.

Faiz, J., Manoochehry, M., and Shahgholian, G. (2011). Performance improvement of permanent magnet linear synchronous motor drive using space vector modulated-direct thrust force control. *Electrical Review*, 87:239–244.

Falcão, A. F. d. O. (2008). Phase control through load control of oscillating-body wave energy converters with hydraulic pto system. *Ocean Engineering*, 35(3):358–366.

Falcão, A. F. d. O. (2010). Wave energy utilization: A review of the technologies. *Renew. Sustainable Energy Rev.*, 14(3):899–918.

Falnes, J. (1995). On non-causal impulse response functions related to propagating water waves. *Appl. Ocean Res.*, 17(6):379–389.

Falnes, J. (2002). *Ocean waves and oscillating systems: linear interactions including wave-energy extraction*. Cambridge university press.

Falnes, J. (2007). A review of wave-energy extraction. *Marine Structures*, 20(4):185–201.

Falnes, J. and Budal, K. (1978). Wave-power conversion by point absorbers. *Norwegian Maritime Research*, 6(4):2–11.

Falnes, J. and Hals, J. (2012). Heaving buoys, point absorbers and arrays. *Philosophical Transactions of the Royal Society of London A: Mathematical, Physical and Engineering Sciences*, 370(1959):246–277.

Ferri, F. (2014). *Wave-to-wire modelling of wave energy converters: Critical assessment, developments and applicability for economical optimisation*. PhD thesis, Department of Civil Engineering, Aalborg University.

Fischer, B., Kracht, P., and Perez-Becker, S. (2012). Online-algorithm using adaptive filters for short-term wave prediction and its implementation. In *Proceedings of the 4th International Conference on Ocean Energy (ICOE)*, volume 1719, pages 1–6.

Folley, M. (2016). *Numerical Modelling of Wave Energy Converters: State-of-the-Art Techniques for Single Devices and Arrays*. Academic Press.

Folley, M. and Whittaker, T. (2010). Spectral modelling of wave energy converters. *Coast. Eng.*, 57(10):892–897.

Forehand, D. I., Kiprakis, A. E., Nambiar, A. J., and Wallace, A. R. (2016). A fully coupled wave-to-wire model of an array of wave energy converters. *IEEE Transactions on Sustainable Energy*, 7(1):118–128.

French, M. (1979). A generalized view of resonant energy transfer. *Journal of Mechanical Engineering Science*, 21(4):299–300.

Fu, X. and Lecchini-Visintini, A. (2016). Optimisation of restricted complexity control for wave energy conversion. In *Control (CONTROL), 2016 UKACC 11th International Conference on*, pages 1–5. IEEE.

Fusco, F. and Ringwood, J. (2011a). A model for the sensitivity of non-causal control of wave energy converters to wave excitation force prediction errors. In *Proceedings of the 9th European Wave and Tidal Energy Conference (EWTEC)*, pages 1–10.

Fusco, F. and Ringwood, J. (2011b). Quantification of the prediction requirements in reactive control of wave energy converters. *IFAC Proceedings Volumes*, 44(1):11483–11488.

Fusco, F. and Ringwood, J. (2011c). Suboptimal causal reactive control of wave energy converters using a second order system model. In *Proceedings of the 21st (2011) International Offshore and Polar Engineering Conference*, pages 687–694. International Society of Offshore and Polar Engineers (ISOPE).

Fusco, F. and Ringwood, J. V. (2010). Short-term wave forecasting for real-time control of wave energy converters. *IEEE Trans. Sustain. Energy*, 1(2):99–106.

Fusco, F. and Ringwood, J. V. (2014). Hierarchical robust control of oscillating wave energy converters with uncertain dynamics. *IEEE Transactions on Sustainable Energy*, 5(3):958–966.

Gao, Z. and Moan, T. (2009). Mooring system analysis of multiple wave energy converters in a farm configuration. In *8th European Wave and Tidal Energy Conference (EWTEC), Uppsala, Sweden*, pages 509–518.

Garcia-Rosa, P. B., Bacelli, G., and Ringwood, J. V. (2015). Control-informed geometric optimization of wave energy converters: The impact of device motion and force constraints. *Energies*, 8(12):13672–13687.

Garcia-Rosa, P. B. and Ringwood, J. V. (2016). On the sensitivity of optimal wave energy device geometry to the energy maximizing control system. *IEEE Transactions on Sustainable Energy*, 7(1):419–426.

Garcia-Rosa, P. B., Vilela Soares Cunha, J. P., Lizarralde, F., Estefen, S. F., Machado, I. R., and Watanabe, E. H. (2014). Wave-to-wire model and energy storage analysis of an ocean wave energy hyperbaric converter. *IEEE J. Ocean Eng.*, 39(2):386–397.

Ge, M. and Kerrigan, E. C. (2016). Short-term ocean wave forecasting using an autoregressive moving average model. In *2016 UKACC 11th International Conference on Control (CONTROL)*, pages 1–6. IEEE.

GemsSensors (2015). *3300 Series Compact Low Pressure OEM Pressure Transmitters*. Gems Sensors & Controls, Lennox Road, Basingstokes, Hampshire, RG22 4AW, England, 1 edition. General Note.

Genest, R., Bonnefoy, F., Clément, A. H., and Babarit, A. (2014). Effect of non-ideal power take-off on the energy absorption of a reactively controlled one degree of freedom wave energy converter. *Applied Ocean Research*, 48:236–243.

Genest, R. and Ringwood, J. (2016a). Receding horizon pseudospectral optimal control for wave energy conversion. In *Control (CONTROL), 2016 UKACC 11th International Conference on*, pages 1–6. IEEE.

Genest, R. and Ringwood, J. V. (2016b). A critical comparison of model-predictive and pseudospectral control for wave energy devices. *Journal of Ocean Engineering and Marine Energy*, pages 1–15.

Gieske, P. (2007). Model predictive control of a wave energy converter: Archimedes wave swing. Master's thesis, Delft University of Technology, Delft, The Netherlands.

Giorgi, G. and Ringwood, J. V. (2016). Implementation of latching control in a numerical wave tank with regular waves. *Journal of Ocean Engineering and Marine Energy*, 2(2):211–226.

Giorgi, S., Davidson, J., and Ringwood, J. (2015). Identification of nonlinear excitation force kernels using numerical wave tank experiments. In *Proceedings of the 11th European Wave and Tidal Energy Conference*, pages 09C1–1–1–09C1–1–10.

Giorgi, S., Davidson, J., and Ringwood, J. V. (2016). Identification of wave energy device models from numerical wave tank data—part 2: Data-based model determination. *IEEE Transactions on Sustainable Energy*, 7(3):1020–1027.

Girard, P. (1799). Pour divers moyens d'employer les vagues de la mer, comme moteurs. *French Patent, July*, 12:1799.

Goggins, J. and Finnegan, W. (2014). Shape optimisation of floating wave energy converters for a specified wave energy spectrum. *Renewable Energy*, 71:208–220.

Greenhow, M. and White, S. (1997). Optimal heave motion of some axisymmetric wave energy devices in sinusoidal waves. *Appl. Ocean Res.*, 19(3-4):141–159.

Griffiths, D. J. (1999). *Introduction to Electrodynamics*. Prentice-Hall.

Gudmestad, O. T. and Moe, G. (1996). Hydrodynamic coefficients for calculation of hydrodynamic loads on offshore truss structures. *Marine Structures*, 9(8):745–758.

Gunn, K. and Stock-Williams, C. (2012). Quantifying the global wave power resource. *Renewable Energy*, 44:296–304.

Guo, B., Patton, R., Jin, S., Gilbert, J., and Parsons, D. (2017). Non-linear modelling and verification of a heaving point absorber for wave energy conversion. *IEEE Transactions on Sustainable Energy*. doi: 10.1109/TSTE.2017.27413410.

Halliday, J. R., Dorrell, D. G., and Wood, A. R. (2011). An application of the fast fourier transform to the short-term prediction of sea wave behaviour. *Renew. Energy*, 36(6):1685–1692.

Hals, J., Falnes, J., and Moan, T. (2011a). A comparison of selected strategies for adaptive control of wave energy converters. *Journal of Offshore Mechanics and Arctic Engineering*, 133(3):031101–1–031101–12.

Hals, J., Falnes, J., and Moan, T. (2011b). Constrained optimal control of a heaving buoy wave-energy converter. *Journal of Offshore Mechanics and Arctic Engineering*, 133(1):011401.

Hansen, R. H. and Kramer, M. M. (2011). Modelling and control of the wavestar prototype. In *The 9th European Wave and Tidal Energy Conference: EWTEC 2011*, pages 1–10.

Henderson, R. (2006). Design, simulation, and testing of a novel hydraulic power take-off system for the pelamis wave energy converter. *Renew. energy*, 31(2):271–283.

Hodgins, N., Keysan, O., McDonald, A. S., and Mueller, M. A. (2012). Design and testing of a linear generator for wave-energy applications. *IEEE Transactions on Industrial Electronics*, 59(5):2094–2103.

Hong, Y., Waters, R., Boström, C., Eriksson, M., Engström, J., and Leijon, M. (2014). Review on electrical control strategies for wave energy converting systems. *Renewable and Sustainable Energy Reviews*, 31:329–342.

Huang, L., Yu, H., Hu, M., Zhao, J., and Cheng, Z. (2011). A novel flux-switching permanent-magnet linear generator for wave energy extraction application. *IEEE Transactions on Magnetics*, 47(5):1034–1037.

Ilyas, A., Kashif, S. A., Saqib, M. A., and Asad, M. M. (2014). Wave electrical energy systems: Implementation, challenges and environmental issues. *Renewable and Sustainable Energy Reviews*, 40:260–268.

Inoue, M. and Sato, K. (2000). An approach to a suitable stator length for minimizing the detent force of permanent magnet linear synchronous motors. *IEEE Transactions on Magnetics*, 36(4):1890–1893.

Jin, S., Guo, B., Patton, R., Gilbert, J., and Abdelrahman, M. (2016). Non-linear analysis of a point absorber wave energy converter. In *The Second International Conference on Offhshore Renewable Energy*, pages 1–6. ASRANet.

Josset, C., Babarit, A., and Clément, A. (2007). A wave-to-wire model of the searev wave energy converter. *Proceedings of the institution of mechanical engineers, Part M: Journal of Engineering for the Maritime Environment*, 221(2):81–93.

Kaźmierkowski, M., JasiIński, M., and Sorensen, H. C. (2008). Ocean waves energy converter-wave dragon mw. *Elektrotech.*, 84(2):8–13.

Kofoed, J. P. and Antonishen, M. P. (2009). The crest wing wave energy device: 2nd phase testing. Technical Report 59, Department of Civil Engineering, Aalborg University.

Kofoed, J. P., Frigaard, P., Friis-Madsen, E., and Sørensen, H. C. (2006). Prototype testing of the wave energy converter wave dragon. *Renewable energy*, 31(2):181–189.

Korde, U. (1999). On providing a reaction for efficient wave energy absorption by floating devices. *Applied Ocean Research*, 21(5):235–248.

Korde, U. A. and Ringwood, J. (2016). *Hydrodynamic Control of Wave Energy Devices*. Cambridge University Press.

Korvin-Kroukovsky, B. V. and Jacobs, W. R. (1957). Pitching and heaving motions of a ship in regular waves. Technical report, DTIC Document.

Kramer, M., Marquis, L., and Frigaard, P. (2011). Performance evaluation of the wavestar prototype. In *The 9th European Wave and Tidal Energy Conference: EWTEC 2011*, pages 1–9.

Krishnan, R. (2010). *Permanent magnet synchronous and brushless DC motor drives*. CRC Press/Taylor & Francis.

Kristiansen, E., Hjulstad, Å., and Egeland, O. (2005). State-space representation of radiation forces in time-domain vessel models. *Ocean Eng.*, 32(17):2195–2216.

Kundur, P., Balu, N. J., and Lauby, M. G. (1994). *Power system stability and control*, volume 7. McGraw-hill New York.

Kung, S.-Y. (1978). A new identification and model reduction algorithm via singular value decomposition. In *Proceedings of the 12th Asilomar conference on circuits, systems and computers, Pacific Grove*, pages 705–714.

Kurniawan, A., Pedersen, E., and Moan, T. (2012). Bond graph modelling of a wave energy conversion system with hydraulic power take-off. *Renewable energy*, 38(1):234–244.

Lan, J. and Patton, R. J. (2015). Integrated design of robust fault estimation and fault-tolerant control for linear systems. In *2015 IEEE 54th Annual Conference on Decision and Control (CDC)*, pages 5105–5110. IEEE.

Lan, J. and Patton, R. J. (2017). Integrated design of fault-tolerant control for nonlinear systems based on fault estimation and t–s fuzzy modeling. *IEEE Transactions on Fuzzy Systems*, 25(5):1141–1154.

Langhamer, O., Haikonen, K., and Sundberg, J. (2010). Wave power—sustainable energy or environmentally costly? a review with special emphasis on linear wave energy converters. *Renewable and Sustainable Energy Reviews*, 14(4):1329–1335.

Le Crom, I., Brito-Melo, A., Neumann, F., and Sarmento, A. (2009). Numerical estimation of incident wave parameters based on the air pressure measurements in pico owc plant. In *Proceedings of the 8th European Wave and Tidal Energy Conference*, pages 130–139.

Leijon, M., Danielsson, O., Eriksson, M., Thorburn, K., Bernhoff, H., Isberg, J., Sundberg, J., Ivanova, I., Sjöstedt, E., and Ågren, O. (2006). An electrical approach to wave energy conversion. *Renewable energy*, 31(9):1309–1319.

LHEEA (2016). Nemoh. Available from http://lheea.ec-nantes.fr/doku.php/emo/nemoh/start (accessed on 9 October 2016).

Li, G. and Belmont, M. R. (2014a). Model predictive control of sea wave energy converters–part i: A convex approach for the case of a single device. *Renewable Energy*, 69:453–463.

Li, G. and Belmont, M. R. (2014b). Model predictive control of sea wave energy converters–part ii: The case of an array of devices. *Renewable Energy*, 68:540–549.

Li, Y. and Yu, Y.-H. (2012). A synthesis of numerical methods for modeling wave energy converter-point absorbers. *Renew. Sustainable Energy Rev.*, 16(6):4352–4364.

Lin, Y., Bao, J., Liu, H., Li, W., Tu, L., and Zhang, D. (2015). Review of hydraulic transmission technologies for wave power generation. *Renewable and Sustainable Energy Reviews*, 50:194–203.

Liu, C., Yu, H., Hu, M., Liu, Q., and Zhou, S. (2013). Detent force reduction in permanent magnet tubular linear generator for direct-driver wave energy conversion. *IEEE Transactions on Magnetics*, 49(5):1913–1916.

Lopes, M., Hals, J., Gomes, R., Moan, T., Gato, L., and Falcao, A. d. O. (2009). Experimental and numerical investigation of non-predictive phase-control strategies for a point-absorbing wave energy converter. *Ocean Engineering*, 36(5):386–402.

López, I., Andreu, J., Ceballos, S., de Alegría, I. M., and Kortabarria, I. (2013). Review of wave energy technologies and the necessary power-equipment. *Renewable and Sustainable Energy Reviews*, 27:413–434.

Mann, L. D. (2011). Application of ocean observations & analysis: The ceto wave energy project. In *Operational Oceanography in the 21st Century*, pages 721–729. Springer.

Maragos, P., Kaiser, J. F., and Quatieri, T. F. (1993). Energy separation in signal modulations with application to speech analysis. *IEEE Trans. Signal Process.*, 41(10):3024–3051.

Margheritini, L., Vicinanza, D., and Frigaard, P. (2009). Ssg wave energy converter: Design, reliability and hydraulic performance of an innovative overtopping device. *Renewable Energy*, 34(5):1371–1380.

Marjani, A. (2008). *Advancement in smoothed particle hydrodynamics for applying to ocean wave energy conversion*. PhD thesis, North Carolina State University.

Marquis, L., Kramer, M., and Frigaard, P. (2010). First power production figures from the wave star roshage wave energy converter. In *Proceedings of the 3rd International Conference on Ocean Energy (ICOE-2010), Bilbao, Spain*, volume 68, pages 1–5.

Marton, L. and Lantos, B. (2007). Modeling, identification, and compensation of stick-slip friction. *IEEE Transactions on Industrial Electronics*, 54(1):511–521.

Masuda, Y. (1986). An experience of wave power generator through tests and improvement. In *Hydrodynamics of ocean wave-energy utilization*, pages 445–452. Springer.

Maxwell, A. (2016). 16.2: Maxwell 2d technical notes–transient simulation. *Maxwell Online Help*.

McCabe, A., Bradshaw, A., Meadowcroft, J., and Aggidis, G. (2006). Developments in the design of the ps frog mk 5 wave energy converter. *Renewable Energy*, 31(2):141–151.

McCormick, M. (1981). *Ocean wave energy conversion*. Wiley-Interscience, New York, NY.

McCormick, M. E. (1973). *Ocean engineering wave mechanics*. John Wiley & Sons.

MeasurementComputing (2014). *USB-1608FS User's Guide*. Measurement Computing Ltd, One Technology Way, P.O. Box 9106, Norwood, MA 02062-9160, U.S.A., 7 edition. Document Revision 7A.

Mehlum, E. (1986). Tapchan. In *Hydrodynamics of Ocean Wave-Energy Utilization*, pages 51–55. Springer.

Mei, C. C. (1976). Power extraction from water waves. *Journal of Ship Research*, 20:63–66.

Mendoza, E., Chávez, X., Alcérreca-Huerta, J. C., and Silva, R. (2015). Hydrodynamic behavior of a new wave energy convertor: The blow-jet. *Ocean Engineering*, 106:252–260.

Merigaud, A., Gilloteaux, J.-C., and Ringwood, J. V. (2012). A nonlinear extension for linear boundary element methods in wave energy device modelling. In *ASME 2012 31st International Conference on Ocean, Offshore and Arctic Engineering*, pages 615–621. American Society of Mechanical Engineers.

MoceanEnergy (2017). Mocean energy is developing a hinged-raft wave energy converter (wec). Available from http://www.moceanenergy.com/technology.html (accessed on 3 June 2017).

Mohammadpour, A. and Parsa, L. (2011). Svm-based direct thrust control of permanent magnet linear synchronous motor with reduced force ripple. In *Industrial Electronics (ISIE), 2011 IEEE International Symposium on*, pages 756–760. IEEE.

Morison, J., Johnson, J., and Schaaf, S. (1950). The force exerted by surface waves on piles. *Journal of Petroleum Technology*, 2(05):149–154.

Mouwen, F. (2008). Presentation on wavebob to engineers ireland. Available from https://www.engineersireland.ie/EngineersIreland/media/SiteMedia/groups/Divisions/new-energy/Wavebob-Development_of_a_Wave_Energy_Converter.pdf?ext=.pdf (accessed on 3 June 2017).

Mueller, M. and Baker, N. J. (2002). A low speed reciprocating permanent magnet generator for direct drive wave energy converters. In *2002 International Conference on Power Electronics, Machines and Drives (Conf. Publ. No. 487)*, pages 468–473.

Mueller, M., Polinder, H., and Baker, N. (2007). Current and novel electrical generator technology for wave energy converters. In *Electric Machines & Drives Conference, 2007. IEMDC'07. IEEE International*, volume 2, pages 1401–1406. IEEE.

Mueller, M. A., Baker, N. J., Ran, L., Chong, N. G., Wei, H., Tavner, P. J., and McKeever, P. (2008). Experimental tests of an air-cored pm tubular generator for direct drive wave energy converters. In *2008 4th IET Conference on Power Electronics, Machines and Drives*, pages 747–751.

Mundon, T., Murray, A., and Wallace, R. (2011). Toward a biologically inspired, neural control mechanism for multiple degree of freedom wave energy converters. In *Proc. 9th European Wave Tidal Energy Conf*, pages 1–7.

NationalInstruments (2009). *DAQ M Series NI USB-621x User Manual*. National Instruments Corporation, 11500 North Mopac Expressway, Austin, Texas, U.S.A., 1 edition. 371931F-01.

Nebel, P. (1992). Maximizing the efficiency of wave-energy plant using complex-conjugate control. *Proceedings of the Institution of Mechanical Engineers, Part I: Journal of Systems and Control Engineering*, 206(4):225–236.

Neumann, F., Brito-Melo, A., Didier, E., and Sarmento, A. (2007). Pico owc recovery project: recent activities and performance data. In *Proceedings of the 7th European wave and tidal energy conference, Porto, Portugal*, pages 1–7.

Newman, J. N. (1962). The exciting forces on fixed bodies in waves. *J. Ship Res.*, 6:10–17.

Newman, J. N. (1977). *Marine hydrodynamics*. MIT press.

OES (2014). Ocean energy systems annual report 2014. Technical report, Technical Report for Ocean Energy Systems.

OES (2015). Ocean energy systems annual report 2015. Technical report, Technical Report for Ocean Energy Systems.

Ogilvie, T. F. (1964). Recent progress toward the understanding and prediction of ship motions. In *5th Symposium on naval hydrodynamics*, volume 1, pages 2–5. Bergen, Norway.

Ogilvie, T. F. and Tuck, E. O. (1969). A rational strip theory of ship motions: part i. Technical Report 013, University of Michigan.

O'Hagan, A., Huertas, C., O'Callaghan, J., and Greaves, D. (2016). Wave energy in europe: Views on experiences and progress to date. *International Journal of Marine Energy*, 14:180–197.

Omholt, T. (1978). A wave activated electric generator. In *OCEANS'78*, pages 585–589. IEEE.

Ovadia, S. (1995). System for conversion of sea wave energy. US Patent 5,461,862.

Papini, G. P. R., Vertechy, R., and Fontana, M. (2013). Dynamic model of dielectric elastomer diaphragm generators for oscillating water column wave energy converters. In *ASME 2013 Conference on Smart Materials, Adaptive Structures and Intelligent Systems*, pages V001T03A038–V001T03A038. American Society of Mechanical Engineers.

Parsons, D. (2016). Total environment simulator at the deep. Available from http://www2.hull.ac.uk/science/geography/research/deep.aspx (accessed on 9 October 2016).

Pecher, A., Kofoed, J. P., Espedal, J., and Hagberg, S. (2010). Results of an experimental study of the langlee wave energy converter. In *The Twentieth International Offshore and Polar Engineering Conference*, pages 877–885. International Society of Offshore and Polar Engineers.

Pelfrene, J. (2011). Study of the sph method for simulation of regular and breaking waves. Master's thesis, Universiteit Gent.

Pelrine, R., Kornbluh, R., Pei, Q., and Joseph, J. (2000). High-speed electrically actuated elastomers with strain greater than 100%. *Science*, 287(5454):836–839.

Pena, R., Clare, J., and Asher, G. (1996). Doubly fed induction generator using back-to-back pwm converters and its application to variable-speed wind-energy generation. *IEE Proceedings-Electric Power Applications*, 143(3):231–241.

Peñalba, M., Giorgi, G., and Ringwood, J. (2015). A review of non-linear approaches for wave energy converter modelling. In *Proceedings of European Wave and Tidal Energy Conference, Nantes, France*, pages 08C1–3–1–08C1–3–10.

Penalba, M. and Ringwood, J. V. (2016). A review of wave-to-wire models for wave energy converters. *Energies*, 9(7):506.

Penalba Retes, M., Mérigaud, A., Gilloteaux, J.-C., and Ringwood, J. (2015). Nonlinear froude-krylov force modelling for two heaving wave energy point absorbers. In *Proceedings of the 11th European Wave and Tidal Energy Conference*, pages 08C1–4–1–08C1–4–10.

Pérez, T. and Fossen, T. I. (2008). Time-vs. frequency-domain identification of parametric radiation force models for marine structures at zero speed. *Modeling, Identification and Control*, 29(1):1–19.

Perez, T. and Fossen, T. I. (2009). A matlab toolbox for parametric identification of radiation-force models of ships and offshore structures. *Modeling, Identification and Control*, 30(1):1.

Perez, T. and Fossen, T. I. (2011). Practical aspects of frequency-domain identification of dynamic models of marine structures from hydrodynamic data. *Ocean Engineering*, 38(2):426–435.

Pierson, W. J. and Moskowitz, L. (1964). A proposed spectral form for fully developed wind seas based on the similarity theory of sa kitaigorodskii. *J. Geophys. Res.*, 69(24):5181–5190.

Piscopo, V., Benassai, G., Cozzolino, L., Della Morte, R., and Scamardella, A. (2016). A new optimization procedure of heaving point absorber hydrodynamic performances. *Ocean Engineering*, 116:242–259.

Polinder, H., Damen, M. E., and Gardner, F. (2004). Linear pm generator system for wave energy conversion in the aws. *IEEE transactions on energy conversion*, 19(3):583–589.

Polinder, H., Damen, M. E., Gardner, F., and de Sousa Prado, M. G. (2005a). Archimedes wave swing linear permanent-magnet generator system performance. In *6th European Wave and Tidal Energy Conference, Glasgow*, pages 383–387.

Polinder, H., Mecrow, B. C., Jack, A. G., Dickinson, P. G., and Mueller, M. A. (2005b). Conventional and tfpm linear generators for direct-drive wave energy conversion. *IEEE Transactions on Energy Conversion*, 20(2):260–267.

Polinder, H., Mueller, M., Scuotto, M., and Goden de Sousa Prado, M. (2007). Linear generator systems for wave energy conversion. In *Proceedings of the 7th European Wave and Tidal Energy Conference, Porto, Sept.*, pages 1–8. IDMEC-Institute de Engenharia Mecânica.

Pontes, T. and Falcão, A. (2001). Ocean energy conversion. In *Proceedings of the 18th World Energy Council*, pages 1–27.

Prado, M. and Polinder, H. (2011). Direct drive in wave energy conversion—aws full scale prototype case study. In *Power and Energy Society General Meeting, 2011 IEEE*, pages 1–7. IEEE.

Rafiee, A. and Fiévez, J. (2015). Numerical prediction of extreme loads on the ceto wave energy converter. In *Proceedings of the 11th European Wave and Tidal Energy Conference (EWTEC)*, pages 09A1–2–1–09A1–2–10.

Rhinefrank, K., Schacher, A., Prudell, J., Brekken, T. K., Stillinger, C., Yen, J. Z., Ernst, S. G., von Jouanne, A., Amon, E., and Paasch, R. (2012). Comparison of direct-drive power takeoff systems for ocean wave energy applications. *IEEE Journal of Oceanic Engineering*, 37(1):35–44.

Richter, M., Magana, M. E., Sawodny, O., and Brekken, T. K. (2013). Nonlinear model predictive control of a point absorber wave energy converter. *IEEE Transactions on Sustainable Energy*, 4(1):118–126.

Ringwood, J. V., Bacelli, G., and Fusco, F. (2014). Energy-maximizing control of wave-energy converters: the development of control system technology to optimize their operation. *IEEE Control Systems*, 34(5):30–55.

Roessling, A. and Ringwood, J. (2015). Finite order approximations to radiation forces for wave energy applications. *Renewable Energies Offshore*, pages 359–366.

Ruellan, M., BenAhmed, H., Multon, B., Josset, C., Babarit, A., and Clement, A. (2010). Design methodology for a searev wave energy converter. *IEEE Transactions on Energy Conversion*, 25(3):760–767.

Safonov, M. and Chiang, R. (1988). A schur method for balanced model reduction. In *American Control Conference*, pages 1036–1040. IEEE.

Salter, S. (1979). Power conversion systems for ducks. In *International Conference on Future Energy Concepts*, volume 1, pages 100–108.

Salter, S. H. (1974). Wave power. *Nature*, 249(5459):720–724.

Salter, S. H., Taylor, J., and Caldwell, N. (2002). Power conversion mechanisms for wave energy. *Proceedings of the Institution of Mechanical Engineers, Part M: Journal of Engineering for the Maritime Environment*, 216(1):1–27.

Sarmento, A. (1993). Model-test optimization of an owc wave power plant. *International Journal of Offshore and Polar Engineering*, 3(01):66–72.

Sarpkaya, T. (1986). Force on a circular cylinder in viscous oscillatory flow at low keulegan—carpenter numbers. *Journal of Fluid Mechanics*, 165:61–71.

Schauder, C. and Mehta, H. (1993). Vector analysis and control of advanced static var compensators. In *IEE Proceedings C (Generation, Transmission and Distribution)*, volume 140, pages 299–306. IET.

Schoen, M. P., Hals, J., and Moan, T. (2008a). Robust control of heaving wave energy devices in irregular waves. In *Control and Automation, 2008 16th Mediterranean Conference on*, pages 779–784. IEEE.

Schoen, M. P., Hals, J., and Moan, T. (2008b). Wave prediction and fuzzy logic control of wave energy converters in irregular waves. In *Control and Automation, 2008 16th Mediterranean Conference on*, pages 767–772. IEEE.

SEAI (2017). Marine farm accelerator. Available from http://www.seai.ie/Renewables/Ocean-Energy/Ocean-Energy-Test-Sites-in-Ireland/ (accessed on 24 May 2017).

Shek, J. K.-H., Macpherson, D. E., Mueller, M. A., and Xiang, J. (2007). Reaction force control of a linear electrical generator for direct drive wave energy conversion. *IET Renew. Power Gen.*, 1(1):17–24.

Sheng, W., Alcorn, R., and Lewis, A. (2015). On improving wave energy conversion, part i: Optimal and control technologies. *Renewable Energy*, 75:922–934.

Sinha, A., Karmakar, D., and Soares, C. G. (2016). Performance of optimally tuned arrays of heaving point absorbers. *Renewable Energy*, 92:517–531.

Sjolte, J., Bjerke, I., Crozier, A., Tjensvoll, G., and Molinas, M. (2012). All-electric wave energy power take off system with improved power quality at the grid connection point. In *Transmission and Distribution Conference and Exposition (T&D), 2012 IEEE PES*, pages 1–7. IEEE.

St Dinis, M. and Pierson Jr, W. J. (1953). On the motions of ships in confused seas. *SNAME Trans*, 61:280–357.

Taghipour, R., Perez, T., and Moan, T. (2008). Hybrid frequency–time domain models for dynamic response analysis of marine structures. *Ocean Eng.*, 35(7):685–705.

Tedd, J. and Kofoed, J. P. (2009). Measurements of overtopping flow time series on the wave dragon, wave energy converter. *Renew. Energy*, 34(3):711–717.

Tedeschi, E., Carraro, M., Molinas, M., and Mattavelli, P. (2011). Effect of control strategies and power take-off efficiency on the power capture from sea waves. *IEEE Trans. Energy Convers.*, 26(4):1088–1098.

Thorpe, T. (1999). An overview of wave energy technologies: status, performance and costs. *Wave power: moving towards commercial viability*, 26:50–120.

Timman, R. and Newman, J. (1962). The coupled damping coefficients of a symmetric ship. Technical Report 1672, DTIC Document.

Tiron, R., Mallon, F., Dias, F., and Reynaud, E. G. (2015). The challenging life of wave energy devices at sea: A few points to consider. *Renewable and Sustainable Energy Reviews*, 43:1263–1272.

Tom, N. and Yeung, R. W. (2013). Nonlinear model predictive control applied to a generic ocean-wave energy extractor. In *Proc. of the ASME 32nd International Conference on Ocean, Offshore and Arctic Engineering*, pages 1–13. American Society of Mechanical Engineers.

Tustin, A. (1947). The effects of backlash and of speed-dependent friction on the stability of closed-cycle control systems. *Electrical Engineers-Part IIA: Automatic Regulators and Servo Mechanisms, Journal of the Institution of*, 94(1):143–151.

Unneland, K., Fossen, T. I., Van Dooren, P., and Egeland, O. (2006). Low order potential damping models for surface vessels. In *Proceedings of Seventh IFAC Conference on Manoeuvering and Control of Marine Craft, September*, pages 20–25.

Valério, D., Beirão, P., and Da Costa, J. S. (2007). Optimisation of wave energy extraction with the archimedes wave swing. *Ocean Eng.*, 34(17):2330–2344.

Valério, D., Ortigueira, M. D., and Da Costa, J. S. (2008). Identifying a transfer function from a frequency response. *Journal of computational and nonlinear dynamics*, 3(2):021207.

Vantorre, M., Banasiak, R., and Verhoeven, R. (2004). Modelling of hydraulic performance and wave energy extraction by a point absorber in heave. *Applied Ocean Research*, 26(1):61–72.

Vertechy, R., Fontana, M., Papini, G. R., and Bergamasco, M. (2013). Oscillating-water-column wave-energy-converter based on dielectric elastomer generator. In *SPIE Smart Structures and Materials Nondestructive Evaluation and Health Monitoring*, pages 1–13.

Vicinanza, D. and Frigaard, P. (2008). Wave pressure acting on a seawave slot-cone generator. *Coastal Engineering*, 55(6):553–568.

Wang, J., Howe, D., and Jewell, G. W. (2003a). Fringing in tubular permanent-magnet machines: Part ii. cogging force and its minimization. *IEEE Transactions on Magnetics*, 39(6):3517–3522.

Wang, J., Inoue, M., Amara, Y., and Howe, D. (2005). Cogging-force-reduction techniques for linear permanent-magnet machines. *IEE Proceedings-Electric Power Applications*, 152(3):731–738.

Wang, S., Yuan, P., Li, D., and Jiao, Y. (2011). An overview of ocean renewable energy in china. *Renewable and Sustainable Energy Reviews*, 15(1):91–111.

Wang, X., Yang, Y., and Fu, D. (2003b). Study of cogging torque in surface-mounted permanent magnet motors with energy method. *Journal of magnetism and magnetic materials*, 267(1):80–85.

Washio, Y., Osawa, H., Nagata, Y., Fujii, F., Furuyama, H., and Fujita, T. (2000). The offshore floating type wave power device mighty whale: Open sea tests. In *Proceedings of the Tenth International Offshore and Polar Engineering Conference*, volume 1, pages 373–380. International Society of Offshore and Polar Engineers.

Washio, Y., Osawa, H., and Ogata, T. (2001). The open sea tests of the offshore floating type wave power device" mighty whale"-characteristics of wave energy absorption and power generation. In *OCEANS, 2001. MTS/IEEE Conference and Exhibition*, volume 1, pages 579–585. IEEE.

WaveHub (2016). Wave hub limited adcancing offshore renewable energy. Available from http://www.wavehub.co.uk/ (accessed on 4 August 2016).

Weber, J., Mouwen, F., Parish, A., and Robertson, D. (2009). Wavebob–research & development network and tools in the context of systems engineering. In *Proc. Eighth European Wave and Tidal Energy Conference, Uppsala, Sweden*, pages 416–420.

WEC-Commission (1993). *Renewable energy resources: opportunities and constraints 1990-2020*. World Energy Council, London.

Wehausen, J. V. (1992). Causality and the radiation condition. *J. Eng. Math*, 26(1):153–158.

WES (2017a). Forth innovation call for wave energy scotland on control systems. Available from http://www.waveenergyscotland.co.uk/ (accessed on 25 May 2017).

WES (2017b). Programmes. Available from http://www.waveenergyscotland.co.uk/programmes/ (accessed on 24 May 2017).

Witt, M., Sheehan, E., Bearhop, S., Broderick, A., Conley, D., Cotterell, S., Crow, E., Grecian, W., Halsband, C., and Hodgson, D. (2012). Assessing wave energy effects on biodiversity: the wave hub experience. *Phil. Trans. R. Soc. A*, 370(1959):502–529.

Wolgamot, H. A. and Fitzgerald, C. J. (2015). Nonlinear hydrodynamic and real fluid effects on wave energy converters. *Proceedings of the Institution of Mechanical Engineers, Part A: Journal of Power and Energy*, 229(7):772–794.

Yang, Y., Wang, X., Zhu, C., and Huang, C. (2009). Study of magnet asymmetry for reduction of cogging torque in permanent magnet motors. In *Industrial Electronics and Applications, 2009. ICIEA 2009. 4th IEEE Conference on*, pages 2325–2328. IEEE.

Yu, Y.-H. and Li, Y. (2011). A rans simulation of the heave response of a two-body floating-point wave absorber. In *The Twenty-first International Offshore and Polar Engineering Conference*, pages 1–7. International Society of Offshore and Polar Engineers.

Yu, Z. and Falnes, J. (1995). State-space modelling of a vertical cylinder in heave. *Appl. Ocean Res.*, 17(5):265–275.

Zhou, G., Huang, J., Yue, T., Luo, Q., and Zhang, G. (2015). Temporal-spatial distribution of wave energy: A case study of beibu gulf, china. *Renewable Energy*, 74:344–356.

Zhu, Y.-W. and Cho, Y.-H. (2007). Thrust ripples suppression of permanent magnet linear synchronous motor. *IEEE Transactions on Magnetics*, 43(6):2537–2539.

Appendix A

Mechanical design

The 1/50 scale PAWEC is design in SOLIDWORKS®. The sketch details are given as follows.

Table A.1 List of mechanical components.

Item No	Component Label	Quantity	Description
1	Bottom	1	Stainless Steel 316, weld with 7&8
2	EndProtection	2	Stainless Steel 316
3	HexBar1	5	Stainless Steel 316
4	HexBar2	2	Stainless Steel 316
5	Lid	1	Stainless Steel 316
6	Disc	1	Stainless Steel 316
7	Side	1	Stainless Steel 316, weld with 1&8
8	Top	1	Stainless Steel 316, weld with 1&7
9	CircularBar	1	Stainless Steel 316

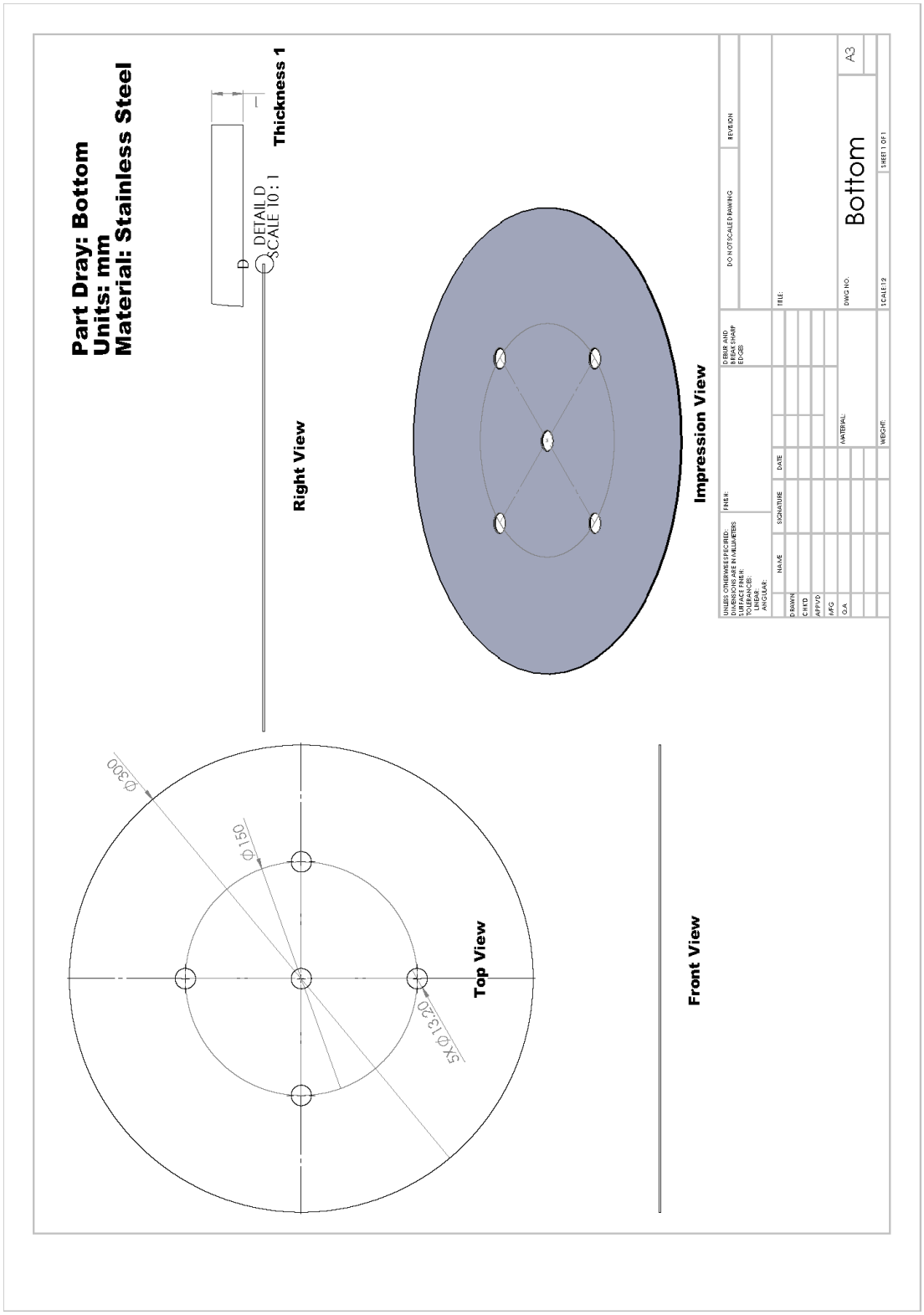

Fig. A.1 Sketch of the bottom component.

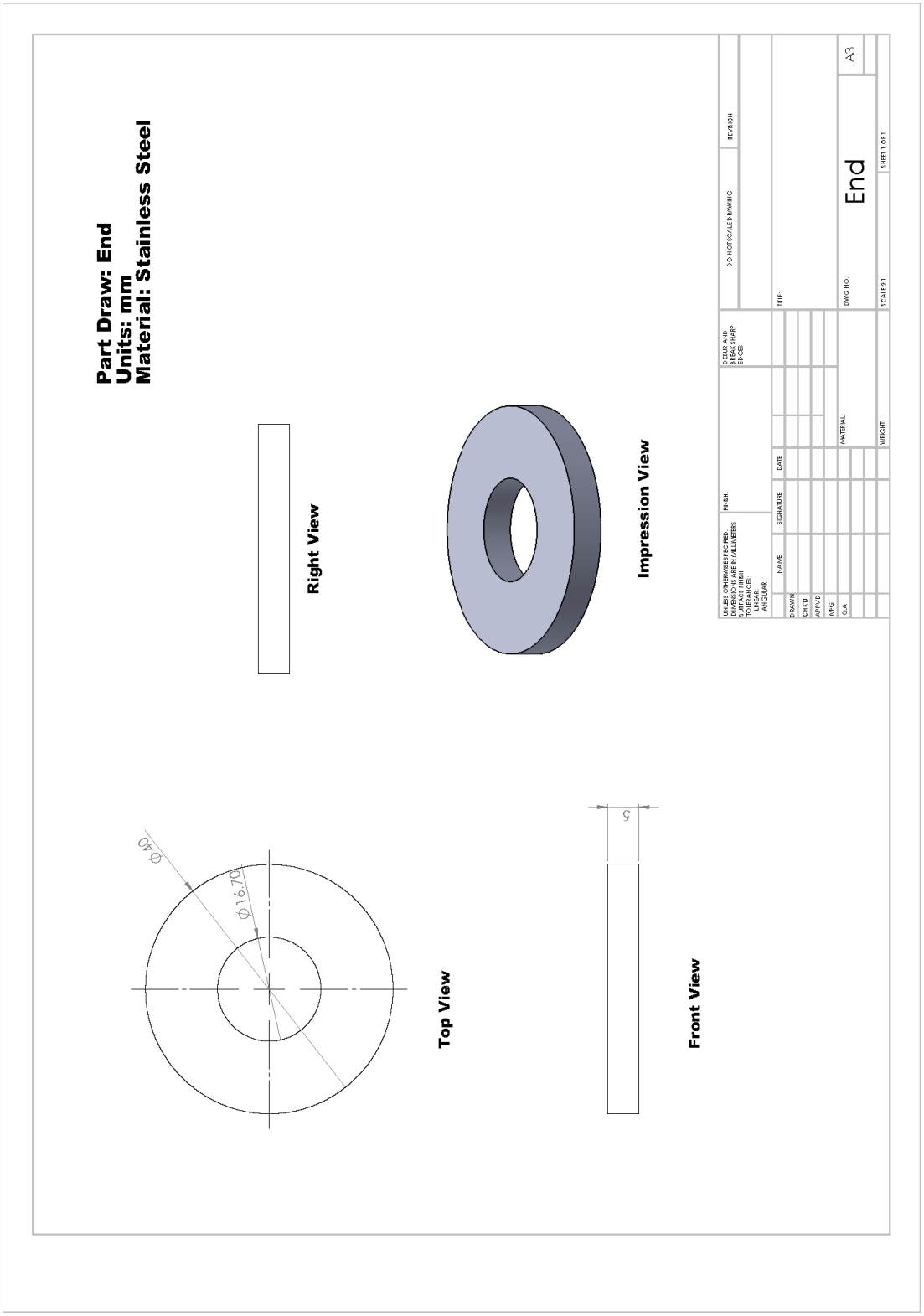

Fig. A.2 Sketch of the end-protection component.

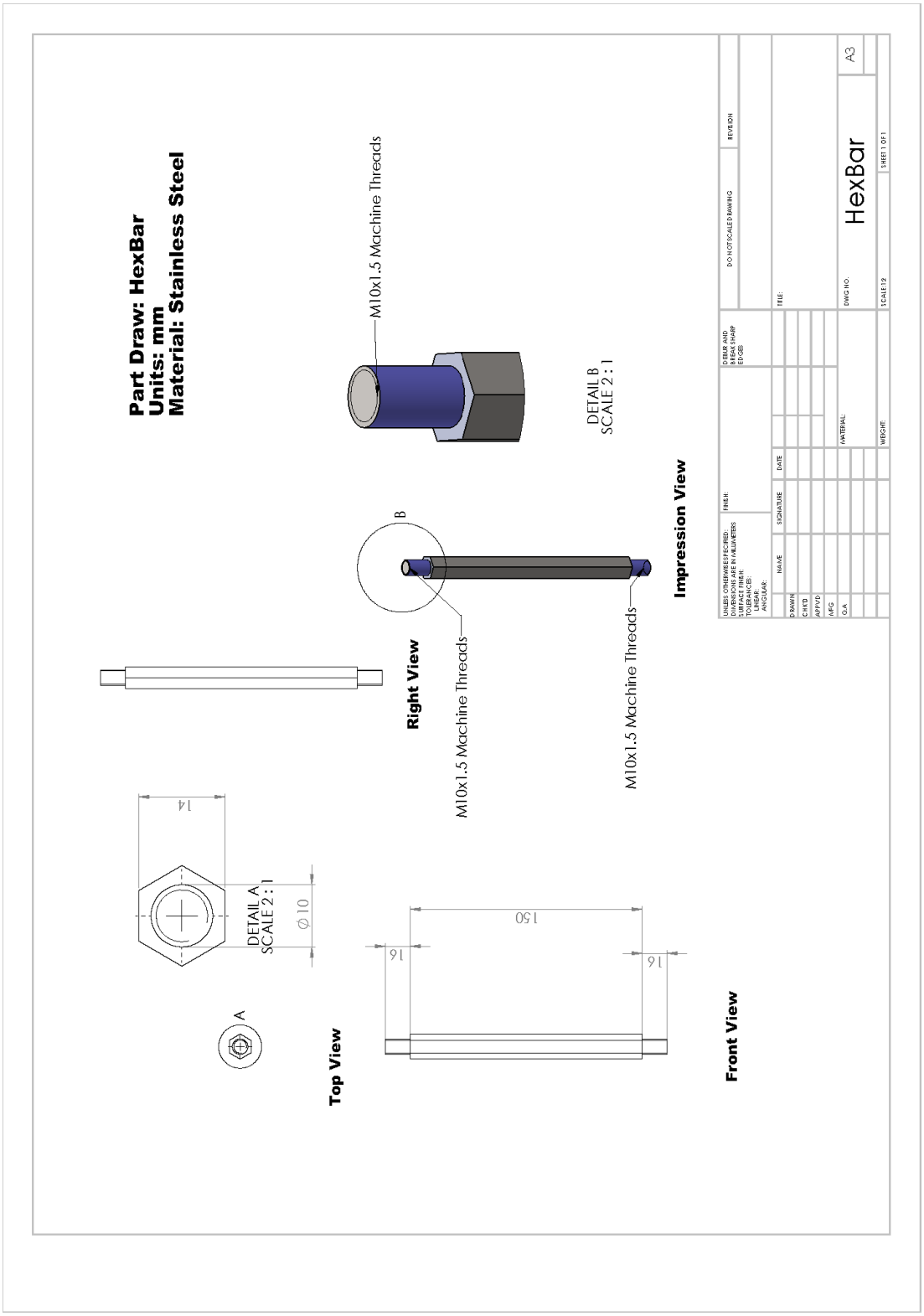

Fig. A.3 Sketch of the hex-bar1 component.

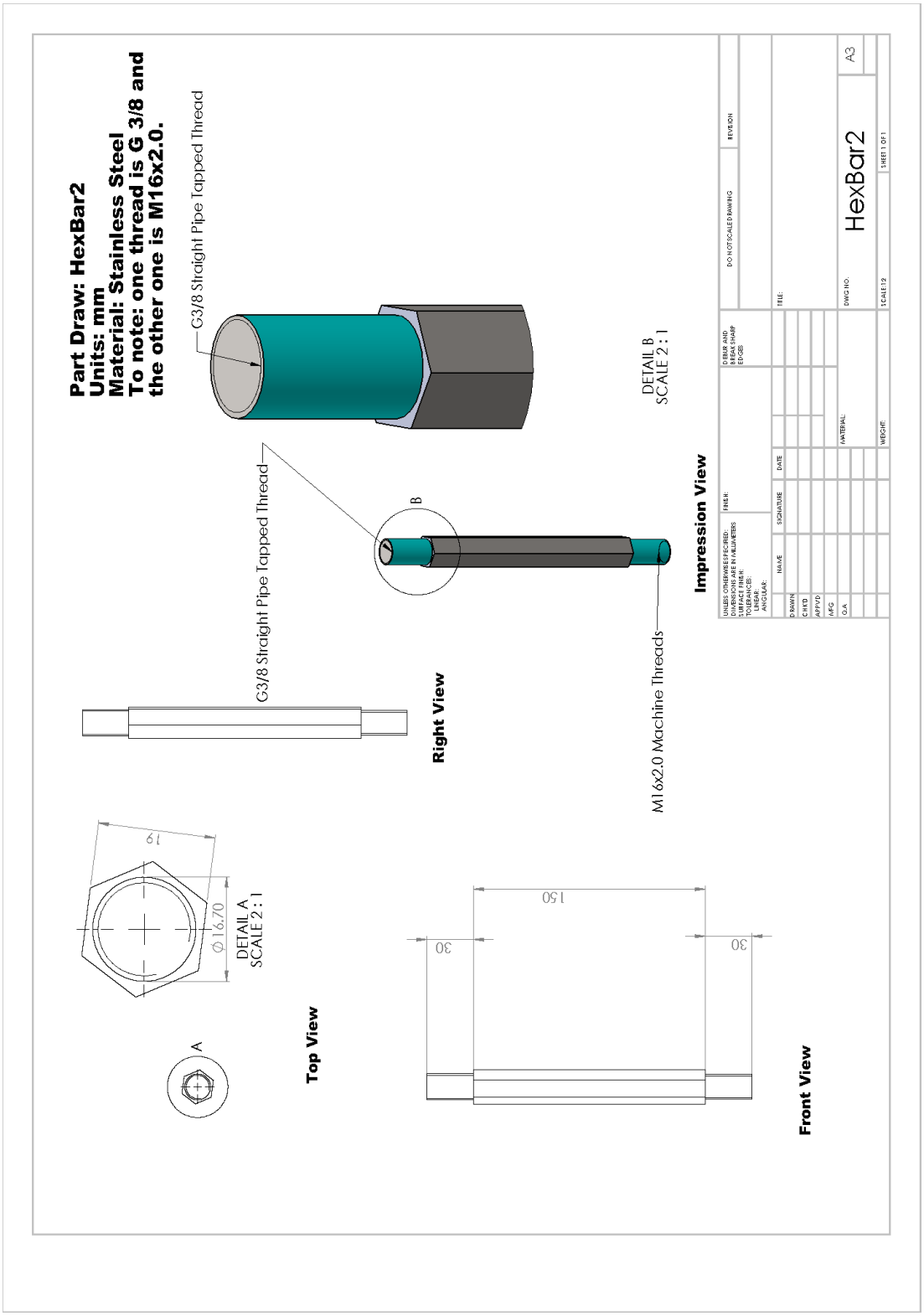

Fig. A.4 Sketch of the hex-bar2 component.

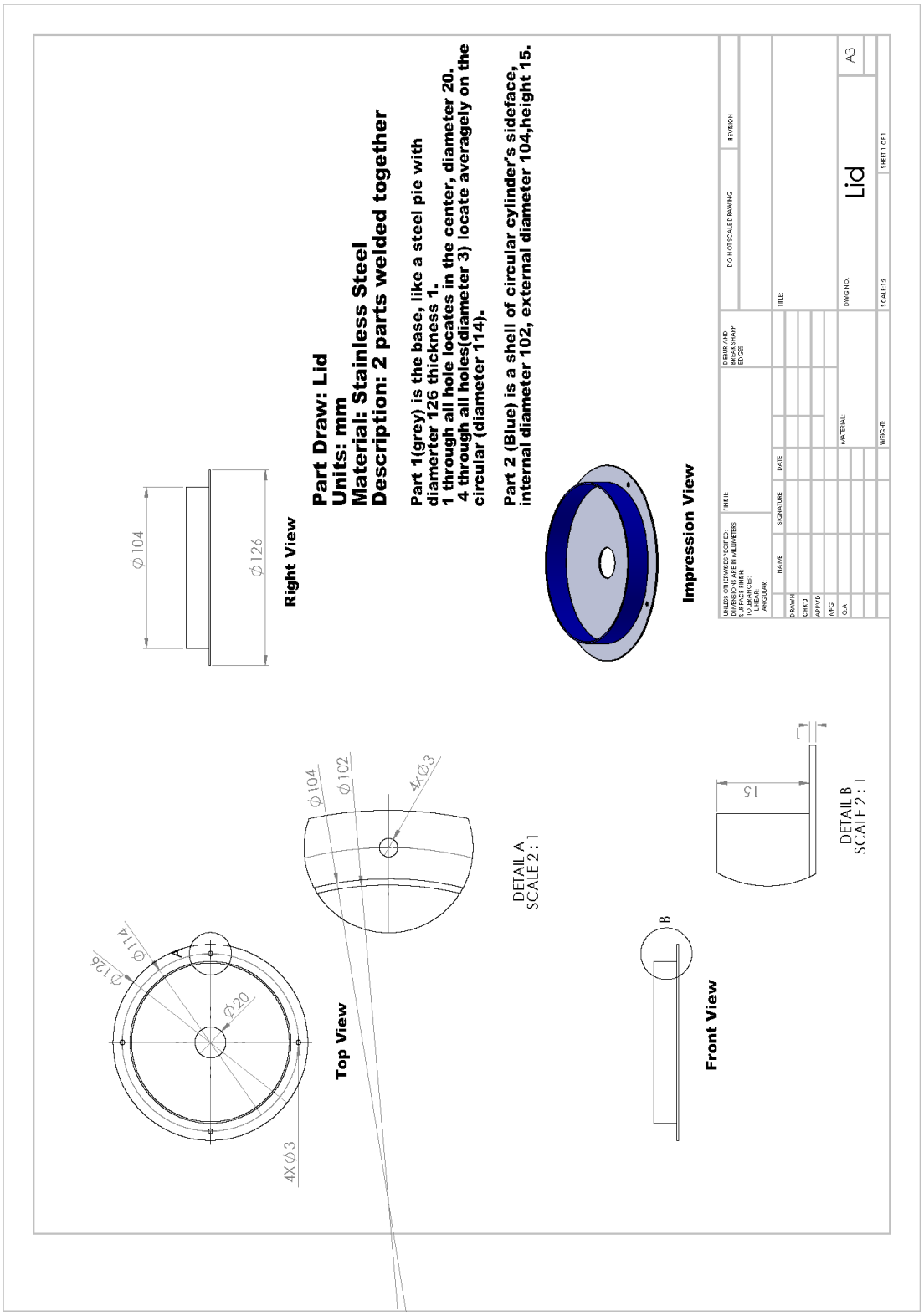

Fig. A.5 Sketch of the lid component.

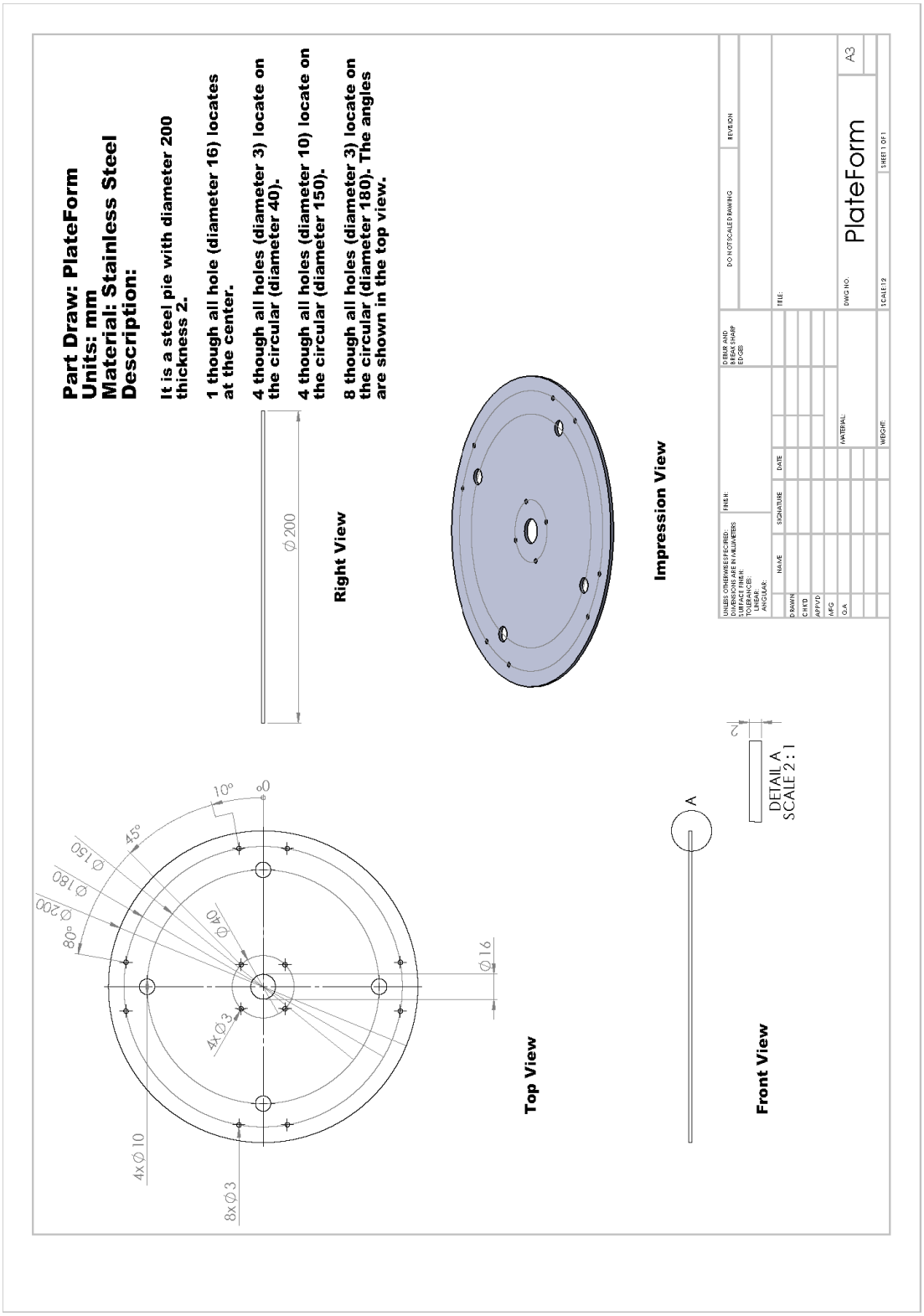

Fig. A.6 Sketch of the disc component.

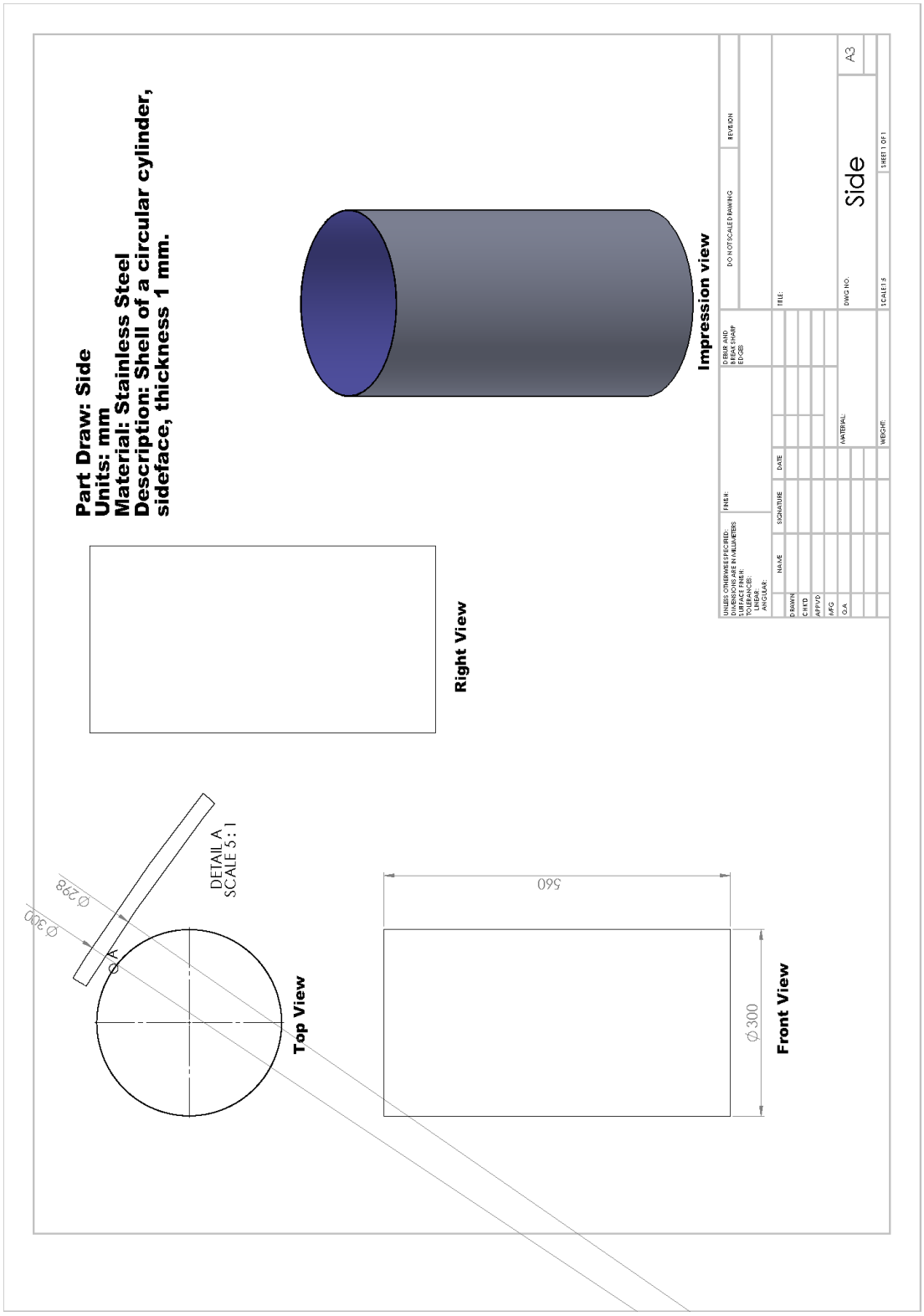

Fig. A.7 Sketch of the side component.

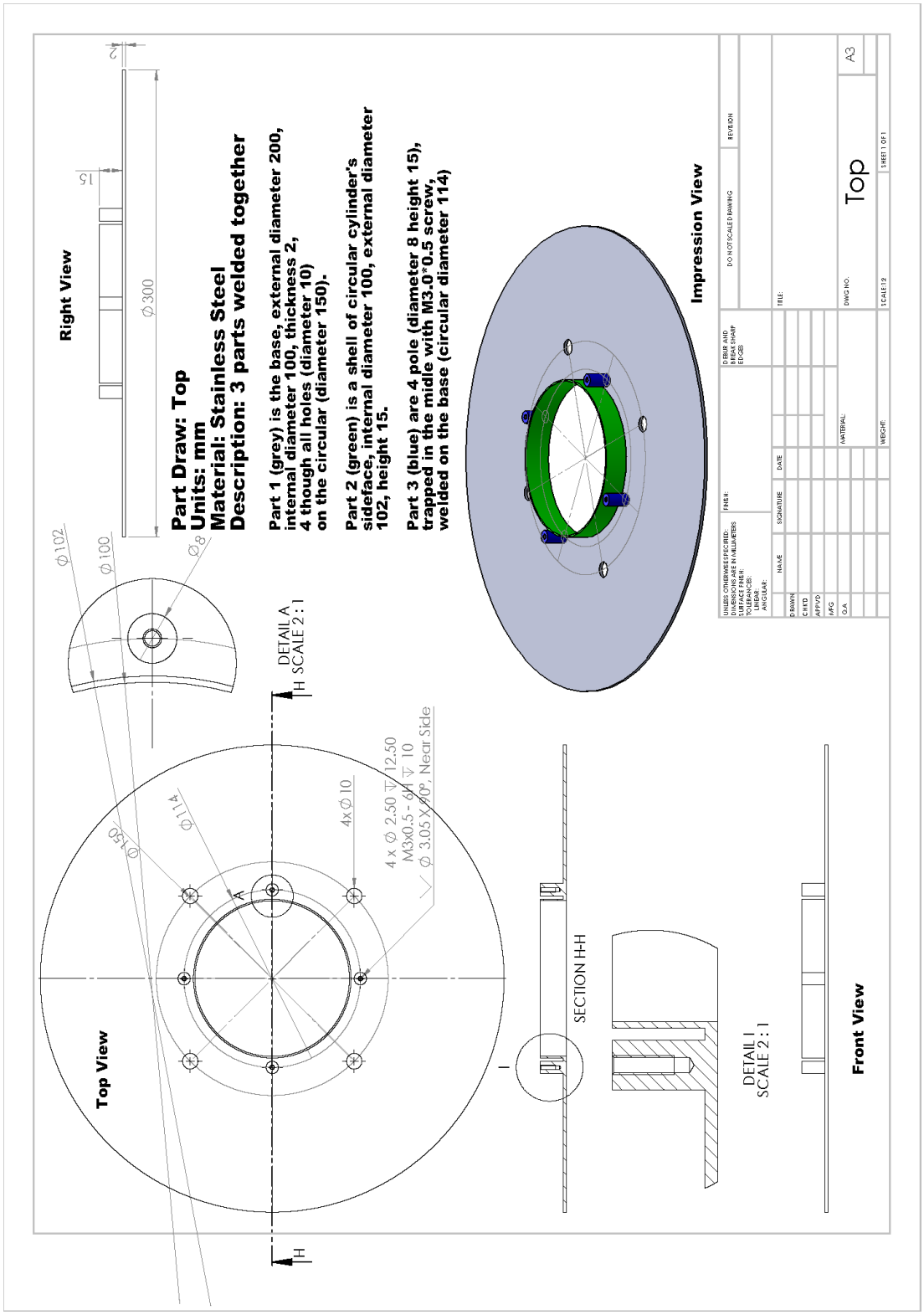

Fig. A.8 Sketch of the top component.

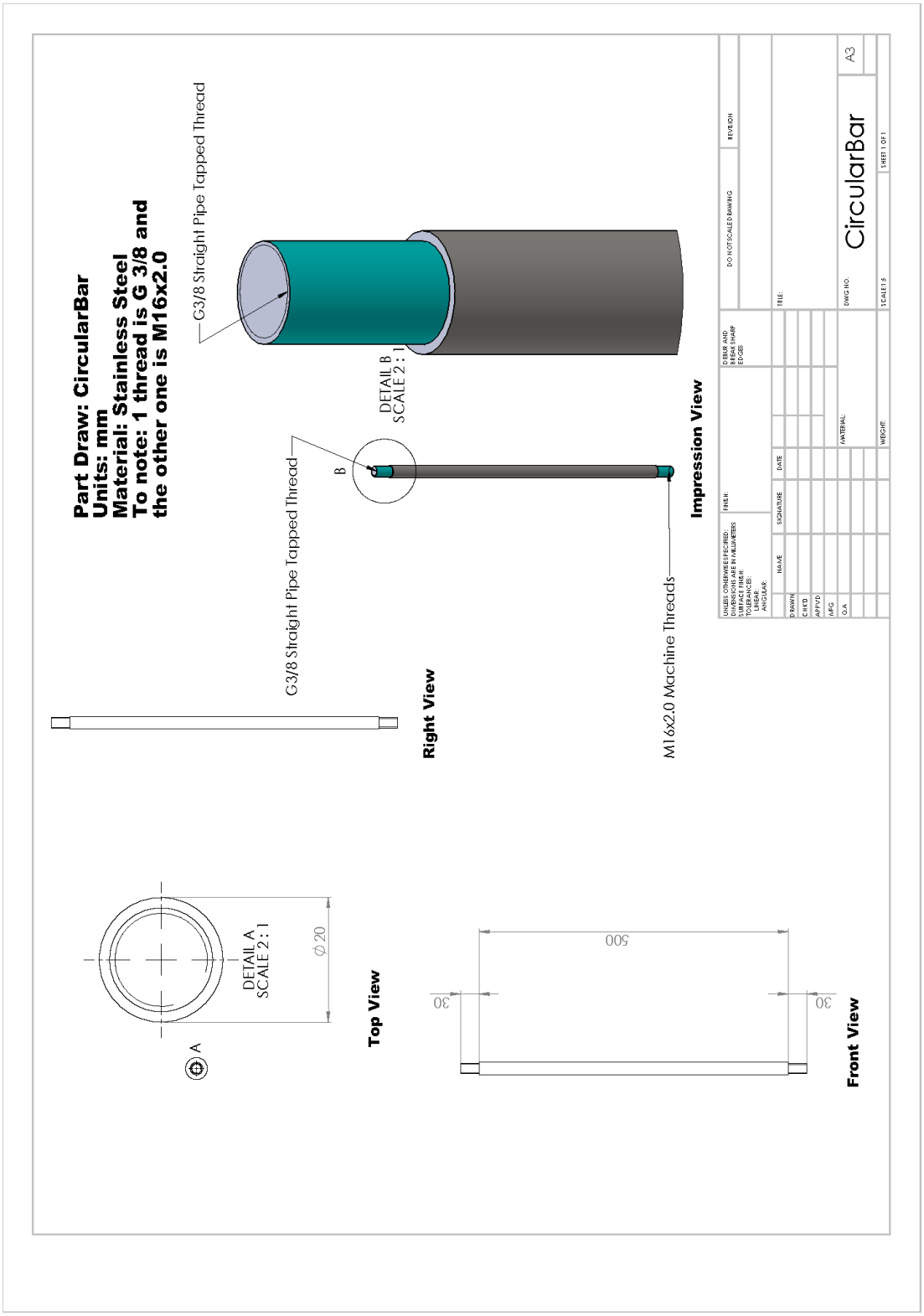

Fig. A.9 Sketch of the circular-bar component.

Appendix B

Electrical sketch

The circuits are design in ALTIUM DESIGNER™. The sketch details are given as follows.

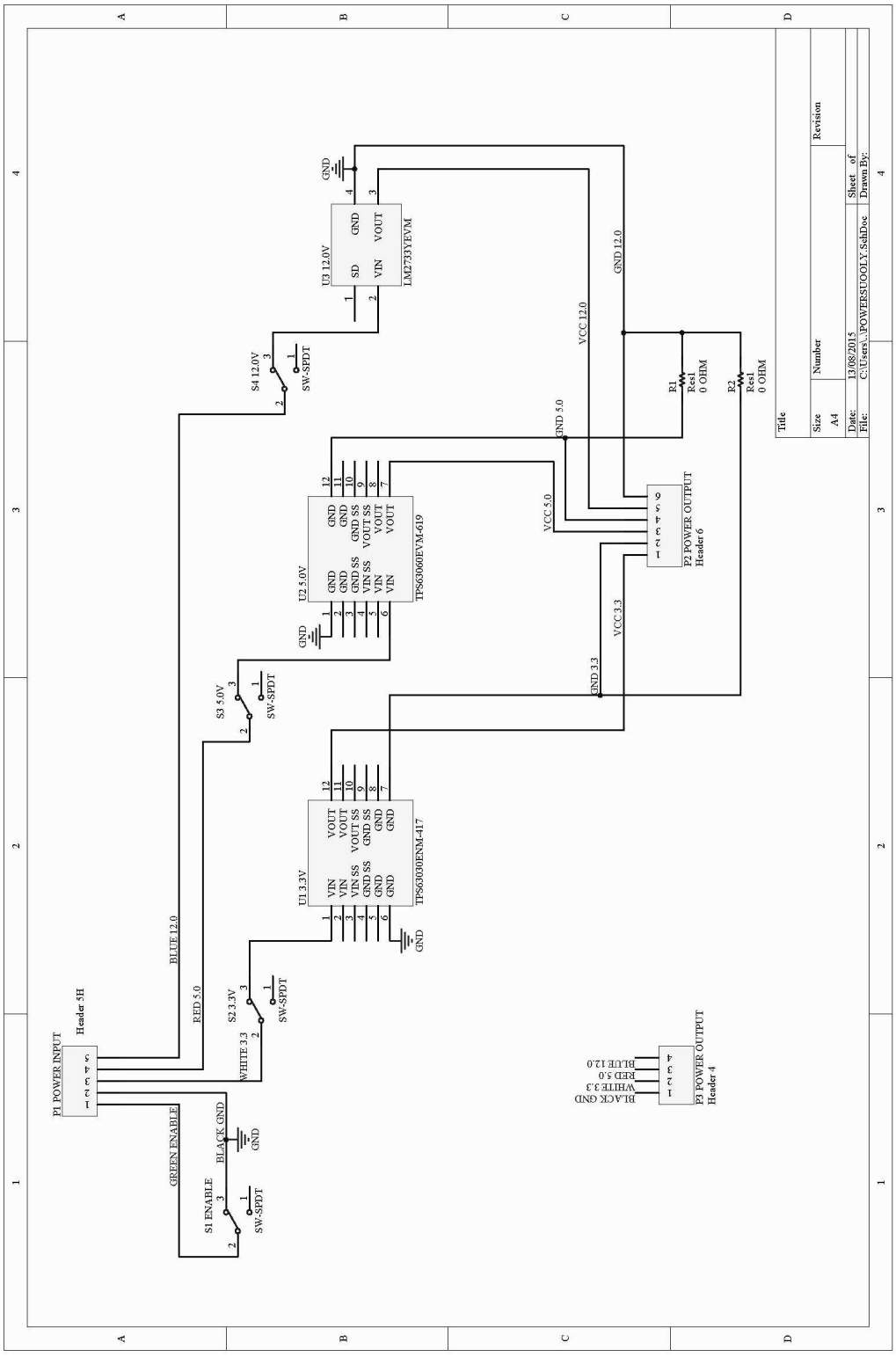

Fig. B.1 Sketch of the power supply board.

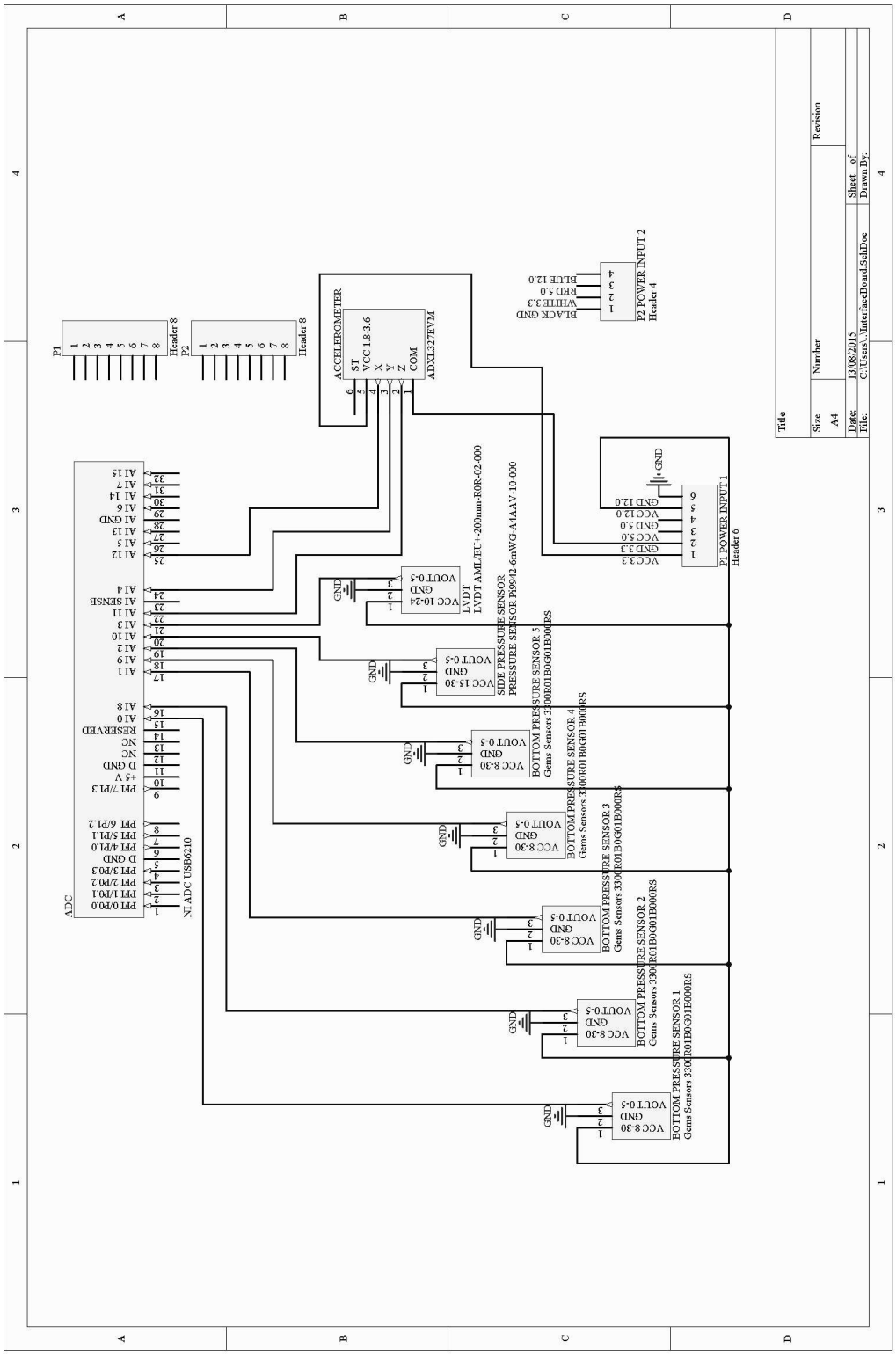

Fig. B.2 Sketch of the interface board.

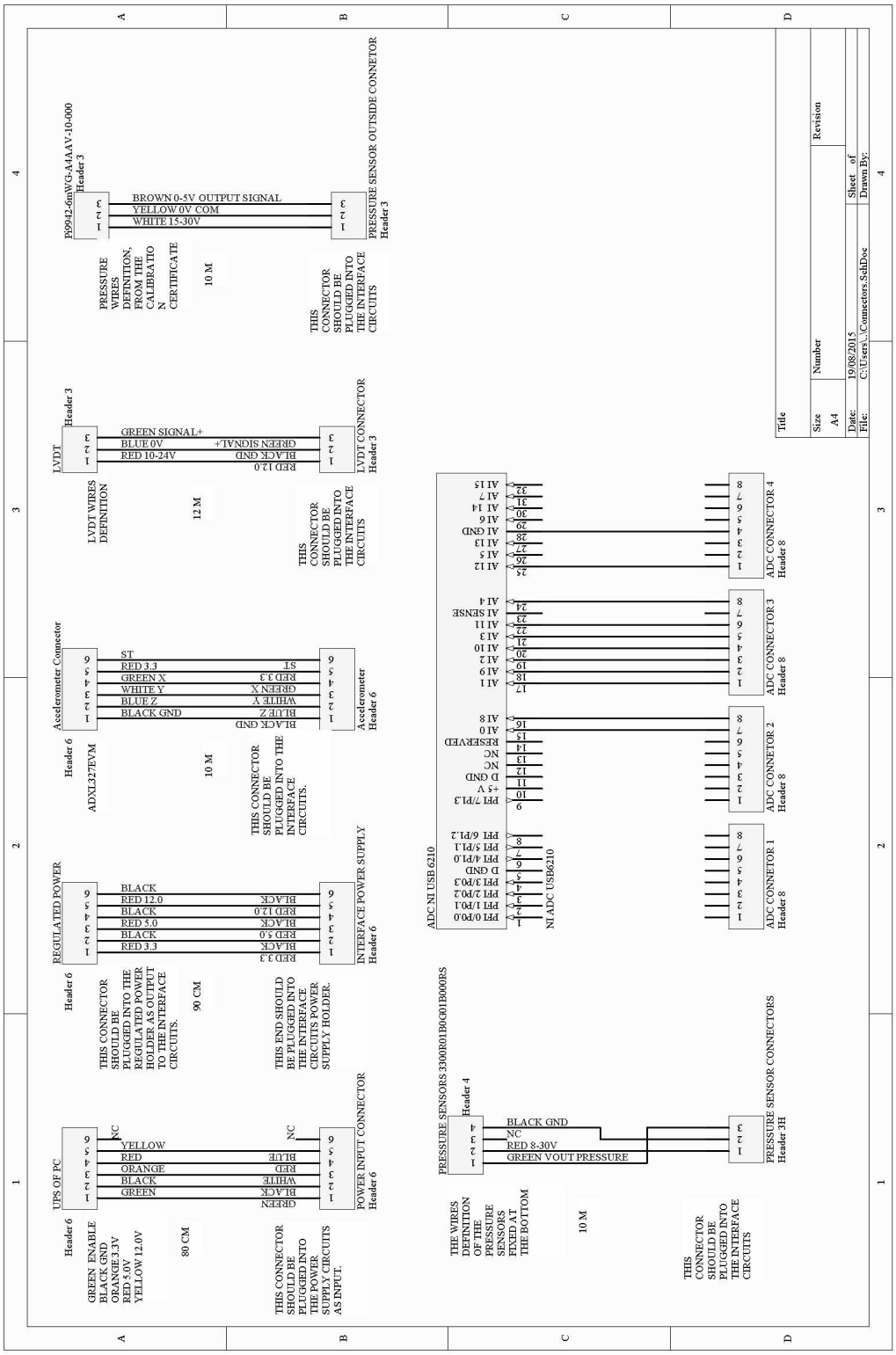

Fig. B.3 Sketch of the connectors.

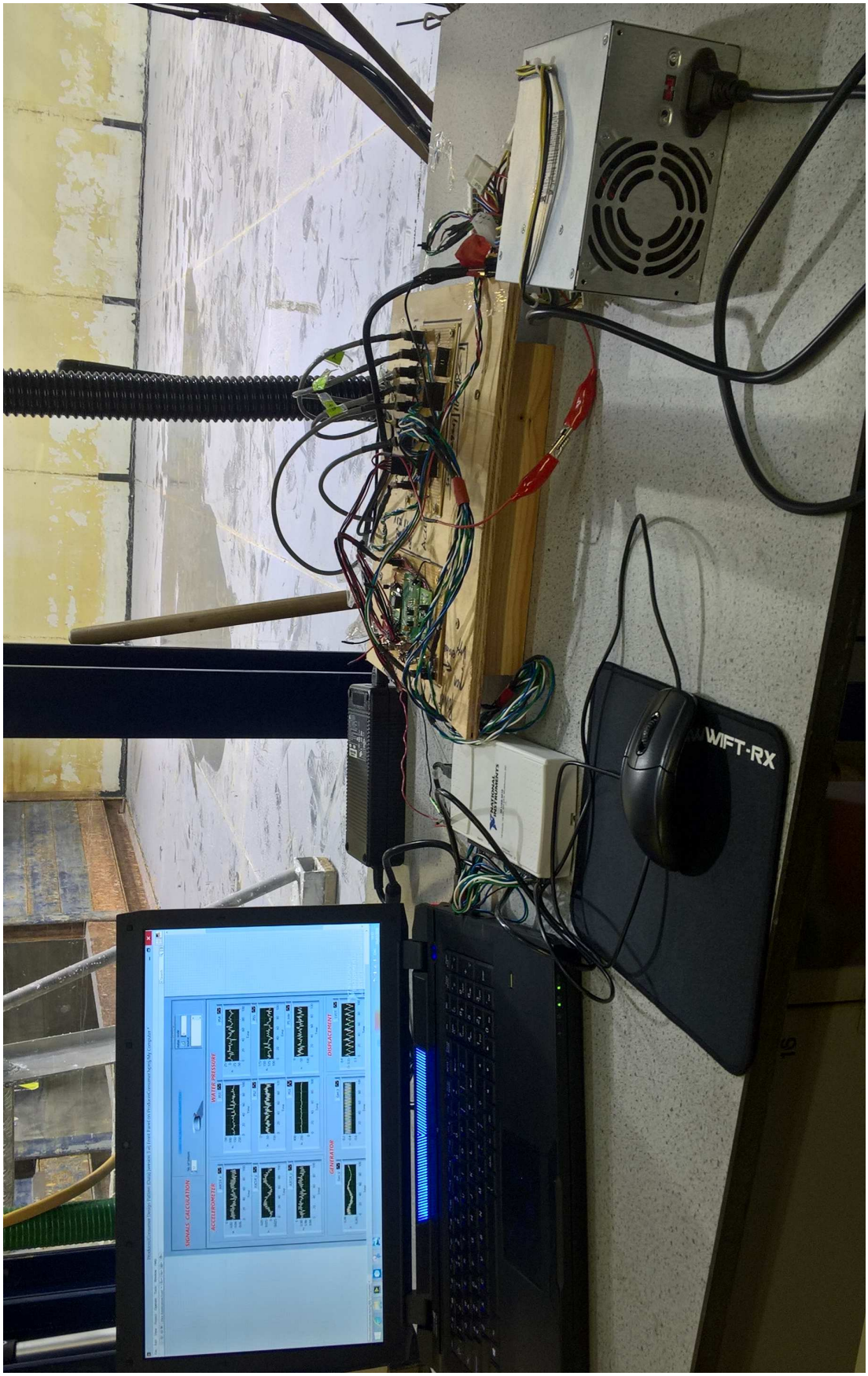

Fig. B.4 Connection of the sensing system.

Appendix C

Material properties for TPMLG design

The B-H curve of the NdFeB35 is downloaded from https://www.hkcm.de/tesla/?l= on 13^{th} May, 2017, shown as Fig. C.1.

The B-H curve of the B50A470 is downloaded from https://www.baosteel.com on 13^{th} May, 2017, shown as Fig. C.1.

The AWG wire standard is downloaded from https://www.solaris-shop.com on 13^{th} May, 2017, shown as Fig. C.3.

BH-diagram (de-magnetisation curve)

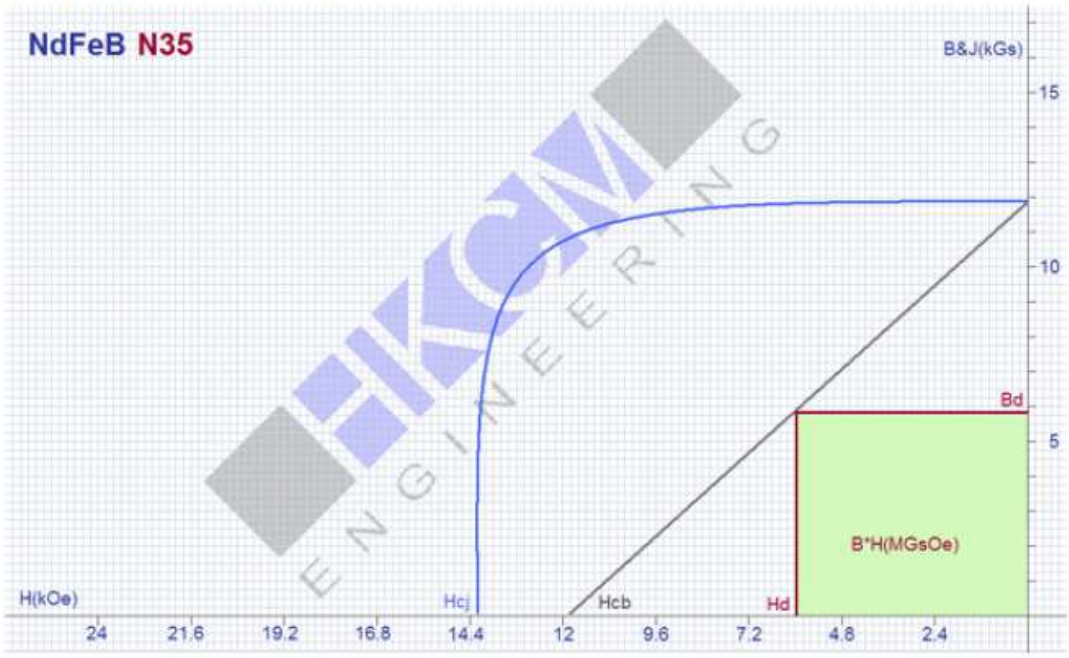

ENERGY PRODUCT = Hd*Bd = 35 Mega Gauss * Oersted (MGO)

Grade	N35	
Residual Induction Br	11.7-12.2 (1170-1220)	KG (mT)
Coercive Force Hcb	10.9 (868)	kOe(KA/m)
Intrinsic Coercive Force Hcj	12.0 (955)	kOe(KA/m)
Energy Product BHmax	33-36 (263-287)	MGO(KJ/m3)
Max. Operating Temp.	80	°C

Fig. C.1 B-H curve of the NdFeB35 material.

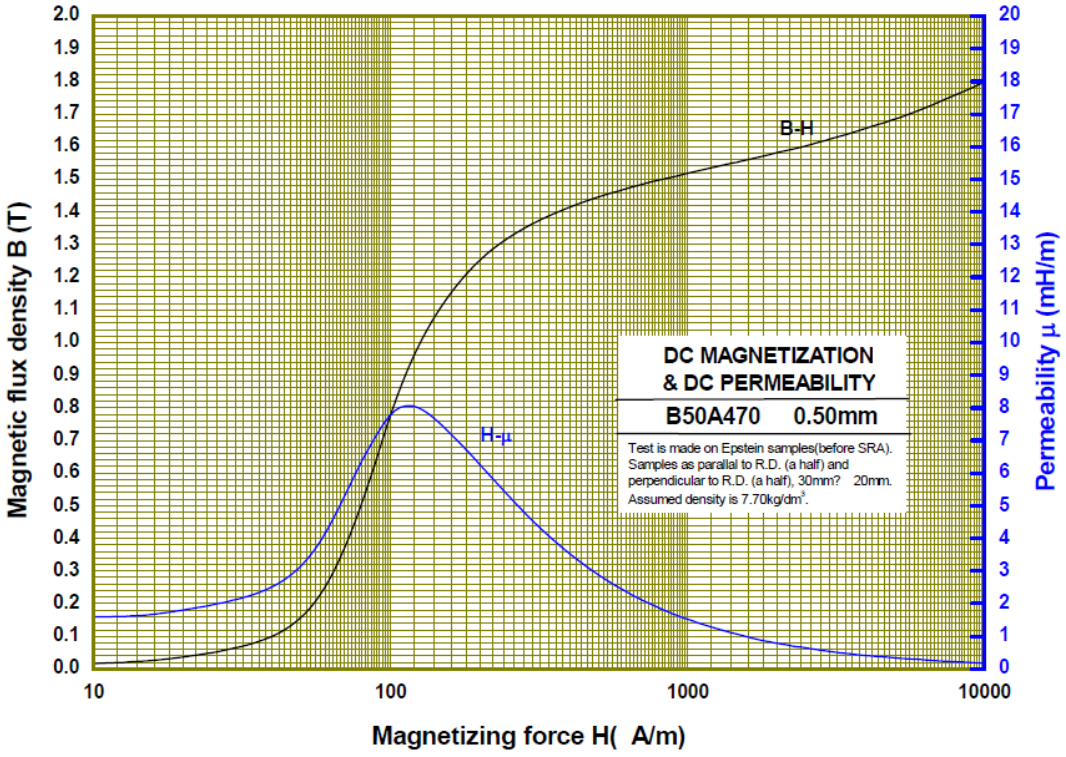

Fig. C.2 B-H curve of the B50A470 material.

AWG	Diameter [inches]	Diameter [mm]	Area [mm^2]	Resistance [Ohms / 1000 ft]	Resistance [Ohms / km]	Max Current [Amperes]	Max Frequency for 100% skin depth
0000 (4/0)	0.46	11.684	107	0.049	0.16072	302	125 Hz
000 (3/0)	0.4096	10.40384	85	0.0618	0.202704	239	160 Hz
00 (2/0)	0.3648	9.26592	67.4	0.0779	0.255512	190	200 Hz
0 (1/0)	0.3249	8.25246	53.5	0.0983	0.322424	150	250 Hz
1	0.2893	7.34822	42.4	0.1239	0.406392	119	325 Hz
2	0.2576	6.54304	33.6	0.1563	0.512664	94	410 Hz
3	0.2294	5.82676	26.7	0.197	0.64616	75	500 Hz
4	0.2043	5.18922	21.2	0.2485	0.81508	60	650 Hz
5	0.1819	4.62026	16.8	0.3133	1.027624	47	810 Hz
6	0.162	4.1148	13.3	0.3951	1.295928	37	1100 Hz
7	0.1443	3.66522	10.5	0.4982	1.634096	30	1300 Hz
8	0.1285	3.2639	8.37	0.6282	2.060496	24	1650 Hz
9	0.1144	2.90576	6.63	0.7921	2.598088	19	2050 Hz
10	0.1019	2.58826	5.26	0.9989	3.276392	15	2600 Hz
11	0.0907	2.30378	4.17	1.26	4.1328	12	3200 Hz
12	0.0808	2.05232	3.31	1.588	5.20864	9.3	4150 Hz
13	0.072	1.8288	2.62	2.003	6.56984	7.4	5300 Hz
14	0.0641	1.62814	2.08	2.525	8.282	5.9	6700 Hz
15	0.0571	1.45034	1.65	3.184	10.44352	4.7	8250 Hz
16	0.0508	1.29032	1.31	4.016	13.17248	3.7	11 k Hz
17	0.0453	1.15062	1.04	5.064	16.60992	2.9	13 k Hz
18	0.0403	1.02362	0.823	6.385	20.9428	2.3	17 kHz
19	0.0359	0.91186	0.653	8.051	26.40728	1.8	21 kHz
20	0.032	0.8128	0.518	10.15	33.292	1.5	27 kHz
21	0.0285	0.7239	0.41	12.8	41.984	1.2	33 kHz
22	0.0254	0.64516	0.326	16.14	52.9392	0.92	42 kHz
23	0.0226	0.57404	0.258	20.36	66.7808	0.729	53 kHz
24	0.0201	0.51054	0.205	25.67	84.1976	0.577	68 kHz
25	0.0179	0.45466	0.162	32.37	106.1736	0.457	85 kHz
26	0.0159	0.40386	0.129	40.81	133.8568	0.361	107 kHz
27	0.0142	0.36068	0.102	51.47	168.8216	0.288	130 kHz

Fig. C.3 AWG wire electro-mechanical standard.